



Universidade de Aveiro

Departamento de Física



Universidade do Porto

Faculdade de Ciências

2012

**Miguel Rodrigues
Zilhão Nogueira**

New frontiers in Numerical Relativity

arXiv:1301.1509v1 [gr-qc] 8 Jan 2013



Universidade de Aveiro

Departamento de Física

Universidade do Porto

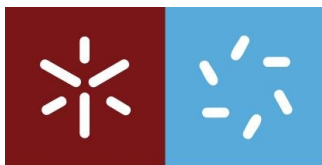
Faculdade de Ciências

2012

**Miguel Rodrigues
Zilhão Nogueira**

New frontiers in Numerical Relativity

Dissertação apresentada ao Programa Doutoral MAP-fis para cumprimento dos requisitos necessários à obtenção do grau de Doutor em Física, realizada sob a orientação científica de Carlos Herdeiro, Professor do Departamento de Física da Universidade de Aveiro, e co-orientação de Vitor Cardoso, Professor do Instituto Superior Técnico.



Universidade do Minho
Escola de Ciências

Setembro de 2012

Agradecimentos

For long you live and high you fly
And smiles you'll give and tears you'll cry
And all you touch and all you see
Is all your life will ever be

Pink Floyd
Breathe

Estes últimos quatro anos foram extraordinariamente enriquecedores para mim e tenho, felizmente, várias razões para estar grato por esta jornada que agora finda. Começo por deixar aqui um agradecimento aos meus amigos e orientadores Carlos e Vitor, com quem muito aprendi e com quem é um prazer trabalhar. O ritmo de trabalho e entusiasmo de ambos por Física, e Ciência em geral, são para mim fontes de inspiração. O Carlos merece ainda especial destaque uma vez que, entre Mecânica Quântica e Relatividade Geral, com ele aprendi as bases da Física moderna. Só tenho pena de esta pequena nota não reflectir todo o meu reconhecimento a ambos.

O trabalho que tenho vindo a desenvolver, e que esta tese resume, resulta na sua maior parte de trabalho feito em colaboração também com o Uli, a Helvi, o Leonardo e o Andrea, a quem queria deixar também o meu reconhecimento. Não poderia ter escolhido um melhor grupo de trabalho.

Durante os últimos quatro anos tive a felicidade de poder passar períodos de tempo a visitar outros grupos e instituições, o que muito enriqueceu este trabalho. Gostaria em particular de agradecer ao Vitor e ao pessoal do CENTRA por ter sido sempre bem acolhido nas minhas várias idas ao Instituto Superior Técnico; ao Emanuele, ao Marco, e ao Departamento de Física e Astronomia da Universidade do Mississippi pela hospitalidade durante a minha visita; ao Uli, Carlos e grupo do CSIC-IEEC pelo período que com eles estive em Barcelona; ao Luis e ao Perimeter Institute for Theoretical Physics pela óptima experiência que foram os quatro meses que lá passei; e por último, queria também agradecer ao Crispino e ao grupo em Belém do Pará pelas duas magníficas semanas em que nos receberam na Amazónia, mesmo na recta final deste trabalho.

Sendo o conteúdo desta tese um resumo de trabalho feito nos últimos quatro anos, a realidade é que esta acaba por ser o culminar de todo o meu processo educativo formal—um percurso escolar iniciado há vinte anos na Escola Primária de Lavadores—que tem aqui um ponto final,

e para o qual várias pessoas foram importantes. Assim, deixo aqui também uma palavra de reconhecimento a quem neste percurso me acompanhou, com destaque para os meus colegas e professores na Escola Secundária Inês de Castro. Gostaria em particular de mencionar os meus colegas de turma, o Patrício, o Norberto, o Ricardo, a Annie, a Mariana, e especialmente a Joana. Da interacção com todos eles resulta a pessoa que hoje sou, e estou-lhes por isso grato.

A minha formação em Física começa depois no Departamento de Física da Faculdade de Ciências da Universidade do Porto, onde passei a maior parte do meu percurso escolar, e considero ter tido muito boa formação. Fica então aqui o meu obrigado aos meus professores e, em especial, aos meus colegas de curso, Mariana, Joana, Raul, Lino, Coelho, João Nuno, e com destaque particular para o Carlos—tanto por tudo o que fomos aprendendo a estudar para os exames durante a licenciatura, como pelas conversas que fomos conseguindo manter nestes últimos anos.

A maior parte deste trabalho foi efectuado no Centro de Física do Porto (CFP), onde tive sempre boas condições e ambiente para trabalhar. Agradeço a todos os elementos do Centro, e destaco em particular o João Nuno, meu colega de gabinete, e o Luís Filipe, tanto pela colaboração num outro projecto, como por nunca haver um momento aborrecido na sua companhia.

O meu obrigado também ao Departamento de Física da Universidade de Aveiro onde também nada me faltou. À Carmen, ao Marco e ao Flávio agradeço o bom ambiente que sempre lá temos.

A temporada que passei em Waterloo tornou-se muito mais agradável na companhia dos amigos que lá fiz, com as nossas longas discussões ao jantar. Fica aqui então o meu obrigado ao Federico, ao Francesco, ao João, ao Jon, ao Mehdi, ao Siavash, ao Farbod, ao Anton, e especialmente à Yasaman.

Aos portugueses que pagam os seus impostos e à Fundação para a Ciência e a Tecnologia (FCT) agradeço o apoio financeiro para todo este trabalho, através da bolsa SFRH/BD/43558/2008 com co-financiamento do POPH/FSE.

Nem só de ciência vive um aluno de doutoramento. Assim, e apesar de não ter frequentado aulas durante estes quatro anos, não posso deixar de agradecer ao Mota, ao Cesário, ao Paulo, e ao resto do pessoal da Escola de Música de Canidelo. Lá tive a minha formação em música—que foi extremamente importante para mim—formação essa que me acompanha e sempre acompanhará. Fica também uma palavra para os meus companheiros da Associação Porto Céltico, com quem nunca nos aborrecemos.

Para último deixo a minha gratidão à minha família, que é a minha constante do movimento: à Nair—que faz parte de mim; aos meus pais, Adriano e Alexandra—que sempre me apoiaram; aos meus irmãos, Nuno e Luís—que nunca mudem; aos meus avós, Manuel, Aurora, Domingos e em especial à Alice—que foi a minha primeira professora; e à Rosa. Nada que eu possa aqui escrever alguma vez faria justiça à importância que estas pessoas tiveram neste meu percurso, pelo que posso apenas terminar dedicando-lhes este trabalho.

Abstract

The first attempts at solving a binary black hole spacetime date back to the 1960s, with the pioneering works of Hahn and Lindquist. In spite of all the computational advances and enormous efforts by several groups, the first stable, long-term evolution of the orbit and merger of two black holes was only accomplished over 40 years later, in 2005. Since then, the field of Numerical Relativity has matured, and been extensively used to explore and uncover a plethora of physical phenomena in various scenarios.

In this thesis, we take this field to new frontiers by exploring its extensions to higher dimensions, non-asymptotically flat spacetimes and Einstein-Maxwell theory. We start by reviewing the usual formalism and tools, including the “3+1” decomposition, initial data construction, the BSSN evolution scheme and standard wave extraction procedures. We then present a dimensional reduction procedure that allows one to use existing numerical codes (with minor adaptations) to evolve higher-dimensional systems with enough symmetry, and show corresponding results obtained for five-dimensional head-on collisions of black holes. Finally, we show evolutions of black holes in non-asymptotically flat spacetimes, and in Einstein-Maxwell theory.

Resumo

As primeiras tentativas de evolução da geometria de um sistema binário de buracos negros datam da década de 60, com o trabalho pioneiro de Hahn e Lindquist. Apesar de todos os avanços computacionais e enormes esforços por parte de vários grupos, as primeiras evoluções estáveis da órbita e coalescência de dois buracos negros foram conseguidas apenas 40 anos depois, em 2005. Desde então, o campo da Relatividade Numérica amadureceu, e tem sido usado extensivamente para explorar e descobrir fenómenos físicos em vários cenários.

Nesta tese, levamos este campo a novas fronteiras e exploramos extensões a dimensões extra, espaços não-assimptoticamente planos e teoria de Einstein-Maxwell. Começamos por rever o formalismo e ferramentas usuais, incluindo a decomposição “3+1”, construção de dados iniciais, o esquema de evolução BSSN e os procedimentos padrão de extracção de radiação. Seguidamente apresentamos um procedimento de redução dimensional que permite o uso de códigos numéricos existentes (com adaptações menores) para evoluir sistemas em dimensões mais elevadas com simetria suficiente, apresentando ainda os correspondentes resultados obtidos para colisões frontais de buracos negros em cinco dimensões. Finalmente, mostramos resultados em espaços não-assimptoticamente planos e teoria de Einstein-Maxwell.

Contents

1	Introduction	14
1.1	Motivation and historical background	14
1.2	The new frontiers	19
1.2.1	Higher-dimensional gravity	19
1.2.2	Non-asymptotically flat geometries	20
1.2.3	Einstein-Maxwell	21
1.3	Structure	22
1.4	Preliminaries	22
2	$(D - 1) + 1$ decomposition	25
2.1	Hypersurfaces	25
2.1.1	Definition	25
2.1.2	Normal vector	26
2.1.3	Induced metric	26
2.1.4	Orthogonal projector	26
2.1.5	Intrinsic curvature	27
2.1.6	Extrinsic curvature	28
2.2	Foliations	28
2.2.1	The lapse function	28
2.2.2	Normal evolution vector	29
2.2.3	Eulerian observers	29
2.2.4	Evolution of $\gamma_{\alpha\beta}$	29
2.3	Gauss, Codazzi and Ricci equations	30

2.3.1	Gauss equation	30
2.3.2	Codazzi equation	30
2.3.3	Ricci equation	30
2.4	Einstein equations	31
2.4.1	Decomposition of the stress-energy tensor	31
2.4.2	Projection of the Einstein equations	31
2.5	Choice of coordinates	32
2.6	The PDE system	33
3	Initial data	35
3.1	Conformal decomposition	36
3.1.1	Conformal transformations	36
3.2	Initial data for vacuum spacetimes	37
3.2.1	Brill-Lindquist initial data	38
3.2.2	Bowen-York initial data	40
3.3	Final remarks	44
4	Numerical implementation	45
4.1	BSSN formulation	46
4.2	Gauge conditions	48
4.2.1	1+log slicing	49
4.2.2	Gamma driver	49
4.3	Numerical code	50
4.A	<i>D</i> -dimensional BSSN equations	51
5	Wave extraction and horizon finding	52
5.1	Wave extraction	52
5.1.1	Newman-Penrose formalism	54
5.1.2	Kodama-Ishibashi	57
5.2	Horizon finding	59
6	Higher-dimensional numerical relativity	61

6.1	Dimensional reduction	62
6.1.1	General formalism	62
6.1.2	Examples	64
6.2	Dimensional reduction on a $(D - 4)$ -sphere and 3+1 split	66
6.2.1	BSSN formulation	70
6.3	Higher-dimensional initial data	70
6.3.1	Coordinate transformation	71
6.3.2	Four dimensional initial data for a general D head-on collision	72
6.3.3	Single puncture with linear momentum	73
6.3.4	Two punctures with linear momentum	77
6.4	Numerical evolutions	81
6.4.1	Code tests	82
6.4.2	Head-on collisions	84
6.4.3	Head-on collision from rest in $D = 5$	86
6.5	Discussion	91
6.A	Ricci tensor	92
6.B	Equations of motion: Einstein frame	95
7	Non-asymptotically flat spacetimes	97
7.1	de Sitter	97
7.1.1	Evolution equations	98
7.1.2	Schwarzschild-de Sitter	98
7.1.3	Numerical Setup	100
7.1.4	Numerical Results	101
7.1.5	Final Remarks	105
7.2	Black holes in a box	106
7.2.1	Numerical setup	106
7.2.2	Gravitational wave signal	108
7.2.3	Interaction of the wave pulse with the remnant black hole	108
7.2.4	Final remarks	109
7.3	Black holes in cylinders	110

7.3.1	Setup	110
7.3.2	Initial data	111
7.3.3	Results	112
7.3.4	Final remarks	113
8	Einstein-Maxwell	114
8.1	Evolution equations	115
8.1.1	3+1 decomposition	116
8.1.2	Initial data	117
8.2	Wave Extraction	118
8.3	Analytic predictions	118
8.4	Numerical Results	121
8.4.1	Code tests	122
8.4.2	Collisions of two black holes: the “static” components and infall time	123
8.4.3	Waveforms: infall, merger and ringdown	124
8.4.4	Radiated energy and fluxes	127
8.5	Conclusions	129
9	Final remarks	131
A	List of publications	133
	Bibliography	135

List of Tables

6.1	ADM mass obtained with equation (6.3.47)	78
6.2	Grid structure and initial parameters of the head-on collisions starting from rest in $D = 5$	87
8.1	Grid structure, coordinate distance, proper horizon-to-horizon distance, charge, gravitational and electromagnetic radiated energy for our set of simulations .	121
8.2	Comparison of the ringdown frequencies	126

List of Figures

6.1	D -dimensional representation of two types of black hole collisions	68
6.2	Convergence plot for the $b/r_S = 30.185$, $P/r_S^{D-3} = \pm 0.80$ cases.	79
6.3	u function for $D = 4, \dots, 7$ plotted along the z -axis	80
6.4	Violation of the Hamiltonian constraint along the z -axis	81
6.5	$D = 5$ Tangherlini black hole, geodesic slicing	83
6.6	$D = 5$ single black hole, constraint violation	83
6.7	$D = 5$ black hole collision from rest	84
6.8	Estimates for the time it takes for two equal-mass black holes to collide in $D = 5$	88
6.9	The $l = 2$ and $l = 4$ mode of the KI function	89
6.10	$l = 2$ components of the KI function as generated by a head-on collision of black holes	90
6.11	Energy flux in the $l = 2$ component of the KI wave function $\Phi_{,t}$	91
7.1	Conformal factor for a single black hole evolution with $H = 0.8H_{\text{crit}}$	101
7.2	Critical coordinate distance for small mass binaries	102
7.3	Hamiltonian constraint violation	103
7.4	Proper distance between the black hole horizons as a function of time	104
7.5	Snapshots at different times of a simulation with $H = 1.05H_{\text{crit}}$	105
7.6	Illustration of a (Lego-)spherical outer boundary.	107
7.7	Real part of the $l = m = 2$ mode of $rM\Psi_0$ and $rM\Psi_4$	108
7.8	Time evolution of the (relative) mass of the black hole	109
7.9	Illustration of the coordinate system for the Minkowski space-time $\mathbb{M}^{1,3} \times S^1$	110
7.10	Illustration of the correspondence between real space and covering space for a single black hole and a situation of head on collision	111

7.11	Hamiltonian constraint along the x and z axis, for the $L/r_S = 32$ case. . . .	112
7.12	Puncture z coordinate as function of time for the outgoing and $L/r_S = 16$ cases.	113
8.1	Numerical profiles for γ_{zz} and E^z obtained in geodesic slicing	122
8.2	Convergence analysis for simulation d08q05	123
8.3	Monopole ϕ_1^{00} and quadrupole ϕ_1^{20} of the radial part of the electromagnetic field Φ_1	124
8.4	Time for apparent horizon formation	125
8.5	Real part of the $(2, 0)$ mode of Ψ_4 and Φ_2	125
8.6	Power spectrum for the gravitational and electromagnetic quadrupole	127
8.7	Radiated fluxes	128
8.8	Energy radiated in the gravitational and electromagnetic quadrupole	128

Chapter 1

Introduction

Why you care about small things? World very simple place. World only have two things: things you can eat and things you no can eat.

Quina

FINAL FANTASY IX

1.1 Motivation and historical background

Formulated by Einstein in 1915 [1, 2, 3], general relativity is one of the most beautiful theories ever discovered. Its very elegance, however, can also be a disadvantage. We are able to do purely analytical calculations—sometimes using just pen and paper—in highly symmetrical ideal examples where exact solutions are known, or limits where gravity is weak. Alas, Nature is not that simple.

To attack more complicated problems—such as those with strong and dynamical gravitational fields—one will eventually need to perform numerical computations. The quintessential example is the two-body problem. With well known solutions in terms of conics in Newtonian gravity, the equivalent problem in general relativity—the evolution of a black hole binary—posses no (known) closed-form solution. Perturbative analytical techniques do exist and some are very well suited to study certain stages of this problem. In particular, the inspiral phase (before the merger) is well modelled by post-Newtonian methods; the ringdown phase (after merger) can be described by perturbative methods using the *quasi-normal modes* of the final black hole. Full numerical simulations are required, however, to evolve the system during the merger.

Much of the motivation to understand the nature of such systems and the corresponding energy emitted via gravitational radiation originally came from the gravitational wave astronomy field. A first generation of highly sensitive gravitational waves detectors—LIGO [4],

Virgo [5], GEO [6] and TAMA [7]—have been operational and a second generation of even more sensitive detectors is under construction. These detectors may allow us to study signals produced from strong-field systems, which carry the specific signature of the system that produced them. The analysis of these signals may then provide us with a new window to the universe. For that, however, we rely on source modelling: templates of theoretical waveforms from likely sources are needed if one wishes to reconstruct the signal.

Numerical relativity can be regarded as a tool to study spacetimes that cannot be studied by analytical means. It dates back to the mid 1960s with Hahn and Lindquist’s attempts of numerically evolving Einstein’s field equations for a binary black hole spacetime [8]. Their computer power was very limited, however, and not much physics could be extracted from the simulation. More reliable simulations were only performed in the late 1970s by Smarr [9] and Eppley [10], which again attempted the head-on collision of two black holes. Though almost a decade after Hahn and Lindquist, the available computer power was still only enough to evolve low resolution simulations.

With the development of faster computers and the extra motivation of returning to the two-body problem coming from LIGO, the 1990s finally witnessed the simulation of a head-on collision of two black holes [11, 12] as well as the study of more complex systems. To name just a few: simulations of rapidly rotating neutron stars [13], the formation of a toroidal event horizon in the collapse of a system containing a toroidal distribution of particles [14, 15] and one of the most influential results, gravitational collapse and its relation with critical phenomena [16]. For a more comprehensive overview see, for example, [17].

In spite of all these successes, the real breakthrough came only in 2005 with the first simulations of stable, long-term evolutions of the inspiral and merger of two black holes [18, 19, 20]. For an overview of the two-body problem in general relativity see [21].

Since then, numerical codes have considerably improved and much progress has been made. In particular, we have witnessed numerical evolutions of (see e.g. [22] for a thorough overview of some recent results):

- binary black hole mergers lasting for 15 orbits before merger [23, 24]. The corresponding waveforms, which include the infall, non-linear merger and ringdown phase, have been used in comparisons with post-Newtonian results.
- black hole binaries with mass ratios up to 1 : 100 [25, 26]. Waveforms for high mass ratios are essential, since they are expected to be the most common, astrophysically. Computationally, however, they are much more demanding than comparable mass cases.
- rotating black holes with near extremal spin [27, 28].
- zoom-whirl orbits—characterised by black hole trajectories that alternate between a whirling quasi-circular motion and a highly eccentric quasi-elliptical zooming out [29, 30].
- so called “superkick” configurations—equal mass black holes with (initially) opposite

spin vectors lying in the orbital plane—where the post-merger recoil velocity can reach up to ~ 4000 km/s [31, 32]. Recently [33], this effect was combined with the “hangup” configuration [34]—where the black holes have spin aligned with the orbital angular momentum—to predict maximum recoils up to ~ 5000 km/s. Given that such velocities are enough to eject a black hole from the centre of a galaxy [35], these results could have important consequences for astronomy (such as in structure formation), see e.g. [36, 37, 38, 39].

- high velocity collisions of black holes—head-on collisions up to $0.94c$ [40], where the radiated energy was found to be around 14% when extrapolating the relative velocity between the black holes to c ; as well as non-head-on collisions [41, 42], where the impact parameter for black hole merger was determined in the limit where the relative velocity approaches c .

As we can observe from these previous examples, numerical relativity has now reached a state of maturity and, at least in the four-dimensional asymptotically flat vacuum case, is largely under control allowing us to evolve a large class of different configurations.

Motivation to study gravity in the dynamical/strong field regime is not restricted to the evolution of the two-body problem or variations thereof, and computation of the respective waveform. Indeed, incentive to study such systems also comes from fields other than gravity itself. In the following we mention some of these topics and briefly describe how numerical relativity can be expected to shed light on some outstanding issues.

Tests of cosmic censorship hypothesis

It has been known for some time from the Penrose-Hawking singularity theorems that, quite generically, solutions of Einstein’s field equations with physically reasonable matter content can develop singularities [43]. If such singularities are visible to the rest of spacetime (i.e., no horizon is covering them), predictability may break down. Originally formulated by Penrose in 1969 [44], what is known as the *weak cosmic censorship conjecture* roughly states that, generically, singularities of gravitational collapse are covered by an event horizon and therefore have no causal contact with distant observers.

In the absence of a generic proof*, one can try and put the conjecture to the test in specific configurations. The ability to perform full blown non-linear numerical simulations in arbitrary spacetimes could here prove invaluable.

With such simulations, the conjecture has been shown to hold under extremely violent events—the ultra-relativistic collision of black holes [40]. In higher-dimensional gravity, it was shown by Lehner and Pretorius that cosmic censorship does not seem to hold generically, even in vacuum [45]. Specifically, it was shown that five dimensional black strings (solutions of five dimensional vacuum gravity, known to be unstable [46]) display, when perturbed, a self-similar behaviour that ultimately gives rise to naked singularities

*Indeed, the conjecture has not even been stated in a rigorous way—as often happens, that is part of the task.

in rather generic conditions. Also in higher dimensions, results by Okawa et al. [47] seem to indicate that in a high-velocity scattering of five-dimensional black holes, curvature radius shorter than the Planck length can be observed (i.e., no horizon is covering this region). This could be regarded as an effective singularity in classical gravity.

Stability of (higher-dimensional) black hole solutions

Higher dimensional gravity has a much richer diversity of black object solutions than its four dimensional counterpart. Spherical topology is not the only allowed topology for objects with a horizon and one can also have, e.g., black rings (with a donut-like topology) [48, 49] and even regular solutions with disconnected horizons, such as the “black Saturn” [50], the “black di-ring” [51] or the “bicycling black rings” [52].

The study of these objects is relevant for a number of reasons. Other than the obvious intrinsic value that such studies carry and the possibly interesting mathematical properties that some of these objects may have, the understanding of these solutions can also be helpful for: (i) quantum gravity—the calculations of black hole entropy within string theory were first performed in five dimensional spacetimes, and only afterwards extended to four dimensions; (ii) gauge/gravity correspondence, which maps properties of D -dimensional black holes to strongly coupled field theories in $D - 1$ dimensions; (iii) large extra dimensions scenarios, suggesting that (microscopic) higher-dimensional black objects could be formed in particle collisions with centre of mass energy \gtrsim TeV (such as at the LHC). See the review article [53] for more details and further motivation.

The stability of these higher-dimensional black objects is now starting to be explored. It had been conjectured that for $D \geq 6$ ultra-spinning Myers-Perry black holes will be unstable [54], and this instability has been confirmed by an analysis of linearised axi-symmetric perturbations in $D = 7, 8, 9$ [55].

Clearly, the study of the non-linear development of these instabilities and determination of the respective endpoint requires numerical methods. Such studies have been recently presented for a non axi-symmetric perturbation in $D = 5$ [56] and $D = 6, 7, 8$ [57], where it was found that the single spinning Myers-Perry black hole is unstable, for sufficiently large rotation parameter.

AdS/CFT correspondence

In 1997–98, a powerful tool known as the AdS/CFT correspondence (or the gauge/gravity duality, or even, more generically, as *holography*) was introduced [58]. This holographic correspondence (if true in general) is extremely powerful since it maps the dynamics of a non-perturbative, strongly coupled regime of certain gauge theories in D dimensions to $(D + 1)$ -dimensional classical gravity. This means that, for such gauge theories, we can map strongly coupled quantum field theory dynamics to systems of partial differential equations, which can in principle be solved (numerically, if needed).

In particular, high energy collisions of black holes are said to have a dual description in terms of high energy collisions with balls of de-confined plasma surrounded by a confining phase. These are the type of events that may have direct observational consequences for the experiments at Brookhaven’s Relativistic Heavy Ion Collider (RHIC) [59, 60].

Numerical relativity in anti-de Sitter (AdS) is notoriously difficult, and therefore progress has been slow in applying its techniques to the aforementioned problems. Nevertheless, some exciting results have been recently put forth [61, 62, 63].

TeV-scale gravity scenarios

As first pointed out by 't Hooft [64], if two point particles collide at energies above the Planck energy, it is expected that gravity should dominate the interaction and thus, quite remarkably, the process should be well described by general relativity.

Thorne's *Hoop Conjecture* [65] further tells us that if one traps a given amount of Energy E in a region of space such that a circular hoop with radius R encloses this matter *in all directions*, a black hole is formed if its Schwarzschild radius $R_S \equiv \left(\frac{16\pi GE}{(D-2)\mathcal{A}_{D-2}c^4} \right)^{\frac{1}{D-3}} > R$. This conjecture (or rather, the classical variant thereof) has recently gained more support with the work by Choptuik and Pretorius [66], where it was shown that collisions of boson stars *do* form black holes, for sufficiently high boost parameter.

If this conjecture does hold, it would imply that particle collisions could produce black holes [67, 68]. As argued above, the production of black holes at trans-Planckian collision energies (compared to the fundamental Planck scale) should be well described by using classical general relativity (see also [69] and references therein). Writing down the exact solution describing the collision of two ultra-relativistic particles in general relativity is not feasible, however, and approximations have to be used. One possible approximation (good for its simplicity) is to use black holes, and model the scattering of point particles by black hole collisions.

This gains further relevance in the context of the so-called TeV-gravity scenarios. Such models were proposed as a possible solution to the *hierarchy problem*, i.e., the relative weakness of gravity by about 40 orders of magnitude compared to the other fundamental interactions. It has been proposed that this can be resolved if one adopts the idea that the Standard Model is confined to a brane in a higher dimensional space, such that the extra dimensions are much larger than the four dimensional Planck scale (they may be large up to a sub-millimetre scale) [70, 71, 72]. In a different version of the model, the extra dimensions are infinite, but the metric has an exponential factor introducing a finite length scale [73, 74].

In such models, the fundamental Planck scale could be as low as 1 TeV. Thus, high energy colliders, such as the Large Hadron Collider (LHC), may directly probe strongly coupled gravitational physics [75, 76, 68, 67, 77, 78]. In fact, such tests may even be routinely available in the collisions of ultra-high energy cosmic rays with the Earth's atmosphere [79, 80, 81], or in astrophysical black hole environments [82, 83, 84] (for reviews see [85, 86, 69]).

Numerical simulations of high energy black hole collisions in higher dimensional space-times, then, could give an accurate estimate of the fractions of the collision energy and angular momentum that are lost in the higher-dimensional space by emission of

gravitational waves; such information would be extremely important to improve the modelling of microscopic black hole production, and of the ensuing evaporation phase, which might be observed during LHC collisions.

The challenge is then to use the classical framework to determine the cross section for production and, for each initial setup, the fractions of the collision energy and angular momentum that are lost in the higher dimensional space by emission of gravitational waves. This information will be of paramount importance to improve the modelling of microscopic black hole production in event generators such as TRUENOIR [67], CHARYBDIS2 [87], CATFISH [88] or BLACKMAX [89, 90]. The event generators will then provide a description of the corresponding evaporation phase, which might be observed during LHC collisions.

For a thorough review of these topics, challenges and how tools coming from numerical relativity can help see [91].

1.2 The new frontiers

With these motivations in mind, we propose in this thesis to extend current numerical relativity tools to new frontiers.

1.2.1 Higher-dimensional gravity

The first such frontier, in light of our discussion in the previous section, is higher-dimensional gravity. We start by emphasising that full blown $4 + 1$, $5 + 1$, etc. numerical simulations of Einstein’s field equations without symmetry are currently (and in the near future) not possible due to the heavy computational costs. We have thus developed a framework and a numerical code that can, in principle, be applied to different spacetime dimensions (with enough symmetry) with little adaptations. This is achieved by taking the D dimensional vacuum spacetime to have an isometry group fit to include a large class of interesting problems. If this isometry group is sufficiently large, it allows a dimensional reduction of the problem to $3+1$ dimensions, where our originally higher-dimensional problem now appears as (four dimensional) general relativity coupled to source terms. Thus, the different spacetime dimensions manifest themselves only in the different “matter” content of the four dimensional theory. An obvious advantage of this approach is that we can use existing numerical codes with small adaptations: taking a working four-dimensional code, the four dimensional equations need to be coupled to the appropriate source terms and some issues related to the chosen coordinates must be addressed. Incidentally, other issues possibly related with the choice of gauge conditions further complicate the problem.

We should here point out that alternative approaches have been proposed to evolve numerically Einstein’s equations in higher dimensions, as well as other codes tailored to study specific problems. In particular we note the previously mentioned pioneering works concerned with

the non-linear development of the Gregory-Laflamme instability [46] of cosmic strings [92, 45]; studies of gravitational collapse [93, 94]; static situations [95]; and the alternative approach, based on the *Cartoon method* [96], that has been developed and tested by Yoshino and Shibata [97, 57]. For a review of numerical relativity in higher-dimensions see also [98, 99].

1.2.2 Non-asymptotically flat geometries

Another frontier has to do with numerical evolutions in non-asymptotically flat spacetimes.

de Sitter

Going back to four dimensions, an obvious first choice of a non-asymptotically flat spacetime is *de Sitter*, the simplest model for an accelerating universe. de Sitter is a maximally symmetric solution of Einstein's equations with a positive cosmological constant, describing a Friedmann-Robertson-Walker (FRW) cosmology with a constant Hubble parameter. There is now a large body of observational evidence for a present cosmological acceleration well modelled by a positive cosmological constant Λ [100].

Cosmological dynamics should leave imprints in gravitational phenomena, such as gravitational radiation emitted in a black hole binary coalescence. Identifying such signatures can thus be phenomenologically relevant in view of ongoing efforts to directly detect gravitational radiation.

Studying the dynamics of black holes in asymptotically de Sitter spacetimes can also potentially teach us about more fundamental questions such as cosmic censorship, as in the following scenario. Consider two black holes of sufficiently large mass in a de Sitter spacetime. If, upon merger, the final black hole is too large to fit in its cosmological horizon the end state of such an evolution would be a naked singularity. This possibility begs for a time evolution of such a configuration, which we will show and discuss.

Black holes in a box

As argued above, having a framework to solve Einstein's equations in asymptotically Anti-de Sitter geometries would be of major help for studies of AdS/CFT duality, in particular in dynamical settings. This is no easy task, however, and a major reason for that is the "active role" played by the boundary of AdS spaces. This is easily visualised in the Penrose diagram of AdS, which has a timelike boundary. Null geodesics in AdS reach the boundary in a finite affine parameter, and one therefore often refers to an asymptotically AdS space as a "box", having in mind that AdS boundary conditions directly affect the bulk physics [101, 102, 103].

As a first step to model the role of the boundary in evolutions, we will here give an overview of the work reported in [104] where a toy model for AdS was considered. Therein, as we will explain, the cosmological constant is set to zero and mirror-like boundary conditions are imposed on a box containing the dynamical system, which mimics the global AdS geometry.

Inside this box, black hole binaries are evolved, producing an inspiralling merger. Such systems are very well tested in standard asymptotically flat spacetimes with purely outgoing boundary conditions, and differences to these cases can be clearly seen.

Black holes in cylinders

Again in the topic of higher-dimensional gravity, now in scenarios with compact extra dimensions, a natural question to ask is how the compactness of the extra dimensions changes the dynamics of such scenarios (as opposed to the asymptotically flat cases) and understanding the role of the compactness of the extra dimensions in the aforementioned TeV gravity scenarios.

There is considerable literature on Kaluza-Klein black holes and black holes on cylinders [105, 106, 107, 108], but, to the best of our knowledge, the full non-linear dynamics of black holes in such spacetimes remain unexplored.

In this spirit, using the formalism developed for higher-dimensional spacetimes, we have started exploring what happens when one of the directions is compactified.

1.2.3 Einstein-Maxwell

Finally, we have started exploring the electrovacuum Einstein-Maxwell system. We first note that while the dynamics of black holes interacting with electromagnetic fields and plasmas have been the subject of a number of numerical studies (e.g. [109, 110]), dynamics of charged (Reissner-Nordström) black holes have remained rather unexplored.

Studying the dynamics of charged black holes is relevant for a number of reasons. In the context of astrophysics, charged black holes may actually be of interest in realistic systems. First, a rotating black hole in an external magnetic field will accrete charged particles up to a given value, $Q = 2B_0J$ [111]. It is thus conceivable that astrophysical black holes could have some (albeit rather small) amount of electrical charge. It is then of interest to understand the role of this charge in the Blandford-Znajek mechanism [112], which has been suggested for extracting spin energy from the hole, or in a related mechanism capable of extracting energy from a moving black hole [110, 113] to power outflows from accretion disk-fed black holes. Also of interest is investigating the role of charge in post-merger recoil velocities of black hole binaries, and see if the recently predicted recoils of ~ 5000 km/s [33] could be exceeded.

Incentive to study such systems also comes from outside of astrophysics. In particular, as already mentioned above, it was argued by 't Hooft [64], that in trans-Planckian particle collisions, gravity should dominate the interaction and thus the process should be well described by general relativity—we can say that, for ultra high energy collisions, *matter does not matter* [66]. Calculations of shock wave collisions, however, seem to suggest that even though other interactions—say charge—may become irrelevant in the ultra-relativistic limit, the properties of the final black hole (and of the associated emission of gravitational radiation) will in fact depend on the amount of charge carried by the colliding particles [114, 115]. One then wonders whether the often repeated *matter does not matter* scenario is actually true.

Light can be shed in this issue by performing highly boosted collisions of charged black holes (analogous to the ones performed in vacuum [40, 41]) and comparing the results—in particular the profile of the corresponding waveform—against equivalent electrically neutral systems.

With these incentives, we will report on the first steps taken in the numerical evolution of Reissner-Nordström black holes, building on previous numerical evolutions of the Einstein-Maxwell system [116, 109, 117, 118].

1.3 Structure

The structure of this thesis is as follows. We start by reviewing, in chapter 2, standard differential geometry results, summarise the formalism of the “ $(D-1)+1$ ” decomposition* and conformal decomposition to write Einstein’s equations in a dynamical systems form. In chapter 3 we then review the construction of relevant initial data for the class of problems we will be interested on and discuss, in chapter 4, the numerical implementation of Einstein’s equations: first, we need to re-write the evolution equations in the so-called BSSN (Baumgarte, Shapiro, Shibata, Nakamura) form; we next discuss the gauge conditions and finish by giving a very brief overview of the numerical code we use for the simulations. In chapter 5 we review the usual procedures to extract the physical results from numerical simulations: wave extracting and horizon finding. These chapters consist mostly of review material found in the usual literature (e.g. [119, 120, 121]). Finally, in chapter 6, we introduce a dimensional reduction procedure that allows us to reduce higher-dimensional systems (with enough symmetry) to effective four-dimensional theories with source terms. This enables us to perform numerical evolutions of such higher-dimensional systems by adapting existing numerical codes. We also discuss the construction of initial data and present results. Chapter 7 is dedicated to evolutions in non-asymptotically flat spacetimes: we present the aforementioned collisions of black holes in asymptotically de Sitter spacetimes, black holes in a box and black holes in asymptotically cylindrical spacetimes. In chapter 8 we report on evolutions of charged black holes, in electrovacuum Einstein-Maxwell theory, and we end with some final remarks and future directions in chapter 9.

1.4 Preliminaries

Let us consider a D -dimensional pseudo-Riemannian manifold (\mathcal{M}, g) , that is, a differentiable manifold \mathcal{M} equipped with a smooth, symmetric metric tensor g with signature $(- + \cdots +)$. We further assume that the manifold is covered by a set of coordinates $\{x^\mu\}$, $\mu = 0, \dots, D-1$.

A *coordinate basis* of the *tangent space* of \mathcal{M} at p , $T_p\mathcal{M}$, is given by $\partial_\mu \equiv \partial/\partial x^\mu$. A *vector*

*Usually found in the literature as “3+1” decomposition. Here we will keep the D arbitrary, but the differences are minimal.

$V \in T_p\mathcal{M}$ can be written in the form

$$V = V^\mu \partial_\mu, \quad (1.4.1)$$

where V^μ are the components of V in the basis ∂_μ . When a vector V acts on a function f it produces the directional derivative of f along V :

$$V(f) = V^\mu \partial_\mu f. \quad (1.4.2)$$

A 1-form $\omega \in T_p^*\mathcal{M}$ (the *cotangent space* at p) is an object which is dual to a vector, i.e., it produces a number when acting on a vector. The simplest example of such an object is the differential df of a function f . The action of df on V is defined to be

$$\langle df, V \rangle \equiv V(f) = V^\mu \partial_\mu f. \quad (1.4.3)$$

Since $df = \partial_\mu f dx^\mu$, $\{dx^\mu\}$ is a natural choice as a basis of $T_p^*\mathcal{M}$. We thus naturally expand an arbitrary 1-form ω as

$$\omega = \omega_\mu dx^\mu. \quad (1.4.4)$$

The metric tensor g allows us to define a scalar product between two vectors U and V

$$U \cdot V \equiv g(U, V) = g(\partial_\mu, \partial_\nu) U^\mu V^\nu \equiv g_{\mu\nu} U^\mu V^\nu, \quad (1.4.5)$$

which induces an isomorphism between vectors and 1-forms, corresponding in the index notation to the usual raising and lowering of indices: if U is a vector, one can define a 1-form U_b through

$$\langle U_b, V \rangle \equiv g(U, V) = g_{\mu\nu} U^\mu V^\nu \equiv (U_b)_\nu V^\nu \quad \forall V. \quad (1.4.6)$$

Analogously, given a 1-form ω we can map it to a vector ω^\sharp through

$$\langle \sigma, \omega^\sharp \rangle \equiv g^{-1}(\sigma, \omega) = g^{-1}(\sigma_\mu dx^\mu, \omega_\nu dx^\nu) = g^{\mu\nu} \sigma_\mu \omega_\nu \equiv \sigma_\mu (\omega^\sharp)^\mu \quad \forall \sigma. \quad (1.4.7)$$

Since we will be working mostly in the index notation, and the placement of the index makes clear whether one is dealing with vectors or 1-forms, we will omit the flat and sharp symbols throughout.

The metric further allows us to determine the distance between two nearby points in the manifold according to

$$ds^2 = g_{\mu\nu} dx^\mu dx^\nu. \quad (1.4.8)$$

Notice that a basis of $T_p\mathcal{M}$ (and of $T_p^*\mathcal{M}$) need not be coordinate. One can have, for instance, the combination $e_\alpha \equiv A_\alpha^\mu \partial_\mu$. $\{e_\alpha\}$ is an example of a *non-coordinate basis*.

We now introduce a (generic) non-coordinate basis obeying

$$[e_\alpha, e_\beta] = c_{\alpha\beta}^\delta e_\delta, \quad (1.4.9)$$

where the *Lie bracket* $[X, Y]$ is defined by

$$[X, Y]f = X(Y(f)) - Y(X(f)). \quad (1.4.10)$$

The connection coefficients $\Gamma^\alpha{}_{\beta\gamma}$ then take the form

$$\Gamma^\alpha{}_{\beta\gamma} = \frac{1}{2}g^{\alpha\delta} (g_{\delta\beta,\gamma} + g_{\delta\gamma,\beta} - g_{\beta\gamma,\delta} + c_{\delta\beta\gamma} + c_{\delta\gamma\beta} - c_{\beta\gamma\delta}), \quad (1.4.11)$$

where $\Gamma^\alpha{}_{[\beta\gamma]} = -\frac{1}{2}c_{\beta\gamma}{}^\alpha$. When using coordinate basis ($c_{\beta\gamma}{}^\alpha = 0$), these are usually called the Christoffel symbols.

We now define the Riemann curvature tensor

$$R^\alpha{}_{\beta\gamma\delta} = \Gamma^\alpha{}_{\beta\delta,\gamma} - \Gamma^\alpha{}_{\beta\gamma,\delta} + \Gamma^\alpha{}_{\lambda\gamma}\Gamma^\lambda{}_{\beta\delta} - \Gamma^\alpha{}_{\lambda\delta}\Gamma^\lambda{}_{\beta\gamma} - \Gamma^\alpha{}_{\beta\lambda}c_{\gamma\delta}{}^\lambda. \quad (1.4.12)$$

Mind the notation

$$T_{\alpha,\beta} \equiv \partial_{e_\beta} T_\alpha \equiv e_\beta(T_\alpha). \quad (1.4.13)$$

Thus, $T_{\alpha,\sigma\lambda} = \partial_{e_\lambda}\partial_{e_\sigma}T_\alpha \neq \partial_{e_\sigma}\partial_{e_\lambda}T_\alpha$.

General relativity is a geometric theory of gravity which relates the curvature of spacetime to its matter content via the Einstein field equations, which read

$$G_{\mu\nu} \equiv R_{\mu\nu} - \frac{1}{2}R g_{\mu\nu} = 8\pi T_{\mu\nu}, \quad (1.4.14)$$

where $R_{\mu\nu} \equiv R^\lambda{}_{\mu\lambda\nu}$ is the Ricci curvature tensor, R its trace (the Ricci scalar), $g_{\mu\nu}$ the metric tensor and $T_{\mu\nu}$ the stress-energy tensor. All these quantities are D -dimensional.

Throughout this work we will always use the $(- + \dots +)$ metric signature and geometrised units $G = 1 = c$.

Chapter 2

$(D - 1) + 1$ decomposition

We start by briefly stating some known results from differential geometry that will be of use to us. In this chapter we use the following conventions: Greek indices $(\alpha, \beta, \gamma, \dots)$ run from 0 to $D - 1$; Latin indices (i, j, k, \dots) run from 1 to $D - 1$.

We work on a D -dimensional manifold \mathcal{M} with a metric $g_{\mu\nu}$. We denote the torsion-free Levi-Civita connection on \mathcal{M} associated with $g_{\mu\nu}$ by ${}^D\nabla$. All quantities defined relative to the manifold \mathcal{M} will have a leading D superscript, e.g., the Riemann curvature tensor on \mathcal{M} is denoted by ${}^DR^\mu{}_{\alpha\beta\gamma}$.

2.1 Hypersurfaces

2.1.1 Definition

A codimension 1 hypersurface Σ is a $(D - 1)$ -dimensional submanifold of \mathcal{M} , defined as the image of a $(D - 1)$ -dimensional manifold $\hat{\Sigma}$ by an embedding Φ , $\Sigma = \Phi(\hat{\Sigma})$ [122, 119]. Given a scalar field t on \mathcal{M} , we can select a particular hypersurface Σ by putting a restriction on the coordinates

$$t(x^\alpha) = 0, \tag{2.1.1}$$

or by giving parametric equations

$$x^\mu = x^\mu(y^i), \tag{2.1.2}$$

where y^i are coordinates intrinsic to the hypersurface.

2.1.2 Normal vector

The 1-form $\partial_\mu t$ is normal to the hypersurface. We can introduce a unit normal n_μ (if the hypersurface is not null) as

$$n_\mu = \frac{1}{\sqrt{|\partial_\alpha t \partial^\alpha t|}} \partial_\mu t. \quad (2.1.3)$$

With this definition

$$n^\mu n_\mu \equiv \sigma = \begin{cases} -1 & \text{if } \Sigma \text{ is spacelike} \\ +1 & \text{if } \Sigma \text{ is timelike} \end{cases}. \quad (2.1.4)$$

2.1.3 Induced metric

We obtain the *induced metric on* Σ by restricting the line element to displacements confined to the hypersurface. Using the parametric equations $x^\mu = x^\mu(y^i)$, we define the vectors

$$e_i^\mu = \frac{\partial x^\mu}{\partial y^i} \quad (2.1.5)$$

that are tangent to the curves in Σ . For displacements confined to Σ we have

$$\begin{aligned} ds_\Sigma^2 &= g_{\mu\nu} dx^\mu dx^\nu \\ &= g_{\mu\nu} \left(\frac{\partial x^\mu}{\partial y^i} dy^i \right) \left(\frac{\partial x^\nu}{\partial y^j} dy^j \right) \\ &= \gamma_{ij} dy^i dy^j, \end{aligned} \quad (2.1.6)$$

where

$$\gamma_{ij} \equiv \left(\frac{\partial x^\mu}{\partial y^i} \right) \left(\frac{\partial x^\nu}{\partial y^j} \right) g_{\mu\nu} \quad (2.1.7)$$

is the induced metric of the hypersurface (also called the *first fundamental form of* Σ). Notice that if $u, v \in \Sigma$,

$$u \cdot v = g_{\mu\nu} u^\mu v^\nu = \gamma_{ij} u^i v^j.$$

2.1.4 Orthogonal projector

The *orthogonal projector onto* Σ is a concept closely related with that of the induced metric. For a hypersurface Σ with unit normal n^μ we define it as

$$P_{\mu\nu} = g_{\mu\nu} - \sigma n_\mu n_\nu. \quad (2.1.8)$$

To see that this definition makes sense, we note that, for any vector v^μ in \mathcal{M} (or, more correctly, in $T_p\mathcal{M}$, the *tangent space* of \mathcal{M} at p), $P_{\mu\nu}$ will project it tangent to the hypersurface, i.e., orthogonal to n^μ :

$$(P_{\mu\nu} v^\mu) n^\nu = 0. \quad (2.1.9)$$

Notice also that the projector is idempotent:

$$P^\mu{}_\lambda P^\lambda{}_\nu = P^\mu{}_\nu. \quad (2.1.10)$$

Finally, note that for $u, v \in \Sigma$, $P_{\mu\nu}$ acts just like the metric:

$$P_{\mu\nu} u^\mu v^\nu = g_{\mu\nu} u^\mu v^\nu = \gamma_{ij} u^i v^j. \quad (2.1.11)$$

Thus, we see that the orthogonal projector $P_{\mu\nu}$ is the natural extension of the induced metric γ_{ij} for all vectors in $T_p\mathcal{M}$. As such, from now on we will no longer make any distinction between these two concepts, and will denote both by $\gamma_{\mu\nu}$ (defined as $\gamma_{\mu\nu} = g_{\mu\nu} - \sigma n_\mu n_\nu$). This way we adopt a D -dimensional point of view, where we treat all tensor fields defined on Σ as if they were defined on \mathcal{M} and we avoid the need to introduce a specific coordinate system on Σ .

Note that we can project an arbitrary tensor on \mathcal{M} onto Σ in the following way. Let $T^{\mu_1 \dots \mu_p}{}_{\nu_1 \dots \nu_q}$ be a tensor field on \mathcal{M} . Denoting $(\gamma T)^{\alpha_1 \dots \alpha_p}{}_{\beta_1 \dots \beta_q}$ another tensor in \mathcal{M} such that

$$(\gamma T)^{\alpha_1 \dots \alpha_p}{}_{\beta_1 \dots \beta_q} = \gamma^{\alpha_1}{}_{\mu_1} \dots \gamma^{\alpha_p}{}_{\mu_p} \gamma^{\nu_1}{}_{\beta_1} \dots \gamma^{\nu_q}{}_{\beta_q} T^{\mu_1 \dots \mu_p}{}_{\nu_1 \dots \nu_q}, \quad (2.1.12)$$

we easily see that $(\gamma T)^{\alpha_1 \dots \alpha_p}{}_{\beta_1 \dots \beta_q}$ is in Σ .

2.1.5 Intrinsic curvature

We now want to define a covariant derivative associated with $\gamma_{\mu\nu}$ on Σ , ∇ , that has the “usual properties” of a covariant derivative, in particular that it is torsion-free and satisfies

$$\nabla_\alpha \gamma_{\mu\nu} = 0. \quad (2.1.13)$$

The easiest way to define it is just to project the covariant derivative ${}^D\nabla$ onto Σ using (2.1.8):

$$\nabla_\rho T^{\alpha_1 \dots \alpha_p}{}_{\beta_1 \dots \beta_q} = \gamma^{\alpha_1}{}_{\mu_1} \dots \gamma^{\alpha_p}{}_{\mu_p} \gamma^{\nu_1}{}_{\beta_1} \dots \gamma^{\nu_q}{}_{\beta_q} \gamma^\sigma{}_\rho {}^D\nabla_\sigma T^{\mu_1 \dots \mu_p}{}_{\nu_1 \dots \nu_q}. \quad (2.1.14)$$

It can be shown [119] that this definition of the covariant derivative has all the properties we want (linearity, Leibniz’ rule, its torsion vanishes, ...) and it satisfies (2.1.13).

We can now define the Riemann tensor associated with this connection, $R^\alpha{}_{\beta\gamma\delta}$, as the measure of the non-commutativity of this covariant derivative, associated with the $\gamma_{\mu\nu}$ metric on Σ ,

$$\nabla_\alpha \nabla_\beta v^\gamma - \nabla_\beta \nabla_\alpha v^\gamma = R^\gamma{}_{\mu\alpha\beta} v^\mu, \quad (2.1.15)$$

where $v^\mu \in \Sigma$.

$R^\alpha{}_{\beta\gamma\delta}$ represents the *intrinsic curvature* of Σ .

2.1.6 Extrinsic curvature

The intrinsic curvature of the hypersurface Σ , as the name implies, is a property of the hypersurface itself. We will now define the *extrinsic curvature*, which depends on how Σ is embedded on \mathcal{M} . We define it as* [123]

$$K_{\mu\nu} = -\gamma^\alpha{}_\mu \gamma^\beta{}_\nu \nabla_\alpha n_\beta. \quad (2.1.16)$$

It can be shown that $K_{\mu\nu} = K_{\nu\mu}$. Defining

$$a^\mu = n^\nu \nabla_\nu n^\mu, \quad (2.1.17)$$

we have, after some simple algebra,

$$K_{\mu\nu} = -\nabla_\mu n_\nu + \sigma n_\mu a_\nu. \quad (2.1.18)$$

We will always consider spacelike hypersurfaces, so from now on we will work with $\sigma = -1$. Note that, by definition, $K_{\mu\nu}$ lives on Σ .

2.2 Foliations

We assume that our spacetime can be foliated by a family of spacelike hypersurfaces Σ_t , that is, there exists a smooth scalar field \hat{t} on \mathcal{M} such that

$$\Sigma_t \equiv \{p \in \mathcal{M}, \hat{t}(p) = t\}. \quad (2.2.1)$$

In the following we will not distinguish between t and \hat{t} .

2.2.1 The lapse function

We write the unit normal vector as

$$n_\mu \equiv -\alpha \partial_\mu t, \quad (2.2.2)$$

where

$$\alpha \equiv \frac{1}{\sqrt{-\partial_\nu t \partial^\nu t}} \quad (2.2.3)$$

is called the *lapse function*.

*Our definition, with the minus sign, agrees with the standard convention used in the numerical relativity community, but note that some authors use different conventions.

2.2.2 Normal evolution vector

We define the *normal evolution vector* as

$$m^\mu \equiv \alpha n^\mu. \quad (2.2.4)$$

We can easily see that

$$m^\mu D\nabla_\mu t = 1,$$

which means that m^μ , unlike n^μ , is adapted to the scalar field t . It can be shown [119] that the hypersurfaces Σ_t are *Lie dragged* by m^μ . As consequence of this, if v^μ is in Σ , $\mathcal{L}_m v$ is also in Σ .

2.2.3 Eulerian observers

We can identify the unit timelike vector n^μ as the velocity (or the “ D -velocity”...) of some observer, that we will call the *Eulerian observer*. The worldlines of these observers are orthogonal to the hypersurfaces Σ_t , which means that, for a given t , the hypersurface Σ_t is the set of events that are simultaneous from the point of view of the Eulerian observer.

We define the acceleration of the Eulerian observer the usual way,

$$a^\mu = n^\nu \nabla_\nu n^\mu. \quad (2.2.5)$$

Let us now list some formulæ that will be useful for the following sections:

$$a_\mu = \nabla_\mu \log \alpha, \quad (2.2.6)$$

$$D\nabla_\beta n_\alpha = -K_{\alpha\beta} - n_\beta \nabla_\alpha \log \alpha, \quad (2.2.7)$$

$$D\nabla_\beta m^\alpha = -\alpha K^\alpha{}_\beta - n_\beta \nabla^\alpha \alpha + n^\alpha D\nabla_\beta \alpha. \quad (2.2.8)$$

2.2.4 Evolution of $\gamma_{\alpha\beta}$

From the definition of Lie derivative and equation (2.2.8), one can show

$$\mathcal{L}_m \gamma_{\alpha\beta} = -2\alpha K_{\alpha\beta}, \quad (2.2.9)$$

and

$$\mathcal{L}_m \gamma^\alpha{}_\beta = 0, \quad (2.2.10)$$

which means that, for any tensor field T on Σ_t , its Lie derivative along m is also a tensor field on Σ_t .

2.3 Gauss, Codazzi and Ricci equations

We still need a way to relate quantities defined on the hypersurface to those defined on the manifold \mathcal{M} ; in particular, we would like to have a relation between the D -dimensional Riemann curvature tensor, the $(D - 1)$ -dimensional Riemann tensor on the hypersurface and the extrinsic curvature. Such relations are common in differential geometry—known as the equations of Gauss, Codazzi and Ricci—which we now state without proof (see, e.g., [119]).

2.3.1 Gauss equation

The starting point is equation (2.1.15). We just need to use equation (2.1.14) to relate $\nabla_\alpha v^\gamma$ with ${}^D\nabla_\alpha v^\gamma$. After some algebra we arrive at

$$\gamma^\mu{}_\alpha \gamma^\nu{}_\beta \gamma^\gamma{}_\rho \gamma^\sigma{}_\delta {}^D R^\rho{}_{\sigma\mu\nu} = R^\gamma{}_{\delta\alpha\beta} + K^\gamma{}_\alpha K_{\delta\beta} - K^\gamma{}_\beta K_{\alpha\delta}, \quad (2.3.1)$$

which is called the *Gauss equation*. Contracting this equation on γ and α we get

$$\gamma^\mu{}_\alpha \gamma^\nu{}_\beta {}^D R_{\mu\nu} + \gamma_{\alpha\mu} \gamma^\rho{}_\beta n^\nu n^\sigma {}^D R^\mu{}_{\nu\rho\sigma} = R_{\alpha\beta} + K K_{\alpha\beta} - K_{\alpha\mu} K^\mu{}_\beta, \quad (2.3.2)$$

where we defined $K \equiv K^\mu{}_\mu = K^i{}_i$ (where the equality comes from the fact that $K_{\mu\nu}$ lives on Σ). Taking the trace of this expression we have (noting that $K_{\mu\nu} K^{\mu\nu} = K_{ij} K^{ij}$)

$${}^D R + 2{}^D R_{\mu\nu} n^\mu n^\nu = R + K^2 - K_{ij} K^{ij}. \quad (2.3.3)$$

2.3.2 Codazzi equation

We now start with the following equation

$$\nabla_\alpha \nabla_\beta n^\gamma - \nabla_\beta \nabla_\alpha n^\gamma = R^\gamma{}_{\mu\alpha\beta} n^\mu, \quad (2.3.4)$$

and we project it onto Σ using (2.1.12). Using equation (2.1.18) and after some algebra we arrive at

$$\gamma^\gamma{}_\rho \gamma^\mu{}_\alpha \gamma^\nu{}_\beta n^\sigma {}^D R^\rho{}_{\sigma\mu\nu} = \nabla_\beta K^\gamma{}_\alpha - \nabla_\alpha K^\gamma{}_\beta, \quad (2.3.5)$$

which is called the *Codazzi equation*. Contracting this equation on β and γ we have

$$\gamma^\mu{}_\alpha n^\nu {}^D R_{\mu\nu} = \nabla_\alpha K - \nabla_\mu K^\mu{}_\alpha. \quad (2.3.6)$$

2.3.3 Ricci equation

We still need one more projection of the Riemann tensor (in fact, the last non-trivial projection). Again, we start with equation (2.3.4), but this time we project it only twice onto Σ_t and one time along n^μ :

$$\gamma_{\alpha\mu} n^\sigma \gamma^\nu{}_\beta ({}^D\nabla_\nu {}^D\nabla_\sigma n^\mu - {}^D\nabla_\sigma {}^D\nabla_\nu n^\mu) = \gamma_{\alpha\mu} n^\sigma \gamma^\nu{}_\beta n^\rho {}^D R^\mu{}_{\rho\nu\sigma}. \quad (2.3.7)$$

Using equations (2.2.7), (2.2.8) and some properties of the Lie derivative we arrive at

$$\gamma_{\alpha\mu}\gamma^\nu{}_\beta n^\rho n^\sigma D R^\mu{}_{\rho\nu\sigma} = \frac{1}{\alpha}\mathcal{L}_m K_{\alpha\beta} + \frac{1}{\alpha}\nabla_\alpha\partial_\beta\alpha + K_{\alpha\mu}K^\mu{}_\beta, \quad (2.3.8)$$

which is called the *Ricci equation*. We can combine equation (2.3.8) with equation (2.3.2) to get

$$\gamma^\mu{}_\alpha\gamma^\nu{}_\beta D R_{\mu\nu} = -\frac{1}{\alpha}\mathcal{L}_m K_{\alpha\beta} - \frac{1}{\alpha}\nabla_\alpha\partial_\beta\alpha + R_{\alpha\beta} + K K_{\alpha\beta} - 2K_{\alpha\mu}K^\mu{}_\beta. \quad (2.3.9)$$

2.4 Einstein equations

Our goal now is to write the Einstein equations in an explicit dynamical system form. Let us start by writing the equations themselves in their “traditional” form,

$$D R_{\mu\nu} - \frac{1}{2}D R g_{\mu\nu} = 8\pi T_{\mu\nu}. \quad (2.4.1)$$

The alternative form

$$D R_{\mu\nu} = 8\pi \left(T_{\mu\nu} - \frac{T}{D-2}g_{\mu\nu} \right), \quad (2.4.2)$$

where $T \equiv g^{\mu\nu}T_{\mu\nu}$, will also be useful to us.

2.4.1 Decomposition of the stress-energy tensor

We define

$$E \equiv T_{\mu\nu}n^\mu n^\nu, \quad (2.4.3)$$

$$j_\alpha \equiv -T_{\mu\nu}n^\mu\gamma^\nu{}_\alpha, \quad (2.4.4)$$

$$S_{\alpha\beta} \equiv T_{\mu\nu}\gamma^\mu{}_\alpha\gamma^\nu{}_\beta, \quad (2.4.5)$$

which correspond to the *matter energy density*, the *matter momentum density* and the *matter stress density*, respectively, as measured by the Eulerian observer. We further define $S \equiv g^{\mu\nu}S_{\mu\nu} = \gamma^{ij}S_{ij}$ and note that $T = S - E$.

2.4.2 Projection of the Einstein equations

2.4.2.1 Projection onto Σ_t

Using equation (2.3.9) we project equation (2.4.2) onto Σ_t . We get

$$\mathcal{L}_m K_{\alpha\beta} = -\nabla_\alpha\nabla_\beta\alpha + \alpha \left[R_{\alpha\beta} + K K_{\alpha\beta} - 2K_{\alpha\mu}K^\mu{}_\beta + \frac{8\pi}{D-2}(S - E)\gamma_{\alpha\beta} - 8\pi S_{\alpha\beta} \right]. \quad (2.4.6)$$

Note that every single term in this equation lives in Σ_t . Thus, we can restrict the indices to spacial ones,

$$\mathcal{L}_m K_{ij} = -\nabla_i\nabla_j\alpha + \alpha \left[R_{ij} + K K_{ij} - 2K_{ik}K^k{}_j + \frac{8\pi}{D-2}(S - E)\gamma_{ij} - 8\pi S_{ij} \right]. \quad (2.4.7)$$

2.4.2.2 Projection along n^μ

This step is easy, we just need to contract equation (2.4.1) with $n^\mu n^\nu$ and use (2.3.3), yielding

$$R + K^2 - K_{ij}K^{ij} = 16\pi E. \quad (2.4.8)$$

This equation is called the *Hamiltonian constraint*.

2.4.2.3 Mixed projection

Finally, we need to project equation (2.4.1) once onto Σ_t and once along n^μ . Using equation (2.3.6) we get

$$\nabla_j (K^{ij} - \gamma^{ij}K) = 8\pi j^i. \quad (2.4.9)$$

This equation is called the *momentum constraint*.

2.5 Choice of coordinates

Equations (2.4.7) ($(D - 1)D/2$ equations), (2.4.8) (1 equation) and (2.4.9) ($D - 1$ equations) contain the same information as equation (2.4.1) (it can be checked that the number of independent components is the same: $(D - 1)D/2 + 1 + (D - 1) = D(D + 1)/2$). Before we can cast these equations in a dynamical system form, however, we have to introduce a specific coordinate system, something we have not yet done.

We will introduce coordinates adapted to the foliation Σ_t in the following way [119]. On each hypersurface Σ_t we have a coordinate system $x^i = x^1, x^2, \dots, x^{D-1}$ that is varying smoothly between neighbouring hypersurfaces, so that $x^\alpha = t, x^1, x^2, \dots, x^{D-1}$ is a well behaved coordinate system on \mathcal{M} . In this coordinate system

$$n_\mu = (-\alpha, 0, \dots, 0). \quad (2.5.1)$$

We define the *shift vector* β as

$$\beta \equiv \partial_t - m, \quad (2.5.2)$$

or in components, $\beta^\mu \equiv \delta^\mu_t - m^\mu$. Note that $n_\mu \beta^\mu = 0$, so β lives on Σ_t ($\beta^t = 0$). Using (2.5.2) we can also write

$$n^\mu = \frac{1}{\alpha} (1, -\beta^i). \quad (2.5.3)$$

Notice also that

$$\partial_t \cdot \partial_t = -\alpha^2 + \beta^\mu \beta_\mu = -\alpha^2 + \beta^k \beta_k.$$

We are now able to write the metric components $g_{\mu\nu}$ relative to this coordinate system,

$$\begin{aligned} g_{00} &= g_{\mu\nu} (\partial_t)^\mu (\partial_t)^\nu = \partial_t \cdot \partial_t = -\alpha^2 + \beta^k \beta_k, \\ g_{0i} &= g_{\mu\nu} (\partial_t)^\mu (\partial_i)^\nu = (m + \beta) \cdot \partial_i = \beta \cdot \partial_i = \beta_j \delta^j_i = \beta_i, \\ g_{ij} &= g_{\mu\nu} (\partial_i)^\mu (\partial_j)^\nu = \gamma_{kl} (\partial_i)^k (\partial_j)^l = \gamma_{ij}. \end{aligned}$$

The line element is thus

$$g_{\mu\nu} dx^\mu dx^\nu = -\alpha^2 dt^2 + \gamma_{ij} (dx^i + \beta^i dt) (dx^j + \beta^j dt), \quad (2.5.4)$$

or, in matrix form,

$$g_{\mu\nu} = \begin{pmatrix} -\alpha^2 + \beta_k \beta^k & \beta_i \\ \beta_j & \gamma_{ij} \end{pmatrix}. \quad (2.5.5)$$

The inverse metric takes the form

$$g^{\mu\nu} = \begin{pmatrix} -\frac{1}{\alpha^2} & \frac{\beta^i}{\alpha^2} \\ \frac{\beta^j}{\alpha^2} & \gamma^{ij} - \frac{\beta^i \beta^j}{\alpha^2} \end{pmatrix}. \quad (2.5.6)$$

The determinants of $g_{\mu\nu}$ and γ_{ij} are related by

$$\sqrt{-g} = \alpha \sqrt{\gamma}, \quad (2.5.7)$$

where

$$g \equiv \det g_{\mu\nu}, \quad \gamma \equiv \det \gamma_{ij}.$$

2.6 The PDE system

Using the properties of the Lie derivative and the definition of shift vector, equation (2.5.2), we can write

$$\mathcal{L}_m K_{ij} = \partial_t K_{ij} - \mathcal{L}_\beta K_{ij}. \quad (2.6.1)$$

Equation (2.2.9) can also be put in the form

$$(\partial_t - \mathcal{L}_\beta) \gamma_{ij} = -2\alpha K_{ij}. \quad (2.6.2)$$

We now have our full system, which we rewrite here

$$(\partial_t - \mathcal{L}_\beta) \gamma_{ij} = -2\alpha K_{ij}, \quad (2.6.3a)$$

$$(\partial_t - \mathcal{L}_\beta) K_{ij} = -\nabla_i \nabla_j \alpha + \alpha \left[R_{ij} + K K_{ij} - 2K_{ik} K^k_j + \frac{8\pi}{D-2} (S - E) \gamma_{ij} - 8\pi S_{ij} \right], \quad (2.6.3b)$$

$$R + K^2 - K_{ij} K^{ij} = 16\pi E, \quad (2.6.3c)$$

$$\nabla_j (K^{ij} - \gamma^{ij} K) = 8\pi j^i. \quad (2.6.3d)$$

Note that we can write the covariant derivatives ∇_k and the Lie derivatives \mathcal{L}_β in terms of partial derivatives of the coordinates x^i , and the Ricci tensor R_{ij} and Ricci scalar R in terms of γ_{ij} and its derivatives in the usual way. This way, assuming that the source terms E , j_i , S_{ij} are given, we have a second-order non-linear system of PDEs with the unknowns γ_{ij} , K_{ij} , α , β^i .

The above equations (2.6.3) are known in the numerical relativity community as the *ADM equations*, after the work of Arnowitt, Deser and Misner [124] on their Hamiltonian formulation of general relativity. In this form, however, the equations were in fact first written by York [125] (in four spacetime dimensions), and are thus sometimes referred to as the ADM-York equations.

By now we have cast the Einstein equations on an explicit $(D - 1)$ -dimensional dynamical system form. Note, however, that whereas equations (2.6.3a) and (2.6.3b) are evolution equations, equations (2.6.3c) and (2.6.3d) are not. These last two equations constitute *constraints* that the system must satisfy at all times. In particular, these constraints must be satisfied at $t = 0$. So we would now need to specify the relevant initial conditions, satisfying equations (2.6.3c) and (2.6.3d), and then evolve them using equations (2.6.3a) and (2.6.3b), while making sure that equations (2.6.3c) and (2.6.3d) always hold.

The question arises: given a specific physical problem (say, a head-on collision of two black holes), how does one specify the initial conditions that correspond to the problem we have in mind? This is the *initial data* problem which will be the focus of the next chapter.

Chapter 3

Initial data

On any dynamical system, to perform an evolution one needs to supply the initial conditions. In our case, this amounts to providing a snapshot of the gravitational fields on some hypersurface—the *initial data*. Then, one evolves this data to neighbouring hypersurfaces and so on.

In general relativity initial data cannot be freely specified. As we have seen in chapter 2, not all of Einstein’s equations are evolution equations. We also have a set of constraint equations that must be satisfied at all times, the Hamiltonian (2.6.3c) and momentum (2.6.3d) constraints. In particular, these equations need to be solved at $t = 0$ for the (γ_{ij}, K_{ij}) that represent the physical system we are interested in evolving. We then feed these values to the evolution equations themselves.

In general, this step is far from trivial. There is no unique recipe for the writing of initial data corresponding to an arbitrary gravitational system. For some systems, however,—such as vacuum spacetimes with moving black holes—recipes do exist. Actually, for the four-dimensional case, several methods for constructing initial data for different systems have been explored over the years (see [126] for a review). For higher-dimensional systems, however, only recently the “standard” way of constructing initial data for moving black holes in the vacuum was generalised [127, 128].

In this chapter we will give an overview of the procedure of *conformal decomposition* first introduced by York and Lichnerowicz [129, 130, 131, 132] which rearranges the degrees of freedom contained in the three-metric γ_{ij} and extrinsic curvature K_{ij} via a conformal transformation and a split of the curvature into trace and traceless part followed by a transverse-traceless decomposition of the conformally rescaled traceless extrinsic curvature.

We will focus specifically on initial data for vacuum spacetimes, generalising the well-known Brill-Lindquist [133] and Bowen-York [134, 135] initial data along the lines of [127, 128]. For alternative procedures to tackle the initial data problem we refer the reader to Cook’s review [126], Alcubierre’s book [120], the recent book by Baumgarte & Shapiro [121] and references therein.

As in the previous chapter, Greek indices are spacetime indices running from 0 to $D - 1$; Latin indices are spatial indices, running from 1 to $D - 1$.

3.1 Conformal decomposition

3.1.1 Conformal transformations

We start by recalling a known general result: given an N -dimensional manifold with metric $g_{\mu\nu}$, if one performs the conformal transformation

$$g_{\mu\nu} = \phi(x^\alpha) \hat{g}_{\mu\nu}, \quad (3.1.1)$$

the Ricci scalars relative to the metrics $g_{\mu\nu}$ and $\hat{g}_{\mu\nu}$ are related by

$$R = \frac{\hat{R}}{\phi} + \frac{1-N}{\phi^2} \hat{\nabla}^\alpha \partial_\alpha \phi - \frac{\partial_\alpha \phi \partial^\alpha \phi}{4\phi^3} (1-N)(6-N), \quad (3.1.2)$$

where $\hat{\nabla}$ is the covariant derivative associated with the conformal metric $\hat{g}_{\mu\nu}$.

Let us now consider our case, where we have a $(D-1)$ -dimensional spacelike slice with induced metric γ_{ij} and “conformal metric” $\hat{\gamma}_{ij}$. We have $N = D - 1$, and we make

$$\phi = \psi^p, \quad p = \frac{4}{D-3}.$$

We have

$$R = \psi^{-p} \hat{R} + (2-D)p \psi^{-p-1} \hat{\nabla}^k \partial_k \psi. \quad (3.1.3)$$

We further decompose the extrinsic curvature in trace and trace-free parts,

$$K_{ij} \equiv A_{ij} + \frac{K}{D-1} \gamma_{ij}, \quad (3.1.4)$$

where $K \equiv \gamma^{ij} K_{ij}$ and, by definition, $\gamma^{ij} A_{ij} = 0$. Defining $A^{ij} = \gamma^{ik} \gamma^{jl} A_{kl}$, we can also write

$$K^{ij} \equiv A^{ij} + \frac{K}{D-1} \gamma^{ij}. \quad (3.1.5)$$

3.1.1.1 Conformal decomposition of the Hamiltonian and momentum constraint

Under such a transformation, it is a matter of simple substitution to show that the Hamiltonian constraint equation (2.6.3c) takes the form

$$\hat{\Delta} \psi + \frac{\psi}{p(2-D)} \hat{R} - \frac{\psi^{p+1}}{p(2-D)} A^{ij} A_{ij} - \frac{\psi^{p+1}}{p(D-1)} K^2 = 16\pi E \frac{\psi^{p+1}}{p(2-D)}, \quad (3.1.6)$$

where $\hat{\Delta} \equiv \hat{\nabla}^k \hat{\nabla}_k$.

With a straightforward calculation we can easily show that

$$\nabla_i A^{ij} = \psi^{-q} \hat{\nabla}_k (\psi^q A^{kj}), \quad (3.1.7)$$

with $q \equiv 2\frac{D+1}{D-3}$. Thus, we define

$$\hat{A}^{ij} \equiv \psi^q A^{ij} \equiv \psi^{2\frac{D+1}{D-3}} A^{ij}, \quad (3.1.8)$$

and we will lower its indices with $\hat{\gamma}_{ij}$,

$$\hat{A}_{ij} \equiv \hat{\gamma}_{ik} \hat{\gamma}_{jl} \hat{A}^{kl} = \psi^2 A_{ij}. \quad (3.1.9)$$

We thus have

$$\nabla_i K^{ij} = \psi^{-q} \hat{\nabla}_i \hat{A}^{ij} + \frac{\psi^{-p}}{D-1} \hat{\nabla}^j K.$$

Equation (2.4.9) is then written in the form

$$\hat{\nabla}_i \hat{A}^{ij} - \frac{D-2}{D-1} \psi^{2\frac{D-1}{D-3}} \hat{\nabla}^j K = 8\pi \psi^{2\frac{D+1}{D-3}} j^j. \quad (3.1.10)$$

All we need now is to write equation (3.1.6) as function of \hat{A}_{ij} , which is very easy. Our system is now

$$\hat{\Delta} \psi - \frac{D-3}{4(D-2)} \psi \hat{R} + \frac{D-3}{4(D-2)} \psi^{-\frac{3D-5}{D-3}} \hat{A}^{ij} \hat{A}_{ij} - \frac{D-3}{4(D-1)} \psi^{\frac{D+1}{D-3}} K^2 = -4\pi E \frac{D-3}{D-2} \psi^{\frac{D+1}{D-3}}, \quad (3.1.11)$$

$$\hat{\nabla}_i \hat{A}^{ij} - \frac{D-2}{D-1} \psi^{2\frac{D-1}{D-3}} \hat{\nabla}^j K = 8\pi \psi^{2\frac{D+1}{D-3}} j^j, \quad (3.1.12)$$

where

$$g_{\mu\nu} dx^\mu dx^\nu = -\alpha^2 dt^2 + \psi^{\frac{4}{D-3}} \hat{\gamma}_{ij} (dx^i + \beta^i dt) (dx^j + \beta^j dt).$$

3.2 Initial data for vacuum spacetimes

Let us now consider the equations (3.1.11) and (3.1.12) for the particular case of vacuum solutions ($j^i = 0 = E$). We further impose that the ‘‘conformal metric’’ $\hat{\gamma}_{ij}$ is flat (and, thus, $\hat{R} = 0$) and the ‘‘maximum slicing condition’’, $K = 0$ (to be discussed in section 4.2.1). The equations (3.1.11) and (3.1.10) greatly simplify, and we are left with

$$\partial_i \hat{A}^{ij} = 0, \quad (3.2.1)$$

$$\hat{\Delta} \psi + \frac{D-3}{4(D-2)} \psi^{-\frac{3D-5}{D-3}} \hat{A}^{ij} \hat{A}_{ij} = 0, \quad (3.2.2)$$

where $\hat{\Delta} \equiv \partial_i \partial^i$ is now the flat space Laplace operator.

Here we make a pause to recall that the Schwarzschild-Tangherlini metric in D dimensions is

$$ds^2 = - \left(1 - \frac{\mu}{r^{D-3}} \right) dt^2 + \frac{dr^2}{1 - \frac{\mu}{r^{D-3}}} + r^2 d\Omega_{D-2}^2, \quad (3.2.3)$$

where $\mu = \frac{16\pi M}{(D-2)\mathcal{A}_{D-2}}$, M being the mass of the black hole and $\mathcal{A}_{N-1} = \frac{2\pi^{N/2}}{\Gamma(N/2)}$ the area of the hypersphere. By performing the coordinate transformation

$$r = R \left(1 + \frac{\mu}{4R^{D-3}} \right)^{\frac{2}{D-3}}$$

we can write it in isotropic coordinates as

$$ds^2 = - \left(1 - \frac{16R^{3+D}\mu}{(4R^D + R^3\mu)^2} \right) dt^2 + \left(1 + \frac{\mu}{4R^{D-3}} \right)^{\frac{4}{D-3}} (dR^2 + R^2 d\Omega_{D-2}^2). \quad (3.2.4)$$

We will shortly make use of this geometry.

3.2.1 Brill-Lindquist initial data

We now assume that the extrinsic curvature vanishes identically, $K_{ij} = 0$, a condition that holds for *time-symmetric* initial data. It can be shown [119] that if $K_{ij} = 0$ and we choose coordinates such that $\alpha = 1$, we have

$$\mathcal{L}_m g_{\alpha\beta} = 0,$$

which means that, locally, m^μ is a Killing vector. m^μ is also orthogonal to the hypersurface $\Sigma_{t=0}$, and as such this configuration is static. This property only holds locally (on $\Sigma_{t=0}$) and we therefore call this configuration *momentarily static*.

For $K_{ij} = 0$ equation (3.2.1) is automatically satisfied, and (3.2.2) reduces to the standard $D - 1$ -dimensional flat space Laplace equation,

$$\hat{\Delta}\psi = 0. \quad (3.2.5)$$

We impose the following conditions on ψ

$$\lim_{r \rightarrow \infty} \psi = 1, \quad (3.2.6)$$

which is the asymptotic flatness condition (remember that $\gamma_{ij} = \psi^{\frac{4}{D-3}} \hat{\gamma}_{ij}$).

Let $r_{(i)} \equiv |r - x_{(i)}|$, where the $x_{(i)}$ are arbitrary points in our spacetime. A solution to equation (3.2.5) is given by

$$\psi = 1 + \sum_{i=1}^N \frac{C_{(i)}}{r_{(i)}^{D-3}}, \quad (3.2.7)$$

where the $C_{(i)}$ are arbitrary constants. Note that equation (3.2.7) obeys the condition (3.2.6). The spatial metric takes the form (recall that the conformal metric $\hat{\gamma}_{ij}$ is flat)

$$\gamma_{ij} dx^i dx^j = \left(1 + \sum_{i=1}^N \frac{C_{(i)}}{r_{(i)}^{D-3}} \right)^{\frac{4}{D-3}} (dr^2 + r^2 d\Omega_{D-2}^2). \quad (3.2.8)$$

This solution is asymptotically flat (by construction), and if we compare this expression with (3.2.4), we can identify $\mu = 4 \sum_{i=1}^N C_{(i)}$, which is the mass parameter measured in the “principal sheet” (anticipating the interpretation).

We now have to analyse what happens as $r \rightarrow x_{(i)}$, for a given i . When $r \rightarrow x_{(i)}$, $r_{(i)} \rightarrow 0$ and $r_{(j)} \rightarrow r_{(i)(j)} \equiv |x_{(i)} - x_{(j)}|$. Setting the origin of our coordinate system at $r = r_{(i)}$ ($x_{(i)} = 0$) we have

$$ds^2 = \left(\frac{C_{(i)}}{r_{(i)}^{D-3}} \right)^{\frac{4}{D-3}} \left[1 + \frac{r_{(i)}^{D-3}}{C_{(i)}} \left(1 + \sum_{j \neq i}^N \frac{C_{(j)}}{r_{(j)}^{D-3}} \right) \right]^{\frac{4}{D-3}} \left(dr_{(i)}^2 + r_{(i)}^2 d\Omega_{D-2}^2 \right),$$

and when $r_{(i)} \rightarrow 0$

$$ds^2 \rightarrow \left(\frac{C_{(i)}}{r_{(i)}^{D-3}} \right)^{\frac{4}{D-3}} \left[1 + A_{(i)} \frac{r_{(i)}^{D-3}}{C_{(i)}} \right]^{\frac{4}{D-3}} \left(dr_{(i)}^2 + r_{(i)}^2 d\Omega_{D-2}^2 \right),$$

where we defined $A_{(i)} \equiv 1 + \sum_{j \neq i}^N \frac{C_{(j)}}{r_{(i)(j)}^{D-3}}$. With the coordinate transformation $r'_{(i)} = \frac{C_{(i)}^{\frac{2}{D-3}}}{r_{(i)}}$ we have

$$ds^2 \xrightarrow[r'_{(i)} \rightarrow \infty]{r_{(i)} \rightarrow 0} \left(1 + A_{(i)} \frac{C_{(i)}}{r'_{(i)}^{D-3}} \right) \left(dr'_{(i)}{}^2 + r'_{(i)}{}^2 d\Omega_{D-2}^2 \right). \quad (3.2.9)$$

This shows that in this limit the space is also asymptotically flat. Thus, our solution (3.2.8) describes a space with $N + 1$ asymptotically flat regions. Note that all “lower sheets” are separate, i.e., there is no way to travel from one sheet to the other except through the “upper sheet” (or “principal sheet”). Equation (3.2.9) shows that each sheet, asymptotically, has a Schwarzschild-Tangherlini form, with the mass measured in the i th sheet being given by

$$\bar{\mu}_{(i)} = 4A_{(i)}C_{(i)} = 4 \left(C_{(i)} + \sum_{j \neq i}^N \frac{C_{(i)}C_{(j)}}{r_{(i)(j)}^{D-3}} \right). \quad (3.2.10)$$

The observer located on the principal sheet (the $(N + 1)$ th sheet) is the only one that sees a system of N black holes, with total mass $\mu_{\text{ADM}} = \mu_{N+1} = 4 \sum_{i=1}^N C_{(i)}$, as we had already mentioned. Thus we identify $\mu_{(i)} \equiv 4C_{(i)}$ and rewrite our expressions in terms of $\mu_{(i)}$,

$$\begin{aligned} \psi &= 1 + \sum_{i=1}^N \frac{\mu_{(i)}}{4r_{(i)}^{D-3}}, \\ \bar{\mu}_{(i)} &= \mu_{(i)} \left(1 + \sum_{j \neq i}^N \frac{\mu_{(j)}}{4r_{(i)(j)}^{D-3}} \right), \\ \mu_{\text{ADM}} &= \sum_{i=1}^N \mu_{(i)}, \end{aligned}$$

where $r_{(i)} \equiv |r - x_{(i)}|$ and $r_{(i)(j)} \equiv |x_{(i)} - x_{(j)}|$. The points $x_{(i)}$ are called *punctures*.

Note that $\mu \neq \sum_i^N \bar{\mu}_{(i)}$. This difference can be attributed to the interaction energy between the black holes. It is important to note that μ_i , as we have defined it, is just a convenient label for the mass of the i th black hole (but is *not* the mass). The mass of the i th black hole as measured on the i th sheet (its “bare mass”), is given by $\bar{\mu}_{(i)}$.*

3.2.2 Bowen-York initial data

Brill-Lindquist initial data is very useful because it provides us with an analytical solution for the constraint equations. However, it also has little physical relevance. Generally, one is interested in solutions with black holes that are spinning and moving and as such Brill-Lindquist data is clearly not enough.

In order to have a more general configuration, i.e. one that is not momentarily static, we cannot impose $K_{ij} = 0$. Let us recall that our assumptions are: $K = 0$ —the maximum slicing condition; $\hat{\gamma}_{ij}$ is flat—the conformal flatness condition; and $\lim_{r \rightarrow \infty} \psi = 1$ —the asymptotic flatness condition.

We now start by writing \hat{A}^{ij} in the form

$$\hat{A}^{ij} = (\hat{L}X)^{ij} + \hat{A}_{\text{TT}}^{ij}, \quad (3.2.11)$$

where

$$(\hat{L}X)^{ij} \equiv \hat{\nabla}^i X^j + \hat{\nabla}^j X^i - \frac{2}{D-1} \hat{\nabla}_k X^k \hat{\gamma}^{ij}. \quad (3.2.12)$$

By construction, $(\hat{L}X)^{ij} \hat{\gamma}_{ij} = 0$, and we impose $\hat{\gamma}_{ij} \hat{A}_{\text{TT}}^{ij} = 0 = \hat{\nabla}_j \hat{A}_{\text{TT}}^{ij}$. We will also restrict ourselves to the case $\hat{A}_{\text{TT}}^{ij} = 0$. The equations (3.2.1) and (3.2.2) take the form

$$\hat{\Delta} X^j + \frac{D-3}{D-1} \partial^j \partial_i X^i = 0, \quad (3.2.13)$$

$$\hat{\Delta} \psi + \frac{D-3}{4(D-2)} \psi^{-\frac{3D-5}{D-3}} \hat{A}^{ij} \hat{A}_{ij} = 0, \quad (3.2.14)$$

$$\hat{A}^{ij} = (\hat{L}X)^{ij}. \quad (3.2.15)$$

Thus, we have to solve (3.2.13), plug X^j in (3.2.15) and then solve (3.2.14). We will see that, even though we will be able to solve (3.2.13) analytically, we generally have to use numerical methods to solve (3.2.14).

To solve (3.2.13) we make the following decomposition [128], which introduces functions λ and V_j ,

$$X_j = \frac{3D-5}{D-3} V_j - \left(\partial_j \lambda + x^k \partial_j V_k \right). \quad (3.2.16)$$

*There seems to be some mismatch in the literature as to the definition of “bare mass”. Brill and Lindquist [133] clearly define it as $\bar{\mu}_{(i)}$, in our notation, and they even point out that the sum of the bare masses is different from the total mass. However, Brandt and Brügmann [135] seem to define bare mass as $\mu_{(i)}$.

Equation (3.2.13) then gets the form

$$\frac{3D-5}{D-3}\hat{\Delta}V_j - x^k\partial_j\hat{\Delta}V_k - 2\frac{D-2}{D-1}\partial_j\hat{\Delta}\lambda - \frac{D-3}{D-1}\partial_j(x^k\hat{\Delta}V_k) = 0,$$

which is solved if

$$\begin{cases} \hat{\Delta}V_j = 0 \\ \hat{\Delta}\lambda = 0 \end{cases}. \quad (3.2.17)$$

We have reduced our problem to solving two flat space Laplace equations, which have known analytical solutions. In the following we analyse some possible solutions [128].

3.2.2.1 Moving black holes

We start by choosing a solution for the system (3.2.17) of the form

$$V_j = -\frac{2\pi}{(D-2)\mathcal{A}_{D-2}}\frac{P_j}{r^{D-3}}, \quad \lambda = 0. \quad (3.2.18)$$

\mathcal{A}_N stands for the area of the N -dimensional hypersphere. P_j are constants that, as we shall see, will be the linear momentum of the black hole in the j direction.

For such an *ansatz* we have, from equation (3.2.16),

$$X_j = -\frac{2\pi}{(D-2)\mathcal{A}_{D-2}}\frac{1}{r^{D-3}}\left(\frac{3D-5}{D-3}P_j + (D-3)n^k P_k n_j\right), \quad (3.2.19)$$

where $n_j \equiv \frac{x_j}{r}$, and from equations (3.2.15) and (3.2.12)

$$\hat{A}^{ij} = \frac{4\pi(D-1)}{(D-2)\mathcal{A}_{D-2}}\frac{1}{r^{D-2}}\left(n^i P^j + n^j P^i - n_k P^k \hat{\gamma}_{ij} + (D-3)n^i n^j P^k n_k\right). \quad (3.2.20)$$

The ADM linear momentum is given by [134, 128, 119]

$$P_i^{\text{ADM}} = \frac{1}{8\pi}\int_{r\rightarrow\infty}(K_{ij}n^j - Kn_i)\sqrt{q}d^{D-2}y, \quad (3.2.21)$$

where we perform the integration on a hypersphere at infinity; $\sqrt{q}d^{D-2}y$ denotes the induced metric on the hypersphere—using spherical coordinates $\sqrt{q}d^{D-2}y = r^{D-2}d\Omega_{D-2}$ (we can write the induced metric on a hypersphere \mathcal{S} of radius r as $ds_{\mathcal{S}}^2 = q_{AB}dy^A dy^B = r^2 d\Omega_{D-2}^2$, and thus $q = \det q_{AB} = (r^2)^{D-2} d\Omega_{D-2}^2$); n^j is its unit normal vector.

Reminding ourselves that

$$\begin{aligned} \hat{A}^{ij} &= \psi^{\frac{2D+1}{D-3}} A^{ij}, \\ \hat{A}_{ij} &= \psi^2 A_{ij}, \\ K_{ij} &= A_{ij} \quad (\text{we are considering } K = 0), \\ \psi &= 1 + O\left(\frac{1}{r}\right), \end{aligned}$$

we see that we can calculate the ADM linear momentum without knowing ψ . Plugging (3.2.20) into (3.2.21) we have that $P_i^{\text{ADM}} = P_i$, as expected.

Finally, we note that, as the equation (3.2.1) is linear, we can superimpose N solutions of the type (3.2.21) corresponding to N Schwarzschild black holes,

$$\hat{A}_P^{ab} = \sum_{i=1}^N \hat{A}_{P(i)}^{ab}, \quad (3.2.22)$$

where

$$\hat{A}_{P(i)}^{ab} = \frac{4\pi(D-1)}{(D-2)A_{D-2}} \frac{1}{r_{(i)}^{D-2}} \left(n_{(i)}^a P_{(i)}^b + n_{(i)}^b P_{(i)}^a - (n_{(i)})_k P_{(i)}^k \hat{\gamma}_{ab} + (D-3)n_{(i)}^a n_{(i)}^b P_{(i)}^k (n_{(i)})_k \right), \quad (3.2.23)$$

where $n_{(i)}^a \equiv \frac{x^a - x_{(i)}^a}{r_{(i)}}$ and the parameters $P_{(i)}^a$ correspond to the ADM momentum of the i th black hole when the separation of the holes is very large.

3.2.2.2 Spinning black holes

Let us now try a solution of (3.2.17) of the form

$$V_j = \frac{(D-3)\pi}{(D-2)A_{D-2}} \frac{J_{jk} n^k}{r^{D-2}}, \quad \lambda = 0, \quad (3.2.24)$$

where $J_{jk} = -J_{kj}$ will be the angular momentum tensor of the black hole. We have

$$X_j = \frac{4\pi}{A_{D-2}} J_{jk} \frac{x^k}{r^{D-1}}, \quad (3.2.25)$$

and

$$\hat{A}^{ij} = -\frac{4\pi(D-1)}{A_{D-2}} \frac{1}{r^{D-1}} \left(J^{jk} n_k n^i + J^{ik} n_k n^j \right). \quad (3.2.26)$$

The ADM angular momentum is given by (when $K = 0$) [134, 128, 119]

$$J_{ik}^{\text{ADM}} = \frac{1}{8\pi} \int_{r \rightarrow \infty} (x_i K_{jk} - x_j K_{ik}) n^k \sqrt{q} d^{D-2}y. \quad (3.2.27)$$

We can check that $J_{ik}^{\text{ADM}} = J_{ik}$.

For $D = 4$ we can define the angular momentum vector in the usual way,

$$J^i = \frac{1}{2} \epsilon^{ijk} J_{kl}. \quad (3.2.28)$$

As in the previous section, we can now superimpose N solutions of the type (3.2.26),

$$\hat{A}_J^{ab} = \sum_{i=1}^N \hat{A}_{J(i)}^{ab}, \quad (3.2.29)$$

where

$$\hat{A}_{J(i)}^{ab} = -\frac{4\pi(D-1)}{A_{D-2}} \frac{1}{r_{(i)}^{D-1}} \left(J_{(i)}^{bk}(n_{(i)})_k n_{(i)}^a + J_{(i)}^{ak}(n_{(i)})_k n_{(i)}^b \right). \quad (3.2.30)$$

The parameters $J_{(i)}^{ab}$ correspond to the ADM angular momentum of the i th black hole when the separation of the holes is very large.

3.2.2.3 General case

We can now combine the results from the two previous sections to build a solution of N black holes with arbitrary linear momentum and spin,

$$\hat{A}^{ab} = \sum_{i=1}^N \left(\hat{A}_{P(i)}^{ab} + \hat{A}_{J(i)}^{ab} \right), \quad (3.2.31)$$

where $\hat{A}_{P(i)}^{ab}$ and $\hat{A}_{J(i)}^{ab}$ are given by equations (3.2.23) and (3.2.30).

Note: This solution reduces to the Brill-Lindquist momentarily static solution ($K_{ij} = 0$) when $P_{(i)}^a = 0 = J_{(i)}^{ab}$. For $N = 1$, $J^{ab} \neq 0$ and $P^a = 0$, however, we do *not* have a slice of a Kerr (or, for the higher-dimensional case, Myers-Perry) spacetime. It has actually been shown [136] that there is no foliation of the Kerr spacetime that is axisymmetric, conformally flat, and reduces smoothly to the Schwarzschild solution in the non-rotating limit.* This means that our Bowen-York solution with $J^{ab} \neq 0$ does represent a rotating black hole, but not a stationary one. For the four-dimensional case, when we evolve the data, the system emits gravitational radiation and eventually settles down to the Kerr solution [137, 138] (the higher-dimensional case has not been studied as of yet). This spurious gravitational radiation has no desirable physical properties and is often referred to as “junk radiation”.

3.2.2.4 Conformal factor

We still need to solve equation (3.2.14) to get the full initial data, and now there is no hope of finding an analytical solution. Let us rewrite the equation we need to solve,

$$\hat{\Delta}\psi + \frac{D-3}{4(D-2)} \psi^{-\frac{3D-5}{D-3}} \hat{A}^{ij} \hat{A}_{ij} = 0, \quad (3.2.32)$$

with \hat{A}_{ij} given by (3.2.31).

Along the lines of [135] and [128] we write

$$\psi = \psi_{\text{BL}} + u, \quad (3.2.33)$$

*For the four-dimensional Kerr solution, but there is no reason to believe that the higher-dimensional case is any different.

where

$$\psi_{\text{BL}} \equiv 1 + \sum_{i=1}^N \frac{\mu^{(i)}}{4r^{(i)D-3}}. \quad (3.2.34)$$

Equation (3.2.32) then takes the form

$$\hat{\Delta}u + \frac{D-3}{4(D-2)} \hat{A}^{ab} \hat{A}_{ab} \psi^{-\frac{3D-5}{D-3}} = 0. \quad (3.2.35)$$

For the four-dimensional case, Brandt and Brügmann [135] were able to show the existence and uniqueness of C^2 solutions for the above equations. Furthermore, the solution for u is found on an Euclidean manifold; we do not need to impose inner boundary conditions to avoid singularities. Brandt and Brügmann also show that this solution is the “natural” generalisation of the Brill-Lindquist initial data, i.e., each puncture represents the infinity of another asymptotically flat region of the spacetime and there is no way to travel from one sheet to the other except through the “upper” sheet. The higher-dimensional case has not been thoroughly studied, but it is believed that the situation is not radically different [128].

3.3 Final remarks

In this chapter we introduced tools for the construction of initial data for higher-dimensional numerical relativity. As we mentioned, even though the four-dimensional case has been thoroughly studied, the study of initial data for higher-dimensional systems started only very recently. As of yet, only Brill-Lindquist and Bowen-York initial data have been generalised, but with these two approaches one is already able to construct quite interesting systems for vacuum spacetimes. In particular, the Bowen-York approach allows us to write initial data for spacetimes with an arbitrary number of moving and spinning black holes.

For the four-dimensional case there are also powerful computer codes to solve the elliptic equation (3.2.35), such as the spectral method presented by Ansorg et al. [139].

In upcoming chapters we will present a generalisation of the spectral solver in [139] that solves (3.2.35) for black hole binaries in $D \geq 5$ dimensions with non-vanishing initial boost, and preserves the spectral convergence properties observed in four dimensions.

Chapter 4

Numerical implementation

In chapter 2, we have written Einstein’s field equations explicitly in a form (usually referred to as ADM equations (2.6.3)) which one could easily give to a computer to evolve. As can be seen from this system of equations, though, we are still not quite ready to perform numerical evolutions: we still need to say what happens with the variables α (lapse) and β^i (shift). The Einstein equations have not imposed any evolution equation for these variables. This reflects our coordinate freedom: fixing the lapse function and shift vector is a gauge choice, which one could in principle do arbitrarily. It turns out, though, that a good choice is crucial to achieve a stable numerical integration. We will in this chapter briefly discuss why this is the case and write down the equations we will be using throughout this work.

It also turns out, as researchers eventually found out empirically in the 1990s when full three-dimensional evolutions were attempted using the ADM equations, that this system of evolution equations is not well suited to obtain long-term stable numerical simulations. This is now known to be due to the fact that the ADM equations are only weakly hyperbolic.* People started experimenting with reformulations of the ADM equations and in 1998 Baumgarte and Shapiro—revisiting an earlier formulation based on conformal transformations by Nakamura, Oohara and Kojima [140] and Shibata and Nakamura [141]—showed that this formulation behaved much better than ADM for all cases considered [142]. This formulation became known as BSSN (Baumgarte, Shapiro, Shibata and Nakamura) and is today the most popular scheme used to evolve Einstein’s equations.

It was later realised that indeed the BSSN scheme can be shown to be strongly hyperbolic, as opposed to only weakly hyperbolic like in the ADM case, and thus well-posed, e.g. [143, 144].

We should also mention that other successful evolution schemes do exist. Most notably, the *generalised harmonic coordinates* approach, e.g. [145], was successfully used by Pretorius in the first ever evolutions of binary black holes through several orbits [18]. Giving a full overview of such topics falls outside of the scope of this work. We will in this chapter merely introduce the BSSN evolution equations and we refer the interested reader to, e.g., [120, 121]

*The ADM equations do allow stable evolutions in spherical symmetry, though (see e.g. [120]).

for comprehensive overviews.

We close this chapter by introducing the numerical code itself used for all the simulations to be presented.

In this chapter, we restrict ourselves to the four-dimensional case (for completeness, we present in appendix 4.A the higher-dimensional BSSN scheme), and therefore spatial (Latin) indices are here restricted to $i = 1, 2, 3$.

4.1 BSSN formulation

As we have just mentioned, if we were to try and evolve Einstein's equations in the ADM formulation (2.6.3) (supplemented with the gauge conditions we will introduce in the next section) we would find out that the system is severely unstable. In this section we recast the evolution equations in the BSSN form, which allows for stable numerical evolutions.

We start by performing a conformal decomposition of the spatial metric γ_{ij} in the following way (observe it is going to be a different decomposition from the one performed in the study of the initial data)

$$\tilde{\gamma}_{ij} \equiv \chi \gamma_{ij}. \quad (4.1.1)$$

The conformal factor χ can in principle be freely prescribed. In the BSSN scheme, one imposes that the determinant of the conformal metric be equal to the determinant of the flat metric η_{ij} ,

$$\chi = \left(\frac{\gamma}{\eta} \right)^{-1/3}. \quad (4.1.2)$$

By construction, we have

$$\det \tilde{\gamma}_{ij} = \eta. \quad (4.1.3)$$

Since we will stick to Cartesian coordinate systems throughout this work, we will always have $\eta = 1 = \det \tilde{\gamma}_{ij}$, which makes χ a scalar density with weight $-2/3$.

Just like in equation (3.1.4), we decompose the extrinsic curvature K_{ij} into trace and trace-free parts and apply the conformal transformation we used for the metric to the traceless part,

$$K_{ij} \equiv \chi^{-1} \left(\tilde{A}_{ij} + \frac{K}{3} \tilde{\gamma}_{ij} \right). \quad (4.1.4)$$

Let us now find evolution equations for the variables we have introduced $(\chi, \tilde{\gamma}_{ij}, K, \tilde{A}_{ij})$. Inserting (4.1.1) and (4.1.4) into (2.6.3a) and (2.6.3b) we have, taking the trace,

$$\partial_t \chi = \beta^k \partial_k \chi + \frac{2}{3} \chi (\alpha K - \partial_k \beta^k), \quad (4.1.5)$$

and

$$\partial_t K = \beta^k \partial_k K - \nabla^k \partial_k \alpha + \alpha \left(\tilde{A}^{ij} \tilde{A}_{ij} + \frac{1}{3} K^2 \right) + 4\pi \alpha (E + S), \quad (4.1.6)$$

where in this last equation we have already used the constraint (2.6.3c) to eliminate the Ricci scalar. Substituting back we can compute the remaining evolution equations, which take the form

$$\partial_t \tilde{\gamma}_{ij} = \beta^k \partial_k \tilde{\gamma}_{ij} + 2\tilde{\gamma}_{k(i} \partial_{j)} \beta^k - \frac{2}{3} \tilde{\gamma}_{ij} \partial_k \beta^k - 2\alpha \tilde{A}_{ij}, \quad (4.1.7)$$

and

$$\begin{aligned} \partial_t \tilde{A}_{ij} = & \beta^k \partial_k \tilde{A}_{ij} + 2\tilde{A}_{k(i} \partial_{j)} \beta^k - \frac{2}{3} \tilde{A}_{ij} \partial_k \beta^k + \chi (\alpha R_{ij} - \nabla_i \partial_j \alpha)^{\text{TF}} \\ & + \alpha \left(K \tilde{A}_{ij} - 2\tilde{A}_i{}^k \tilde{A}_{kj} \right) - 8\pi\alpha \left(\chi S_{ij} - \frac{S}{3} \tilde{\gamma}_{ij} \right), \end{aligned} \quad (4.1.8)$$

where $^{\text{TF}}$ denotes the trace-free part, e.g., $R_{ij}^{\text{TF}} = R_{ij} - \frac{1}{3} \gamma_{ij} R$.

We further need to decompose the Ricci tensor in two parts,

$$R_{ij} = \tilde{R}_{ij} + R_{ij}^\chi \quad (4.1.9)$$

where R_{ij}^χ only depends on χ and \tilde{R}_{ij} is the Ricci tensor associated with the metric $\tilde{\gamma}_{ij}$. This term contains mixed second derivatives of the metric, something that is undesirable. For stable numerical integration, the following ‘‘conformal connection’’ variable was introduced [141, 142]

$$\tilde{\Gamma}^i \equiv \tilde{\gamma}^{jk} \tilde{\Gamma}_{jk}^i = -\partial_j \tilde{\gamma}^{ij}. \quad (4.1.10)$$

In terms of this conformal connection, the conformal Ricci tensor then takes the form

$$\tilde{R}_{ij} = -\frac{1}{2} \tilde{\gamma}^{kl} \partial_l \partial_k \tilde{\gamma}_{ij} + \tilde{\gamma}_{k(i} \partial_{j)} \tilde{\Gamma}^k - \partial_k \tilde{\gamma}_{l(i} \partial_{j)} \tilde{\gamma}^{kl} + \frac{1}{2} \tilde{\Gamma}^k \partial_k \tilde{\gamma}_{ij} - \tilde{\Gamma}_{ik}^l \tilde{\Gamma}_{jl}^k. \quad (4.1.11)$$

As we can see, the first term in this expression, which involves a Laplacian, is the only explicit second order derivative operator acting on $\tilde{\gamma}_{ij}$. All the mixed second derivatives have been absorbed in derivatives of $\tilde{\Gamma}^i$. Since the BSSN scheme considers $\tilde{\Gamma}^i$ to be an independent variable, we need an evolution equation for it. Acting on (4.1.10) and interchanging the time and space derivatives we get

$$\partial_t \tilde{\Gamma}^i = -\partial_j \left(\beta^k \partial_k \tilde{\gamma}^{ij} - 2\tilde{\gamma}^{k(j} \partial_k \beta^{i)} + \frac{2}{3} \tilde{\gamma}^{ij} \partial_k \beta^k + 2\alpha \tilde{A}^{ij} \right). \quad (4.1.12)$$

We further use the momentum constraint (2.6.3d) to do away with the divergence of the extrinsic curvature and obtain

$$\begin{aligned} \partial_t \tilde{\Gamma}^i = & \beta^k \partial_k \tilde{\Gamma}^i - \tilde{\Gamma}^k \partial_k \beta^i + \frac{2}{3} \tilde{\Gamma}^i \partial_k \beta^k + 2\alpha \tilde{\Gamma}_{jk}^i \tilde{A}^{jk} + \frac{1}{3} \tilde{\gamma}^{ij} \partial_j \partial_k \beta^k + \tilde{\gamma}^{jk} \partial_j \partial_k \beta^i \\ & - \frac{4}{3} \alpha \tilde{\gamma}^{ij} \partial_j K - \tilde{A}^{ij} (3\alpha \chi^{-1} \partial_j \chi + 2\partial_j \alpha) - 16\pi\alpha \chi^{-1} j^i. \end{aligned} \quad (4.1.13)$$

The full system of evolution equations is then

$$\partial_t \tilde{\gamma}_{ij} = \beta^k \partial_k \tilde{\gamma}_{ij} + 2\tilde{\gamma}_{k(i} \partial_j) \beta^k - \frac{2}{3} \tilde{\gamma}_{ij} \partial_k \beta^k - 2\alpha \tilde{A}_{ij}, \quad (4.1.14a)$$

$$\partial_t \chi = \beta^k \partial_k \chi + \frac{2}{3} \chi (\alpha K - \partial_k \beta^k), \quad (4.1.14b)$$

$$\begin{aligned} \partial_t \tilde{A}_{ij} = & \beta^k \partial_k \tilde{A}_{ij} + 2\tilde{A}_{k(i} \partial_j) \beta^k - \frac{2}{3} \tilde{A}_{ij} \partial_k \beta^k + \chi (\alpha R_{ij} - \nabla_i \partial_j \alpha)^{\text{TF}} \\ & + \alpha \left(K \tilde{A}_{ij} - 2\tilde{A}_i{}^k \tilde{A}_{kj} \right) - 8\pi\alpha \left(\chi S_{ij} - \frac{S}{3} \tilde{\gamma}_{ij} \right), \end{aligned} \quad (4.1.14c)$$

$$\partial_t K = \beta^k \partial_k K - \nabla^k \partial_k \alpha + \alpha \left(\tilde{A}^{ij} \tilde{A}_{ij} + \frac{1}{3} K^2 \right) + 4\pi\alpha (E + S), \quad (4.1.14d)$$

$$\begin{aligned} \partial_t \tilde{\Gamma}^i = & \beta^k \partial_k \tilde{\Gamma}^i - \tilde{\Gamma}^k \partial_k \beta^i + \frac{2}{3} \tilde{\Gamma}^i \partial_k \beta^k + 2\alpha \tilde{\Gamma}_{jk}^i \tilde{A}^{jk} + \frac{1}{3} \tilde{\gamma}^{ij} \partial_j \partial_k \beta^k + \tilde{\gamma}^{jk} \partial_j \partial_k \beta^i \\ & - \frac{4}{3} \alpha \tilde{\gamma}^{ij} \partial_j K - \tilde{A}^{ij} (3\alpha \chi^{-1} \partial_j \chi + 2\partial_j \alpha) - 16\pi\alpha \chi^{-1} j^i, \end{aligned} \quad (4.1.14e)$$

where $R_{ij} = \tilde{R}_{ij} + R_{ij}^\chi$

$$\begin{aligned} \tilde{R}_{ij} = & -\frac{1}{2} \tilde{\gamma}^{kl} \partial_l \partial_k \tilde{\gamma}_{ij} + \tilde{\gamma}_{k(i} \partial_j) \tilde{\Gamma}^k - \partial_k \tilde{\gamma}_{l(i} \partial_j) \tilde{\gamma}^{kl} + \frac{1}{2} \tilde{\Gamma}^k \partial_k \tilde{\gamma}_{ij} - \tilde{\Gamma}_{ik}^l \tilde{\Gamma}_{jl}^k, \\ R_{ij}^\chi = & \frac{1}{2} \chi^{-1} \left(\partial_i \partial_j \chi - \partial_k \chi \tilde{\Gamma}_{ij}^k \right) - \frac{1}{4} \chi^{-2} \partial_i \chi \partial_j \chi - \frac{1}{2} \tilde{\gamma}_{ij} \chi^{-1} \partial_k \chi \tilde{\Gamma}^k \\ & + \frac{1}{2} \tilde{\gamma}_{ij} \tilde{\gamma}^{kl} \chi^{-1} \left(\partial_k \partial_l \chi - \frac{3}{2} \chi^{-1} \partial_k \chi \partial_l \chi \right). \end{aligned} \quad (4.1.15)$$

Source terms are determined by

$$\begin{aligned} E & \equiv n^\alpha n^\beta T_{\alpha\beta}, & j_i & \equiv -\gamma_i^\alpha n^\beta T_{\alpha\beta}, \\ S_{ij} & \equiv \gamma^\alpha{}_i \gamma^\beta{}_j T_{\alpha\beta}, & S & \equiv \gamma^{ij} S_{ij}. \end{aligned} \quad (4.1.16)$$

The above system of evolution equations (4.1.14) is known as the BSSN evolution scheme and has proven to be extremely robust for numerical evolutions of Einstein's field equations. Numerous other schemes do exist; most, however, offer no substantial advantage over BSSN, which has remained extremely popular. We will use BSSN for all our numerical evolutions.

4.2 Gauge conditions

We now turn our attention to the gauge conditions. The first question to ask is: what is a "good" choice for α and β^i ? An obvious first choice, also the simplest possible, is to impose the so-called *geodesic slicing* (also known as *Gaussian normal coordinates*),

$$\alpha = 1, \quad \beta^i = 0. \quad (4.2.1)$$

This choice was in fact used in the pioneering work by Hahn and Lindquist [8]; it is now known, however, that it is actually a very bad choice for long-term evolutions. We can

intuitively understand why this is the case. First we note from equation (2.2.6) that the Eulerian observers have zero acceleration and thus follow geodesics (hence the name of this slicing). In the presence of black holes (or other gravitational sources), geodesics tend to focus. Coordinate observers will then collide with each other, consequently forming coordinate singularities and crashing the numerical evolution. We thus need better gauge choices. It falls outside the scope of this work to give an overview on the merits and disadvantages of the different conditions that have been proposed throughout the years. We will simply state and motivate the conditions we will be using.

4.2.1 1+log slicing

A famous choice for the lapse function is known as *maximal slicing*, which corresponds to imposing that the trace of the extrinsic curvature vanishes throughout the evolution,

$$K = 0. \quad (4.2.2)$$

A nice property of this condition is its *singularity avoidance*. We can see this by taking the trace of equation (2.1.18), which with (4.2.2) implies $\nabla_\mu n^\mu = 0$, an incompressibility condition on the velocity field of the Eulerian observers. This prevents the observers from converging and the subsequent appearance of a coordinate singularity, as in the geodesic slicing case. Such a property is very much desirable, making maximal slicing an attractive choice. There is an enormous disadvantage, however, which is the need to solve an elliptic equation at every time step during the numerical evolution in order to ensure (4.2.2). We therefore would like to have conditions that mimic this property of maximal slicing, yet with a hyperbolic character.

Such a choice is the so-called *1+log slicing*,

$$(\partial_t - \mathcal{L}_\beta)\alpha = -2\alpha K, \quad (4.2.3)$$

which, being a hyperbolic equation, is trivial to implement numerically, has been shown to be extremely robust and mimics the singularity avoidance properties of maximal slicing [146].

This condition gets its name from the fact that, when imposing $\beta^i = 0$, equation (4.2.3) can be integrated to give

$$\alpha = 1 + \log \gamma, \quad (4.2.4)$$

where we recall that $\gamma \equiv \det \gamma_{ij}$.

4.2.2 Gamma driver

Having chosen a condition for the lapse function, it remains then to say what happens to the shift.

A possible choice, known as the *Gamma freezing* condition, is the following

$$\partial_t \tilde{\Gamma}^i = 0. \quad (4.2.5)$$

Using equation (4.1.14e), we can write the above condition as an elliptic equation for β^i . This condition is related to the “minimal distortion” shift condition [147], which attempts to choose coordinates such that the time derivative of the 3-metric $\partial_t \gamma_{ij}$ is minimised. The disadvantage is once again the need to solve an elliptic equation at each time step.

Researchers have therefore proposed alternative conditions, using parabolic or hyperbolic equations, that mimic the minimal distortion condition with good approximation. The following choice (and variations thereof) is now extremely popular

$$(\partial_t - \mathcal{L}_\beta) \beta^i = \tilde{\Gamma}^i - \eta_\beta \beta^i, \quad (4.2.6)$$

where η_β is a function of spacetime. This is known as the *Gamma driver* condition [148].

Use of these gauge choices proved crucial for the 2005 breakthroughs using the *moving puncture* technique [20, 19].

4.3 Numerical code

Having chosen a set of evolution equations (4.1.14), gauge conditions (4.2.3), (4.2.6) and prescriptions for setting initial data (see chapter 3), it remains then to assemble everything on a numerical code. Such a task is far from trivial. One of the main reasons is that the presence of very different scales in the spacetimes that are usually evolved requires the use of *mesh refinement*. The problem is further complicated by the need to use parallel computing and to store large amounts of data.

All numerical simulations that will be presented in subsequent chapters have been performed by adapting the LEAN code [149], initially designed for 3 + 1 vacuum spacetimes by U. Sperhake. LEAN is based on the CACTUS computational toolkit [150], it employs the BSSN formulation of the Einstein equations [141, 142] (with fourth order discretisation in the spatial derivatives) with the moving puncture method [20, 19], uses the CARPET package for Berger-Oliger mesh refinement [151, 152], the spectral solver described in [139] for 3 + 1 initial data and Thornburg’s AHFINDERDIRECT [153, 154] for horizon finding (see section 5.2).

For a given numerical simulation our numerical grid will consist of two types of cubic refinement levels: n outer levels centred on the origin (remaining stationary throughout the simulation), and m inner levels centred around each black hole (and following these as the simulation progresses). The following notation (which we will make frequent use of)

$$\{(256, 128, 74, 24, 12, 6) \times (1.5, 0.75), h = 1/48\}$$

specifies a grid with six fixed outer components of “radius” 256, 128, 74, 24, 12 and 6 respectively and two refinement levels with two components each with radius 1.5 and 0.75 centred around either black hole. The resolution is $h = 1/48$ on the finest level and successively decreases to $2^7/48 = 8/3$ on the outermost level. Further details about LEAN may be found in [149].

4.A D -dimensional BSSN equations

For completeness, we here write the full D -dimensional BSSN equations, as first written in [97]. These equations can be derived in a procedure entirely analogous to the one outlined in section 4.1.

$$\partial_t \tilde{\gamma}_{ij} = \beta^k \partial_k \tilde{\gamma}_{ij} + 2\tilde{\gamma}_{k(i} \partial_j) \beta^k - \frac{2}{D-1} \tilde{\gamma}_{ij} \partial_k \beta^k - 2\alpha \tilde{A}_{ij}, \quad (4.A.1a)$$

$$\partial_t \chi = \beta^k \partial_k \chi + \frac{2}{D-1} \chi (\alpha K - \partial_k \beta^k), \quad (4.A.1b)$$

$$\begin{aligned} \partial_t \tilde{A}_{ij} = & \beta^k \partial_k \tilde{A}_{ij} + 2\tilde{A}_{k(i} \partial_j) \beta^k - \frac{2}{D-1} \tilde{A}_{ij} \partial_k \beta^k + \chi (\alpha R_{ij} - \nabla_i \partial_j \alpha)^{\text{TF}} \\ & + \alpha \left(K \tilde{A}_{ij} - 2\tilde{A}_i^k \tilde{A}_{kj} \right) - 8\pi \alpha \left(\chi S_{ij} - \frac{S}{D-1} \tilde{\gamma}_{ij} \right), \end{aligned} \quad (4.A.1c)$$

$$\partial_t K = \beta^k \partial_k K - \nabla^k \partial_k \alpha + \alpha \left(\tilde{A}^{ij} \tilde{A}_{ij} + \frac{1}{D-1} K^2 \right) + \frac{8\pi}{D-2} \alpha [(D-3)E + S], \quad (4.A.1d)$$

$$\begin{aligned} \partial_t \tilde{\Gamma}^i = & \beta^k \partial_k \tilde{\Gamma}^i - \tilde{\Gamma}^k \partial_k \beta^i + \frac{2}{D-1} \tilde{\Gamma}^i \partial_k \beta^k + 2\alpha \tilde{\Gamma}_{jk}^i \tilde{A}^{jk} + \frac{1}{D-1} \tilde{\gamma}^{ij} \partial_j \partial_k \beta^k + \tilde{\gamma}^{jk} \partial_j \partial_k \beta^i \\ & - 2\frac{D-2}{D-1} \alpha \tilde{\gamma}^{ij} \partial_j K - \tilde{A}^{ij} \left((D-1)\alpha \frac{\partial_j \chi}{\chi} + 2\partial_j \alpha \right) - 16\pi \alpha \chi^{-1} j^i, \end{aligned} \quad (4.A.1e)$$

where $^{\text{TF}}$ denotes the trace-free part and the Ricci tensor R_{ij} is further split into $R_{ij} = \tilde{R}_{ij} + R_{ij}^X$, where

$$\begin{aligned} \tilde{R}_{ij} = & -\frac{1}{2} \tilde{\gamma}^{kl} \partial_l \partial_k \tilde{\gamma}_{ij} + \tilde{\gamma}_{k(i} \partial_j) \tilde{\Gamma}^k - \partial_k \tilde{\gamma}_{l(i} \partial_j) \tilde{\gamma}^{kl} + \frac{1}{2} \tilde{\Gamma}^k \partial_k \tilde{\gamma}_{ij} - \tilde{\Gamma}_{ik}^l \tilde{\Gamma}_{jl}^k \\ R_{ij}^X = & \frac{D-3}{2} \chi^{-1} \left(\partial_i \partial_j \chi - \partial_k \chi \tilde{\Gamma}_{ij}^k \right) - \frac{D-3}{4} \chi^{-2} \partial_i \chi \partial_j \chi - \frac{1}{2} \tilde{\gamma}_{ij} \chi^{-1} \partial_k \chi \tilde{\Gamma}^k \\ & + \frac{1}{2} \tilde{\gamma}_{ij} \tilde{\gamma}^{kl} \chi^{-1} \left(\partial_k \partial_l \chi - \frac{(D-1)}{2} \chi^{-1} \partial_k \chi \partial_l \chi \right) \end{aligned} \quad (4.A.2)$$

Equations (4.1.14) can be recovered with $D = 4$.

Chapter 5

Wave extraction and horizon finding

We have thus far covered, essentially, all the main tools necessary to successfully evolve Einstein's equations on a computer. Assuming then that we can specify some arbitrary initial configuration and evolve it for as long as we like, we are still faced with the most important task: how to extract the relevant physical information. Recalling that the coordinate system used throughout the evolution is designed to be well suited to the numerical evolution and not for human-readability, we easily convince ourselves that it is not trivial to read physical information from the numerical output. For this purpose, tools were developed to enable the extraction of the gravitational wave information from a numerical simulation and, when dealing with black hole spacetimes, information about the black hole's horizon.

In this chapter we will briefly outline the two main methods of extracting gravitational wave information and the corresponding waveforms: the gauge invariant formalism of Kodama and Ishibashi [155, 156]—itself a generalisation to higher-dimensional spacetimes of the Regge-Wheeler-Zerilli formalism [157, 158], later put in a gauge-invariant form by Moncrief [159]—and the *Newman-Penrose formalism* [160]. We will also mention the very basics regarding finding (apparent) black hole horizons.

5.1 Wave extraction

Gravitational waves are ripples in the shape of spacetime that propagate information at finite speed, just as water waves are ripples in the shape of an ocean's surface. They are one of the most important predictions of general relativity. These waves have never been directly detected; there is, however, strong indirect evidence for its existence since the discovery of the famous binary pulsar PSR 1913+16 (also known as the Hulse-Taylor binary pulsar after its discoverers [161]), whose orbital period change is consistent with the general relativistic prediction for energy loss via gravitational wave emission. Other systems have since been

uncovered, allowing for even more stringent tests, e.g. [162, 163].

These waves are generated by dynamical gravitational fields—roughly speaking, accelerated bodies in non-spherically symmetric motion will emit gravitational waves*. As they propagate throughout spacetime, they carry with them information about the physical properties of the system that produced them. By measuring them with gravitational wave detectors—such as the already mentioned LIGO, Virgo, GEO and TAMA—we can have a brand new window opening up to the universe. The likelihood of such detections is greatly enhanced if one can use theoretical gravitational wave signals coming from possible astrophysical sources as templates. Our task here is to briefly introduce the techniques used to generate such templates from numerical simulations.

Before we begin, let us make one last comment. We have mentioned energy carried away by gravitational radiation, but as we know there is no notion of local energy of a gravitational field, so some care has to be taken here. The usual procedure is to write a stress-energy tensor for the metric fluctuations that is second-order in said fluctuations (the same way that the stress-energy tensor associated with a scalar or electromagnetic field is second order in the fields). Modulo some subtleties, such a quantity can be constructed, and meaningful quantities can be extracted from it. We will not be giving details on its derivation or the subtleties involved (see, e.g., [164, 165, 166]), but merely present the relevant formulæ that will be of use to us.

We will start by recalling known four-dimensional results that will be of use. In the weak-field limit, we can write the metric tensor as the Minkowski metric plus perturbations,

$$g_{\mu\nu} = \eta_{\mu\nu} + h_{\mu\nu}, \quad |h_{\mu\nu}| \ll 1. \quad (5.1.1)$$

To first order in $h_{\mu\nu}$, the Riemann tensor is

$${}^{(4)}R_{\alpha\beta\mu\nu} = \frac{1}{2}(\partial_\beta\partial_\mu h_{\alpha\nu} + \partial_\alpha\partial_\nu h_{\beta\mu} - \partial_\beta\partial_\nu h_{\alpha\mu} - \partial_\alpha\partial_\mu h_{\beta\nu}). \quad (5.1.2)$$

It is useful to introduce the usual *trace reversed perturbation*

$$\bar{h}_{\mu\nu} \equiv h_{\mu\nu} - \frac{h}{2}\eta_{\mu\nu}. \quad (5.1.3)$$

Imposing the *Lorenz gauge*

$$\partial_\mu \bar{h}^{\mu\nu} = 0, \quad (5.1.4)$$

the linearised field equations reduce to

$$\square \bar{h}_{\mu\nu} = -16\pi T_{\mu\nu}, \quad (5.1.5)$$

where \square is the d'Alembertian operator in flat space. In vacuum we get the usual wave equation

$$\square \bar{h}_{\mu\nu} = 0. \quad (5.1.6)$$

*For a system to emit gravitational waves the third time derivative of its quadrupole moment has to be non-zero.

Since the Lorenz gauge does not completely fix our degrees of freedom, we can further impose the *transverse-traceless (TT) gauge*

$$u^\nu \bar{h}_{\mu\nu}^{\text{TT}} = 0, \quad \bar{h}^{\text{TT}\mu}{}_\mu = 0, \quad (5.1.7)$$

where, to simplify, we can use a Cartesian coordinate system $\eta_{\mu\nu} = \text{diag}(-1, 1, 1, 1)$ and u^ν is a unit timelike vector. The second equation reflects the fact that there is no propagating scalar mode in general relativity. Note that in this gauge $\bar{h}_{\mu\nu} = h_{\mu\nu}$. With the constraints (5.1.4) and (5.1.7) we are left with two degrees of freedom (in four dimensions; generically, in D -dimensions, we have $D(D-3)/2$ degrees of freedom). We can write the plane-wave solution of equation (5.1.6) subject to the constraints (5.1.7) in the usual form

$$h_{\mu\nu}^{\text{TT}} = A_{\mu\nu} e^{ik_\sigma x^\sigma}, \quad (5.1.8)$$

taking $k^\mu = (1, 0, 0, 1)$ and where

$$A_{\mu\nu} = \begin{pmatrix} 0 & 0 & 0 & 0 \\ 0 & h_+ & h_\times & 0 \\ 0 & h_\times & -h_+ & 0 \\ 0 & 0 & 0 & 0 \end{pmatrix}. \quad (5.1.9)$$

h_+ and h_\times are the two independent polarisations of the gravitational wave, known as “plus” and “cross” polarisations.

It can be shown (e.g. [166, 123, 121]) that the outgoing energy flux carried by the gravitational radiation is given by

$$F_{\text{GW}} = \frac{dE_{\text{GW}}}{dt} = \lim_{r \rightarrow \infty} \frac{r^2}{16\pi} \int \left(\dot{h}_+^2 + \dot{h}_\times^2 \right) d\Omega. \quad (5.1.10)$$

To derive this formula, we need to expand Einstein’s equations up to second order perturbations. Terms that are quadratic in the first order perturbations of the metric, after suitable averaging, can then be viewed as sources, constituting an effective stress-energy tensor for gravitational waves. This stress-energy tensor can then be used to compute energy and momentum carried away by the gravitational radiation.

5.1.1 Newman-Penrose formalism

We now briefly describe the Newman-Penrose formalism. This formalism (also known as the *spin-coefficient formalism*) introduced by Newman and Penrose in 1962 [160] is an alternative way to write Einstein’s equations which has proven to be extremely useful in many situations in general relativity, such as in searches of exact solutions, black hole perturbation theory and studies of gravitational radiation. There is a whole literature devoted to this formalism. For its application in numerical simulations, we mention for instance the books by Alcubierre [120], Baumgarte & Shapiro [121] and references therein. Here we will only state the basic equations that we will need and refer the reader to relevant publications where appropriate.

In this section we restrict ourselves to four-dimensional spacetimes since this formalism has not been generalised to higher dimensions.*

This formalism starts with introducing a null complex tetrad $\{l, k, m, \bar{m}\}$ satisfying

$$-l \cdot k = 1 = m \cdot \bar{m}, \quad (5.1.11)$$

where \bar{m} is the complex conjugate of m and all other inner products vanish.

We further note that the four-dimensional Riemann tensor ${}^{(4)}R^\alpha{}_{\beta\gamma\delta}$ has 20 independent components. Its trace, the Ricci tensor ${}^{(4)}R_{\alpha\beta}$ has 10. The remaining degrees of freedom are encoded in the Weyl tensor ${}^{(4)}C_{\alpha\beta\gamma\delta}$, defined as

$${}^{(4)}C_{\alpha\beta\gamma\delta} \equiv {}^{(4)}R_{\alpha\beta\gamma\delta} - {}^{(4)}g_{\alpha[\gamma}{}^{(4)}R_{\delta]\beta} + {}^{(4)}g_{\beta[\gamma}{}^{(4)}R_{\delta]\alpha} + \frac{1}{3}{}^{(4)}g_{\alpha[\gamma}{}^{(4)}g_{\delta]\beta}{}^{(4)}R. \quad (5.1.12)$$

The Newman-Penrose formalism encodes these degrees of freedom in a set of complex scalars, often called *Newman-Penrose scalars*. The ten independent components of the Weyl tensor are encoded in the five complex scalars Ψ_0, \dots, Ψ_4 (often also called *Weyl scalars*).[†] All of these scalars are formed by contracting the Weyl tensor (and the Ricci) with the complex null tetrad. Since there is no unique choice for a null tetrad satisfying (5.1.11), the choice of this tetrad will affect the Weyl scalars and their physical interpretation.

For a class of such tetrads, the so-called *quasi-Kinnersley frames*, Ψ_1 and Ψ_3 both vanish, and we can interpret Ψ_0 and Ψ_4 as measures of the incoming and outgoing gravitational radiation, whereas Ψ_2 can be interpreted as the ‘‘Coulombic’’ part. Ψ_4 and Ψ_0 are defined as[‡]

$$\Psi_0 \equiv {}^{(4)}C_{\alpha\beta\gamma\delta} l^\alpha m^\beta l^\gamma m^\delta. \quad (5.1.13)$$

$$\Psi_4 \equiv {}^{(4)}C_{\alpha\beta\gamma\delta} k^\alpha \bar{m}^\beta k^\gamma \bar{m}^\delta. \quad (5.1.14)$$

Since (for the suitable tetrad we mentioned above) the latter quantity encodes the outgoing gravitational wave signal, this will be of particular use to us (Ψ_0 will also be of use in section 7.2).

In practice, we construct l , k and m from an orthonormal triad $e_{\hat{r}}, e_{\hat{\theta}}, e_{\hat{\phi}}$ orthogonal to the unit timelike vector $e_{\hat{t}}$

$$\begin{aligned} l &= \frac{1}{\sqrt{2}} (e_{\hat{t}} + e_{\hat{r}}), \\ k &= \frac{1}{\sqrt{2}} (e_{\hat{t}} - e_{\hat{r}}), \\ m &= \frac{1}{\sqrt{2}} (e_{\hat{\theta}} + ie_{\hat{\phi}}). \end{aligned} \quad (5.1.15)$$

*A related formalism also based on spin-coefficients, the *Geroch-Held-Penrose* (GHP) [167] formalism, has been extended to higher dimensions [168].

[†]The ten independent components of the Ricci tensor are analogously written in terms of four scalars and three complex scalars, but we will never make use of these quantities in this work.

[‡]Different sign conventions exist in the literature.

We refer the reader to [169] for a review of the formalism; here we merely note that asymptotically the triad vectors $e_{\hat{r}}$, $e_{\hat{\theta}}$, $e_{\hat{\phi}}$ behave as the unit radial, polar and azimuthal vectors.

Having chosen our tetrad, we can now compute an explicit expression for Ψ_4 using the definition (5.1.14). In the TT gauge, this can be shown to be, for outgoing waves [120, 121]

$$\Psi_0 = 0, \quad (5.1.16)$$

$$\Psi_4 = -\ddot{h}_+ + i\ddot{h}_\times, \quad (5.1.17)$$

whereas for ingoing waves, we have instead

$$\Psi_0 = \ddot{h}_+ - i\ddot{h}_\times, \quad (5.1.18)$$

$$\Psi_4 = 0, \quad (5.1.19)$$

where $\dot{}$ denotes a time derivative and h_+ and h_\times are the amplitudes of the plus and cross polarisation of the gravitational wave (5.1.8), (5.1.9). Herein lies the usefulness of the Ψ_4 scalar.

It is useful to perform a multipolar decomposition by projecting Ψ_4 onto spherical harmonics of spin weight $s = -2$ (cf., e.g., appendix D of [120]):

$$\Psi_4(t, \theta, \phi) = \sum_{l,m} \psi^{lm}(t) Y_{lm}^{-2}(\theta, \phi). \quad (5.1.20)$$

In terms of these multipoles, the radiated flux is given by the expressions [160, 170]

$$F_{\text{GW}} = \frac{dE_{\text{GW}}}{dt} = \lim_{r \rightarrow \infty} \frac{r^2}{16\pi} \sum_{l,m} \left| \int_{-\infty}^t dt' \psi^{lm}(t') \right|^2. \quad (5.1.21)$$

In Einstein-Maxwell theory, the right-hand-side of Einstein's equations reads

$$T_{\mu\nu} = \frac{1}{4\pi} \left[F_{\mu}{}^{\lambda} F_{\nu\lambda} - \frac{1}{4} g_{\mu\nu} F^{\lambda\sigma} F_{\lambda\sigma} \right], \quad (5.1.22)$$

where $F^{\mu\nu}$ is the Maxwell-Faraday tensor. In such cases, we can analogously extract the electromagnetic wave signal in the form of the scalar functions, Φ_1 and Φ_2 [160, 170], defined as

$$\Phi_1 \equiv \frac{1}{2} F_{\mu\nu} (l^\mu k^\nu + \bar{m}^\mu \bar{m}^\nu), \quad (5.1.23)$$

$$\Phi_2 \equiv F_{\mu\nu} \bar{m}^\mu k^\nu. \quad (5.1.24)$$

For outgoing waves at infinity, these quantities behave as

$$\Phi_1 \sim \frac{1}{2} (E_{\hat{r}} + iB_{\hat{r}}), \quad \Phi_2 \sim E_{\hat{\theta}} - iE_{\hat{\phi}}. \quad (5.1.25)$$

Again, it is useful to perform a multipolar decomposition by projecting Φ_1 and Φ_2 onto spherical harmonics of spin weight 0 and -1 respectively:

$$\Phi_1(t, \theta, \phi) = \sum_{l,m} \phi_1^{lm}(t) Y_{lm}^0(\theta, \phi), \quad (5.1.26)$$

$$\Phi_2(t, \theta, \phi) = \sum_{l,m} \phi_2^{lm}(t) Y_{lm}^{-1}(\theta, \phi). \quad (5.1.27)$$

In terms of these multipoles, the radiated flux is given by the expressions [160, 170]

$$F_{\text{EM}} = \frac{dE_{\text{EM}}}{dt} = \lim_{r \rightarrow \infty} \frac{r^2}{4\pi} \sum_{l,m} \left| \phi_2^{lm}(t) \right|^2. \quad (5.1.28)$$

We see from (5.1.25) that Φ_2 encodes the radiative modes.

5.1.2 Kodama-Ishibashi

A different approach to extract gravitational wave perturbations is that of the gauge-invariant Moncrief formalism [159]. This has been generalised to higher dimensions by Kodama and Ishibashi (KI) [155, 156], and we will review this approach in the following.

In the KI formalism, we start by writing the metric element as a background metric plus a perturbation

$$\bar{g}_{AB} = \bar{g}_{AB}^{(0)} + \delta\bar{g}_{AB}. \quad (5.1.29)$$

The background spacetime has the form

$$d\bar{s}^{2(0)} = \bar{g}_{AB}^{(0)} dx^A dx^B = g_{ab}^{(0)} dx^a dx^b + r^2 d\Omega_{D-2} = g_{ab}^{(0)} dx^a dx^b + r^2 \Omega_{\bar{a}\bar{b}} dx^{\bar{a}} dx^{\bar{b}}, \quad (5.1.30)$$

where the x^A coordinates refer to the whole spacetime ($A = 0, \dots, D-1$), $x^a = t, r$ and $\Omega_{\bar{a}\bar{b}}$ is the metric on the unit $(D-2)$ -sphere S^{D-2} .

The procedure now is to expand the metric perturbations \bar{g}_{AB} into harmonic functions. These exist in three flavours—scalar, vector and tensor harmonics. Metric perturbations can then be written in terms of gauge invariant quantities [155]:

Tensor harmonics $\mathbb{T}_{\bar{a}\bar{b}}$ satisfy

$$\left(\hat{\Delta} + k^2 \right) \mathbb{T}_{\bar{a}\bar{b}} = 0, \quad (5.1.31)$$

with the properties

$$\mathbb{T}^{\bar{a}}_{\bar{a}} = 0, \quad \mathbb{T}^{\bar{a}}_{\bar{b};\bar{a}} = 0. \quad (5.1.32)$$

where $\hat{\Delta}$ is the Laplace-Beltrami operator on S^{D-2} and $;\bar{a}$ denotes the covariant derivative with respect to the metric $\Omega_{\bar{a}\bar{b}}$ on the sphere. Note that we will omit the index labelling the harmonic throughout this discussion.

For tensor-type perturbations, the metric perturbations $\delta\bar{g}_{AB} = h_{AB}$ are expanded in the following way

$$h_{ab} = 0, \quad h_{a\bar{a}} = 0, \quad h_{\bar{a}\bar{b}} = 2r^2 H_T \mathbb{T}_{\bar{a}\bar{b}}, \quad (5.1.33)$$

where $H_T = H_T(t, r)$ (again, we leave the harmonic labels implicit), and note that there is sum over the indices of the harmonics in this expression.

Vector harmonics $\mathbb{V}_{\bar{a}}$ satisfy

$$\left(\hat{\Delta} + k^2\right) \mathbb{V}_{\bar{a}} = 0, \quad (5.1.34)$$

$$\mathbb{V}^{\bar{a}}{}_{;\bar{a}} = 0. \quad (5.1.35)$$

from this, vector-type harmonic tensors can further be defined

$$\mathbb{V}_{\bar{a}\bar{b}} = -\frac{1}{2k} (\mathbb{V}_{\bar{a};\bar{b}} + \mathbb{V}_{\bar{b};\bar{a}}). \quad (5.1.36)$$

We expand the vector-type perturbations as

$$h_{ab} = 0, \quad h_{a\bar{a}} = r f_a \mathbb{V}_{\bar{a}}, \quad h_{\bar{a}\bar{b}} = 2r^2 H_T \mathbb{V}_{\bar{a}\bar{b}}, \quad (5.1.37)$$

where $f_a = f_a(t, r)$.

Scalar harmonics \mathbb{S} satisfy

$$\left(\hat{\Delta} + k^2\right) \mathbb{S} = 0, \quad (5.1.38)$$

from which we can build scalar-type vector harmonics

$$\mathbb{S}_{\bar{a}} = -\frac{1}{k} \mathbb{S}_{;\bar{a}}, \quad (5.1.39)$$

and scalar-type harmonic tensors

$$\mathbb{S}_{\bar{a}\bar{b}} = \frac{1}{k^2} \mathbb{S}_{;\bar{a}\bar{b}} + \frac{1}{D-2} \Omega_{\bar{a}\bar{b}} \mathbb{S}. \quad (5.1.40)$$

We expand scalar-type perturbations as

$$h_{ab} = f_{ab} \mathbb{S}, \quad h_{a\bar{a}} = r f_a \mathbb{S}_{\bar{a}}, \quad h_{\bar{a}\bar{b}} = 2r^2 (H_L \Omega_{\bar{a}\bar{b}} \mathbb{S} + H_T \mathbb{S}_{\bar{a}\bar{b}}), \quad (5.1.41)$$

where $f_{ab} = f_{ab}(t, r)$.

For $l > 1$, the metric perturbations can be expressed in terms of the following gauge-invariant variables [155]

$$F = H_L + \frac{1}{D-2} H_T + \frac{1}{r} X_a r^{|a}, \quad (5.1.42)$$

$$F_{ab} = f_{ab} + X_{a|b} + X_{b|a},$$

where we have defined

$$X_a = \frac{r}{k} \left(f_a + \frac{r}{k} H_{T|a} \right), \quad (5.1.43)$$

and we denote the covariant derivative with respect to the metric $g_{ab}^{(0)}$ with a subscript $|a$.

Impressively, a *master function* Φ can be defined that, from the perturbed Einstein equations, can be shown to obey the simple wave equation [156]

$$(\square - V(r))\Phi = 0, \quad (5.1.44)$$

where \square is the d'Alembertian operator with respect to $g_{ab}^{(0)}$, and the form of the potential $V(r)$ depends on whether one is considering scalar, vector or tensor perturbations.

The master function Φ is specially useful since it encodes the gravitational waveform; the energy emitted via gravitational radiation can also be computed quite effortlessly. Writing the index l explicitly, the energy flux in each l -multipole is [171]

$$\frac{dE_l}{dt} = \frac{1}{32\pi} \frac{D-3}{D-2} k^2 (k^2 - D + 2) (\Phi_{,t}^l)^2. \quad (5.1.45)$$

The total energy emitted in the process is then

$$E = \sum_{l=2}^{\infty} \int_{-\infty}^{+\infty} dt \frac{dE_l}{dt}. \quad (5.1.46)$$

5.2 Horizon finding

When evolving black hole spacetimes, besides the wave extraction tools, physical information can also be read from its horizon properties. A black hole is a region of spacetime from which no future directed null geodesic can reach an outside observer. Its surface, the *event horizon*, acts therefore as a one-way membrane. In asymptotically flat spacetimes, the event horizon can be defined as the boundary of the causal past of future null infinity. It is thus a global concept, requiring information from the whole spacetime to be located. From the point of view of a numerical evolution, this is not very useful since one would like to know about the location of the black hole as the simulation progresses.

A more useful concept in this regard is that of the *apparent horizon*. It is defined as the *outermost marginally trapped surface* on a given spatial hypersurface—a closed surface on which the expansion of (outgoing) null geodesics vanishes. The apparent horizon is a local concept, depending only on information present on the given hypersurface, making it an ideal diagnostic tool for numerical evolutions.

Given a spatial section Σ of a spacetime with 3-metric γ_{ij} and extrinsic curvature K_{ij} , the expansion of null geodesics can be shown to be

$$\Theta_{\pm} = \pm \nabla_i s^i + K_{ij} s^i s^j - K \quad (5.2.1)$$

where ∇ is the covariant derivative with respect to the 3-metric γ_{ij} and s^i is the spatial normal to the apparent horizon surface within Σ . Θ_+ is the expansion of the outgoing null geodesics, Θ_- the expansion of the ingoing ones. The (black hole) apparent horizon is then defined by the following equation

$$\nabla_i s^i + K_{ij} s^i s^j - K = 0. \quad (5.2.2)$$

General purpose tools exist to solve this equation during numerical evolutions; for an overview see e.g. [172] and references therein.

Finally, we emphasise that apparent horizons are slicing dependent. It is possible, for instance, to foliate the Schwarzschild spacetime in such a way that there is no apparent horizon [173] (the event horizon, being a global quantity, is an intrinsic property of the geometry and is thus always present). The presence of an apparent horizon, however, does imply the existence of a section of an event horizon exterior to it (assuming cosmic censorship and $R_{\mu\nu}k^\mu k^\nu \geq 0$ for all null k^μ [174]).

Chapter 6

Higher-dimensional numerical relativity

As mentioned in the Introduction, the ability to perform fully non-linear numerical evolutions of Einstein’s field equations in higher-dimensional scenarios has tremendous potential to answer fundamental questions in physics, with possible applications including studies of the AdS/CFT duality, explorations of TeV-gravity scenarios and the study of higher-dimensional black hole solutions.

Numerical relativity in higher dimensions has only recently started being explored, with pioneering works including those in [92, 97, 175, 57, 176]. In this chapter, we will describe the approach of [175, 176].

The formalism we will present allows us to consider two classes of models, which are generalisations of axial symmetry to higher dimensional spacetimes: a $D \geq 5$ dimensional vacuum spacetime with an $SO(D - 2)$ isometry group, and a $D \geq 6$ dimensional vacuum spacetime with an $SO(D - 3)$ isometry group. The former class allows studies of head-on collisions of non-spinning black holes. The latter class allows to model black hole collisions with impact parameter and with spinning black holes, as long as all the dynamics take place on a single plane. This class includes the most interesting physical configurations relevant to accelerator—and cosmic ray—physics (in the context of TeV-scale gravity), and to the theoretical properties of higher-dimensional black objects (such as stability and phase diagrams).

In section 6.1, we introduce a general dimensional reduction procedure from D -dimensional vacuum general relativity to a lower dimension model; in section 6.2 we specialise the equations obtained to the case where the D -dimensional spacetime has an $SO(D - 2)$ isometry group, perform the 3+1 splitting of space and time and write down a system of evolution equations; in section 6.3 we outline the construction of relevant initial data, following the approach of [177]; in section 6.4, we discuss some code tests, introduce a wave extraction procedure and present results. We end this chapter with a discussion in 6.5.

We note that in this chapter, due to the necessity of introducing multiple covariant derivatives, we shall explain the notation as we go along.

6.1 Dimensional reduction

The starting point of our formalism is a dimensional reduction from D -dimensional general relativity in vacuum to a lower dimensional model.

The isometry group of a Schwarzschild (or, for $D > 4$, Tangherlini [178]) black hole is $SO(D-1) \times \mathbb{R}$. For a head-on collision of two non-rotating black holes, the isometry is further reduced to $SO(D-2)$: indeed, neither the time direction nor the direction of the collision correspond to symmetries, but a rotation of the remaining $D-2$ spatial directions leaves the spacetime invariant.

One can take advantage of this symmetry to reduce the spacetime dimensionality. This can be accomplished by writing Einstein's equations in D dimensions in a coordinate system which makes the symmetry manifest, allowing for a lower dimensional interpretation of the D -dimensional Einstein's equations (in the spirit of the Kaluza-Klein reduction). We remark, however, that we do not perform a compactification; rather, we perform a dimensional reduction by isometry, as first proposed by Geroch [179]. The extra dimensions manifest themselves in the lower dimensionality as a source of Einstein's equations, defined on the lower dimensional manifold.

In the original proposal of Geroch [179] the symmetry space was $SO(2)$. This approach has been applied to numerical relativity, see for instance [180, 181, 182]; a five dimensional extension, with the same symmetry space, has been derived in [183]. A generalisation to coset manifolds (like the sphere S^n) was given by Cho in [184, 185], but in these papers the complete form of Einstein's equations was not presented.

Following the approach by Cho [184], we will start by deriving the general equations obtained doing a dimensional reduction by isometry. We will afterwards focus on the isometry group of the S^n sphere and present the equations obtained with a dimensional reduction to four dimensions, as well as their numerical implementation.

6.1.1 General formalism

The most general D -dimensional metric \bar{g}_{AB} , $A = 0, \dots, d-1, \dots, (D-1)$, can be written in the following form (in the coordinate basis $\partial_A = (\partial_\mu, \partial_{\bar{i}})$)

$$d\bar{s}^2 = \bar{g}_{AB} dx^A dx^B = \left(g_{\mu\nu} + e^2 \kappa^2 g_{\bar{i}\bar{j}} \bar{B}_\mu^{\bar{i}} \bar{B}_\nu^{\bar{j}} \right) dx^\mu dx^\nu + 2e\kappa \bar{B}_\mu^{\bar{i}} g_{\bar{i}\bar{j}} dx^\mu dx^{\bar{j}} + g_{\bar{i}\bar{j}} dx^{\bar{i}} dx^{\bar{j}}, \quad (6.1.1)$$

where $\mu = 0, \dots, d-1$ and $\bar{i} = d, \dots, D-1$. κ is a scale parameter and e a coupling constant. This metric is fully general and *not* an *ansatz*.

Assume that \bar{g}_{AB} admits an m -dimensional isometry G , generated by m Killing vector fields which we express as (assuming $D - d$ is large enough)

$$\xi_a = K_a^{\bar{i}} \partial_{\bar{i}}, \quad (6.1.2)$$

$a = 1, \dots, m \equiv \dim G$. The Killing vector fields form the Lie algebra of G , satisfying

$$\mathcal{L}_{\xi_a} \bar{g}_{AB} = 0, \quad (6.1.3)$$

$$[\xi_a, \xi_b] = \frac{1}{\kappa} f^c{}_{ab} \xi_c. \quad (6.1.4)$$

Defining

$$[\xi_a, \partial_{\bar{i}}] \equiv F_{a\bar{i}}^{\bar{j}} \partial_{\bar{j}} = - \left(\partial_{\bar{i}} K_a^{\bar{j}} \right) \partial_{\bar{j}},$$

and the “dual” form $\phi_{\bar{i}}^a$ to the Killing fields ξ_a by

$$\phi_{\bar{i}}^a K_a^{\bar{j}} = \delta_{\bar{i}}^{\bar{j}},$$

we can derive, from (6.1.3),

$$\begin{aligned} \partial_{\bar{i}} g_{\bar{j}\bar{k}} &= F_{\bar{i}\bar{j}}^{\bar{l}} g_{\bar{l}\bar{k}} + F_{\bar{i}\bar{k}}^{\bar{l}} g_{\bar{j}\bar{l}}, \\ \partial_{\bar{j}} B_{\bar{\mu}}^{\bar{k}} &= -F_{\bar{j}\bar{i}}^{\bar{k}} B_{\bar{\mu}}^{\bar{i}}, \\ \partial_{\bar{i}} g_{\bar{\mu}\bar{\nu}} &= 0, \end{aligned} \quad (6.1.5)$$

where $F_{\bar{i}\bar{j}}^{\bar{k}} \equiv \phi_{\bar{i}}^a F_{a\bar{j}}^{\bar{k}}$.

Our goal is to compute the Ricci tensor of metric (6.1.1), which is more easily done in a non-coordinate basis. Details of the computation can be found in appendix 6.A; here we mention only the final result.

We first *define* the “covariant derivatives” $\nabla_{\bar{\mu}}$ and $\nabla_{\bar{j}}$ as

$$\nabla_{\bar{\sigma}} T_{\bar{k}\bar{\mu}}^{\bar{i}\alpha} \equiv D_{\bar{\sigma}} T_{\bar{k}\bar{\mu}}^{\bar{i}\alpha} + \mathcal{F}_{\bar{\sigma}\bar{i}}^{\bar{l}} T_{\bar{k}\bar{\mu}}^{\bar{l}\alpha} - \mathcal{F}_{\bar{\sigma}\bar{k}}^{\bar{l}} T_{\bar{l}\bar{\mu}}^{\bar{i}\alpha} + \Gamma_{\lambda\bar{\sigma}}^{\alpha} T_{\bar{k}\bar{\mu}}^{\bar{i}\lambda} - \Gamma_{\bar{\mu}\bar{\sigma}}^{\lambda} T_{\bar{k}\bar{\lambda}}^{\bar{i}\alpha}, \quad (6.1.6)$$

$$\nabla_{\bar{j}} T_{\bar{k}\bar{\mu}}^{\bar{i}\alpha} \equiv \partial_{\bar{j}} T_{\bar{k}\bar{\mu}}^{\bar{i}\alpha} + \Gamma_{\bar{l}\bar{j}}^{\bar{i}} T_{\bar{k}\bar{\mu}}^{\bar{l}\alpha} - \Gamma_{\bar{k}\bar{j}}^{\bar{l}} T_{\bar{l}\bar{\mu}}^{\bar{i}\alpha}, \quad (6.1.7)$$

where

$$\begin{aligned} D_{\bar{\mu}} &\equiv \partial_{\bar{\mu}} - e\kappa B_{\bar{\mu}}^{\bar{i}} \partial_{\bar{i}} \\ \mathcal{F}_{\bar{\mu}\bar{i}}^{\bar{k}} &\equiv e\kappa \partial_{\bar{i}} B_{\bar{\mu}}^{\bar{k}} = -e\kappa F_{\bar{i}\bar{j}}^{\bar{k}} B_{\bar{\mu}}^{\bar{j}}, \\ \mathcal{F}_{\bar{i}\bar{j}}^{\bar{k}} &\equiv 0, \\ \mathcal{F}_{\bar{\mu}\bar{\nu}}^{\bar{k}} &\equiv -e\kappa G_{\bar{\mu}\bar{\nu}}^{\bar{k}} \equiv -e\kappa \left(\partial_{\bar{\mu}} B_{\bar{\nu}}^{\bar{k}} - \partial_{\bar{\nu}} B_{\bar{\mu}}^{\bar{k}} + e\kappa t_{\bar{i}\bar{j}}^{\bar{k}} B_{\bar{\mu}}^{\bar{i}} B_{\bar{\nu}}^{\bar{j}} \right), \\ t_{\bar{j}\bar{k}}^{\bar{i}} &\equiv F_{\bar{j}\bar{k}}^{\bar{i}} - F_{\bar{k}\bar{j}}^{\bar{i}}, \end{aligned} \quad (6.1.8)$$

and both connections are metric,

$$\begin{aligned} \nabla_{\bar{\sigma}} g_{\bar{\mu}\bar{\nu}} &= \partial_{\bar{\sigma}} g_{\bar{\mu}\bar{\nu}} - \Gamma_{\bar{\mu}\bar{\sigma}}^{\lambda} g_{\lambda\bar{\nu}} - \Gamma_{\bar{\nu}\bar{\sigma}}^{\lambda} g_{\bar{\mu}\lambda} = 0, \\ \nabla_{\bar{k}} g_{\bar{i}\bar{j}} &\equiv \partial_{\bar{k}} g_{\bar{i}\bar{j}} - \Gamma_{\bar{i}\bar{k}}^{\bar{l}} g_{\bar{l}\bar{j}} - \Gamma_{\bar{j}\bar{k}}^{\bar{l}} g_{\bar{i}\bar{l}} = 0. \end{aligned}$$

Note however that

$$\nabla_\sigma g_{\bar{i}\bar{j}} \equiv D_\sigma g_{\bar{i}\bar{j}} - \mathcal{F}^{\bar{k}}_{\sigma\bar{i}} g_{\bar{k}\bar{j}} - \mathcal{F}^{\bar{k}}_{\sigma\bar{j}} g_{\bar{i}\bar{k}} \neq 0.$$

The Ricci tensor of (6.1.1) is (see appendix 6.A)

$$\bar{R}_{\bar{i}\bar{j}} = R_{\bar{i}\bar{j}} - \frac{1}{4} g^{\bar{k}\bar{l}} \nabla_\beta g_{\bar{k}\bar{l}} \nabla^\beta g_{\bar{i}\bar{j}} + \frac{1}{2} g^{\bar{k}\bar{l}} \nabla_\beta g_{\bar{i}\bar{k}} \nabla^\beta g_{\bar{j}\bar{l}} + \frac{1}{4} g^{\alpha\lambda} g^{\beta\rho} g_{\bar{j}\bar{k}} g_{\bar{i}\bar{l}} \mathcal{F}^{\bar{k}}_{\beta\lambda} \mathcal{F}^{\bar{l}}_{\rho\alpha} - \frac{1}{2} \nabla^\beta \nabla_\beta g_{\bar{i}\bar{j}}, \quad (6.1.9)$$

$$\begin{aligned} \bar{R}_{\bar{\mu}\bar{i}} &= e\kappa \bar{R}_{\bar{i}\bar{j}} B_{\bar{\mu}}^{\bar{j}} + \frac{1}{2} g^{\alpha\lambda} \nabla_\alpha \left(g_{\bar{i}\bar{k}} \mathcal{F}^{\bar{k}}_{\lambda\mu} \right) + \frac{1}{4} g^{\bar{k}\bar{l}} \nabla_\beta g_{\bar{k}\bar{l}} g^{\beta\lambda} \mathcal{F}^{\bar{m}}_{\lambda\mu} g_{\bar{i}\bar{m}} + \frac{1}{2} \nabla_{\bar{k}} \left(g^{\bar{k}\bar{l}} \nabla_\mu g_{\bar{l}\bar{i}} \right) \\ &\quad - \frac{1}{2} \nabla_{\bar{i}} \left(g^{\bar{k}\bar{l}} \nabla_\mu g_{\bar{k}\bar{l}} \right) = \bar{R}_{\bar{i}\bar{\mu}}, \end{aligned} \quad (6.1.10)$$

$$\begin{aligned} \bar{R}_{\bar{\mu}\bar{\nu}} &= R_{\bar{\mu}\bar{\nu}} + 2e\kappa B_{(\bar{\mu}}^{\bar{i}} \bar{R}_{\bar{\nu})\bar{i}} - e^2 \kappa^2 \bar{R}_{\bar{i}\bar{j}} B_{\bar{\mu}}^{\bar{j}} B_{\bar{\nu}}^{\bar{i}} - \frac{1}{2} g^{\alpha\lambda} g_{\bar{i}\bar{j}} \mathcal{F}^{\bar{i}}_{\lambda\mu} \mathcal{F}^{\bar{j}}_{\alpha\nu} - \frac{1}{2} \nabla_\nu \left(g^{\bar{i}\bar{j}} \nabla_\mu g_{\bar{i}\bar{j}} \right) \\ &\quad - \frac{1}{4} g^{\bar{i}\bar{j}} g^{\bar{k}\bar{l}} \nabla_\mu g_{\bar{i}\bar{k}} \nabla_\nu g_{\bar{j}\bar{l}} - \frac{1}{2} \nabla_{\bar{k}} \mathcal{F}^{\bar{k}}_{\bar{\mu}\bar{\nu}}, \end{aligned} \quad (6.1.11)$$

and

$$\begin{aligned} \bar{R} &= R + \tilde{R} - \frac{1}{4} g_{\bar{k}\bar{l}} g^{\alpha\lambda} g^{\mu\nu} \mathcal{F}^{\bar{l}}_{\lambda\mu} \mathcal{F}^{\bar{k}}_{\alpha\nu} - \nabla^\mu \left(g^{\bar{k}\bar{l}} \nabla_\mu g_{\bar{k}\bar{l}} \right) - \frac{1}{4} g^{\bar{k}\bar{i}} g^{\bar{j}\bar{l}} \nabla^\mu g_{\bar{k}\bar{l}} \nabla_\mu g_{\bar{i}\bar{j}} \\ &\quad - \frac{1}{4} g^{\bar{k}\bar{l}} g^{\bar{i}\bar{j}} \nabla^\mu g_{\bar{k}\bar{l}} \nabla_\mu g_{\bar{i}\bar{j}}. \end{aligned} \quad (6.1.12)$$

These are the expressions we were looking for. Equivalent forms can be found in [183, 184].

6.1.2 Examples

6.1.2.1 S^1

As a first (trivial) exercise, we can reproduce the standard Kaluza-Klein expressions. Remember that the Kaluza-Klein metric has the form

$$d\bar{s}^2 = g_{\mu\nu} dx^\mu dx^\nu + e^{2\phi} (dx^5 + A_\mu dx^\mu)^2. \quad (6.1.13)$$

We can easily recover this case from our formalism by making $d = 4$, $D = 5$, $g_{\bar{i}\bar{j}} \rightarrow e^{2\phi}$, $g^{\bar{i}\bar{j}} \rightarrow e^{-2\phi}$, $e\kappa B_{\bar{\mu}}^{\bar{i}} \rightarrow A_\mu$, and $\mathcal{F}^{\bar{i}}_{\bar{\mu}\bar{\nu}} \rightarrow -F_{\mu\nu} \equiv -(\partial_\mu A_\nu - \partial_\nu A_\mu)$ (cf. equations (6.1.8)). Remember also that for the Kaluza-Klein case nothing depends on the ‘‘fifth’’ dimension, and as such $\mathcal{F}^{\bar{i}}_{\bar{\mu}\bar{j}} = 0$. We get the usual Kaluza-Klein expressions,

$$\begin{aligned} \bar{R}_{\bar{i}\bar{j}} &\rightarrow e^{2\phi} \left(\frac{1}{4} e^{2\phi} F^{\alpha\beta} F_{\alpha\beta} - \partial_\alpha \phi \partial^\alpha \phi - \nabla^\alpha \partial_\alpha \phi \right) \equiv \bar{R}_{55}, \\ \bar{R}_{\bar{\mu}\bar{i}} &\rightarrow A_\mu \bar{R}_{55} + \frac{3}{2} \partial^\alpha e^{2\phi} F_{\mu\alpha} + e^{2\phi} \nabla^\alpha F_{\mu\alpha} \equiv \bar{R}_{\mu 5}, \\ \bar{R}_{\bar{\mu}\bar{\nu}} &\rightarrow R_{\bar{\mu}\bar{\nu}} + 2A_{(\bar{\mu}} \bar{R}_{\bar{\nu})5} - A_\mu A_\nu \bar{R}_{55} - \frac{1}{2} e^{2\phi} F^\alpha_{\bar{\mu}} F_{\alpha\nu} - \nabla_\nu \partial_\mu \phi - \partial_\mu \phi \partial_\nu \phi, \\ \bar{R} &\rightarrow R - \frac{1}{4} e^{2\phi} F^{\alpha\beta} F_{\alpha\beta} - 2\nabla^\alpha \partial_\alpha \phi - 2\partial_\alpha \phi \partial^\alpha \phi. \end{aligned}$$

6.1.2.2 S^n

A more interesting case is performing the dimensional reduction on the S^n sphere, $n \equiv D - d \geq 2$. For such an isometry, the Killing vectors ξ_a , $a = 1, \dots, (n+1)n/2$ satisfy

$$[\xi_a, \xi_b] = \epsilon_{ab}{}^c \xi_c, \quad (6.1.14)$$

where $\epsilon_{ab}{}^c$ are the structure constants of $SO(n+1)$. Because the fibre has the minimal dimension necessary to accommodate $n(n+1)/2$ independent Killing vector fields, we may assume without loss of generality that the Killing vector fields have components exclusively along the fibre: $\xi_a = \xi_a^{\bar{i}} \partial_{\bar{i}}$. Furthermore, we may normalise the Killing vectors so that they only depend on the coordinates of the fibre, i.e. $\partial_\mu \xi_a^{\bar{i}} = 0$.

Equation (6.1.3) gives the following conditions

$$\mathcal{L}_{\xi_a} g_{\bar{i}\bar{j}} = 0, \quad (6.1.15)$$

$$\mathcal{L}_{\xi_a} B_{\bar{\mu}}^{\bar{i}} = 0, \quad (6.1.16)$$

$$\mathcal{L}_{\xi_a} g_{\mu\nu} = 0. \quad (6.1.17)$$

These expressions can be interpreted either as Lie derivatives of rank-2 tensors defined on the D -dimensional spacetime, or as Lie derivatives of a rank-2 tensor, a vector and a scalar, which are defined on S^n .

Together with (6.1.14), conditions (6.1.15)-(6.1.17) have the following implications:

-

$$g_{\bar{i}\bar{j}} = f(x^\mu) h_{\bar{i}\bar{j}}^{S^n}, \quad (6.1.18)$$

because, from (6.1.15), $g_{\bar{i}\bar{j}}$ admits the maximal number of Killing vector fields and thus must be the metric on a maximally symmetric space at each x^μ . Due to (6.1.14) this space must be the S^n sphere. $h_{\bar{i}\bar{j}}^{S^n}$ denotes the metric on an S^n with unit radius;

-

$$g_{\mu\nu} = g_{\mu\nu}(x^\mu), \quad (6.1.19)$$

because the Killing vector fields ξ_a act transitively on the fibre and therefore the base space metric must be independent of the fibre coordinates;

-

$$B_{\bar{\mu}}^{\bar{i}} = 0, \quad (6.1.20)$$

because equation (6.1.16) is equivalent to

$$[\xi_a, B_{\bar{\mu}}] = 0, \quad (6.1.21)$$

and there exist no non-trivial vector fields on S^n for $n \geq 2$ that commute with all Killing vector fields on the sphere.

We write the metric on the sphere as

$$g_{\bar{i}\bar{j}} dx^{\bar{i}} dx^{\bar{j}} = e^{2\phi} h_{\bar{i}\bar{j}} dx^{\bar{i}} dx^{\bar{j}}, \quad (6.1.22)$$

with $\phi = \phi(x^\mu)$. Our D -dimensional metric has a block diagonal form. Making $g_{\bar{i}\bar{j}} = e^{2\phi} h_{\bar{i}\bar{j}}$ and $B_{\mu}^{\bar{i}} = 0$ in the expressions (6.1.9)-(6.1.12) we get

$$\begin{aligned} \bar{R}_{\bar{i}\bar{j}} &= R_{\bar{i}\bar{j}} - e^{2\phi} h_{\bar{i}\bar{j}} (n \partial^\alpha \phi \partial_\alpha \phi + \nabla^\alpha \partial_\alpha \phi), \\ \bar{R}_{\mu\bar{i}} &= 0, \\ \bar{R}_{\mu\nu} &= R_{\mu\nu} - n \nabla_\nu \partial_\mu \phi - n \partial_\mu \phi \partial_\nu \phi, \\ \bar{R} &= R + \tilde{R} - 2n \nabla^\mu \partial_\mu \phi - n(n+1) \partial^\mu \phi \partial_\mu \phi, \end{aligned} \quad (6.1.23)$$

where $R_{\bar{i}\bar{j}}$ and \tilde{R} are the Ricci tensor and Ricci scalar for the metric (6.1.22). They evaluate to

$$R_{\bar{j}\bar{l}} = (n-1) h_{\bar{j}\bar{l}}, \quad \tilde{R} = n(n-1) e^{-2\phi}. \quad (6.1.24)$$

For D -dimensional vacuum spacetimes $\bar{R}_{AB} = 0 = \bar{R}_{\mu\nu} = \bar{R}_{\bar{i}\bar{j}}$. Using also (6.1.24) on (6.1.23) we get two coupled equations,

$$\begin{aligned} e^{2\phi} (n \partial^\alpha \phi \partial_\alpha \phi + \nabla^\alpha \partial_\alpha \phi) &= n-1 \\ R_{\mu\nu} &= n \nabla_\nu \partial_\mu \phi + n \partial_\mu \phi \partial_\nu \phi \end{aligned} \quad (6.1.25)$$

These equations can also be obtained from the following action

$$\mathcal{S} = \frac{1}{16\pi G_d} \int d^d x \sqrt{-g} e^{n\phi} \left[R + n(n-1) e^{-2\phi} + n(n-1) \partial_\mu \phi \partial^\mu \phi \right]. \quad (6.1.26)$$

Performing the substitution $e^{2\phi} = \lambda^p$ will be useful for the upcoming numerical implementation. We get

$$\begin{aligned} p \lambda^{p-1} \left[\left(\frac{np}{2} - 1 \right) \lambda^{-1} \partial^\alpha \lambda \partial_\alpha \lambda + \nabla^\alpha \partial_\alpha \lambda \right] &= 2(n-1), \\ R_{\mu\nu} &= \frac{np}{2} \lambda^{-1} \nabla_\nu \partial_\mu \lambda + \frac{np}{4} \lambda^{-2} (p-2) \partial_\mu \lambda \partial_\nu \lambda. \end{aligned} \quad (6.1.27)$$

For completeness, we write in appendix 6.B the equations of motion obtained when we write the action (6.1.26) in the Einstein frame.

6.2 Dimensional reduction on a $(D-4)$ -sphere and 3+1 split

In the previous section we were considering a dimensional reduction under the full isometry group of the higher-dimensional spacetime. In the case of head-on black hole collisions, this would produce a reduction down to 3 spacetime dimensions. In practice, we are actually interested in performing a $4 + (D-4)$ split of the D dimensional spacetime. This may be

done as follows. The metric on a unit S^{D-3} may always be written in terms of the line element on a unit S^{D-4} , denoted by $d\Omega_{D-4}$, as follows,

$$h_{\bar{i}\bar{j}}^{S^{D-3}} dx^{\bar{i}} dx^{\bar{j}} = d\theta^2 + \sin^2 \theta d\Omega_{D-4}, \quad (6.2.1)$$

where θ is a polar-like coordinate, $\theta \in [0, \pi]$. Now we introduce four dimensional coordinates, $x^\mu \equiv (x^{\bar{\mu}}, \theta)$, $\mu = 0, 1, 2, 3$, and define a four dimensional metric

$$g_{\mu\nu} dx^\mu dx^\nu = g_{\bar{\mu}\bar{\nu}} dx^{\bar{\mu}} dx^{\bar{\nu}} + f(x^{\bar{\mu}}) d\theta^2, \quad (6.2.2)$$

as well as a new conformal factor

$$\lambda(x^\mu) = \sin^2 \theta g_{\theta\theta}. \quad (6.2.3)$$

As we have seen in the previous sections, the most general D -dimensional metric compatible with $SO(D-2)$ isometry is, for $D \geq 5$

$$ds^2 = g_{\mu\nu} dx^\mu dx^\nu + \lambda(x^\mu) d\Omega_{D-4}. \quad (6.2.4)$$

The geometry (6.2.4) has a manifest $SO(D-3)$ symmetry. We will now perform a dimensional reduction on a $(D-4)$ -sphere, which yields, from the D -dimensional vacuum Einstein equations, a set of $3+1$ dimensional Einstein equations coupled to quasi-matter. In cases with larger symmetry (if $SO(D-2)$ is the full isometry group, for example), the quasi-matter terms do not contain independent degrees of freedom and could in principle be fully determined by the $3+1$ dimensional geometry. For such cases we could perform the dimensional reduction on a $(D-3)$ -sphere instead (which has the full isometry group $SO(D-2)$), which would yield a $2+1$ dimensional system. The former method allows, however, the use of existing numerical codes, with small changes, which justifies our choice.

The $SO(D-3)$ isometry group allows the study of a large class of black hole collisions with impact parameter and with spin: the collisions in which the two black holes always move on the same 2-plane and the only non trivial components of the spin 2-form are on that same 2-plane—see figure 6.1. With our framework we are able, therefore, to describe not only head-on collisions of spinless black holes but also a class of collisions for spinning black holes with impact parameter. As follows from the discussion of (6.1.20), the ansatz (6.2.4) describes general spacetimes with $SO(D-3)$ isometry in $D \geq 6$. We remark that the models with $D \geq 6$ are actually the most interesting for phenomenological studies of large extra dimensions models (see for instance [86]).

Taking (6.2.4) as an ansatz, we see from (6.1.26) that the D -dimensional Einstein-Hilbert action takes the form (for reasons related with the numerical implementation, we now use the variable λ instead of the previously used ϕ)

$$\mathcal{S} = \frac{1}{16\pi G_4} \int d^4x \sqrt{-g} \lambda^{\frac{D-4}{2}} \left[R + (D-4)(D-5) \left(\lambda^{-1} + \frac{1}{4} \lambda^{-2} \partial_\mu \lambda \partial^\mu \lambda \right) \right], \quad (6.2.5)$$

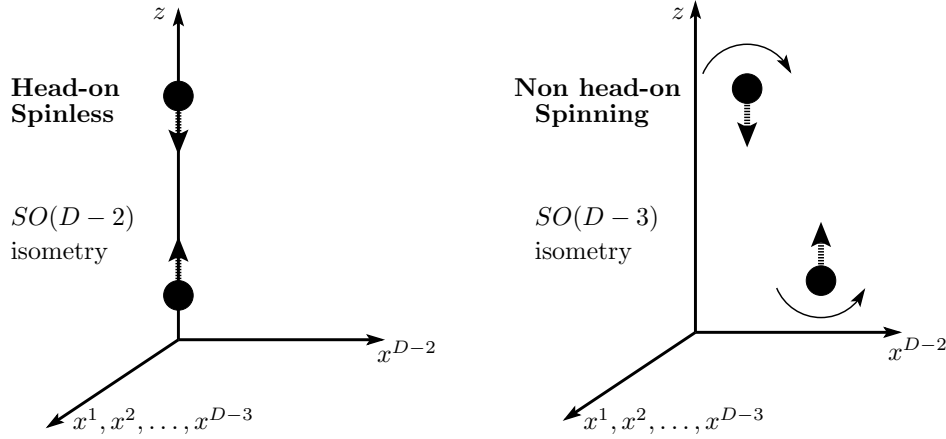


Figure 6.1: D -dimensional representation, using coordinates $(t, x^1, x^2, \dots, x^{D-3}, x^{D-2}, z)$, of two types of black hole collisions: (left panel) head-on for spinless black holes, for which the isometry group is $SO(D-2)$; (right panel) non head-on, with motion on a *single* 2-plane, for black holes spinning in that *same* plane only, for which the isometry group is $SO(D-3)$. The figures make manifest the isometry group in both cases.

where the D -dimensional Newton's constant G_D is related to the four dimensional one G_4 by the area of the unit $D-4$ dimensional sphere: $G_4 = G_D/A^{S^{D-4}}$. Explicitly, the D -dimensional Einstein's equations in vacuum yield the following system of four dimensional equations coupled to a scalar field:

$$R_{\mu\nu} = \frac{D-4}{2\lambda} \left(\nabla_\mu \partial_\nu \lambda - \frac{1}{2\lambda} \partial_\mu \lambda \partial_\nu \lambda \right), \quad (6.2.6)$$

$$\nabla^\mu \partial_\mu \lambda = 2(D-5) - \frac{D-6}{2\lambda} \partial_\mu \lambda \partial^\mu \lambda. \quad (6.2.7)$$

In these equations, all operators are covariant with respect to the four dimensional metric $g_{\mu\nu}$. These could also be obtained from equations (6.1.27) with $p = 1$. The energy momentum tensor is

$$T_{\mu\nu} = \frac{D-4}{16\pi\lambda} \left[\nabla_\mu \partial_\nu \lambda - \frac{1}{2\lambda} \partial_\mu \lambda \partial_\nu \lambda - (D-5)g_{\mu\nu} + \frac{D-5}{4\lambda} g_{\mu\nu} \partial_\alpha \lambda \partial^\alpha \lambda \right]. \quad (6.2.8)$$

With this four dimensional perspective, the usual 3 + 1 split of spacetime can be performed, as outlined in section 2.5. As explained therein, the projection operator $\gamma_{\mu\nu}$ and the normal to the three dimensional hypersurface Σ , n^μ ($n^\mu n_\mu = -1$), are introduced

$$\gamma_{\mu\nu} = g_{\mu\nu} + n_\mu n_\nu, \quad (6.2.9)$$

as well as the lapse α and shift β^μ ,

$$\partial_t = \alpha n + \beta, \quad (6.2.10)$$

where t is the time coordinate. The four dimensional metric is then written in the form

$$ds^2 = g_{\mu\nu} dx^\mu dx^\nu = -\alpha^2 dt^2 + \gamma_{ij} (dx^i + \beta^i dt)(dx^j + \beta^j dt), \quad i, j = 1, 2, 3. \quad (6.2.11)$$

As usual, we introduce the extrinsic curvature $K_{ij} = -\frac{1}{2}\mathcal{L}_n\gamma_{ij}$, which gives the evolution equation for the 3-metric (2.6.2). Defining the variable

$$K_\lambda \equiv -\frac{1}{2}\mathcal{L}_n\lambda = -\frac{1}{2}n^\mu\partial_\mu\lambda, \quad (6.2.12)$$

we further get an evolution equation for λ

$$(\partial_t - \mathcal{L}_\beta)\lambda = -2\alpha K_\lambda. \quad (6.2.13)$$

Using the relation

$$D_\alpha D_\beta\lambda = -K_{\alpha\beta}n^\sigma\partial_\sigma\lambda + \gamma^\mu{}_\alpha\gamma^\nu{}_\beta\nabla_\nu\partial_\mu\lambda, \quad (6.2.14)$$

where D_α denotes now the covariant derivative with respect to the 3-metric $\gamma_{\mu\nu}$ on Σ , and equation (6.2.7) we can get an evolution equation for K_λ . The contraction of equation (6.2.14) with $g^{\alpha\beta}$, yields

$$\square\lambda = \gamma^{ij}D_i\partial_j\lambda - 2KK_\lambda - n^\mu n^\nu\nabla_\nu\partial_\mu\lambda. \quad (6.2.15)$$

Noting that

$$\mathcal{L}_n K_\lambda = n^\mu\partial_\mu K_\lambda = -\frac{1}{2}n^\mu\nabla_\mu n^\nu\partial_\nu\lambda - \frac{1}{2}n^\mu n^\nu\nabla_\mu\partial_\nu\lambda, \quad (6.2.16)$$

and

$$n^\mu\nabla_\mu n^\nu = \frac{1}{\alpha}D^\nu\alpha, \quad (6.2.17)$$

we obtain

$$-n^\mu n^\nu\nabla_\mu\partial_\nu\lambda = 2\mathcal{L}_n K_\lambda + \frac{1}{\alpha}D^\nu\alpha\partial_\nu\lambda. \quad (6.2.18)$$

Noticing also that $D^\nu\alpha\partial_\nu\lambda = \gamma^{ij}\partial_i\alpha\partial_j\lambda$, we write

$$\square\lambda = \gamma^{ij}D_i\partial_j\lambda - 2KK_\lambda + 2\mathcal{L}_n K_\lambda + \frac{1}{\alpha}\gamma^{ij}\partial_i\alpha\partial_j\lambda. \quad (6.2.19)$$

Moreover, from equation

$$D_\mu\lambda = \gamma^\nu{}_\mu\partial_\nu\lambda = \partial_\mu\lambda - 2n_\mu K_\lambda, \quad (6.2.20)$$

we get

$$\partial_\alpha\lambda\partial^\alpha\lambda = \gamma^{ij}\partial_i\lambda\partial_j\lambda - 4K_\lambda^2, \quad (6.2.21)$$

so that the evolution equation for K_λ is

$$\begin{aligned} \frac{1}{\alpha}(\partial_t - \mathcal{L}_\beta)K_\lambda &= -\frac{1}{2\alpha}\gamma^{ij}\partial_i\lambda\partial_j\alpha + (D-5) + KK_\lambda + \frac{D-6}{\lambda}K_\lambda^2 - \frac{D-6}{4\lambda}\gamma^{ij}\partial_i\lambda\partial_j\lambda \\ &\quad - \frac{1}{2}D^k\partial_k\lambda. \end{aligned} \quad (6.2.22)$$

Equations (6.2.13) and (6.2.22) are the evolution equations for the quasi-matter degrees of freedom.

6.2.1 BSSN formulation

For numerical implementation, we write the evolution equations in the BSSN formulation, as introduced in section 4. The evolution equations are those of (4.1.14) with source terms determined by (4.1.16) where the energy momentum tensor is given by equation (6.2.8). A straightforward computation shows that

$$\begin{aligned} \frac{4\pi(E+S)}{D-4} &= -(D-5)\lambda^{-1} + \frac{1}{2}\lambda^{-1}\chi^{3/2}\tilde{\gamma}^{ij}\tilde{D}_i\left(\chi^{-1/2}\partial_j\lambda\right) \\ &\quad + \frac{D-6}{4}\lambda^{-2}\chi\tilde{\gamma}^{ij}\partial_i\lambda\partial_j\lambda - \lambda^{-1}KK_\lambda - (D-5)\lambda^{-2}K_\lambda^2, \end{aligned} \quad (6.2.23a)$$

$$\begin{aligned} \frac{8\pi\chi(S_{ij} - \frac{S}{3}\gamma_{ij})}{D-4} &= \frac{1}{2}\chi\lambda^{-1}\tilde{D}_i\partial_j\lambda + \frac{1}{4}\lambda^{-1}\left(\partial_i\lambda\partial_j\chi + \partial_j\lambda\partial_i\chi - \tilde{\gamma}^{kl}\tilde{\gamma}_{ij}\partial_k\lambda\partial_l\chi\right) - \frac{1}{4}\chi\lambda^{-2}\partial_i\lambda\partial_j\lambda \\ &\quad - \lambda^{-1}K_\lambda\tilde{A}_{ij} - \frac{1}{6}\tilde{\gamma}_{ij}\lambda^{-1}\chi^{3/2}\tilde{\gamma}^{kl}\tilde{D}_k\left(\chi^{-1/2}\partial_l\lambda\right) + \frac{1}{12}\tilde{\gamma}_{ij}\lambda^{-2}\chi\tilde{\gamma}^{kl}\partial_l\lambda\partial_k\lambda, \end{aligned} \quad (6.2.23b)$$

$$\frac{16\pi\chi^{-1}j^i}{D-4} = 2\lambda^{-1}\tilde{\gamma}^{ij}\partial_jK_\lambda - \lambda^{-2}K_\lambda\tilde{\gamma}^{ij}\partial_j\lambda - \tilde{\gamma}^{ik}\tilde{\gamma}^{lj}\tilde{A}_{kl}\lambda^{-1}\partial_j\lambda - \frac{\tilde{\gamma}^{ij}}{3}K\lambda^{-1}\partial_j\lambda, \quad (6.2.23c)$$

where \tilde{D}_i is the covariant derivative with respect to $\tilde{\gamma}_{ij}$.

Finally, the evolution equations for λ and K_λ are

$$(\partial_t - \mathcal{L}_\beta)\lambda = -2\alpha K_\lambda, \quad (6.2.24a)$$

$$\begin{aligned} (\partial_t - \mathcal{L}_\beta)K_\lambda &= \alpha\left\{(D-5) + \frac{6-D}{4}\left[\lambda^{-1}\chi\tilde{\gamma}^{ij}\partial_i\lambda\partial_j\lambda - 4\lambda^{-1}K_\lambda^2\right]\right. \\ &\quad \left.+ KK_\lambda - \frac{1}{2}\chi^{3/2}\tilde{\gamma}^{kl}\tilde{D}_k\left(\chi^{-1/2}\partial_l\lambda\right)\right\} - \frac{1}{2}\chi\tilde{\gamma}^{ij}\partial_j\alpha\partial_i\lambda. \end{aligned} \quad (6.2.24b)$$

As stated before, in the case of head-on collisions of spinless black holes the full symmetry of the D -dimensional system we want to consider makes equations (6.2.24) redundant, by virtue of (6.2.3). This allows to determine the quasi-matter degree of freedom in terms of the three dimensional spatial geometry, at each time slice. The extra symmetry manifests itself in the fact that γ_{ij} possesses, at all times, (at least) one Killing vector field. If one chooses coordinates adapted to this Killing vector field, $\partial/\partial\theta$, the metric can then be written in the form (6.2.2), and then the quasi-matter degree of freedom can be determined from the spatial geometry by (6.2.3). In the numerical implementation, one can either determine, at each time-step, the scalar field through (6.2.3), or impose (6.2.3) only in the initial data, and then evolve the scalar field using equation (6.2.24). We have implemented the latter method.

6.3 Higher-dimensional initial data

Having written our system of evolution equations, we now need to construct relevant initial data. Building on the results outlined in chapter 3 (based on [127, 128]), we now present a

generalisation of the spectral solver in [139] that generates initial data for black hole binaries in $D \geq 5$ dimensions with non-vanishing initial boost [177].

In this section we need to make some changes to our notation. Early lower case Latin indices a, b, c, \dots will here extend from 1 to $D - 1$, late lower case Latin indices i, j, k, \dots run from 1 to 3 and early upper case Latin indices A, B, C, \dots from 4 to $D - 1$.

6.3.1 Coordinate transformation

We start by recalling, from chapter 3 that, for a system of boosted black holes, we can solve the momentum constraint equation (2.6.3d) analytically. It remains then to solve equation (3.2.35), which we re-write here:

$$\hat{\Delta}u + \frac{D-3}{4(D-2)} \hat{A}^{ab} \hat{A}_{ab} \psi^{-\frac{3D-5}{D-3}} = 0. \quad (6.3.1)$$

The numerical solution of this equation will be our task in this section.

First, it is convenient to transform to a coordinate system adapted to the generalised axial symmetry $SO(D-2)$ in $D = 5$ dimensions and $SO(D-3)$ in $D \geq 6$ dimensions as discussed in section 6.2. For this purpose we consider the (flat) conformal spatial metric in cylindrical coordinates

$$\hat{\gamma}_{ab} dx^a dx^b = dz^2 + d\rho^2 + \rho^2 (d\varphi^2 + \sin^2 \varphi d\Omega_{D-4}), \quad (6.3.2)$$

where $d\Omega_{D-4}$ is the metric on the $(D-4)$ -sphere. Observe that φ is a polar rather than an azimuthal coordinate, i.e. $\varphi \in [0, \pi]$. Next, we introduce ‘‘incomplete’’ Cartesian coordinates as

$$x = \rho \cos \varphi, \quad y = \rho \sin \varphi, \quad (6.3.3)$$

where $-\infty < x < +\infty$ and $0 \leq y < +\infty$. The D dimensional initial data for the spatial metric is then

$$\bar{\gamma}_{ab} dx^a dx^b = \psi^{\frac{4}{D-3}} [dx^2 + dy^2 + dz^2 + y^2 d\Omega_{D-4}]. \quad (6.3.4)$$

We can transform the $D - 1$ dimensional Cartesian coordinates $\mathcal{X}^a = (x^1, \dots, x^{D-1})$ to the coordinate system $\mathcal{Y}^a = (x, y, z, \xi_1, \xi_2, \dots, \xi_{D-4})$ with hyperspherical coordinates ξ_1, \dots, ξ_{D-4} by

$$\begin{aligned} x^1 &= x \\ x^2 &= y \cos \xi_1 \\ x^3 &= z \\ x^4 &= y \sin \xi_1 \cos \xi_2 & (D \geq 6) \\ x^5 &= y \sin \xi_1 \sin \xi_2 \cos \xi_3 & (D \geq 7) \\ &\vdots \\ x^{D-3} &= y \sin \xi_1 \cdots \sin \xi_{D-6} \cos \xi_{D-5} & (D \geq 7) \\ x^{D-2} &= y \sin \xi_1 \cdots \sin \xi_{D-5} \cos \xi_{D-4} & (D \geq 6) \\ x^{D-1} &= y \sin \xi_1 \cdots \sin \xi_{D-4} & (D \geq 5) \end{aligned} \quad (6.3.5)$$

Without loss of generality, we can always choose coordinates such that the black holes are initially located on the z axis at z_1 and z_2 and have momenta of equal magnitude in opposite directions $P_{(1)}^a = -P_{(2)}^a$. Inserting the momenta into equation (3.2.23) then provides the conformal traceless extrinsic curvature and the differential equation (6.3.1) which is solved numerically for u .

The class of symmetries covered by the formalism developed in this chapter includes head-on and grazing collisions of non-spinning black holes with initial position and momenta

$$\begin{aligned} x_{(1)}^a &= (0, 0, z_1, 0, \dots, 0), & x_{(2)}^a &= (0, 0, z_2, 0, \dots, 0) \\ P_{(1)}^a &= (P^x, 0, P^z, 0, \dots, 0) = -P_{(2)}^a. \end{aligned} \quad (6.3.6)$$

Note that a non-zero P^y is not compatible with the assumed symmetries. On the other hand, the x -axis can always be oriented such that the collision takes place in the xz plane. Our formalism therefore covers general grazing collisions of non-spinning black hole binaries in D dimensions.

6.3.2 Four dimensional initial data for a general D head-on collision

We will now discuss in detail the case of black holes with momenta in the z direction, that is, the case given by setting $P^x = 0$ in equation (6.3.6). The linear momenta are thus given by

$$P_{(1)}^a = (0, 0, P^z, 0, \dots, 0) = -P_{(2)}^a. \quad (6.3.7)$$

The rescaled trace-free part of the extrinsic curvature for such a configuration is

$$\hat{A}_{ab} = \hat{A}_{ab}^{(1)} + \hat{A}_{ab}^{(2)}, \quad (6.3.8)$$

where $\hat{A}_{ab}^{(1)}$ and $\hat{A}_{ab}^{(2)}$ are given by equation (3.2.23) with (6.3.6) and (6.3.7). Using equation (6.3.5) we can write this in the coordinate system \mathcal{Y}^a adapted to the spacetime symmetry:

$$\hat{A}_{ab}^{(1)} = \frac{4\pi(D-1)P^z}{(D-2)\mathcal{A}_{D-2}(x^2 + y^2 + (z-z_1)^2)^{\frac{D+1}{2}}} \left(\begin{array}{c|c} \hat{a}_{ij}^{(1)} & 0 \\ \hline 0 & \hat{a}_{AB}^{(1)} \end{array} \right), \quad (6.3.9)$$

with

$$\hat{a}_{ij}^{(1)} = \begin{pmatrix} -[-(D-4)x^2 + y^2 + (z-z_1)^2](z-z_1) & (D-3)xy(z-z_1) & x[x^2 + y^2 + (D-2)(z-z_1)^2] \\ (D-3)xy(z-z_1) & -[x^2 - (D-4)y^2 + (z-z_1)^2](z-z_1) & y[x^2 + y^2 + (D-2)(z-z_1)^2] \\ x[x^2 + y^2 + (D-2)(z-z_1)^2] & y[x^2 + y^2 + (D-2)(z-z_1)^2] & [x^2 + y^2 + (D-2)(z-z_1)^2](z-z_1) \end{pmatrix}, \quad (6.3.10)$$

and

$$\hat{a}_{AB}^{(1)} = -y^2(z-z_1)[x^2 + y^2 + (z-z_1)^2]h_{AB}, \quad (6.3.11)$$

where h_{AB} is the metric on the $(D-4)$ -sphere. The expression for $\hat{A}_{ab}^{(2)}$ is analogous, but with z_2 in place of z_1 and $-P^z$ in place of P^z in equation (6.3.9).

We now need to re-express these quantities in terms of our $3+1$ quantities, $(\gamma_{ij}, K_{ij}, \lambda, K_\lambda)$, as introduced in the previous section. These are the variables evolved in time and therefore

the variables we ultimately wish to construct from the initial data calculation. For their extraction we first note that γ_{ij} , K_{ij} and K_λ are related to the $(D-1)$ -dimensional metric $\bar{\gamma}_{ab}$ and extrinsic curvature \bar{K}_{ab} by

$$\begin{aligned}\bar{\gamma}_{ij} &= \gamma_{ij}, & \bar{\gamma}_{AB} &= \lambda h_{AB}, \\ \bar{\gamma}_{iA} &= 0,\end{aligned}\tag{6.3.12}$$

$$\begin{aligned}\bar{K}_{ij} &= K_{ij}, & \bar{K}_{AB} &= \frac{1}{2}K_\lambda h_{AB}, \\ \bar{K}_{iA} &= 0, & \bar{K} &= K + \frac{D-4}{2}\frac{K_\lambda}{\lambda}.\end{aligned}\tag{6.3.13}$$

Using these relations and equation (6.2.4) we can express all “3+1” variables in terms of those describing the initial data

$$\begin{aligned}\gamma_{ij} &= \psi^{\frac{4}{D-3}}\delta_{ij}, & \lambda &= \psi^{\frac{4}{D-3}}y^2, \\ K_{ij} &= \psi^{-2}(\hat{A}_{ij}^{(1)} + \hat{A}_{ij}^{(2)}), & K_\lambda &= 2\psi^{-2}y^2(P^+ + P^-), \\ K &= -\frac{(D-4)K_\lambda}{2\lambda},\end{aligned}\tag{6.3.14}$$

where

$$\begin{aligned}P^+ &\equiv -\frac{4\pi(D-1)P^z(z-z_1)}{(D-2)\mathcal{A}_{D-2}(x^2+y^2+(z-z_1)^2)^{\frac{D-1}{2}}}, \\ P^- &\equiv \frac{4\pi(D-1)P^z(z-z_2)}{(D-2)\mathcal{A}_{D-2}(x^2+y^2+(z-z_2)^2)^{\frac{D-1}{2}}}.\end{aligned}\tag{6.3.15}$$

The conformal factor is

$$\psi = 1 + \frac{\mu_1}{4[x^2+y^2+(z-z_1)^2]^{(D-3)/2}} + \frac{\mu_2}{4[x^2+y^2+(z-z_2)^2]^{(D-3)/2}} + u,\tag{6.3.16}$$

and u is the solution of the equation

$$\left(\partial_{\rho\rho} + \partial_{zz} + \frac{D-3}{\rho}\partial_\rho\right)u = \frac{3-D}{4(D-2)}\hat{A}^{ab}\hat{A}_{ab}\psi^{-\frac{3D-5}{D-3}},\tag{6.3.17}$$

where

$$\hat{A}^{ab}\hat{A}_{ab} = (\hat{A}_{ij}^{(1)} + \hat{A}_{ij}^{(2)})(\hat{A}^{ij(1)} + \hat{A}^{ij(2)}) + (D-4)(P^+ + P^-)^2.\tag{6.3.18}$$

Our numerical construction of the function u will be based on the spectral solver developed in [139]. This solver employs coordinates specifically adapted to the asymptotic behaviour of u at spatial infinity. In order to investigate this behaviour, we next consider a single black hole with non-zero linear momentum.

6.3.3 Single puncture with linear momentum

For a single puncture with momentum P^z located at the origin $z=0$, equation (3.2.23) implies

$$\hat{A}^{ab}\hat{A}_{ab} = \frac{16\pi^2(D-1)^2}{(D-2)^2\mathcal{A}_{D-2}^2 r^{2(D-2)}}P_z^2 \left[2 + D(D-3)\left(\frac{z}{r}\right)^2\right],\tag{6.3.19}$$

so that equation (6.3.17) takes the form

$$\hat{\Delta}u + \frac{8\pi^2(D-1)^2(D-3)}{(D-2)^3\mathcal{A}_{D-2}^2r^{2(D-2)}}P_z^2 \left[1 + \frac{D(D-3)}{2} \left(\frac{z}{r} \right)^2 \right] \psi^{-\frac{3D-5}{D-3}} = 0. \quad (6.3.20)$$

It turns out to be convenient for solving this differential equation to introduce a hyperspherical coordinate system on the $D-1$ dimensional spatial slices, such that the flat conformal metric is

$$d\hat{s}^2 = \hat{\gamma}_{ab}dx^a dx^b = dr^2 + r^2 [d\vartheta^2 + \sin^2\vartheta (d\varphi^2 + \sin^2\varphi d\Omega_{D-4})],$$

with $\cos\vartheta = \frac{z}{r}$. We further introduce the radial coordinate

$$X \equiv \left(1 + \frac{\mu}{4r^{D-3}} \right)^{-1}, \quad (6.3.21)$$

which reduces to the coordinate A of equation (31) in [139] for the case of $D=4$ spacetime dimensions. Expressed in the new coordinate system, equation (6.3.20) becomes

$$\left\{ \partial_{XX} + \frac{2}{X}\partial_X + \frac{1}{(D-3)^2X^2(1-X)^2} \left[\partial_{\vartheta\vartheta} + (D-3)\cot\vartheta\partial_{\vartheta} + \frac{1}{\sin^2\vartheta} (\partial_{\varphi\varphi} + (D-4)\cot\varphi\partial_{\varphi}) \right] \right\} u = -\alpha \left(\frac{P_z}{\mu} \right)^2 X^{-\frac{D-7}{D-3}} (1+uX)^{-\frac{3D-5}{D-3}} \left(1 + \frac{D(D-3)}{2} \cos^2\vartheta \right), \quad (6.3.22)$$

with

$$\alpha \equiv \frac{128\pi^2(D-1)^2}{(D-3)(D-2)^3\mathcal{A}_{D-2}^2}.$$

For $D=4$ we recover equation (40) of [139]. In order to study the behaviour of the solution at spatial infinity, we now perform a Taylor expansion in $v \equiv \frac{P_z}{\mu}$,

$$u = \sum_{j=1}^{\infty} v^{2j} u_j. \quad (6.3.23)$$

Odd powers of v have to vanish in order to satisfy equation (6.3.22). We have the following equation for u_1

$$\left\{ \partial_{XX} + \frac{2}{X}\partial_X + \frac{1}{(D-3)^2X^2(1-X)^2} [\partial_{\vartheta\vartheta} + (D-3)\cot\vartheta\partial_{\vartheta}] \right\} u_1 = -\alpha X^{-\frac{D-7}{D-3}} \left(1 + \frac{D(D-3)}{2} \cos^2\vartheta \right). \quad (6.3.24)$$

In order to solve equation (6.3.24), we make the *ansatz*

$$u_1 = f(X) + g(X)Q_D(\cos\vartheta), \quad (6.3.25)$$

where $Q_D(\cos \vartheta) = (D-1)\cos^2 \vartheta - 1$. By solving equation (6.3.24), we find that the functions $f(X)$ and $g(X)$ take the form

$$f(X) = \frac{32\pi^2(D-3)}{(D-2)^2\mathcal{A}_{D-2}^2} \left(1 - X^{\frac{D+1}{D-3}}\right), \quad (6.3.26)$$

$$\begin{aligned} g(X) = & k_1 \left(\frac{X}{1-X}\right)^{\frac{2}{D-3}} + k_2 \left(\frac{1-X}{X}\right)^{\frac{D-1}{D-3}} \\ & - \alpha \frac{D(D-3)^3}{2(D+1)(D-1)} \left[\frac{1}{D-1} \frac{X^{\frac{D+1}{D-3}}}{(1-X)^{\frac{2}{D-3}}} {}_2F_1\left(-\frac{D-1}{D-3}, \frac{D-1}{D-3}; 2\frac{D-2}{D-3}; X\right) \right. \\ & \left. - \frac{1}{2D} X^{\frac{D+1}{D-3}} (1-X)^{\frac{D-1}{D-3}} {}_2F_1\left(\frac{2}{D-3}, \frac{2D}{D-3}; 3\frac{D-1}{D-3}; X\right) \right], \end{aligned} \quad (6.3.27)$$

where ${}_2F_1(a, b; c; X)$ is the hypergeometric function and $k_{1,2}$ are constants to be fixed by imposing that $g(X=1) = 0$ and $g(X=0)$ is smooth. Requiring analyticity at $X=0$ and using the property $F(a, b, c, 0) = 1$, we immediately find $k_2 = 0$.

We are now interested in the large $X \rightarrow 1$ limit. Therefore, we use the $z \rightarrow 1-z$ transformation law for the hypergeometric functions [186],

$$\begin{aligned} F(a-c+1, b-c+1, 2-c, z) = & (1-z)^{c-a-b} \frac{\Gamma(2-c)\Gamma(a+b-c)}{\Gamma(a-c+1)\Gamma(b-c+1)} F(1-a, 1-b, c-a-b+1, 1-z) \\ & + \frac{\Gamma(2-c)\Gamma(c-a-b)}{\Gamma(1-a)\Gamma(1-b)} F(a-c+1, b-c+1, -c+a+b+1, 1-z). \end{aligned} \quad (6.3.28)$$

Requiring a regular solution we find that k_1 has to satisfy

$$k_1 = \frac{64\pi^2 D(D-3)^2}{(D-2)^3(D+1)\mathcal{A}_{D-2}^2} \frac{\Gamma\left(\frac{2(D-2)}{D-3}\right)^2}{\Gamma\left(\frac{3D-5}{D-3}\right)}. \quad (6.3.29)$$

Let us write these functions explicitly for $D = 4, 5, 7$ (for $D = 6$ the hypergeometric function does not simplify):

- $D = 4$:

$$f(X) = \frac{1}{2} (1 - X^5), \quad (6.3.30)$$

$$g(X) = \frac{(1-X)^2}{10X^3} \left[84(1-X)\log(1-X) + 84X - 42X^2 - 14X^3 - 7X^4 - 4X^5 - 2X^6 \right]; \quad (6.3.31)$$

These are equations (42–44) in [139], with appropriate redefinitions.

- $D = 5$:

$$f(X) = \frac{16}{9\pi^2} (1 - X^3), \quad (6.3.32)$$

$$g(X) = -\frac{80(1-X)^2}{81\pi^2 X^2} \left[4\log(1-X) + 4X + 2X^2 + X^3 \right]; \quad (6.3.33)$$

- $D = 7$:

$$f(X) = \frac{128(1-X^2)}{25\pi^4}, \quad (6.3.34)$$

$$g(X) = \frac{28}{125\pi^4 \sqrt{(1-X)X^3}} \left[-30\sqrt{(1-X)X} + 40\sqrt{(1-X)X^3} - 16\sqrt{(1-X)X^7} \right. \\ \left. + 3\pi X^2 + 6(5 - 10X + 4X^2) \arcsin \sqrt{X} \right]. \quad (6.3.35)$$

Analysing these expressions, we can anticipate the convergence properties of the numerical solutions obtained in terms of pseudo-spectral methods. For instance, analyticity of f and g suggests exponential convergence. As will become clear in the next section, we are interested in the convergence properties in a coordinate A behaving as $A \sim 1 - \frac{1}{r}$, for large r . We thus introduce a coordinate A that satisfies

$$X = (1 + (A^{-1} - 1)^{D-3})^{-1}. \quad (6.3.36)$$

In terms of the A coordinate, we find that the functions f are analytical. For the function g in the vicinity of $A = 1$, the leading terms behave as follows:

- $D = 5$

$$g(A) \sim -\frac{80}{81\pi^2} (1-A)^4 [8\log(1-A) + 7], \quad (6.3.37)$$

- $D = 6$

$$g(A) \sim \frac{19683}{6272\pi^2} (1-A)^5, \quad (6.3.38)$$

- $D = 7$

$$g(A) \sim \frac{84}{25\pi^3} (1-A)^6. \quad (6.3.39)$$

From the behaviour of the functions f and g and equation (6.3.25) we conclude that the first term in the expansion (6.3.23) has a leading-order behaviour $u_1 \sim 1/r^{D-3}$ as $r \rightarrow \infty$. Iteratively solving equation (6.3.22) for higher powers of v is complicated by the presence of the source terms on the right hand side, but under simplifying assumptions indicates that higher-order terms $u_j \geq 2$ acquire additional factors of $1/r$ and therefore the leading-order fall off behaviour is given correctly by that of u_1 . This result is confirmed by our numerical investigation using finite boost parameters as we shall discuss in the next section.

With regard to the analyticity of the solutions and the resulting expectations for the convergence properties of a spectral algorithm, we summarise the results of our analytical study of a single puncture as follows. In $D = 6, 7$, the leading terms are analytic functions in the vicinity of $A = 1$. Actually, for $D = 7$, $g(A)$ is analytic in the vicinity of any point. Therefore, we expect exponential convergence of the pseudo-spectral code. For $D = 5$, one observes the presence of a logarithmic term. This type of term is known to arise in $D = 4$, when punctures have non-vanishing momenta [187, 188] and in that case their presence makes the convergence algebraic in the single puncture case. In the next section we shall investigate the impact of the logarithmic terms on the convergence properties of our spectral solver.

6.3.4 Two punctures with linear momentum

6.3.4.1 Code changes

We first explicitly list the modifications applied to the spectral solver of reference [139] and demonstrate how these modifications enable us to generate initial data for boosted black hole binaries with convergence properties and levels of constraint violation similar to the $D = 4$ case. For this purpose we start by recalling that the spectral solver of [139] employs coordinates

$$A \in [0, 1], \quad B \in [-1, 1], \quad \phi \in [0, 2\pi], \quad (6.3.40)$$

which are defined by equation (62) of [139],

$$\begin{aligned} x &= b \frac{2A}{1-A^2} \frac{1-B^2}{1+B^2} \sin \phi, \\ y &= b \frac{2A}{1-A^2} \frac{1-B^2}{1+B^2} \cos \phi, \\ z &= b \frac{A^2+1}{A^2-1} \frac{2B}{1+B^2}, \end{aligned} \quad (6.3.41)$$

where b is half of the coordinate distance between the punctures. In particular, the coordinate A satisfies

$$r \rightarrow \infty \Leftrightarrow A \rightarrow 1. \quad (6.3.42)$$

The first modification consist in adapting the source term and Laplace operator according to (6.3.17).

Next, we note that the type of high-energy collisions which form the main motivation for this work often start from relatively large initial separations of the holes, $|z_1 - z_2| \gg r_S$. In order to obtain high-precision solutions for such binary configurations, we found it crucial to introduce a coordinate A' defined as

$$A = \frac{\sinh[\kappa(A'+1)/2]}{\sinh \kappa}, \quad (6.3.43)$$

where κ is an adjustable free parameter. Note that for $\kappa = 0$ we obtain $A = \frac{1}{2}(A'+1)$. For $\kappa > 0$, however, the new coordinate A' provides the spectral method with enhanced resolution near $A \sim 0$.

Table 6.1: ADM mass obtained with equation (6.3.47) in units of the “bare” Schwarzschild radius $r_S^{D-3} = r_{S(+)}^{D-3} + r_{S(-)}^{D-3}$. The variation of the ADM mass with resolution is of the order of 10^{-10} for all D and $n \geq 100$ grid points indicating that the accuracy in the ADM mass is limited by round-off errors.

D	b/r_S	P/r_S^{D-3}	$r_{S_{\text{global}}}^{D-3}/r_S^{D-3}$	M_{ADM}/r_S^{D-3}
4	30.185	0.8	3.555	1.78
5	30.185	0.8	1.931	2.27
6	30.185	0.8	1.415	2.96
7	30.185	0.8	1.236	3.81

A further modification is related to the asymptotic fall off of the function u as obtained in the previous section,

$$u \sim \frac{1}{r^{D-3}}. \quad (6.3.44)$$

To naturally accommodate this behaviour with the spectral coordinates used in the code, we have changed the variable U of equation (5) in [139] to

$$u = (A' - 1)^{D-3} U. \quad (6.3.45)$$

Note that this U variable is the variable that the code actually solves for.

Finally, we adjust the calculation of the ADM mass from the numerical solution. For this purpose, we note that, asymptotically

$$\psi = 1 + \frac{\mu_+}{4r_+^{D-3}} + \frac{\mu_-}{4r_-^{D-3}} + u \sim 1 + \frac{\mu}{4r^{D-3}}, \quad (6.3.46)$$

with $\mu \equiv r_{S_{\text{global}}}^{D-3} \equiv \frac{16\pi M_{\text{ADM}}}{\mathcal{A}_{D-2}(D-2)}$ and $\mu_{\pm} \equiv r_{S(\pm)}^{D-3}$. The ADM mass is then obtained from

$$\begin{aligned} r_{S_{\text{global}}}^{D-3} &= r_{S(+)}^{D-3} + r_{S(-)}^{D-3} + 4 \lim_{r \rightarrow \infty} r^{D-3} u \\ &= r_{S(+)}^{D-3} + r_{S(-)}^{D-3} + 4 \left(-2b \frac{\tanh \kappa}{\kappa} \right)^{D-3} U(A' = 1), \end{aligned} \quad (6.3.47)$$

where we have used equation (62) of [139], and equation (6.3.43) and (6.3.45). We show in table 6.1 the values obtained for the ADM mass of some cases we considered.

6.3.4.2 Results

We now study the numerical results as obtained for $D = 4, 5, 6, 7$ with these adaptations of the spectral solver of [139]. Throughout the remainder of this section we will graphically present results in units of the “bare” Schwarzschild radius defined as $r_S^{D-3} = r_{S(+)}^{D-3} + r_{S(-)}^{D-3}$.

We first address the convergence properties of the numerical algorithm by evaluating the quantity

$$\delta_{n,m}(u) = \max |1 - u_n/u_m|, \quad (6.3.48)$$

where the maximum is obtained along the collision axis, i.e. z -axis in our case. Here, the index m refers to a reference solution obtained using a large number m of grid points while n denotes test solutions using a coarser resolution, $n < m$. The result obtained for black hole binaries with initial separation $b/r_S = 30.185$ and boost $P^z/r_S^{D-3} = 0.8$ in $D = 4, 5, 6$ and 7 dimensions is displayed in figure 6.2. We note from this figure, that achieving a given target accuracy $\delta_{n,m}$ requires a larger number of points n as D increases. We emphasise in this context, however, that this increase in computational cost in higher dimensions is unlikely to significantly affect the total computational cost of the simulations which typically are dominated by the time evolution rather than the initial data calculation. Most importantly, we observe exponential convergence up to a level of $\delta_{n,m}(u) \approx 10^{-6}$ for all values of the spacetime dimensionality D . Below that level, the two leftmost curves in figure 6.2, corresponding to $D = 4$ and $D = 5$, respectively, show that the rate of convergence decreases indicating that the logarithmic terms become significant and reduce the convergence to algebraic level similar to the observation in figure 4 of reference [139]. For $D = 6$, the convergence remains exponential, in agreement with the absence of logarithmic terms in the analysis of section 6.3.3. Irrespective of a change to algebraic convergence, however, our algorithm is capable of reducing the quantity $\delta_{m,n}(u)$ for all values of D to a level comparable to the case $D = 4$ and, thus, producing initial data of similar quality as in 3+1 dimensions, provided we use a sufficiently high resolution n .

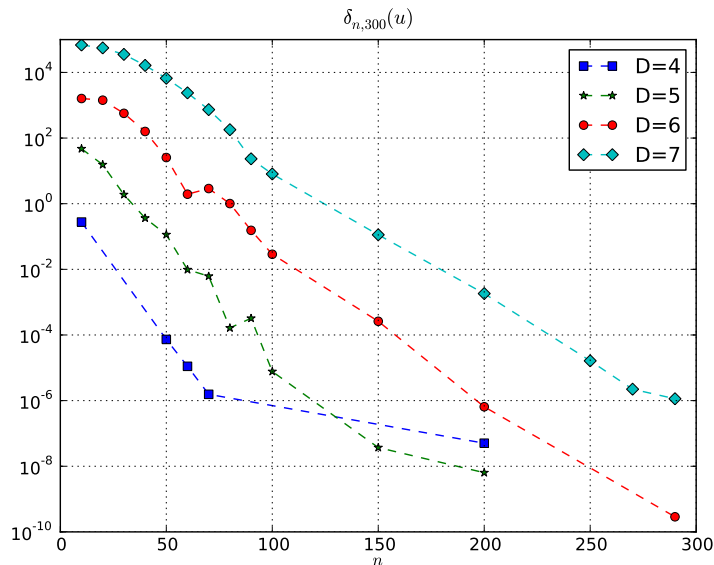


Figure 6.2: Convergence plot for the $b/r_S = 30.185$, $P/r_S^{D-3} = \pm 0.80$ cases.

For illustration, we plot in figure 6.3 the function u obtained for the case of $b/r_S = 30.185$, $P^z/r_S^{D-3} = 0.8$. The behaviour is qualitatively similar for all values of D , but the figure demonstrates the faster fall off for larger D as predicted by (6.3.44). For this plot we have used $n_A = 300$, $n_B = 300$ and $n_\phi = 4$ grid points. The inset in the figure shows the function u in the immediate vicinity of the puncture. While the profile develops multiple extrema for

$D > 4$, the profile remains smooth for all values of D .

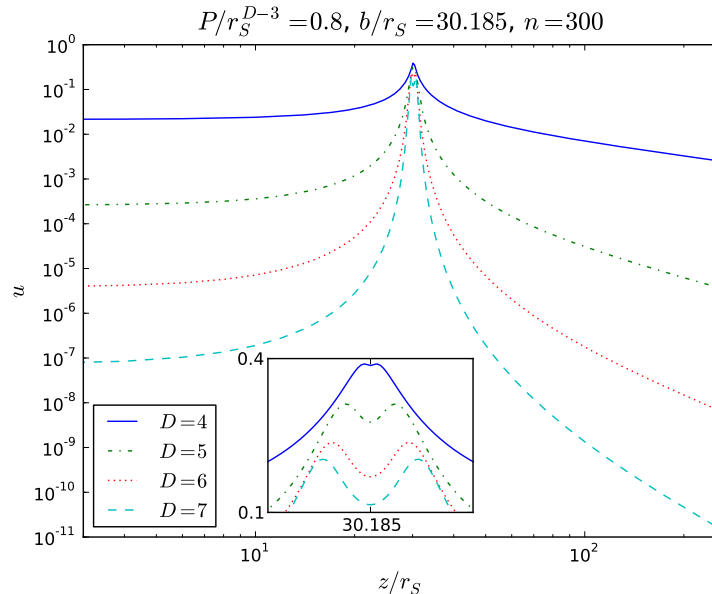


Figure 6.3: u function for $D = 4, \dots, 7$ plotted along the z -axis, in units of r_S . We used $n_A = n_B = n = 300, n_\phi = 4$. We also show a zoom around the puncture.

Finally, we show in figure 6.4, the Hamiltonian constraint corresponding to the solutions presented in figure 6.3 as measured by a fourth-order finite differencing scheme of the LEAN evolution code (section 4.3 and reference [149]). We emphasise that the violation of equation (6.3.1) inside the spectral initial data solver is $< 10^{-12}$ by construction. The independent evaluation of the constraint violation in the evolution code serves two purposes. First, it checks that the differential equation (6.3.1) solved by the spectral method corresponds to the Hamiltonian constraint formulated in ADM variables; an error in coding up the differential equation (6.3.1) could still result in a solution for u of the spectral solver, but would manifest itself in significantly larger violations in figure 6.4. Second, it demonstrates that the remaining numerical error is dominated by the time evolution instead of the initial solver. Note in this context that the relatively large violations of order unity near the puncture location in figure 6.4 are an artifact of the fourth-order discretisation in the diagnostics of the evolution code and are typical for evolutions of the moving-puncture type; see e.g. the right panel in figure 8 in Brown et al. [189].

The solid (blue) curve obtained for the “standard” $D = 4$ case serves as reference. For all values of D the constraint violations are maximal at the puncture location $z_1/r_S \approx 15$ and rapidly decrease away from the puncture. As expected from the higher fall off rate of the grid functions for larger D , the constraints also drop faster for higher dimensionality of the spacetime.

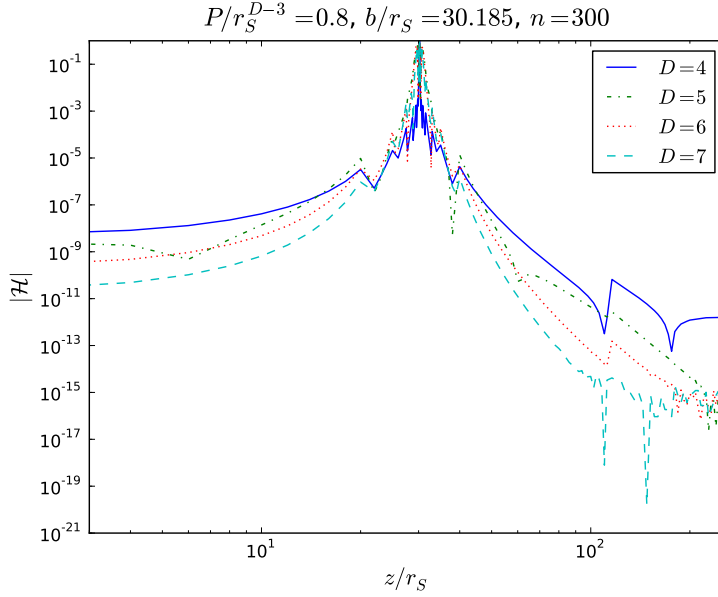


Figure 6.4: Violation of the Hamiltonian constraint along the z -axis, evaluated with a fourth order finite difference scheme. The growth of the constraint violation near the puncture is an artifact of finite-differencing across the puncture; see text for details.

6.4 Numerical evolutions

Having established that our initial data code is working, we will now show some numerical results, obtained by adapting the *LEAN* code introduced in section 4.3. In this section we will begin by briefly commenting on numerical issues generated by the quasi-matter terms arising from the dimensional reduction. We then present some code tests and results.

From the initial data construction of section 6.3, we see that the quasi-matter field λ has a y^2 fall off as $y \rightarrow 0$, that is, on the xz plane (cf. (6.3.14)). From (6.2.23), we see that this leads to divisions by zero on the right-hand side of the BSSN evolution equations; thus, we need to isolate such irregular terms and re-write the equations in terms of variables which are explicitly regular at $y = 0$. In this spirit, we introduce the following evolution variable

$$\zeta \equiv \frac{\chi}{y^2} \lambda, \quad (6.4.1)$$

and corresponding auxiliary variable

$$K_\zeta \equiv -\frac{1}{2\alpha y^2} (\partial_t - \mathcal{L}_\beta)(\zeta y^2) = -\frac{1}{2\alpha} \left(\partial_t \zeta - \beta^m \partial_m \zeta + \frac{2}{3} \zeta \partial_m \beta^m - 2\zeta \frac{\beta^y}{y} \right). \quad (6.4.2)$$

The full quasi-matter terms and evolution equations in terms of these regular variables can be found in Appendices A and B of [175]. Here we note only that, with the above definition, we have the relation

$$K_\lambda = \frac{y^2}{\chi} K_\zeta + \frac{1}{3} \frac{y^2 \zeta}{\chi} K. \quad (6.4.3)$$

Finally, for long term evolutions, we employed the following gauge conditions, which are generalisations of conditions (4.2.3), (4.2.6)

$$\left(\partial_t - \beta^k \partial_k\right) \alpha = -2\alpha(\eta_K K + \eta_{K_\zeta} K_\zeta), \quad (6.4.4)$$

$$\left(\partial_t - \beta^k \partial_k\right) \beta^i = \frac{3}{4} \tilde{\Gamma}^i - \eta \beta^i. \quad (6.4.5)$$

Note the extra term involving K_ζ in the slicing condition compared with standard moving puncture gauge in 3 + 1 dimensions and the additional freedom we have introduced in the form of the parameters η_K and η_{K_ζ} .

6.4.1 Code tests

6.4.1.1 Geodesic slicing

As a first test of our numerical implementation, we have numerically evolved a single $D = 5$ Tangherlini black hole in the so-called *geodesic slicing*, which corresponds to fixing the gauge parameters to (4.2.1) throughout the evolution. Such a gauge choice is not adequate to perform long term numerical evolutions. The advantage of this choice, though, is that one can easily write the Tangherlini metric element in this coordinate system, which we can then match against the numerically obtained solutions [97]. This coordinate system may be achieved by setting a congruence of in-falling radial time-like geodesics, each geodesic starting from rest at radial coordinate r_0 , with r_0 spanning the interval $[\mu, +\infty[$, and using their proper time τ and r_0 as coordinates (instead of the standard t, r Schwarzschild-like coordinates). The line element becomes

$$ds^2 = -d\tau^2 + \frac{\left(r_0(R)^2 + \left(\frac{\mu}{r_0(R)}\right)^2 \tau^2\right)^2}{r_0(R)^2 - \left(\frac{\mu}{r_0(R)}\right)^2 \tau^2} \frac{dR^2}{R^2} + \left(r_0(R)^2 - \left(\frac{\mu}{r_0(R)}\right)^2 \tau^2\right) d\Omega_3, \quad (6.4.6)$$

where $r_0(R)$ is given by

$$r_0(R) = R \left(1 + \frac{\mu^2}{4R^2}\right). \quad (6.4.7)$$

Before the breaking down of the numerical evolution, we can compare our numerical results with the above metric element. This is shown in figure 6.5, where we have plotted one metric component $\tilde{\gamma}_{xx}$ along the x axis (left) and ζ/χ (right), for various values of τ using both the analytical solution and numerical data. The agreement is excellent for $\tilde{\gamma}_{xx}$ and good for ζ/χ . The latter shows some deviations very close to the puncture, but we believe that it is not a problem for two reasons: (i) the agreement improves for higher resolution; (ii) the mismatch does not propagate outside of the horizon.

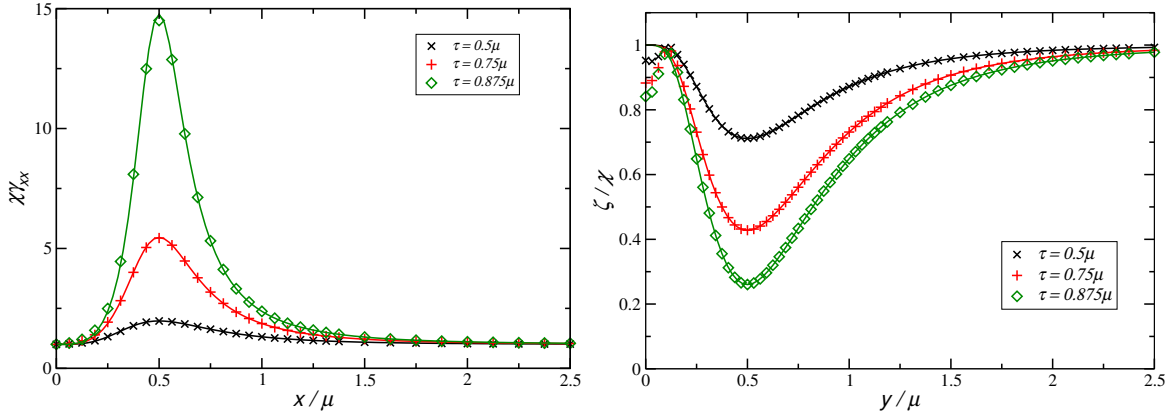


Figure 6.5: Numerical values versus analytical plot of $\tilde{\gamma}_{xx}$ along the x -axis (left panel) and of $\zeta/\chi = \lambda/y^2$ along the y axis (right panel), for various values of τ , for the single Tangherlini black hole in five dimensions. The horizontal axis are in units of μ .

6.4.1.2 Single black hole evolution

To further test our numerical framework, we have performed long term simulations of a single black hole in $D = 5$ using the gauge conditions in (6.4.4) and (6.4.5), the initial data from equations (6.3.14) (with $P^+ = 0 = P^-$) and grid setup (cf. section 4.3)

$$\{(512, 256, 128, 64, 32, 16, 8, 4, 2) \times (), h\},$$

in units of μ with resolutions $h_c = 1/32$ and $h_f = 1/48$. In figure 6.6 we show the Hamiltonian constraint and the y component of the momentum constraint at evolution time $t = 28\mu$. For the Hamiltonian constraint the convergence is essentially 4th order; for the momentum constraint it decreases towards 2nd or 3rd order in patches.

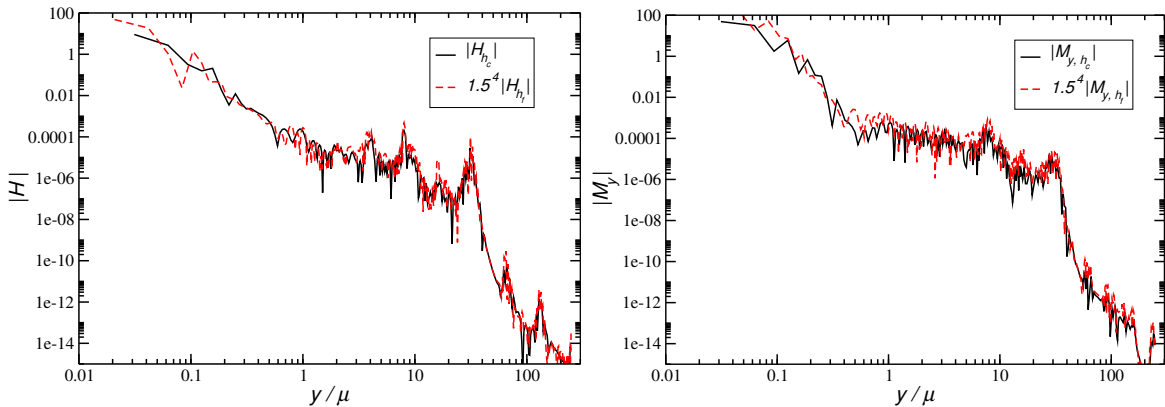


Figure 6.6: Hamiltonian constraint (left panel) and y -component of the momentum constraint (right panel) at time $t = 28\mu$, for the evolution of a single Tangherlini black hole in five dimensions.

6.4.1.3 Head-on collision

Finally, we tested the code capability to evolve a head-on collision from rest. Using again the initial conditions (6.3.14) with $P^+ = 0 = P^-$, we let two black holes with parameters

$$\mu_A^2 = \mu_B^2 \equiv \frac{\mu^2}{2}, \quad (6.4.8)$$

$$z_A = -z_B = 3.185 \mu, \quad (6.4.9)$$

collide from rest, using the grid setup

$$\{(512, 256, 128, 64, 32, 16, 8) \times (2, 1), h = 1/32\},$$

in units of μ . The gauge variables α and β^i were evolved according to equations (6.4.4) and (6.4.5) with parameters $\eta_K = \eta_{K_\zeta} = 1.5$ and $\eta = 0.75$.

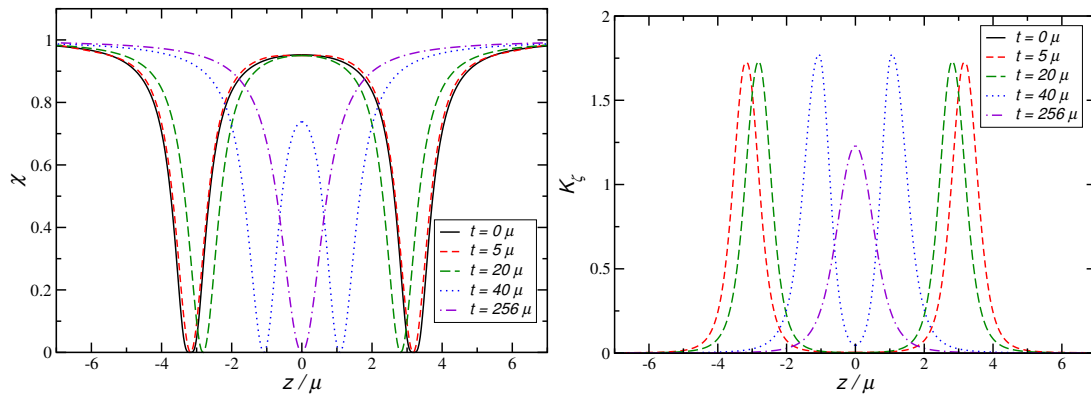


Figure 6.7: The BSSN variable χ (left panel) and the quasi-matter momentum K_ζ (right panel) shown along the axis of collision for a head-on collision at times $t = 0, 5, 20, 40$ and 256μ . Note that $K_\zeta = 0$ at $t = 0$.

In figure 6.7 we show the conformal factor χ and the momentum K_ζ along the axis of collision at various times for such an evolution. At early times, the evolution is dominated by the adjustment of the gauge (cf. the solid and short-dashed curves). The two holes next start approaching each other (long-dashed and dotted curves) and eventually merge and settle down into a single stationary hole (dash-dotted curves). No signs of instabilities were observed.

6.4.2 Head-on collisions

Having established, in the previous section, that our numerical implementation does work (for the five dimensional case) we will now present some results.

Since the final result of a head-on collision of two D dimensional, non-spinning black holes approaches, at late times, a D dimensional Schwarzschild (i.e. Tangherlini) black hole, we can make use of the Kodama-Ishibashi formalism, presented in section 5.1.2 to extract the gravitational wave information. Our remaining task is then to obtain the relevant gauge-invariant quantities from our numerical data. We will give here the main steps for this procedure; the full details can be found in reference [176].

6.4.2.1 Coordinate frames

In the approach developed in section 6.2, we perform a dimensional reduction by isometry on the $(D - 4)$ -sphere S^{D-4} , in such a way that the D dimensional vacuum Einstein equations are rewritten as an effective 3 + 1 dimensional time evolution problem with source terms that involve a scalar field. We focus here on $D \geq 5$ dimensional spacetimes with $SO(D - 2)$ isometry group, which allows us to model head-on collisions of non-spinning black holes; we dub hereafter these spacetimes as *axially symmetric*. Although the corresponding symmetry manifold is the $(D - 3)$ -sphere S^{D-3} , the quotient manifold in our dimensional reduction is its submanifold S^{D-4} . The coordinate frame in which the numerical simulations are performed is

$$(x^\mu, \phi^1, \dots, \phi^{D-4}) = (t, x, y, z, \phi^1, \dots, \phi^{D-4}), \quad (6.4.10)$$

where the angles $\phi^1, \dots, \phi^{D-4}$ describe the quotient manifold S^{D-4} and do not appear explicitly in the simulations. Here, z is the symmetry axis, i.e. the collision line.

Recall that in the frame (6.4.10), the spacetime metric has the form (cf. equation (6.2.4))

$$ds^2 = -\alpha^2 dt^2 + \gamma_{ij}(dx^i + \beta^i dt)(dx^j + \beta^j dt) + \lambda(x^\mu)d\Omega_{D-4}, \quad (6.4.11)$$

Also recall, from equations (6.2.2) and (6.2.3), that with an appropriate transformation of the four dimensional coordinates x^μ , the residual symmetry left after the dimensional reduction on S^{D-4} can be made manifest: $x^\mu \rightarrow (x^{\bar{\mu}}, \theta)$ ($\bar{\mu} = 0, 1, 2$),

$$g_{\mu\nu}(x^\alpha)dx^\mu dx^\nu = g_{\bar{\mu}\bar{\nu}}(x^{\bar{\alpha}})dx^{\bar{\mu}} dx^{\bar{\nu}} + g_{\theta\theta}(x^{\bar{\alpha}})d\theta^2 \quad (6.4.12)$$

and

$$\lambda(x^\mu) = \sin^2 \theta g_{\theta\theta}(x^{\bar{\alpha}}), \quad (6.4.13)$$

so that equation (6.4.11) takes the form $ds^2 = g_{\bar{\mu}\bar{\nu}}dx^{\bar{\mu}}dx^{\bar{\nu}} + g_{\theta\theta}d\Omega_{D-3}$.

To extract the gravitational waves with the KI formalism, spacetime, away from the black holes, is required to be approximately spherically symmetric. In D dimensions this means symmetry with respect to rotations on S^{D-2} , which is manifest in the coordinate frame:

$$(x^a, \bar{\theta}, \theta, \phi^1, \dots, \phi^{D-4}) = (t, r, \bar{\theta}, \theta, \phi^1, \dots, \phi^{D-4}). \quad (6.4.14)$$

Note that $x^a = t, r$ and that we have introduced polar-like coordinates $\bar{\theta}, \theta \in [0, \pi]$ to “build up” the manifold S^{D-2} in the background, together with a radial spherical coordinate r , which is the areal coordinate in the background.

The coordinate frame (6.4.14) is defined in such a way that the metric can be expressed as a stationary background $(ds^{(0)})^2$ (i.e., the Tangherlini metric) plus a perturbation $(ds^{(1)})^2$ which decays faster than $1/r^{D-3}$ for large r , and the formalism from section 5.1.2 can thus be applied [176].

6.4.2.2 Implementation of axisymmetry

In an axially symmetric spacetime, the metric perturbations are symmetric with respect to S^{D-3} . Therefore, the harmonics in the expansion of h_{MN} depend only on the angle $\bar{\theta}$ (which does not belong to S^{D-3}). Furthermore, since there are no off-diagonal terms in the metric, the only non-vanishing $g_{a\bar{i}}$ components are $g_{a\bar{\theta}}$; the only components $g_{\bar{i}\bar{j}}$ are either proportional to $\gamma_{\bar{i}\bar{j}}$, or all vanishing but $g_{\bar{\theta}\bar{\theta}}$. This implies that only scalar spherical harmonics can appear in the expansion of the metric perturbations. Indeed, if

$$\mathbb{V}^{\bar{i}} = (\mathbb{V}^{\bar{\theta}}, 0, \dots, 0), \quad \mathbb{V}^{\bar{i}} = \mathbb{V}^{\bar{i}}(\bar{\theta}), \quad (6.4.15)$$

then equation (5.1.35) gives

$$\mathbb{V}^{\bar{i}}_{;\bar{i}} = \mathbb{V}^{\bar{\theta}}_{;\bar{\theta}} = 0 \Rightarrow \mathbb{V}^{\bar{\theta}} = 0 \Rightarrow \mathbb{V}^{\bar{i}} = 0. \quad (6.4.16)$$

Similarly, from equation (5.1.32) we obtain $\mathbb{T}_{\bar{i}\bar{j}} = 0$.

The scalar harmonics, solutions of equation (5.1.38) and which depend only on the coordinate $\bar{\theta}$, are given by the Gegenbauer polynomials $C_l^{(D-3)/2}$, as discussed in references [171, 190, 127]; writing explicitly the index l , they take the form

$$\mathbb{S}_l(\bar{\theta}) = (K^{lD})^{-1/2} C_l^{(D-3)/2}(\cos \bar{\theta}), \quad (6.4.17)$$

where the normalization K^{lD} is chosen such that

$$\int d\Omega^{D-2} \mathbb{S}_l \mathbb{S}_{l'} = \delta_{ll'}, \quad (6.4.18)$$

and $k^2 = l(l + D - 3)$.

Metric perturbations, and corresponding gauge-invariant functions, can then be computed in terms of these functions [176].

6.4.2.3 Extracting gravitational waves

In the KI framework, the emitted gravitational waves are described by the master function Φ , cf. section 5.1.2. We can compute directly $\Phi_{,t}$ with [156, 176]*

$$\Phi_{,t} = (D-2)r^{(D-4)/2} \frac{-F^r_t + 2rF_{,t}}{k^2 - D + 2 + \frac{(D-2)(D-1)}{2} \frac{r_S^{D-3}}{r^{D-3}}}, \quad (6.4.19)$$

where $k^2 = l(l + D - 3)$. The energy flux can then be computed from expressions (5.1.45), (5.1.46).

6.4.3 Head-on collision from rest in $D = 5$

Having introduced and tested our formalism and numerical code, we now present results obtained for head-on collisions of five-dimensional black holes. The black holes collide

*Note that there is a factor r missing in equation (3.15) of reference [156].

Table 6.2: Grid structure and initial parameters of the head-on collisions starting from rest in $D = 5$. The grid setup is given in terms of the “radii” of the individual refinement levels, in units of r_S , as well as the resolution near the punctures h . d is the initial coordinate separation of the two punctures and L denotes the proper initial separation.

Run	Grid Setup	d/r_S	L/r_S
HD5a	$\{(256, 128, 64, 32, 16, 8, 4) \times (0.5, 0.25), h = r_S/84\}$	1.57	1.42
HD5b	$\{(256, 128, 64, 32, 16, 8, 4) \times (0.5, 0.25), h = r_S/84\}$	1.99	1.87
HD5c	$\{(256, 128, 64, 32, 16, 8, 4) \times (1, 0.5), h = r_S/84\}$	2.51	2.41
HD5d	$\{(256, 128, 64, 32, 16, 8, 4) \times (1, 0.5), h = r_S/84\}$	3.17	3.09
HD5e	$\{(256, 128, 64, 32, 16, 8) \times (2, 1, 0.5), h = r_S/84\}$	6.37	6.33
HD5f	$\{(256, 128, 64, 32, 16, 8) \times (2, 1, 0.5), h = r_S/84\}$	10.37	10.35

from rest, with initial coordinate separation d . Note that in five spacetime dimensions the Schwarzschild radius is related to the ADM mass M via

$$r_S^2 = \frac{8M}{3\pi}. \quad (6.4.20)$$

We therefore define the “total” Schwarzschild radius r_S such that $r_S^2 = r_{S,1}^2 + r_{S,2}^2$. By using this definition, r_S has physical dimension of length and provides a suitable unit for measuring both results and grid setup.

As summarised in table 6.2, we consider a sequence of binaries with initial coordinate separation ranging from $d = 3.17r_S$ to $d = 10.37r_S$. The table further lists the proper separation L along the line of sight between the holes and the grid configurations used for the individual simulations.

6.4.3.1 Newtonian collision time

An estimate of the time at which the black holes “collide” can be obtained by considering a Newtonian approximation of two point particles in $D = 5$. The Newtonian time it takes for two point-masses (with Schwarzschild parameters $r_{S,1}$ and $r_{S,2}$) to collide from rest with initial distance L in D dimensions is given by

$$\frac{t_{\text{free-fall}}}{r_S} = \frac{\mathcal{I}}{D-3} \left(\frac{L}{r_S} \right)^{\frac{D-1}{2}}, \quad (6.4.21)$$

where $r_S^{D-3} = r_{S,1}^{D-3} + r_{S,2}^{D-3}$ and

$$\mathcal{I} = \int_0^1 \sqrt{\frac{z^{\frac{5-D}{D-3}}}{1-z}} dz = \sqrt{\pi} \frac{\Gamma(\frac{1}{2} + \frac{1}{D-3})}{\Gamma(1 + \frac{1}{D-3})}. \quad (6.4.22)$$

For $D = 4$, one recovers the standard result $t_{\text{free-fall}} = \frac{\pi}{2} \sqrt{L^3/r_S^3} r_S$, whereas for $D = 5$ we get

$$t_{\text{free-fall}} = (L/r_S)^2 r_S. \quad (6.4.23)$$

In general relativity, black hole trajectories and merger times are intrinsically observer dependent quantities. For our comparison with Newtonian estimates we have chosen relativistic trajectories as viewed by observers adapted to the numerical coordinate system. While the lack of fundamentally gauge invariant analogues in general relativity prevents us from deriving rigorous conclusions, we believe such a comparison to serve the intuitive interpretation of results obtained within the “moving puncture” gauge. Bearing in mind these caveats, we plot in figure 6.8 the analytical estimate of the Newtonian time of collision, together with the numerically computed time of formation of a common apparent horizon. Also shown in the figure is the time at which the separation between the individual hole’s puncture trajectory decreases below the Schwarzschild parameter r_S . The remarkable agreement provides yet

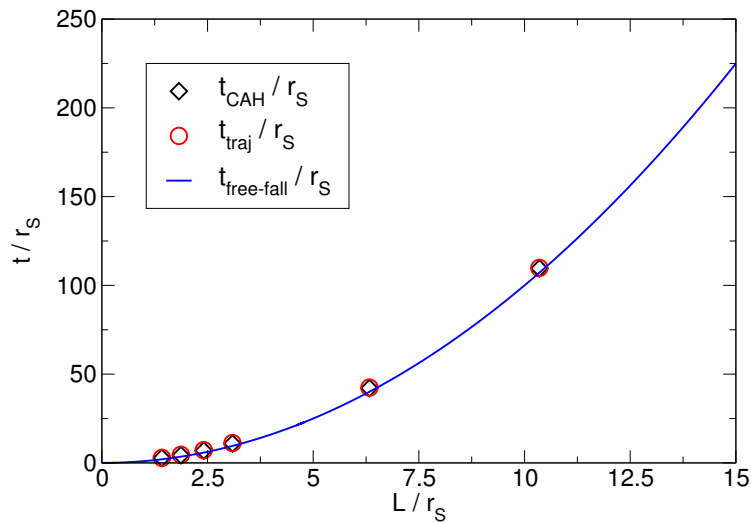


Figure 6.8: Estimates for the time it takes for two equal-mass black holes to collide in $D = 5$. The first estimate is given by the time t_{CAH} elapsed until a single common apparent horizon engulfs both black holes (diamonds), the second estimate is obtained by using the trajectory of the black holes, i.e., the time t_{traj} at which their separation has decreased below the Schwarzschild radius (circles). Finally, these numerical results are compared against a simple Newtonian estimate, given by equation (6.4.23) (blue solid line).

another example of how well numerically successful gauge conditions appear to be adapted to the black hole kinematics.

6.4.3.2 Waveforms

Let us now discuss the gravitational wave signal, extracted with the KI formalism, generated by the head-on collision of two black holes in five dimensions.

In figure 6.9, the $l = 2$ multipole of the KI function Φ_t for model HD5e obtained at different extraction radii is plotted. A small spurious wavepulse due to the initial data construction

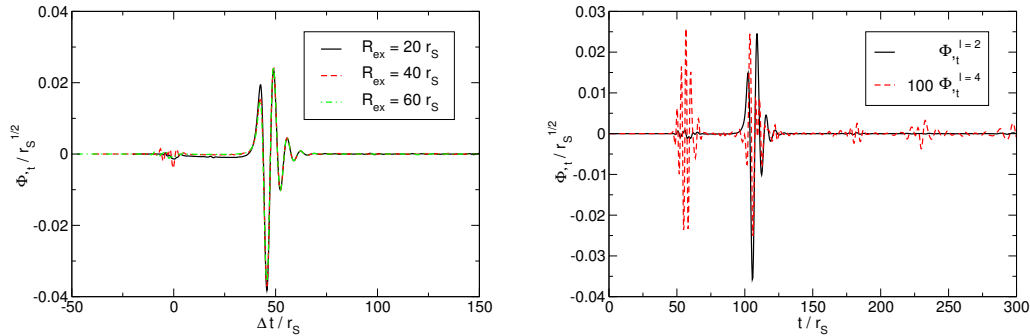


Figure 6.9: Left panel: The $l = 2$ component of the KI waveform for model HD5e extracted at radii $R_{\text{ex}}/r_S = 20, 40$ and 60 and shifted in time by R_{ex}/r_S . Right panel: The $l = 2$ and $l = 4$ mode of the KI function for the same simulation, extracted at $R_{\text{ex}}/r_S = 60$. For clarity, the $l = 4$ component has been re-scaled by a factor of 100.

is visible at $\Delta t \approx 0$, the so-called “junk radiation”. The physical part of the waveform is dominated by the merger signal around $\Delta t = 50r_S$, followed by the (exponentially damped) ringdown, whereas the infall of the holes before $\Delta t = 40r_S$ does not produce a significant amount of gravitational waves. Comparison of the waveforms extracted at different radii demonstrates excellent agreement, in particular for those extracted at $R_{\text{ex}} = 40r_S$ and $60r_S$. Extrapolation of the radiated energy to infinite extraction radius yield a relative error of 5 % at $R_{\text{ex}} = 60r_S$, indicating that such radii are adequate for the analysis presented in this work.

Due to symmetry, no gravitational waves are emitted in the $l = 3$ multipole, so that $l = 4$ represents the second strongest contribution to the wave signal. As demonstrated in the right panel of figure 6.9, however, its amplitude is two orders of magnitude below that of the quadrupole.

In order to assess how accurately we are thus able to approximate an infall from infinity, we have varied the initial separation for models HD5a to HD5f as summarised in table 6.2. As demonstrated in figure 6.10, for models HD5e and HD5f we can safely neglect the spurious radiation as well as the impact of a finite initial separation, provided we use a sufficiently large initial distance $d \gtrsim 6r_S$ of the binary. Here, we compare the radiation emitted during the head-on collision of black holes starting from rest with initial separations $6.37r_S$ and $10.37r_S$. The waveforms have been shifted in time by the extraction radius $R_{\text{ex}} = 60r_S$ and such that the formation of a common apparent horizon occurs at $\Delta t = 0$. The merger signal starting around $\Delta t = 0$ shows excellent agreement for the two configurations and is not affected by the spurious signal visible for HD5e at $\Delta t \approx -50r_S$.

We conclude this discussion with an analysis of the ringdown. After formation of a common horizon, the waveform is dominated by an exponentially damped sinusoid, as the merged hole *rings down* into a stationary state. By fitting our results with an exponentially-damped

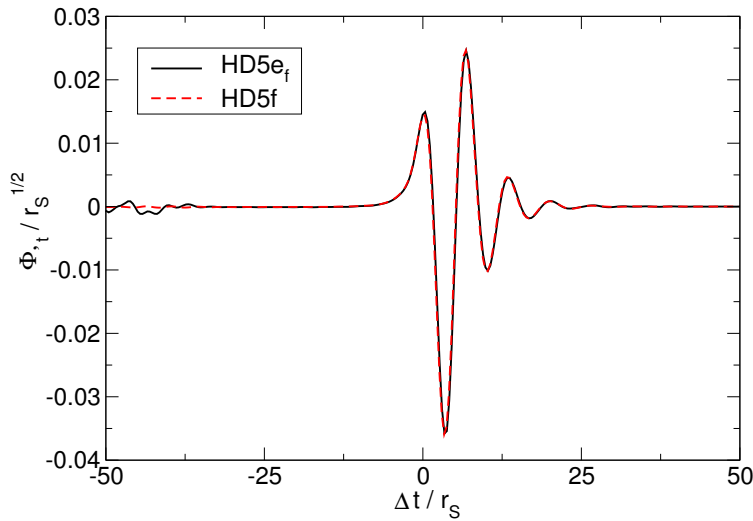


Figure 6.10: $l = 2$ components of the KI function as generated by a head-on collision of black holes with initial (coordinate) distance $d = 6.37r_S$ (black solid line) and $d = 10.37r_S$ (red dashed line). The wave functions have been shifted in time such that the formation of a common apparent horizon corresponds to $\Delta t = 0$ (and taking into account the time it takes for the waves to propagate up to the extraction radius $R_{\text{ex}} = 60r_S$).

sinusoid, we obtain a characteristic frequency

$$r_S \omega = 0.955 \pm 0.005 - i(0.255 \pm 0.005). \quad (6.4.24)$$

This value is in excellent agreement with perturbative calculations, which predict a lowest quasinormal frequency $r_S \omega = 0.9477 - i0.2561$ for $l = 2$ [191, 127, 192].

6.4.3.3 Radiated energy

We now compute the energy flux from the KI master function via equation (5.1.45). The fluxes thus obtained for the $l = 2$ multipole of models HD5e and HD5f in table 6.2, extracted at $R_{\text{ex}} = 60r_S$, are shown in figure 6.11. As in the case of the KI master function in figure 6.10, we see no significant variation of the flux for the two different initial separations. The flux reaches a maximum value of $dE/dt \sim 3.4 \times 10^{-4} r_S$, and is then dominated by the ringdown flux. The energy flux from the $l = 4$ mode is typically four orders of magnitude smaller; this is consistent with the factor of 100 difference of the corresponding wave multipoles observed in figure 6.9, and the quadratic dependence of the flux on the wave amplitude. Integrating, we find that a fraction of $E_{\text{rad}}/M = (8.9 \pm 0.6) \times 10^{-4}$ of the centre of mass energy is emitted in the form of gravitational radiation. We have verified for these models that the amount of energy contained in the spurious radiation is about three orders of magnitude smaller than in the physical merger signal.

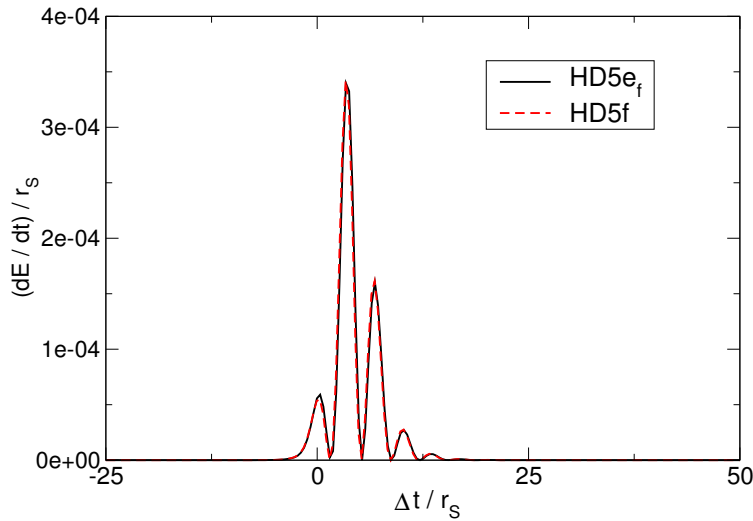


Figure 6.11: Energy flux in the $l = 2$ component of the KI wave function $\Phi_{,t}$, extracted at $R_{\text{ex}} = 60r_S$, for models HD5e (black solid line) and HD5f (red dashed line) in table 6.2. The fluxes have been shifted in time by the extraction radius $R_{\text{ex}} = 60r_S$ and the time t_{CAH} at which the common apparent horizon forms.

6.5 Discussion

In this chapter we have presented a framework that allows the generalisation of the present generation of 3+1 numerical codes to evolve, with relatively minor modifications, spacetimes with $SO(D - 2)$ symmetry in 5 dimensions and $SO(D - 3)$ symmetry in $D \geq 6$ dimensions. The key idea is a dimensional reduction of the problem, along the lines of references [179, 184], that recasts the D -dimensional Einstein vacuum equations in the form of the standard four dimensional equations plus some source terms. The resulting equations can be transformed straightforwardly into the BSSN formulation that has proved remarkably successful in numerical evolutions of black hole configurations in 3+1 spacetimes.

The class of problems that may be studied with our framework includes head-on collisions in $D \geq 5$ and a subset of black hole collisions with impact parameter and spin in $D \geq 6$.

A procedure to construct initial data and a formalism to extract gravitational radiation observables from the numerical simulations were also introduced. With these tools, the numerical implementation was done by adapting the LEAN code and, after a number of tests including the convergence of the Hamiltonian and momentum constraints as well as comparing numerical results with (semi-)analytic expressions for a single Tangherlini black hole in geodesic slicing, we reported results obtained for evolutions of black hole collisions in five-dimensional spacetimes.

As might be expected, stable evolutions of such spacetimes require some modifications of

the underlying methods of the so-called *moving puncture* technique, especially with regard to the gauge conditions used therein. We have successfully modified the slicing condition in order to obtain long-term stable simulations in $D = 5$ dimensions. Unfortunately, these modifications do not appear sufficient to provide long-term stability for arbitrary values of the dimensionality D . This issue remains under investigation.

Besides obtaining the corresponding waveforms for head-on collision of five-dimensional black holes, we have further shown that the total energy released in the form of gravitational waves is approximately $(0.089 \pm 0.006)\%$ of the initial centre of mass energy of the system, for a head-on collision of two black holes starting from rest at very large distances. As a comparison, the analogous process in $D = 4$ releases a slightly smaller quantity: $(0.055 \pm 0.006)\%$.

As yet another test of our implementation, the ringdown part of the waveform was also shown to yield a quasinormal mode frequency in excellent agreement with predictions from black hole perturbation theory.

The numbers reported here for the total energy loss in gravitational waves should increase significantly in high energy collisions, which are the most relevant scenarios for the applications described in the Introduction. Indeed, in the four dimensional case, it is known that ultra-relativistic head-on collisions of equal mass non-rotating black holes release up to 14% of the initial centre of mass energy into gravitational radiation [40]. The analogous number in higher dimensions is as yet unknown, and it remains under investigations using the tools here presented.

Even more energy may be released in high energy collisions with non-vanishing impact parameter. In [41, 42] it was shown that this number can be as large as 35% in $D = 4$. The formalism here developed allows, in principle, the study of analogous processes in $D \geq 6$.

6.A Ricci tensor

In this appendix we give the full details about the computation of the Ricci tensor of section 6.1.1. We start by writing the metric (6.1.1) in block-diagonal form

$$d\bar{s}^2 = \bar{g}_{AB}e^A \otimes e^B = g_{\mu\nu}dx^\mu \otimes dx^\nu + g_{\bar{i}\bar{j}}\Theta^{\bar{i}} \otimes \Theta^{\bar{j}}, \quad (6.A.1)$$

where

$$e_A = (D_\mu, \partial_{\bar{i}}), \quad D_\mu = \partial_\mu - \epsilon\kappa B_\mu^{\bar{i}}\partial_{\bar{i}}, \quad (6.A.2)$$

is now the (non-coordinate) basis. Its dual is

$$e^A = (dx^\mu, \Theta^{\bar{i}}), \quad \Theta^{\bar{i}} = dx^{\bar{i}} + \epsilon\kappa B_\mu^{\bar{i}}dx^\mu. \quad (6.A.3)$$

This basis satisfies

$$[e_A, e_B] = \mathcal{F}^{\bar{k}}{}_{AB}\partial_{\bar{k}}, \quad (6.A.4)$$

where $\mathcal{F}^{\bar{k}}_{AB}$ are given by (6.1.8). In the following we will not explicitly assume the expressions (6.1.8), i.e., we will only assume (unless explicitly mentioned otherwise) that $[e_A, e_B] = \mathcal{F}^k_{AB} e_{\bar{k}} = \mathcal{F}^k_{AB} \partial_{\bar{k}}$, $\partial_i g_{\mu\nu} = 0$ and $\mathcal{F}^{\bar{k}}_{i\bar{j}} = 0$. We will not assume the expression for the e_μ in terms of the coordinate basis (even though we will assume that $e_{\bar{k}} = \partial_{\bar{k}}$).

Important remark: From now on we will work with the non-coordinate basis e_A to simplify the calculations. Note that, for an arbitrary tensor T_A ,

$$T_{A|B} \equiv \partial_{e_B} T_A \equiv e_B(T_A) \neq \partial_B T_A \equiv \frac{\partial T_A}{\partial x^B}.$$

In particular, $e_\mu \equiv D_\mu \equiv \partial_\mu - \epsilon \kappa B_\mu^i \partial_i$, and as such,

$$T_{A|\mu} = \partial_{e_\mu} T_A = D_\mu(T_A) = \partial_\mu T_A - \epsilon \kappa B_\mu^i \partial_i T_A.$$

We must keep in mind that $T_{A|\mu\nu} \neq T_{A|\nu\mu}$. On the other hand, $e_{\bar{k}} = \partial_{\bar{k}}$ and thus

$$T_{A|\bar{k}} = \partial_{\bar{k}} T_A.$$

We recall our definition of the ‘‘covariant derivatives’’ ∇_μ and $\nabla_{\bar{j}}$ as *

$$\nabla_\sigma T^{\bar{i}\alpha}_{\bar{k}\mu} \equiv D_\sigma T^{\bar{i}\alpha}_{\bar{k}\mu} + \mathcal{F}^{\bar{i}}_{\sigma\bar{l}} T^{\bar{l}\alpha}_{\bar{k}\mu} - \mathcal{F}^{\bar{l}}_{\sigma\bar{k}} T^{\bar{i}\alpha}_{\bar{l}\mu} + \Gamma^\alpha_{\lambda\sigma} T^{\bar{i}\lambda}_{\bar{k}\mu} - \Gamma^\lambda_{\mu\sigma} T^{\bar{i}\alpha}_{\bar{k}\lambda}, \quad (6.A.5)$$

$$\nabla_{\bar{j}} T^{\bar{i}\alpha}_{\bar{k}\mu} \equiv \partial_{\bar{j}} T^{\bar{i}\alpha}_{\bar{k}\mu} + \Gamma^{\bar{i}}_{\bar{l}\bar{j}} T^{\bar{l}\alpha}_{\bar{k}\mu} - \Gamma^{\bar{l}}_{\bar{k}\bar{j}} T^{\bar{i}\alpha}_{\bar{l}\mu}, \quad (6.A.6)$$

recall also that both connections are metric,

$$\nabla_\sigma g_{\mu\nu} = \partial_\sigma g_{\mu\nu} - \Gamma^\lambda_{\mu\sigma} g_{\lambda\nu} - \Gamma^\lambda_{\nu\sigma} g_{\mu\lambda} = 0,$$

$$\nabla_{\bar{k}} g_{\bar{i}\bar{j}} \equiv \partial_{\bar{k}} g_{\bar{i}\bar{j}} - \Gamma^{\bar{l}}_{\bar{i}\bar{k}} g_{\bar{l}\bar{j}} - \Gamma^{\bar{l}}_{\bar{j}\bar{k}} g_{\bar{i}\bar{l}} = 0,$$

and that

$$\nabla_\sigma g_{\bar{i}\bar{j}} \equiv D_\sigma g_{\bar{i}\bar{j}} - \mathcal{F}^{\bar{k}}_{\sigma\bar{i}} g_{\bar{k}\bar{j}} - \mathcal{F}^{\bar{k}}_{\sigma\bar{j}} g_{\bar{i}\bar{k}} \neq 0.$$

We now recall some expressions from section 1.4, which we re-write here for convenience: on a non-coordinate basis obeying

$$[e_A, e_B] = c_{AB}{}^D e_D \quad (6.A.7)$$

the torsion-free connection is given by

$$\Gamma^A{}_{BC} = \frac{1}{2} g^{AD} (g_{DB|C} + g_{DC|B} - g_{BC|D} + c_{DBC} + c_{DCB} - c_{BCD}), \quad (6.A.8)$$

where $\Gamma^A{}_{[BC]} = -\frac{1}{2} c_{BC}{}^A$, and the Riemann tensor by

$$R^A{}_{BCD} = \Gamma^A{}_{BD|C} - \Gamma^A{}_{BC|D} + \Gamma^A{}_{EC} \Gamma^E{}_{BD} - \Gamma^A{}_{ED} \Gamma^E{}_{BC} - \Gamma^A{}_{BE} c_{CD}{}^E. \quad (6.A.9)$$

*Note that now, as we are working on a non-coordinate basis, the order of the indices does matter, i.e., $\Gamma^\alpha{}_{\lambda\sigma} \neq \Gamma^\alpha{}_{\sigma\lambda}$ and $\Gamma^{\bar{i}}_{\bar{j}\bar{k}} \neq \Gamma^{\bar{i}}_{\bar{k}\bar{j}}$.

We use the convention

$$\nabla_{e_\alpha} e_\beta = \Gamma^\lambda_{\beta\alpha} e_\lambda.$$

Applying these formulas to our case,

$$c_{AB}^{\bar{i}} = \mathcal{F}^{\bar{i}}_{AB}, \quad c_{AB}^\mu = 0, \quad e_\mu = D_\mu, \quad e_{\bar{k}} = \partial_{\bar{k}},$$

we get from equation (6.A.8)

$$\begin{aligned} \bar{\Gamma}^\alpha_{\mu\nu} &= \frac{1}{2} g^{\alpha\lambda} (g_{\lambda\mu|\nu} + g_{\lambda\nu|\mu} - g_{\mu\nu|\lambda}) = \Gamma^\alpha_{\mu\nu}, \\ \bar{\Gamma}^{\bar{i}}_{\mu\nu} &= -\frac{1}{2} \mathcal{F}^{\bar{i}}_{\mu\nu}, \\ \bar{\Gamma}^\mu_{\bar{i}\nu} &= \frac{1}{2} g^{\mu\lambda} g_{\bar{i}\bar{k}} \mathcal{F}^{\bar{k}}_{\lambda\nu} = \bar{\Gamma}^\mu_{\nu\bar{i}}, \\ \bar{\Gamma}^\mu_{\bar{i}\bar{j}} &= -\frac{1}{2} g^{\mu\lambda} \nabla_\lambda g_{\bar{i}\bar{j}}, \\ \bar{\Gamma}^{\bar{i}}_{\mu\bar{j}} &= \frac{1}{2} g^{\bar{i}\bar{k}} \nabla_\mu g_{\bar{k}\bar{j}}, \\ \bar{\Gamma}^{\bar{i}}_{\bar{j}\mu} &= \frac{1}{2} g^{\bar{i}\bar{k}} \nabla_\mu g_{\bar{k}\bar{j}} + \mathcal{F}^{\bar{i}}_{\mu\bar{j}}, \\ \bar{\Gamma}^{\bar{i}}_{\bar{j}\bar{k}} &= \frac{1}{2} g^{\bar{i}\bar{l}} (g_{\bar{l}\bar{j}|\bar{k}} + g_{\bar{l}\bar{k}|\bar{j}} - g_{\bar{j}\bar{k}|\bar{l}}) = \Gamma^{\bar{i}}_{\bar{j}\bar{k}}. \end{aligned} \tag{6.A.10}$$

From (6.A.9) we compute the Ricci tensor,

$$\bar{R}_{\mu\nu} = R_{\mu\nu} - \frac{1}{2} g^{\alpha\lambda} g_{\bar{i}\bar{j}} \mathcal{F}^{\bar{i}}_{\lambda\mu} \mathcal{F}^{\bar{j}}_{\alpha\nu} - \frac{1}{2} \nabla_\nu (g^{\bar{i}\bar{j}} \nabla_\mu g_{\bar{i}\bar{j}}) - \frac{1}{4} g^{\bar{i}\bar{j}} g^{\bar{k}\bar{l}} \nabla_\mu g_{\bar{i}\bar{k}} \nabla_\nu g_{\bar{j}\bar{l}} - \frac{1}{2} \nabla_{\bar{k}} \mathcal{F}^{\bar{k}}_{\mu\nu}, \tag{6.A.11}$$

$$\bar{R}_{\mu\bar{i}} = \frac{1}{2} g^{\alpha\lambda} \nabla_\alpha (g_{\bar{i}\bar{k}} \mathcal{F}^{\bar{k}}_{\lambda\mu}) + \frac{1}{4} g^{\bar{k}\bar{l}} \nabla_\beta g_{\bar{k}\bar{l}} g^{\beta\lambda} \mathcal{F}^{\bar{m}}_{\lambda\mu} g_{\bar{i}\bar{m}} + \frac{1}{2} \nabla_{\bar{k}} (g^{\bar{k}\bar{l}} \nabla_\mu g_{\bar{l}\bar{i}}) - \frac{1}{2} \nabla_{\bar{i}} (g^{\bar{k}\bar{l}} \nabla_\mu g_{\bar{k}\bar{l}}), \tag{6.A.12}$$

$$\bar{R}_{\bar{i}\mu} = \bar{R}_{\mu\bar{i}} + \mathcal{F}^{\bar{k}}_{\mu\bar{i}|\bar{k}} - \mathcal{F}^{\bar{k}}_{\mu\bar{k}|\bar{i}}, \tag{6.A.13}$$

$$\bar{R}_{\bar{i}\bar{j}} = R_{\bar{i}\bar{j}} - \frac{1}{4} g^{\bar{k}\bar{l}} \nabla_\beta g_{\bar{k}\bar{l}} \nabla^\beta g_{\bar{i}\bar{j}} + \frac{1}{2} g^{\bar{k}\bar{l}} \nabla_\beta g_{\bar{i}\bar{k}} \nabla^\beta g_{\bar{j}\bar{l}} + \frac{1}{4} g^{\alpha\lambda} g^{\beta\rho} g_{\bar{j}\bar{k}} g_{\bar{i}\bar{l}} \mathcal{F}^{\bar{k}}_{\beta\lambda} \mathcal{F}^{\bar{l}}_{\rho\alpha} - \frac{1}{2} \nabla^\beta \nabla_\beta g_{\bar{i}\bar{j}}, \tag{6.A.14}$$

where

$$\begin{aligned} \nabla_{\bar{k}} \mathcal{F}^{\bar{k}}_{\mu\nu} &\equiv \mathcal{F}^{\bar{k}}_{\mu\nu|\bar{k}} + \Gamma^{\bar{k}}_{\bar{j}\bar{k}} \mathcal{F}^{\bar{j}}_{\mu\nu}, \\ \nabla_{\bar{i}} (g^{\bar{k}\bar{l}} \nabla_\mu g_{\bar{k}\bar{l}}) &\equiv \partial_{\bar{i}} (g^{\bar{k}\bar{l}} \nabla_\mu g_{\bar{k}\bar{l}}), \\ \nabla_{\bar{k}} (g^{\bar{k}\bar{l}} \nabla_\mu g_{\bar{l}\bar{i}}) &\equiv \partial_{\bar{k}} (g^{\bar{k}\bar{l}} \nabla_\mu g_{\bar{l}\bar{i}}) + \Gamma^{\bar{k}}_{\bar{j}\bar{k}} g^{\bar{j}\bar{l}} \nabla_\mu g_{\bar{l}\bar{i}} - \Gamma^{\bar{j}}_{\bar{i}\bar{k}} g^{\bar{k}\bar{l}} \nabla_\mu g_{\bar{l}\bar{j}}, \end{aligned}$$

and we also used $\Gamma^{\bar{k}}_{[\bar{i}\bar{j}]} = -\frac{1}{2} c_{\bar{i}\bar{j}}^{\bar{k}} = -\frac{1}{2} \mathcal{F}^{\bar{k}}_{\bar{i}\bar{j}} = 0$ and $\Gamma^\alpha_{[\mu\beta]} = -\frac{1}{2} c_{\mu\beta}^\alpha = -\frac{1}{2} \mathcal{F}^\alpha_{\mu\beta} = 0$.

The Ricci scalar is given by

$$\bar{R} = \bar{g}^{AB} \bar{R}_{AB} = g^{\mu\nu} \bar{R}_{\mu\nu} + g^{\bar{i}\bar{j}} \bar{R}_{\bar{i}\bar{j}}.$$

We have

$$\begin{aligned}\bar{R} &= R + \tilde{R} - \frac{1}{4}g^{\bar{k}\bar{l}}g^{\alpha\lambda}g^{\mu\nu}\mathcal{F}^{\bar{l}}_{\lambda\mu}\mathcal{F}^{\bar{k}}_{\alpha\nu} - \nabla^\mu\left(g^{\bar{k}\bar{l}}\nabla_\mu g_{\bar{k}\bar{l}}\right) - \frac{1}{4}g^{\bar{k}\bar{i}}g^{\bar{j}\bar{l}}\nabla^\mu g_{\bar{k}\bar{l}}\nabla_\mu g_{\bar{i}\bar{j}} \\ &\quad - \frac{1}{4}g^{\bar{k}\bar{l}}g^{\bar{i}\bar{j}}\nabla^\mu g_{\bar{k}\bar{l}}\nabla_\mu g_{\bar{i}\bar{j}},\end{aligned}\tag{6.A.15}$$

where $\tilde{R} = g^{\bar{i}\bar{j}}R_{\bar{i}\bar{j}}$.

We still need to write the components of the Ricci tensor in the coordinate basis $(\partial_\mu, \partial_{\bar{i}})$, so from here on we need to use the specific form of e_μ and, thus, also the algebra in (6.1.8). We perform the basis transformation the usual way,

$$\begin{aligned}\mathbf{R} &= \bar{R}_{AB}e^A \otimes e^B \\ &= \left(\bar{R}_{\mu\nu} + e\kappa\bar{R}_{\bar{i}\bar{\nu}}B_{\bar{\mu}}^{\bar{i}} + e\kappa\bar{R}_{\bar{\mu}\bar{i}}B_{\bar{\nu}}^{\bar{i}} + e^2\kappa^2\bar{R}_{\bar{i}\bar{j}}B_{\bar{\mu}}^{\bar{i}}B_{\bar{\nu}}^{\bar{j}}\right)dx^\mu \otimes dx^\nu \\ &\quad + \left(\bar{R}_{\bar{i}\bar{\mu}} + e\kappa\bar{R}_{\bar{i}\bar{j}}B_{\bar{\mu}}^{\bar{j}}\right)dx^{\bar{i}} \otimes dx^\mu + \left(\bar{R}_{\bar{\mu}\bar{i}} + e\kappa\bar{R}_{\bar{j}\bar{i}}B_{\bar{\mu}}^{\bar{j}}\right)dx^\mu \otimes dx^{\bar{i}} + \bar{R}_{\bar{i}\bar{j}}dx^{\bar{i}} \otimes dx^{\bar{j}},\end{aligned}$$

and thus, in the basis $(\partial_\mu, \partial_{\bar{i}})$ where the metric takes the form (6.1.1), we have

$$\bar{R}_{\bar{i}\bar{j}} = R_{\bar{i}\bar{j}} - \frac{1}{4}g^{\bar{k}\bar{l}}\nabla_\beta g_{\bar{k}\bar{l}}\nabla^\beta g_{\bar{i}\bar{j}} + \frac{1}{2}g^{\bar{k}\bar{l}}\nabla_\beta g_{\bar{i}\bar{k}}\nabla^\beta g_{\bar{j}\bar{l}} + \frac{1}{4}g^{\alpha\lambda}g^{\beta\rho}g_{\bar{j}\bar{k}}g_{\bar{i}\bar{l}}\mathcal{F}^{\bar{k}}_{\beta\lambda}\mathcal{F}^{\bar{l}}_{\rho\alpha} - \frac{1}{2}\nabla^\beta\nabla_\beta g_{\bar{i}\bar{j}},\tag{6.A.16}$$

$$\begin{aligned}\bar{R}_{\bar{\mu}\bar{i}} &= e\kappa\bar{R}_{\bar{i}\bar{j}}B_{\bar{\mu}}^{\bar{j}} + \frac{1}{2}g^{\alpha\lambda}\nabla_\alpha\left(g_{\bar{i}\bar{k}}\mathcal{F}^{\bar{k}}_{\lambda\mu}\right) + \frac{1}{4}g^{\bar{k}\bar{l}}\nabla_\beta g_{\bar{k}\bar{l}}g^{\beta\lambda}\mathcal{F}^{\bar{m}}_{\lambda\mu}g_{\bar{i}\bar{m}} + \frac{1}{2}\nabla_{\bar{k}}\left(g^{\bar{k}\bar{l}}\nabla_\mu g_{\bar{l}\bar{i}}\right) \\ &\quad - \frac{1}{2}\nabla_{\bar{i}}\left(g^{\bar{k}\bar{l}}\nabla_\mu g_{\bar{k}\bar{l}}\right) = \bar{R}_{\bar{i}\bar{\mu}},\end{aligned}\tag{6.A.17}$$

$$\begin{aligned}\bar{R}_{\mu\nu} &= R_{\mu\nu} + 2e\kappa B_{(\mu}^{\bar{i}}\bar{R}_{\nu)\bar{i}} - e^2\kappa^2\bar{R}_{\bar{i}\bar{j}}B_{\bar{\mu}}^{\bar{i}}B_{\bar{\nu}}^{\bar{j}} - \frac{1}{2}g^{\alpha\lambda}g_{\bar{i}\bar{j}}\mathcal{F}^{\bar{i}}_{\lambda\mu}\mathcal{F}^{\bar{j}}_{\alpha\nu} - \frac{1}{2}\nabla_\nu\left(g^{\bar{i}\bar{j}}\nabla_\mu g_{\bar{i}\bar{j}}\right) \\ &\quad - \frac{1}{4}g^{\bar{i}\bar{j}}g^{\bar{k}\bar{l}}\nabla_\mu g_{\bar{i}\bar{k}}\nabla_\nu g_{\bar{j}\bar{l}} - \frac{1}{2}\nabla_{\bar{k}}\mathcal{F}^{\bar{k}}_{\mu\nu},\end{aligned}\tag{6.A.18}$$

and

$$\begin{aligned}\bar{R} &= R + \tilde{R} - \frac{1}{4}g^{\bar{k}\bar{l}}g^{\alpha\lambda}g^{\mu\nu}\mathcal{F}^{\bar{l}}_{\lambda\mu}\mathcal{F}^{\bar{k}}_{\alpha\nu} - \nabla^\mu\left(g^{\bar{k}\bar{l}}\nabla_\mu g_{\bar{k}\bar{l}}\right) - \frac{1}{4}g^{\bar{k}\bar{i}}g^{\bar{j}\bar{l}}\nabla^\mu g_{\bar{k}\bar{l}}\nabla_\mu g_{\bar{i}\bar{j}} \\ &\quad - \frac{1}{4}g^{\bar{k}\bar{l}}g^{\bar{i}\bar{j}}\nabla^\mu g_{\bar{k}\bar{l}}\nabla_\mu g_{\bar{i}\bar{j}}.\end{aligned}\tag{6.A.19}$$

Note: We have used the same indices to label components in both the coordinate and non-coordinate basis. No confusion shall arise, however, since the non-coordinate basis was used merely to simplify the previous computations. In the main text we deal exclusively with the coordinate basis, to which all components refer.

6.B Equations of motion: Einstein frame

We here write the equations of motion obtained when we write the action (6.1.26) in the Einstein frame. To do so, we perform the usual conformal transformation

$$g_{\mu\nu} = \psi^{-\frac{2}{d-2}}\tilde{g}_{\mu\nu}\tag{6.B.1}$$

where in our case $\psi \equiv e^{n\phi}$. The action then takes the form

$$\mathcal{S} = \frac{1}{16\pi G_d} \int d^d x \sqrt{-\tilde{g}} \left[\tilde{R} + k \partial_\mu \tilde{\phi} \partial^\mu \tilde{\phi} + n(n-1) e^{-2\tilde{\phi}} \right] \quad (6.B.2)$$

where $k \equiv n \frac{d(d-4)(n-1)-2(n+2)}{(d-2+n)^2}$ and $\tilde{\phi} = \frac{d-2+n}{d-2} \phi$. From action (6.B.2) we obtain the equations of motion

$$\begin{aligned} k \tilde{\nabla}^\alpha \partial_\alpha \tilde{\phi} + n(n-1) e^{-2\tilde{\phi}} &= 0 \\ \tilde{R}_{\mu\nu} &= -k \partial_\mu \tilde{\phi} \partial_\nu \tilde{\phi} - \frac{n(n-1)}{d-2} e^{-2\tilde{\phi}} \tilde{g}_{\mu\nu} . \end{aligned} \quad (6.B.3)$$

Chapter 7

Non-asymptotically flat spacetimes

7.1 de Sitter

Nonlinear dynamics in cosmological backgrounds has the potential to teach us immensely about our universe, and also to serve as prototype for nonlinear processes in generic curved spacetimes. *de Sitter* spacetime, as already mentioned in the Introduction, is the simplest accelerating universe—a maximally symmetric solution of Einstein’s equations with a positive cosmological constant—which seems to model quite well the present cosmological acceleration [100].

Key questions concerning the evolution towards a de Sitter, spatially homogeneous universe are how inhomogeneities develop in time and, in particular, if they are washed away by the cosmological expansion [193]. Answering them requires controlling the imprint of the gravitational interaction between localised objects on the large-scale expansion. Conversely, the cosmological dynamics should leave imprints in strong gravitational phenomena like primordial black hole formation [194] or the gravitational radiation emitted in a black hole binary coalescence, which carry signatures of the cosmological acceleration as it travels across the universe. Identifying these signatures is not only of conceptual interest but also phenomenologically relevant, in view of the ongoing efforts to directly detect gravitational radiation.

Finally, dynamics in asymptotically de Sitter spacetimes could also teach us about more fundamental questions such as cosmic censorship: two black holes of sufficiently large mass in de Sitter spacetime would, upon merger, give rise to too large a black hole to fit in its cosmological horizon. In this case the end state would be a naked singularity. This possibility begs for a time evolution of such a configuration. Does the time evolution of non-singular data containing two black holes result in a naked singularity, or are potentially offending black holes simply driven away from each other by the cosmological expansion?

In this section, following [195], we report on numerical evolutions of black hole binaries in an asymptotically de Sitter geometry. Even though we consider a range of values for the

cosmological constant far larger than those which are phenomenologically viable, these results provide useful insight on the general features of dynamical black hole processes in spacetimes with a cosmological constant, which can improve our understanding of our universe.

7.1.1 Evolution equations

The Einstein equations with cosmological constant Λ are

$$R_{\mu\nu} - \frac{1}{2}g_{\mu\nu}R = -\Lambda g_{\mu\nu}, \quad (7.1.1)$$

and we will always consider $\Lambda > 0$. We perform the 3+1 decomposition by introducing the projection operator $\gamma_{\mu\nu}$ and the normal to the three dimensional hyper-surface Σ , n^μ ($n^\mu n_\mu = -1$), as outlined in section 2.5 and write the evolution equations in the BSSN form (4.1.14).

From (7.1.1), we straightforwardly compute the source terms

$$\begin{aligned} 8\pi E &= \Lambda, & 8\pi j_i &= 0, \\ 8\pi S_{ij} &= -\Lambda \chi^{-1} \tilde{\gamma}_{ij}, & 8\pi S &= -3\Lambda. \end{aligned} \quad (7.1.2)$$

A new evolution variable $\bar{\chi} = \exp(2\sqrt{\Lambda/3}t)\chi$ has been introduced instead of the usual BSSN variable χ [193]. The reason is that for black hole evolutions it is crucial to impose a floor value on χ , typically 10^{-4} or 10^{-6} , which is inconsistent with the natural behaviour of this variable in a de Sitter spacetime (as we will see below): $\chi^{-1} \sim \exp(2\sqrt{\Lambda/3}t)$. In contrast $\bar{\chi} \rightarrow 1$ when $r \rightarrow \infty$ for all times. The evolution equations are thus

$$\partial_t \tilde{\gamma}_{ij} = [\dots], \quad (7.1.3a)$$

$$\partial_t \bar{\chi} = 2\bar{\chi}(\alpha K - \partial_i \beta^i)/3 + \beta^i \partial_i \bar{\chi} + 2\sqrt{\frac{\Lambda}{3}}\bar{\chi}, \quad (7.1.3b)$$

$$\partial_t K = [\dots] - \alpha \Lambda, \quad (7.1.3c)$$

$$\partial_t \tilde{A}_{ij} = [\dots], \quad (7.1.3d)$$

$$\partial_t \tilde{\Gamma}^i = [\dots]. \quad (7.1.3e)$$

where $[\dots]$ denotes the right-hand side of the BSSN equations (4.1.14) in the absence of source terms.

7.1.2 Schwarzschild-de Sitter

The Schwarzschild-de Sitter spacetime, solution of (7.1.1), written in static coordinates reads

$$ds^2 = -f(R)dT^2 + f(R)^{-1}dR^2 + R^2 d\Omega_2. \quad (7.1.4)$$

The solution is characterised by two parameters: the black hole mass m and the Hubble parameter H ,

$$f(R) = 1 - 2m/R - H^2 R^2, \quad H \equiv \sqrt{\Lambda/3}. \quad (7.1.5)$$

$f(R)$ has two zeros, at $R = R_{\pm}$, $R_- < R_+$, if

$$0 < mH < mH_{\text{crit}} , \quad mH_{\text{crit}} \equiv \sqrt{1/27} . \quad (7.1.6)$$

These zeros are the location of the black hole event horizon (R_-) and of a cosmological horizon (R_+). If $H = 0$, then $R_- = 2m$; if $m = 0$, then $R_+ = 1/H$. If $H, m \neq 0$, then $R_- > 2m$ and $R_+ < 1/H$. Since R is the areal radius, the area of the spatial sections of the cosmological horizon decreases in the presence of a black hole; and the area of the spatial sections of the black hole horizon increases in the presence of a cosmological constant, as one would intuitively anticipate.

The basic dynamics in this spacetime may be inferred by looking at radial timelike geodesics. They obey the equation $(dR/d\tau)^2 = E^2 - f(R)$, where τ is the proper time and E is the conserved quantity associated to the Killing vector field $\partial/\partial T$. In the static patch ($R_- < R < R_+$), E can be regarded as energy. From this equation we see that $f(R)$ is an effective potential. This potential has a maximum at

$$R_{\text{max}} = (m/H^2)^{1/3} . \quad (7.1.7)$$

Geodesics starting from rest (i.e. $dR/d\tau(\tau = \tau_0) = 0$) will fall into the black hole if $R_- < R < R_{\text{max}}$ or move away from the black hole if $R_{\text{max}} < R < R_+$.

As we will discuss in the next section, the initial data for an evolution in the de Sitter universe can be computed in a similar manner as has been done in asymptotically flat space as long as one chooses a foliation with extrinsic curvature K_{ij} having only a trace part. Such a coordinate system is known for Schwarzschild-de Sitter: *McVittie coordinates* [196]. These are obtained from static coordinates by the transformation $(T, R) \rightarrow (t, r)$ given by

$$R = (1 + \xi)^2 a(t)r , \quad T = t + H \int \frac{R dR}{f(R)\sqrt{1 - 2m/R}} , \quad (7.1.8)$$

where $a(t) = \exp(Ht)$ and $\xi \equiv \frac{m}{2a(t)r}$. One obtains McVittie's form for Schwarzschild-de Sitter:

$$ds^2 = - \left(\frac{1 - \xi}{1 + \xi} \right)^2 dt^2 + a(t)^2 (1 + \xi)^4 (dr^2 + r^2 d\Omega_2) . \quad (7.1.9)$$

For $t = \text{constant}$, one can show that indeed $K_j^i = -H\delta_j^i$.

By setting $m = 0$ in McVittie coordinates one recovers an FRW cosmological model with $k = 0$ (flat spatial curvature) and an exponentially growing scale factor. The cosmological horizon \mathcal{H}_C discussed above, located at $R = 1/H$, stands at $r_{\mathcal{H}_C} = 1/(He^{Ht})$. The spatial sections of \mathcal{H}_C seem to be shrinking down in this coordinate system. What happens, in fact, is that the exponentially fast expansion is taking any observer to the outside of \mathcal{H}_C . This is a well known phenomenon in studies of inflation and, as we shall see, has important consequences for the numerical evolution.

7.1.3 Numerical Setup

The cosmological constant introduces a new term (when compared with the vacuum case) in the Hamiltonian constraint obtained after the canonical 3+1 decomposition (2.6.3c),

$$R - K_{ij}K^{ij} + K^2 = 2\Lambda \quad (7.1.10)$$

In references [197, 198] it was observed that imposing a spacetime slicing obeying $K^i_j = -H\delta^i_j$, and a spatial metric of the form $dl^2 = \psi^4\tilde{\gamma}_{ij}dx^i dx^j$, the equations to be solved in order to obtain initial data are equivalent to those in vacuum. In particular, for a system of N black holes momentarily at rest (with respect to the given spatial coordinate patch), the conformal factor ψ takes the form

$$\psi = 1 + \sum_{i=1}^N \frac{m_i}{2|r - r_{(i)}|}. \quad (7.1.11)$$

There are $N + 1$ asymptotically de Sitter regions, as $|r - r_{(i)}| \rightarrow 0, +\infty$; the total mass for observers in the common asymptotic region ($|r - r_{(i)}| \rightarrow +\infty$) is $\sum_i m_i$ [198].

Boundary conditions for all quantities are imposed by looking at the behaviour of massless perturbing fields in a pure de Sitter background. Accordingly, we impose the following asymptotic behaviour for all BSSN variables

$$\partial_t f - \partial_t f_0 + \frac{1}{a(t)}\partial_r f + \frac{f - f_0}{a(t)r} - H(f - f_0) = 0. \quad (7.1.12)$$

We should note that we also performed evolutions using different sets of boundary conditions, to test the independence of the results on boundary conditions imposed in a region with no causal contact with the interaction region. As far as the behaviour and location of the horizons and all quantities discussed in this paper are concerned, no noticeable difference could be found.

Our numerical simulations use the LEAN code [149], see section 4.3. The calculation of Black hole Apparent Horizons (BAHs) and Cosmological Apparent Horizons (CAHs) is performed with AHFINDERDIRECT [153, 154]. We remark that BAHs, found as marginally trapped surfaces, indicate in de Sitter space (with the same legitimacy as in asymptotically flat space) the existence of an event horizon [199]. CAHs are surfaces of zero expansion for *ingoing* null geodesics. In a single black hole case, in McVittie coordinates, the black hole event horizon and cosmological horizon are indeed foliated by apparent horizons.

The “expanding” behaviour of the coordinate system led us to add a new innermost refinement level at periodic time intervals so as to keep the number of points inside the cosmological horizon approximately unchanged. The necessity for adding extra refinement levels effectively limits our ability to follow the evolution on very long timescales, as the number of time steps to cover a fixed portion of physical time grows exponentially. This feature resembles in many ways the recently reported work by Pretorius and Lehner on the follow-up of the black string instability [45].

7.1.4 Numerical Results

As a first test of the numerical implementation, we performed evolutions of a single black hole imposing the McVittie slicing condition; that is, we use (7.1.9) as initial data and impose

$$\partial_t \alpha = 4mrHe^{Ht}/(m + 2re^{Ht})^2, \quad \partial_t \beta^i = 0, \quad (7.1.13)$$

throughout the evolution. The analytical solution (7.1.9) can be compared with the numerical results. For a single black hole evolution with $m = 1$ and $H = 0.8H_{\text{crit}}$, the results are displayed in figure 7.1. Using this slicing, the runs eventually crash (at $t \sim 12m$). By

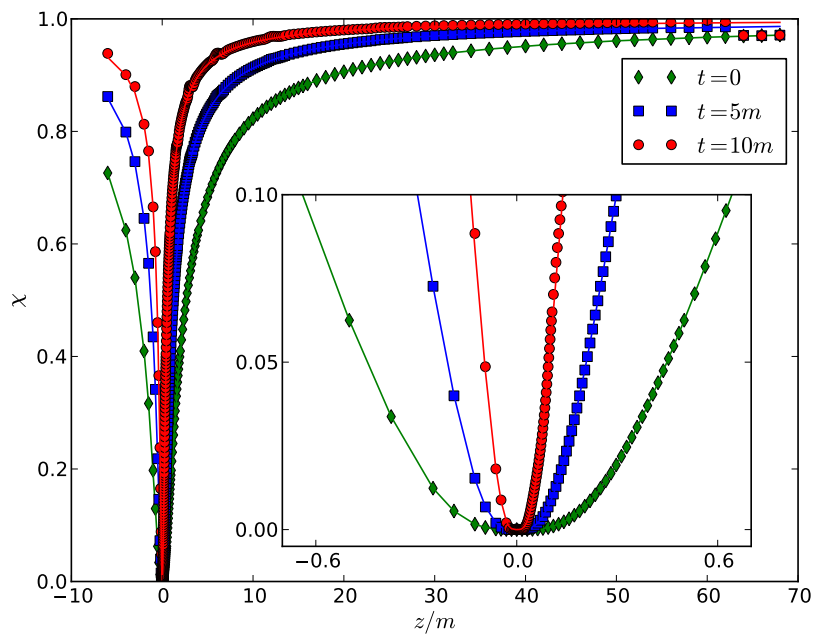


Figure 7.1: Conformal factor χ for a single black hole evolution with $H = 0.8H_{\text{crit}}$ using the McVittie slicing condition, equation (7.1.13). The obtained numerical results are plotted, along the z coordinate (symmetry $\chi(-z) = \chi(z)$ imposed at $z = 0$), against the expected analytical solutions (solid lines).

contrast, the standard “1+log” slicing condition (4.2.3)

$$\partial_t \alpha = \beta^i \partial_i \alpha - 2\alpha (K - K_0), \quad (7.1.14)$$

where $K_0 = -3H = -\sqrt{3\Lambda}$, enables us to have long term stable evolutions. As consistency checks, the areal radii at the apparent horizons (both black hole horizon and cosmological horizon) are constants in time and have the value expected from the analytical solution in a single black hole spacetime. Moreover, the areal radius at fixed coordinate radius evolves with time in the way expected from the exact solution.

For binary black hole initial data, we start by reproducing the results of Nakao et. al [198], where the critical distance between two black holes for the existence of a common BAH

already at $t = 0$ was studied. We thus prepare initial data (7.1.11) with $m_1 = m_2$ and take all quantities in units of the total mass $m = m_1 + m_2$. The two punctures are set initially at symmetric positions along the z axis. The critical value for the cosmological constant, for which the black hole and cosmological horizon coincide is now $mH_{\text{crit}} = 1/\sqrt{27}$. We call *small (large) mass binaries* those, for which $H < H_{\text{crit}}$ ($H > H_{\text{crit}}$). Our results for the critical separation in small mass binaries, at $t = 0$, as function of the Hubble parameter are shown in figure 7.2. The line (diamond symbols) agrees, after a necessary normalisation, with figure 14 of [198].

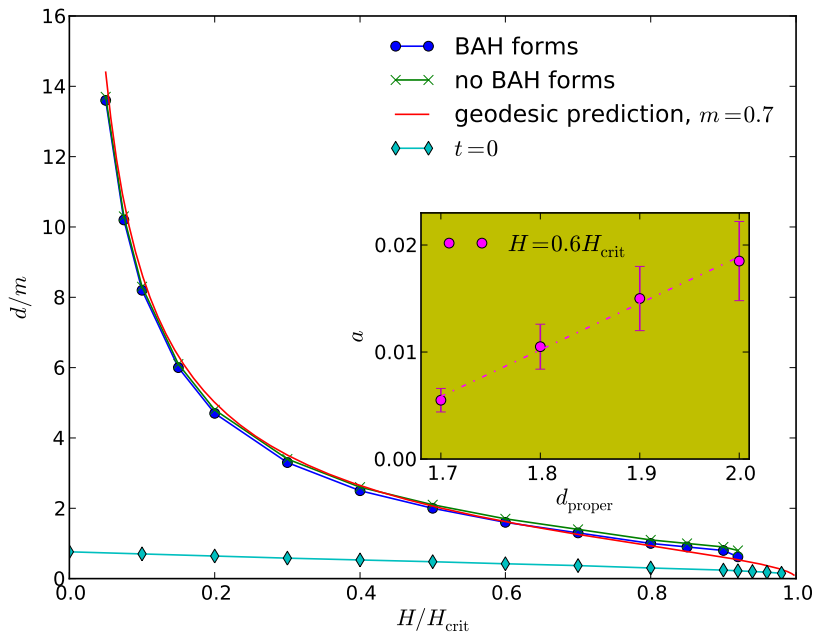


Figure 7.2: Critical coordinate distance for small mass binaries, from both initial data and dynamical evolutions, as well as a point particle estimate, as a function of H/H_{crit} . We obtain this estimate from the coordinate distance to the horizon, equation (7.1.7), for a particular value of m . The $t = 0$ line refers to the critical separation between having or not having a common BAH in the initial data. The inset shows details of the approach to the critical line for $H = 0.6H_{\text{crit}}$, where a is an acceleration parameter.

We now consider head-on collisions of two black holes with no initial momentum, i.e. the time evolution of these data. We have monitored the Hamiltonian constraint violation level for cases with and without cosmological constant. We observe that the constraint violations are comparable in the two cases and plot in figure 7.3 a snapshot of the Hamiltonian constraint violation at $t = 48m$ for parameters $H = 0.9H_{\text{crit}}$ and $d = 0.8m$, a typical case with non-zero cosmological constant. We have used two resolutions, $m/160$ and $m/192$ (on the innermost refinement level) and have rescaled the dashed curve by $Q_2 = (192/160)^2$ as expected for second-order convergence.

For subcritical Hubble constant $H < H_{\text{crit}} = 1/(\sqrt{27}m)$, we monitor the evolution of the

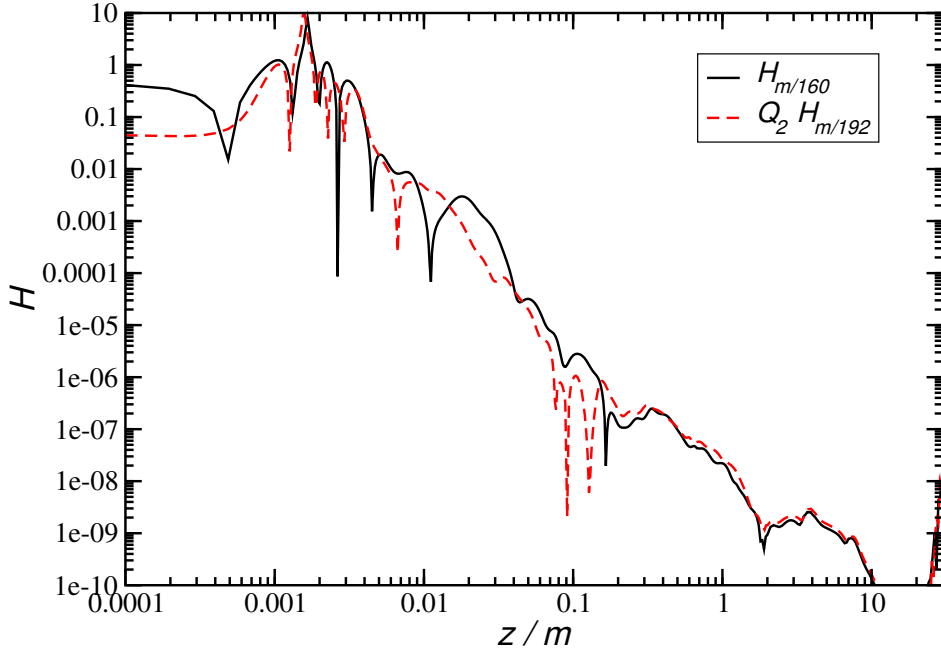


Figure 7.3: Hamiltonian constraint violation along the z -axis at time $t = 48m$ for a simulation with $H = 0.9H_{\text{crit}}$ and initial distance $d = 0.8m$.

areal radius of the BAHs and that of the CAH of an observer at $z = 0$. For instance, for $H = 0.9H_{\text{crit}}$ and proper (initial) separation $3.69m$ we find that the areal radii of the BAH and CAH are approximately constant and equal to $R_{\text{BAH}} \simeq 2.36m$ and $R_{\text{CAH}} \simeq 4.16m$, respectively. As expected the two initial BAHs, as well as the final horizon, are inside the CAH. As a comparison, a Schwarzschild-de Sitter spacetime with the same H has $R_{\text{BAH}} \simeq 2.43m$ and $R_{\text{CAH}} \simeq 4.16m$. This suggests that the interaction effects (binding energy and emission of gravitational radiation) are of the order of a few per cent for this configuration.

As the initial separation grows, so does the total time for merger. For separations larger than a critical value, the two black holes do not merge, but scatter to infinity. For such scattering configurations, the simulations eventually exhibit a regime of exponentially increasing proper distance between the BAH. Just as in scatters of high energy black holes [42], here we find that the immediate merger/scatter regimes are separated by a blurred region, where the holes sit at an almost fixed proper distance for some time; cf. figure 7.4. By performing a large set of simulations for various cosmological parameters H and initial distance d , we have bracketed the critical distance for the merger/scatter region as a function of the Hubble parameter H for the “dynamical” case, i.e., the initial *coordinate* distance between the black holes such that no common BAH forms. The results are displayed in figure 7.2 (circles and \times symbols).

As expected the critical distance becomes larger as compared to the initial data value (“ $t = 0$ ” line): there are configurations for which a common BAH is absent in the initial data but appears during the evolution (just as in asymptotically flat spacetime). The numerical results can be qualitatively well approximated by a point particle prediction—from equation (7.1.7).

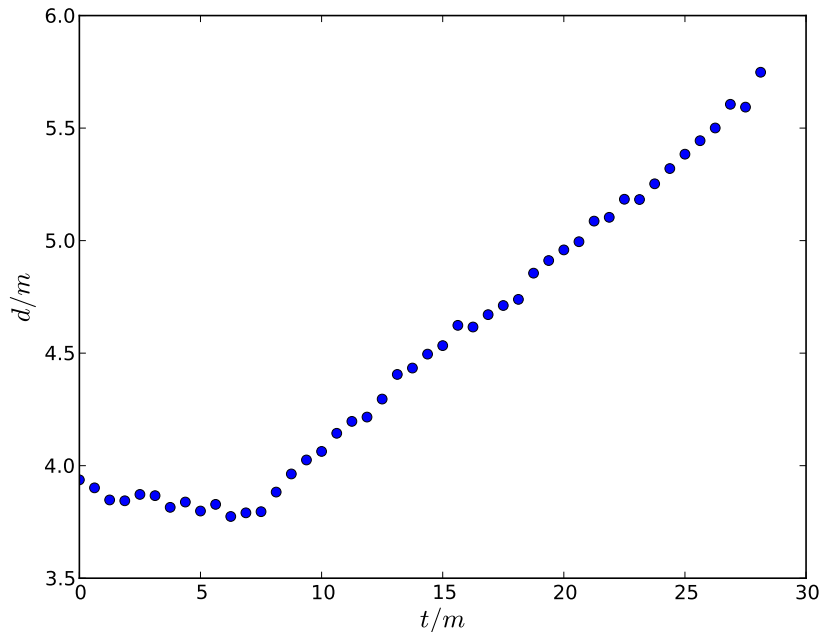


Figure 7.4: Proper distance between the black hole horizons as a function of time for the $H = 0.9H_{\text{crit}}$, and initial (coordinate) distance $d \simeq 0.9m$. The two holes stay at approximately constant distance up to $t \approx 8m$ after which cosmological expansion starts dominating.

To do such comparison a transformation to McVittie coordinates needs to be done; we have performed such transformation at McVittie time $t = 0$. Intriguingly, for a particular value of $m \simeq 0.7$, the point particle approximation matches quantitatively very well the numerical result; the curve obtained from the geodesic prediction in figure 7.2 is barely distinguishable from the numerical results.

A further interesting feature concerns the approach to the critical line. For an initially static binary close to the critical initial separation, the coordinate distance d scales as $d = d_0 + at^2$. In general the acceleration parameter scales as $\log a = C + \Gamma \log(d - d_0)$, where $\Gamma = 1$ in the geodesic approximation. A fit to our numerical results for $H = 0.6H_{\text{crit}}$ (dashed curve in the inset of figure 7.2) for example yields $C = -3.1$, $\Gamma = 0.9$ in rough agreement with this expectation. Details of this regime are given in the inset of figure 7.2.

Finally, we have performed evolutions with $H > H_{\text{crit}}$. On the assumption of weak gravitational wave release, such evolutions can test the cosmic censorship conjecture since the observation of a merger in such case would reveal a violation of the conjecture [200]. From general arguments and from the simulations with $H < H_{\text{crit}}$, we know the cosmological repulsion will dominate for sufficiently large initial distance and in that case we can even expect that a CAH for the observer at $z = 0$ will not encompass the BAHs. This indicates the black holes are no longer in causal contact and therefore can never merge. Our numerical results confirm this overall picture. To test the potentially dangerous configurations, we focus

on the regime in which the black holes are initially very close. A typical example is depicted in figure 7.5, for a supercritical cosmological constant $H = 1.05H_{\text{crit}}$, and an initial coordinate distance $d/m = 1.5002$. Even though the initial separation is very small, we find that the holes move *away* from each other, with a proper separation increasing as the simulation progresses. In fact, further into the evolution, a distorted CAH appears, and remains for as long as the simulation lasts. At late times, this CAH is spherically symmetric, and has an areal radius which agrees, to within 10^{-5} , with that of an empty de Sitter spacetime with the same cosmological constant. The evolution therefore indicates that the spacetime becomes, to an excellent approximation, empty de Sitter space for the observer at $z = 0$ and that the black holes are not in causal contact. Observe that qualitatively similar evolutions can be found in small mass binaries when the initial distance is larger than the critical value

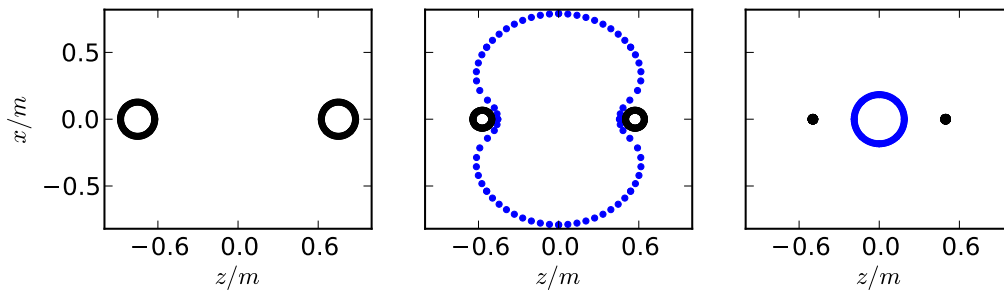


Figure 7.5: Snapshots at different times (from left to right $t/m = 0.0, 8.0156, 20.016$) of a simulation with $H = 1.05H_{\text{crit}}$, and an initial coordinate distance $d/m = 1.5002$. The dotted blue line denotes the CAH (for an observer at $z = 0$) which is first seen in this simulation at $t/m = 8.0156$, highly distorted. At late times, the CAH has an areal radius of $R = 4.94876$, while the “theoretical value” for pure dS is $R = 1/H = 4.94872$, a remarkable agreement showing that the spacetime is accurately empty dS for the observer at $z = 0$ and the black holes are not in causal contact.

7.1.5 Final Remarks

We have presented evidence that the numerical evolution of black hole spacetimes in de Sitter universes is under control. Our results open the door to new studies of strong field gravity in cosmologically interesting scenarios. In closing, we would like to mention that our results are compatible with cosmic censorship in cosmological backgrounds. However, an analytic solution with multiple (charged and extremal) black holes in asymptotically de Sitter spacetime is known, and has been used to study cosmic censorship violations [201]. In *collapsing* universes a potential violation of the conjecture has been reported, although the conclusion relied on singular initial data. To clarify this issue, it would be of great interest to perform numerical evolution of large mass black hole binaries, analogous to those performed herein, but in collapsing universes. This will require adaptations of our setup, since the “expanding” behaviour discussed of the coordinate system will turn into a “collapsing” one,

which raises new numerical challenges.

7.2 Black holes in a box

Anti-de Sitter (AdS) is a non-globally hyperbolic spacetime, which essentially means that it is not enough to prescribe a set of evolution equations and some initial configuration in order to predict what will happen in the future. On such spacetimes, the boundary plays an *active role*, and in order to have a well-defined Cauchy problem the initial data (and evolution equations) must be supplemented by appropriate boundary conditions at the time-like conformal boundary.

In this section, we will give a brief overview of the work presented in [104] where a “toy model” for Anti-de Sitter was considered by imprisoning a black hole binary in a box with mirror-like boundary conditions and thus exploring the active role that boundary conditions play in the evolution of a bulk black hole system.

7.2.1 Numerical setup

The vacuum Einstein equations are written in the BSSN scheme (4.1.14), introduced in section 4.1, with the gauge conditions (4.2.3), (4.2.6). We evolve these equations with the LEAN code [149], see section 4.3.

The work here presented differs from previous implementations of the LEAN code (and most other codes) in the treatment of the outer boundary conditions, which is herein considered to be a reflecting sphere or, rather, an approximation of it by using so-called *Lego* spheres; cf. section 3 in [202]. The numerical implementation of such boundary conditions is schematically illustrated in figure 7.6.

Points outside the outer circle of radius $R_B + \Delta R$ are not required for updating regular points and are simply ignored in the numerical evolution. In practice, we ensure that the boundary shell is always of sufficient thickness to accommodate discretization stencils required for the update of regular gridpoints. The specific boundary condition is then determined by the manner in which we update grid functions on the boundary points marked as \times in the figure.

To mimic the global structure of an AdS spacetime we thus enclose the black hole binary inside the spherical mirror and set

$$\frac{\partial}{\partial t} f = 0, \tag{7.2.1}$$

at each boundary point with f denoting any of the BSSN variables listed in equations (4.1.14). The final ingredient needed for our numerical implementation is related with the spurious radiation present when evolving black hole binaries—often called *junk radiation*—which can be traced back to the methods used to compute the initial data. To avoid contamination of our simulations by such spurious radiation being trapped inside our reflective boundary we employ standard outgoing radiation boundary conditions at early times and only switch on

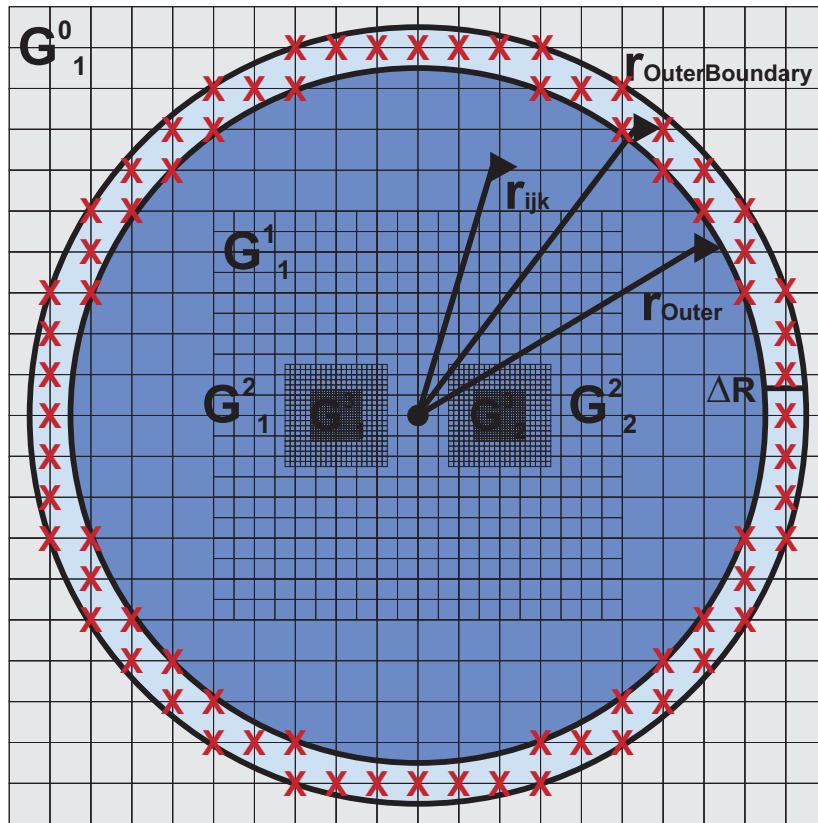


Figure 7.6: Illustration of a (Lego-)spherical outer boundary.

our reflective condition at

$$t_{\text{ref}} = R_B + \Delta t_{\text{pulse}}, \quad (7.2.2)$$

where we estimate the duration of the spurious wave pulse Δt_{pulse} from previous simulations of similar setups in asymptotically flat spacetimes as for example presented in [203, 149, 204]. The spurious radiation is thus given sufficient time to leave the computational domain.

Wave extraction is employed in the fashion outlined in section 5.1.1, where we will herein also measure the Ψ_0 Weyl scalar, which encodes the incoming gravitational wave signal.

The results we will report in the following sections all refer to an inspiral simulation with total mass $M = M_1 + M_2$, where the black hole punctures were set with an initial coordinate distance of $d = 6.517M$ and with Bowen-York momentum parameter $P_i = \pm 0.133M$. The grid structure used was

$$\{(48, 24, 12, 6) \times (1.5, 0.75), h = 1/56\}, \quad (7.2.3)$$

and the Weyl scalars have been extracted at $r_{\text{ex}} = 35M$.

7.2.2 Gravitational wave signal

The nature of our specific configuration is ideal to study both the outgoing (Ψ_4) as well as the ingoing (Ψ_0) gravitational wave pulses.

The gravitational wave signal is dominated by the quadrupole contributions which is shown in figure 7.7. The ingoing signal ψ_{22}^0 has been shifted in time by $\Delta t = 10 M$ to compensate for the additional propagation time from the extraction radius $r_{\text{ex}} = 35 M$ to the boundary $R_B = 40 M$ and back after reflection. The reflection introduces an additional phase shift of $\Delta\phi = \pi$ which has also been taken into account in the figure. Within numerical errors, we find the resulting outgoing and subsequent ingoing pulses to overlap.

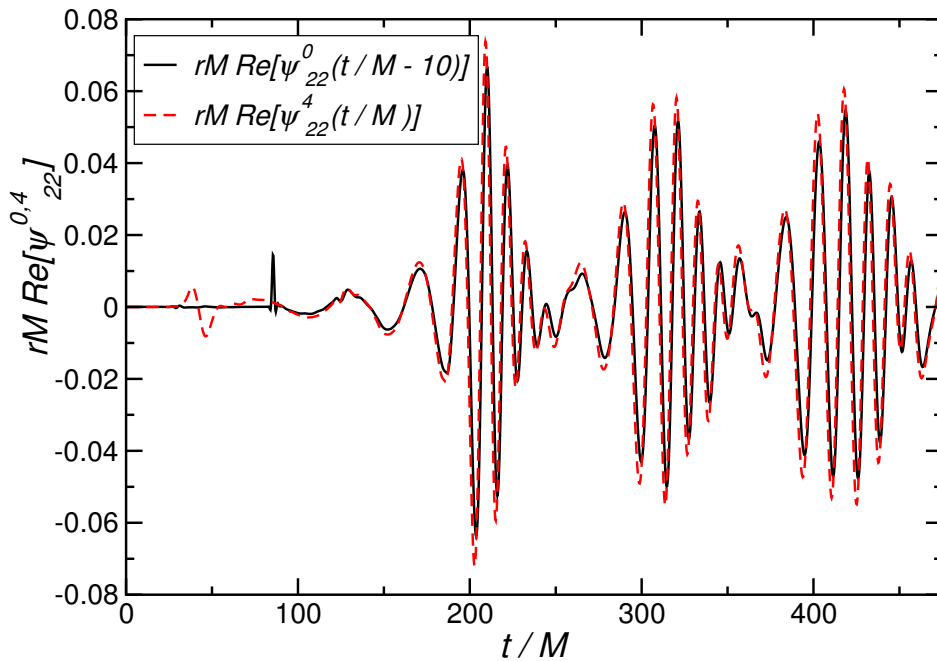


Figure 7.7: Real part of the $l = m = 2$ mode of $rM\Psi_0$ and $rM\Psi_4$. The ingoing signal $rM\Psi_0$ has been shifted in time by $\Delta t = 10M$ and in phase by π (thus equivalent to an extra minus sign) to account for the additional propagation time and the reflection.

7.2.3 Interaction of the wave pulse with the remnant black hole

We define black hole mass in terms of the equatorial radius of the horizon C_e by [205]

$$M = \frac{C_e}{4\pi}. \quad (7.2.4)$$

In figure 7.8 it is shown the fractional deviation $(M - M_0)/M_0$ of the mass of the final black hole from its value immediately after merger together with the irreducible mass and the black hole spin J . The mass remains approximately constant until the pulse returns after its first reflection, then increases, remains constant during the second passage of the pulse and so on.

In contrast, the spin only shows a significant increase during the first scattering of the pulse off the black hole.

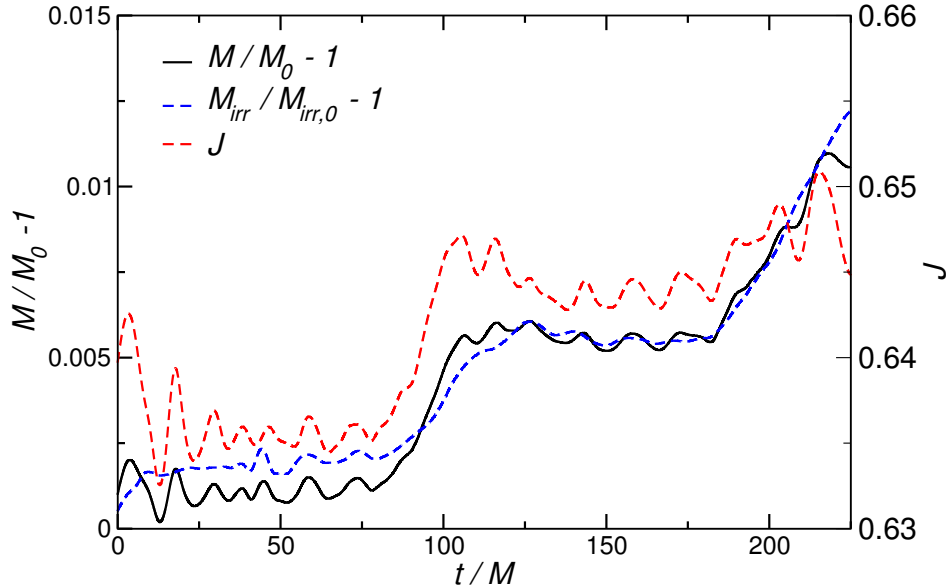


Figure 7.8: Time evolution of the (relative) mass of the black hole (solid) computed by $M = C_e/4\pi$, the irreducible mass (long dashed) and the total spin $J = jM^2$ (dashed curve).

Comparing the increase in the horizon mass with the amount of gravitational wave energy radiated during the last stages of the inspiral, plunge and merger of a corresponding binary system in an asymptotically flat spacetime—which is about 3.5% of the total energy of the system [204, 149]—we estimate that about 15% of the energy emitted during the merger is absorbed by the central spinning black hole per interaction.

7.2.4 Final remarks

In this section, we have given just a brief overview of the work presented in [104] where the global structure of an AdS background was mimicked by introducing a reflecting wall at a finite radius. Inside this cavity a black hole inspiral was evolved.

The results presented are consistent with the intuitive expectations for a wavepacket of radiation (generated during inspiral plus merger) travelling back and forth between the mirror-like wall and the black hole: part of this radiation is absorbed when interacting with the black hole (especially high-frequencies). We estimate that about 15% of the wavepacket's energy is absorbed by the black hole per interaction, at least during the first cycles.

It would be extremely interesting to extend this work to implement the evolution of black holes in real AdS backgrounds, following the recent works in [61, 62, 63].

7.3 Black holes in cylinders

From the gauge/gravity duality to braneworld scenarios, black holes in compactified spacetimes play an important role in fundamental physics. Our current understanding of black hole solutions and their dynamics in such spacetimes is rather poor because analytical tools are capable of handling a limited class of idealised scenarios, only.

In this section, following [206], we wish to study how the compactness of extra dimensions changes the dynamics of such higher-dimensional gravity scenarios. There is considerable literature on Kaluza-Klein black holes and black holes on cylinders [106, 107, 105, 108]; the full non-linear dynamics of black holes on such spacetimes, however, seems to remain unexplored.

7.3.1 Setup

We are interested in describing the evolution of black holes in a five dimensional spacetime with one periodic direction. For a five dimensional cylindrical Minkowski spacetime, $\mathbb{M}^{1,3} \times S^1$, the metric can be written as

$$ds^2 = \underbrace{-dt^2 + dx^2 + dy^2 + y^2 d\phi^2}_{\mathbb{M}^{1,3}} + \underbrace{dz^2}_{S^1}. \quad (7.3.1)$$

The S^1 direction is parameterised by z , which takes values in the interval $[-L, L]$, with the two endpoints identified and $L \in \mathbb{R}^+$. The coordinate ϕ also parameterises a circle, this circle is, however, homotopic to a point, since it shrinks down to zero size at $y = 0$, where y is a radial coordinate in the $y - \phi$ plane which is part of $\mathbb{M}^{1,3}$ —figure 7.9.

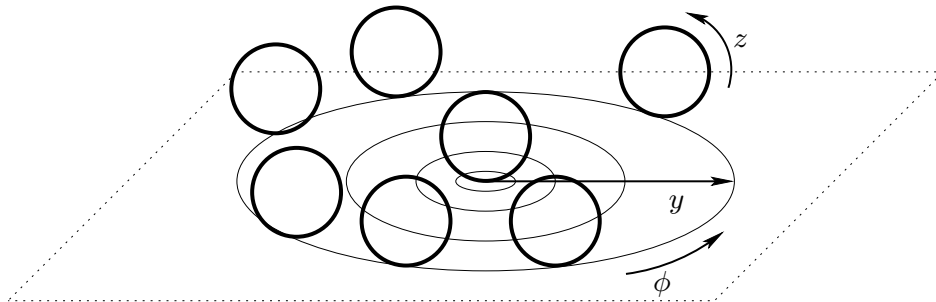


Figure 7.9: Illustration of the coordinate system for the Minkowski spacetime $\mathbb{M}^{1,3} \times S^1$. A slice with $t = \text{constant}$ and $x = \text{constant}$ is shown. y, ϕ parameterise a plane, wherein y is a radial direction and ϕ an azimuthal coordinate. At each point in this plane there is a non-contractible circle parameterised by z . This is illustrated by exhibiting this circle on various points along an orbit of $\partial/\partial\phi$ and also at $y = 0$. Space-time is a (trivial) S^1 bundle over $\mathbb{M}^{1,3}$.

Following the approach outlined in section 6.2, we take our five dimensional metric ansatz to be

$$ds^2 = g_{\mu\nu} dx^\mu dx^\nu + \lambda(x^\mu) d\phi^2, \quad (7.3.2)$$

where $x^\mu = (t, x, y, z)$. We perform a dimensional reduction by isometry on ∂_ϕ and end up with a four dimensional model of gravity coupled to a scalar field. Performing the standard $3 + 1$ decomposition and writing the equations in the BSSN scheme, the evolution equations of the resulting system are those of (4.1.14) with matter terms given by (6.2.23). We here use periodic boundary conditions along the z direction and Sommerfeld radiative boundary conditions along x and y .

7.3.2 Initial data

Following the approach of section 6.3, the four-dimensional Brill-Lindquist initial data appropriate to describe non-spinning, non-rotating black holes momentarily at rest, take the form

$$\gamma_{ij}dx^i dx^j = \psi^2[dx^2 + dy^2 + dz^2], \quad \lambda = y^2\psi^2, \quad K_{ij} = 0 = K_\lambda.$$

In a spacetime with standard topology (wherein z parameterises a line), the initial data for two black holes with horizon radius $r_S^{1,2}$ and punctures placed at $(x, y, z) = (0, 0, \pm a)$, takes the form

$$\psi = 1 + \frac{(r_S^1)^2}{4[x^2 + y^2 + (z - a)^2]} + \frac{(r_S^2)^2}{4[x^2 + y^2 + (z + a)^2]}. \quad (7.3.3)$$

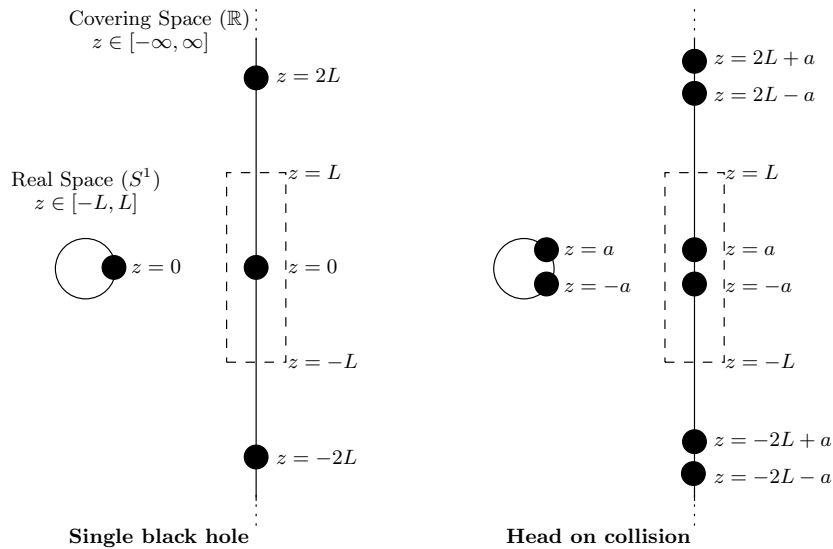


Figure 7.10: Illustration of the correspondence between real space and covering space for a single black hole (left panel) and a situation of head on collision (right panel). The dashed boxes drawn in the covering space contain a single copy of the real space setup and correspond also to what is contained in the numerical grid.

The appropriate initial data to describe a black hole in S^1 can be viewed as having an infinite array of black holes, all with the same mass, separated by coordinate distance $\Delta z = 2L$ —figure 7.10. Since the superposition of various black holes in a line is described by adding up the corresponding initial data, for the infinite array of two black holes in the circle located

at $z = \pm a$ ($0 < a < L$) with horizon radii r_S^i , $i = 1, 2$ (or, equivalently, for two black holes in S^1) the initial data is given by

$$\begin{aligned} \psi &= 1 + \sum_{n=-\infty}^{+\infty} \frac{(r_S^1)^2}{4[x^2 + y^2 + (z - a - 2Ln)^2]} + \sum_{n=-\infty}^{+\infty} \frac{(r_S^2)^2}{4[x^2 + y^2 + (z + a - 2Ln)^2]} \\ &= 1 + \frac{\pi(r_S^1)^2}{8L\rho} \frac{\sinh \frac{\pi\rho}{L}}{\cosh \frac{\pi\rho}{L} - \cos \frac{\pi(z-a)}{L}} + \frac{\pi(r_S^2)^2}{8L\rho} \frac{\sinh \frac{\pi\rho}{L}}{\cosh \frac{\pi\rho}{L} - \cos \frac{\pi(z+a)}{L}}. \end{aligned} \quad (7.3.4)$$

where $\rho^2 \equiv x^2 + y^2$ and in the last equality we have used the result in [105].

7.3.3 Results

Again, we use the LEAN code, introduced in section 4.3, for the numerical evolutions. The main difference to standard implementations of LEAN is the use of periodic boundary conditions, which is also non-trivial to implement in a parallel code.

We will now show some results obtained for a head-on collision (from rest) of black holes with an initial separation of $10.37 r_S$, i.e., $a = 5.185 r_S$. The z ($z \in [-L, L]$) coordinate has been compactified with $L/r_S = 64, 32, 16$. For comparison purposes, we have also performed a simulation with “standard” outgoing boundary conditions ($L \rightarrow \infty$), which will be here referred to as “outgoing”.

All results will be presented in units of the Schwarzschild radius $r_S = r_{S,1} + r_{S,2}$.

7.3.3.1 Hamiltonian constraint

Figure 7.11 shows the Hamiltonian constraint along the x and z axis, respectively, for several time steps for the $L/r_S = 32$ case. As we can see, the constraint is indeed being satisfied with high accuracy.

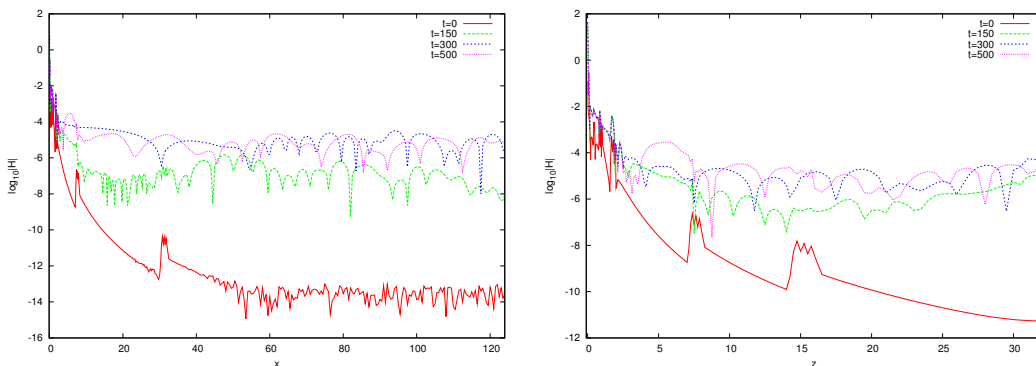


Figure 7.11: Hamiltonian constraint along the x and z axis, for the $L/r_S = 32$ case.

7.3.3.2 Collision time

Next, we study the changes in collision time for different compactification radii. Whereas we do not observe any (noticeable) difference for $L/r_S = 64$ and $L/r_S = 32$ as compared to the outgoing case, the case $L/r_S = 16$ shows already a noticeable difference. The puncture trajectories for these cases are plotted in figure 7.12.

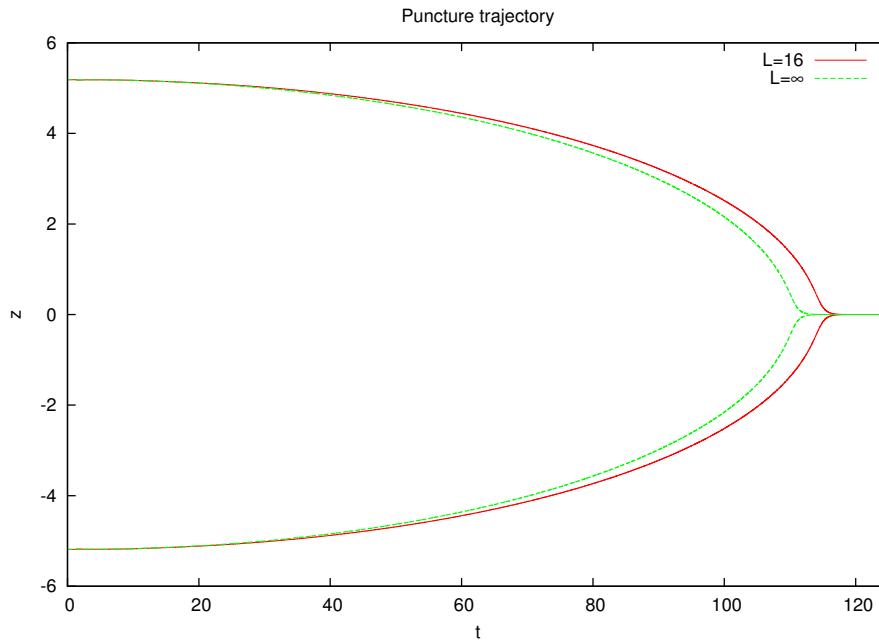


Figure 7.12: Puncture z coordinate as function of time for the outgoing and $L/r_S = 16$ cases.

Recall that one can think of a black hole in a cylindrical space as an array of infinite black holes. Therefore, for a head-on collision on such a cylindrical space, each black hole will also feel the gravitational pull of all the other black holes. Naïvely, one thus expects that for this cylindrical case it will take longer for the black holes to collide, which is what we observe in figure 7.12.

7.3.4 Final remarks

Using the formalism introduced in section 6.1, we were able to reduce the head-on collision of (non-spinning) black holes on cylindrical spacetimes (in any dimension) to an effective $3 + 1$ system with a scalar field, and used this procedure to successfully evolve a head-on collision of two black holes on a five-dimensional cylindrical spacetime.

Further issues that we wish to investigate include monitoring the deformation of the black holes' apparent horizon and computing the energy radiated, along the lines of section 6.4.2.3. We also further plan to perform simulations with smaller compactification radii and study the equivalent six-dimensional system.

Chapter 8

Einstein-Maxwell

In this last chapter we go back to four dimensions once again, this time in Einstein-Maxwell theory, to perform fully non-linear numerical simulations of charged black hole collisions [207].

As mentioned in the Introduction, the dynamics of binary systems of charged, i.e. Reissner-Nordström (RN), black holes have remained rather unexplored territory. Perhaps this is due to the expectation that astrophysical black holes carry zero or very small charge; in particular, black holes with mass M , charge Q and angular momentum aM^2 are expected to discharge very quickly if $Q/M \gtrsim 10^{-13}(a/M)^{-1/2}(M/M_\odot)^{1/2}$ [208, 112]. There is, nevertheless, a good deal of motivation for detailed investigations of the dynamics of charged black holes.

In the context of astrophysics, charged black holes may actually be of interest in realistic systems. First, a rotating black hole in an external magnetic field will accrete charged particles up to a given value, $Q = 2B_0J$ [111]. Thus it is conceivable that astrophysical black holes could have some (albeit rather small) amount of electrical charge. Then it is of interest to understand the role of this charge in the Blandford-Znajek mechanism [112], which has been suggested for extracting spin energy from the hole, or in a related mechanism capable of extracting energy from a moving black hole [110, 113] to power outflows from accretion disk-fed black holes. Numerical simulations of charged black holes interacting with matter and surrounding plasma will enable us to study such effects.

Motivation for the numerical modelling of charged black holes also arises in the context of high energy collisions. It is expected that trans-Planckian particle collisions form black holes; moreover, well above the fundamental Planck scale such processes should be well described by general relativity and other interactions should become negligible [64], an idea poetically stated as *matter does not matter* for ultra high energy collisions [66]. But is this expectation really correct? Calculations of shock wave collisions suggest that even though other interactions—say charge—may become irrelevant in the ultra-relativistic limit, the properties of the final black hole (and of the associated emission of gravitational radiation) do depend on the amount of charge carried by the colliding particles [114, 115]. This issue can be clarified by the simulation of high-energy collisions of charged black holes and the subsequent comparison of the results to those obtained for electrically neutral systems.

Finally we note a variety of conceptual aspects that merit a more detailed investigation of charged black hole systems. In head-on collisions with small velocity, the intuition borrowed from Larmor's formula in Minkowski space suggests a steady growth of the emitted power with the acceleration. However, it is by now well established that for uncharged black holes the gravitational radiation strongly peaks near around time of formation of a common apparent horizon. Does the electromagnetic radiation emission follow a similar pattern? And what is the relative fraction of electromagnetic to gravitational wave emissions? Moreover, a non-head on collision of charged non-spinning black holes will allow us to study, as the end state, a (perturbed) Kerr-Newman geometry, which would be extremely interesting: linearised perturbations around Kerr-Newman black holes do not decouple [209, 192] and so far close to nothing is known about their properties. Among others, the stability of the Kerr-Newman metric is an outstanding open issue. Furthermore, it has been observed that the inspiral phase of an orbiting black-hole-binary system can be well understood via post-Newtonian methods [210] (see also e.g. [23, 211]). The additional radiative channel opened by the presence of electric charge provides additional scope to probe this observation.

With the above motivations in mind we here initiate the numerical study of non-linear dynamics of binary systems of charged black holes, building on previous numerical evolutions of the Einstein-Maxwell system [116, 109, 117, 118]. For reasons of simplicity, we focus in this study on binary systems for which initial data can be constructed by purely analytic means [133, 212]: head-on collisions, starting from rest, of non-spinning black holes with equal charge-to-mass ratio. This implies in particular that the black holes carry a charge of the same sign, so the electromagnetic force will always be repulsive. We extract both gravitational and electromagnetic radiation and monitor their behaviour as the charge-to-mass-ratio parameter of the system is varied.

8.1 Evolution equations

We will adopt the approach outlined in [213, 117] to evolve the electro-vacuum Einstein-Maxwell equations which incorporates suitably added additional fields to ensure the evolution will preserve the constraints. This amounts to considering an enlarged system of the form

$$\begin{aligned} R_{\mu\nu} - \frac{R}{2}g_{\mu\nu} &= 8\pi T_{\mu\nu} , \\ \nabla_{\mu}(F^{\mu\nu} + g^{\mu\nu}\Psi) &= -\kappa n^{\nu}\Psi , \\ \nabla_{\mu}(\star F^{\mu\nu} + g^{\mu\nu}\Phi) &= -\kappa n^{\nu}\Phi , \end{aligned} \tag{8.1.1}$$

where $\star F^{\mu\nu}$ denotes the Hodge dual of the Maxwell-Faraday tensor $F^{\mu\nu}$, κ is a constant and n^{μ} the four-velocity of the Eulerian observer. We recover the standard Einstein-Maxwell system of equations when $\Psi = 0 = \Phi$. With the scalar field Ψ and pseudo-scalar Φ introduced in this way, the natural evolution of this system drives Ψ and Φ to zero (for positive κ), thus ensuring the magnetic and electric constraints are controlled [213, 116]. The electromagnetic

stress-energy tensor takes the usual form

$$T_{\mu\nu} = \frac{1}{4\pi} \left[F_{\mu}{}^{\lambda} F_{\nu\lambda} - \frac{1}{4} g_{\mu\nu} F^{\lambda\sigma} F_{\lambda\sigma} \right]. \quad (8.1.2)$$

8.1.1 3+1 decomposition

We employ the 3 + 1 decomposition, as explained in section 2.5, where we introduced the 3-metric

$$\gamma_{\mu\nu} = g_{\mu\nu} + n_{\mu} n_{\nu}, \quad (8.1.3)$$

and further decompose the Maxwell-Faraday tensor into the more familiar electric and magnetic fields measured by the Eulerian observer moving with four velocity n^{μ}

$$\begin{aligned} F_{\mu\nu} &= n_{\mu} E_{\nu} - n_{\nu} E_{\mu} + \epsilon_{\mu\nu\alpha\beta} B^{\alpha} n^{\beta}, \\ \star F_{\mu\nu} &= n_{\mu} B_{\nu} - n_{\nu} B_{\mu} - \epsilon_{\mu\nu\alpha\beta} E^{\alpha} n^{\beta}, \end{aligned} \quad (8.1.4)$$

where we use the convention $\epsilon_{1230} = \sqrt{-g}$, $\epsilon_{\alpha\beta\gamma} = \epsilon_{\alpha\beta\gamma\delta} n^{\delta}$, $\epsilon_{123} = \sqrt{\gamma}$.

We write the evolution equations in the BSSN form (4.1.14) where, for the case of the electromagnetic energy-momentum tensor of equation (8.1.2), the source terms are given by

$$\begin{aligned} E &\equiv T^{\mu\nu} n_{\mu} n_{\nu} = \frac{1}{8\pi} (E^i E_i + B^i B_i), \\ j_i &\equiv -\gamma_{i\mu} T^{\mu\nu} n_{\nu} = \frac{1}{4\pi} \epsilon_{ijk} E^j B^k, \\ S_{ij} &\equiv \gamma^{\mu}{}_i \gamma^{\nu}{}_j T_{\mu\nu} \\ &= \frac{1}{4\pi} \left[-E_i E_j - B_i B_j + \frac{1}{2} \gamma_{ij} (E^k E_k + B^k B_k) \right], \end{aligned} \quad (8.1.5)$$

and $S \equiv \gamma^{ij} S_{ij}$. The evolution of the electromagnetic fields is determined by equation (8.1.1) whose 3+1 decomposition becomes [118]

$$\begin{aligned} (\partial_t - \mathcal{L}_{\beta}) E^i &= \alpha K E^i + \epsilon^{ijk} \chi^{-1} \left[\tilde{\gamma}_{kl} B^l \partial_j \alpha + \alpha \left(B^l \partial_j \tilde{\gamma}_{kl} + \tilde{\gamma}_{kl} \partial_j B^l - \chi^{-1} \tilde{\gamma}_{kl} B^l \partial_j \chi \right) \right] \\ &\quad - \alpha \chi \tilde{\gamma}^{ij} \partial_j \Psi, \\ (\partial_t - \mathcal{L}_{\beta}) B^i &= \alpha K B^i - \epsilon^{ijk} \chi^{-1} \left[\tilde{\gamma}_{kl} E^l \partial_j \alpha + \alpha \left(E^l \partial_j \tilde{\gamma}_{kl} + \tilde{\gamma}_{kl} \partial_j E^l - \chi^{-1} \tilde{\gamma}_{kl} E^l \partial_j \chi \right) \right] \\ &\quad - \alpha \chi \tilde{\gamma}^{ij} \partial_j \Phi, \\ (\partial_t - \mathcal{L}_{\beta}) \Psi &= -\alpha \nabla_i E^i - \alpha \kappa \Psi, \\ (\partial_t - \mathcal{L}_{\beta}) \Phi &= -\alpha \nabla_i B^i - \alpha \kappa \Phi. \end{aligned} \quad (8.1.6)$$

Here, \mathcal{L}_{β} denotes the Lie derivative along the shift vector β^i . The Hamiltonian and momentum constraint are

$$\begin{aligned} \mathcal{H} &\equiv R + K^2 - K^{ij} K_{ij} - 16\pi E = 0, \\ \mathcal{M}_i &\equiv D_j A_i^j - \frac{3}{2} A_i^j \chi^{-1} \partial_j \chi - \frac{2}{3} \partial_i K - 8\pi j_i = 0, \end{aligned} \quad (8.1.7)$$

where D_i is the covariant derivative associated with the three-metric γ_{ij} .

8.1.2 Initial data

We focus here on black hole binaries with equal charge and mass colliding from rest. For these configurations, it is possible to construct initial using the Brill-Lindquist construction (outlined in section 3.2.1 for the vacuum spacetimes; see [133, 212] for the charged case). The main ingredients of this procedure are as follows.

For a vanishing shift β^i , time symmetry implies $K_{ij} = 0$. Combined with the condition of an initially vanishing magnetic field, the magnetic constraint $D_i B^i = 0$ and momentum constraint are automatically satisfied. By further assuming the spatial metric to be conformally flat

$$\gamma_{ij} dx^i dx^j = \psi^4 (dx^2 + dy^2 + dz^2) , \quad (8.1.8)$$

the Hamiltonian constraint reduces to

$$\Delta\psi = -\frac{1}{4}E^2\psi^5 , \quad (8.1.9)$$

where Δ is the flat space Laplace operator. The electric constraint, Gauss's law, has the usual form

$$D_i E^i = 0 . \quad (8.1.10)$$

Quite remarkably, for systems of black holes with equal charge-to-mass ratio, these equations have known analytical solutions [212]. For the special case of two black holes momentarily at rest with “bare masses” m_1, m_2 and “bare charges” $q_1, q_2 = q_1 m_2 / m_1$ this analytic solution is given by

$$\begin{aligned} \psi^2 &= \left(1 + \frac{m_1}{2|\vec{x} - \vec{x}_1|} + \frac{m_2}{2|\vec{x} - \vec{x}_2|} \right)^2 - \frac{1}{4} \left(\frac{q_1}{|\vec{x} - \vec{x}_1|} + \frac{q_2}{|\vec{x} - \vec{x}_2|} \right)^2 , \\ E^i &= \psi^{-6} \left(q_1 \frac{(\vec{x} - \vec{x}_1)^i}{|\vec{x} - \vec{x}_1|^3} + q_2 \frac{(\vec{x} - \vec{x}_2)^i}{|\vec{x} - \vec{x}_2|^3} \right) , \end{aligned} \quad (8.1.11)$$

where \vec{x}_i is the coordinate location of the i th “puncture”.*

The initial data is thus completely specified in terms of the independent mass and charge parameters m_1, m_2, q_1 and the initial coordinate separation d of the holes. These uniquely determine the remaining charge parameter q_2 via the condition of equal charge-to-mass ratio. In this study we always choose $m_1 = m_2$ and, without loss of generality, position the two holes symmetrically around the origin such that $z_1 = d/2 = -z_2$. The resulting initial three metric γ_{ij} follows from equations. (8.1.8), (8.1.11) while the extrinsic curvature K_{ij} and magnetic field B^i vanish on the initial slice.

We use the same gauge conditions and outer boundary conditions for the BSSN variables as used in vacuum simulations, cf. equations (4.2.3) and (4.2.6). As outer boundary condition for the electric and magnetic fields we have imposed a falloff as $1/r^2$ —from (8.1.11). For the additional scalar fields a satisfactory behaviour is observed by imposing a falloff as $1/r^3$ (which is the expected falloff rate from dimensional grounds).

*We note that this foliation, in isotropic coordinates, only covers the outside of the external horizon.

8.2 Wave Extraction

For a given set of initial parameters $m_1 = m_2$, $q_1 = q_2$, d , the time evolution provides us with the spatial metric γ_{ij} , the extrinsic curvature K_{ij} as well as the electric and magnetic fields E^i , B^i as functions of time. These fields enable us to extract the gravitational and electromagnetic radiation as explained in section 5.1.1. Details concerning the numerical implementation can be found in [149].

We recall that the radiated flux and energy are given by the expressions (5.1.21) and (5.1.28):

$$F_{\text{GW}} = \frac{dE_{\text{GW}}}{dt} = \lim_{r \rightarrow \infty} \frac{r^2}{16\pi} \sum_{l,m} \left| \int_{-\infty}^t dt' \psi^{lm}(t') \right|^2, \quad (8.2.1)$$

$$F_{\text{EM}} = \frac{dE_{\text{EM}}}{dt} = \lim_{r \rightarrow \infty} \frac{r^2}{4\pi} \sum_{l,m} \left| \phi_2^{lm}(t) \right|^2. \quad (8.2.2)$$

As is well known from simulations of uncharged black-hole binaries, initial data obtained from the Brill-Lindquist construction contains “spurious” radiation, which is an artifact of the conformal-flatness assumption. In calculating properties of the radiation, we account for this effect by starting the integration of the radiated flux in equations (8.2.1), (8.2.2) at some finite time Δt after the start of the simulation, thus allowing the spurious pulse to first radiate off the computational domain. In practice, we obtain satisfactory results by choosing $\Delta t = R_{\text{ex}} + 50 M$. Because the physical radiation is very weak for both the gravitational and electromagnetic channel in this early infall stage, the error incurred by this truncation is negligible compared with the uncertainties due to discretization; cf. section 8.4.4.

8.3 Analytic predictions

Before discussing in detail the results of our numerical simulations, it is instructive to discuss the behaviour of the binary system as expected from an analytic approximation. Such an analysis not only serves an intuitive understanding of the binary’s dynamics, but also provides predictions to compare with the numerical results presented below.

For this purpose we consider the electrodynamics of a system of two equal point charges in a Minkowski background spacetime. As in the black hole case, we denote by $q_1 = q_2 \equiv Q/2$ and $m_1 = m_2 \equiv M/2$ the electric charge and mass of the particles which are initially at rest at position $z = \pm d/2$.

It turns out useful to first consider point charges in Minkowski spacetime in the static limit. The expected behaviour of the radial component of the resulting electric field is given by [214]

$$E_{\hat{r}} = 4\pi \sum_{l,m} \frac{l+1}{2l+1} q_{lm} \frac{Y_{lm}(\theta, \varphi)}{r^{l+2}}, \quad (8.3.1)$$

which for a system of two charges of equal magnitude at $z = \pm d/2$ becomes

$$E_{\hat{r}} \simeq \sqrt{4\pi}Q \frac{Y_{00}}{r^2} + \sqrt{\frac{9\pi}{20}}Qd^2 \frac{Y_{20}}{r^4} . \quad (8.3.2)$$

The dipole vanishes in this case due to the reflection symmetry across $z = 0$. This symmetry is naturally preserved during the time evolution of the two-charge system. Furthermore, the total electric charge Q is conserved so that the leading-order behaviour of the electromagnetic radiation is given by variation of the electric quadrupole, just as for the gravitational radiation. Notice that in principle other radiative contributions can arise from the accelerated motion of the charged black holes. From experience with gravitational radiation generated in the collision of electrically neutral black-hole binaries, however, we expect this “Bremsstrahlung” to be small in comparison with the merger signal and hence ignore its contributions in this simple approximation. The good agreement with the numerical results presented in the next section bears out the validity of this *quadrupole approximation*. In consequence, it appears legitimate to regard the “strength” of the collision and the excitation of the black-hole ringdown to be purely kinematic effects.

An estimate for the monopole and quadrupole amplitudes in the limit of two static point charges is then obtained from inserting the radial component of the electric field (8.3.2) into the expression (5.1.25) for Φ_1 and its multipolar decomposition (5.1.26)

$$r^2\phi_1^{00} = \sqrt{\pi}Q \approx 1.77Q , \quad (8.3.3)$$

$$r^4\phi_1^{20} = \sqrt{\frac{9\pi}{80}}Qd^2 \approx 0.59Qd^2 . \quad (8.3.4)$$

The expectation is that these expressions provide a good approximation for the wave signal during the early infall stage when the black holes are moving with small velocities. Equation (8.3.3) should also provide a good approximation for ϕ_1^{00} after the merger and ringdown whereas the quadrupole ϕ_1^{20} should eventually approach zero as a single merged hole corresponds to the case $d = 0$ in equation (8.3.4).

In order to obtain analytic estimates for the collision time and the emitted radiation, we need to describe the dynamic behaviour of the two point charges. Our starting point for this discussion is the combined gravitational and electromagnetic potential energy for two charges $i = 1, 2$ in Minkowski spacetime with mass and charge m_i, q_i at distance r from each other

$$V = -\frac{Gm_1m_2}{r} + \frac{1}{4\pi\epsilon_0} \frac{q_1q_2}{r} . \quad (8.3.5)$$

For the case of two charges with equal mass and charge $m_i = M/2, q_i = Q/2$ and starting from rest at $z_0 = \pm d/2$, conservation of energy implies

$$M\dot{z}^2 - \frac{M^2\mathcal{B}}{4z} = -\frac{M^2\mathcal{B}}{2d} , \quad (8.3.6)$$

where we have used units with $G = 4\pi\epsilon_0 = 1$ and

$$\mathcal{B} \equiv 1 - Q^2/M^2 . \quad (8.3.7)$$

The resulting equation of motion for $z(t)$ is obtained by differentiating equation (8.3.6) which results in

$$M\ddot{z} = -\frac{M^2}{8z^2} + \frac{Q^2}{8z^2} = -M^2\frac{\mathcal{B}}{8z^2} . \quad (8.3.8)$$

An estimate for the time for collision follows from integrating equation (8.3.6) over $z \in [d/2, 0]$

$$\left(\frac{t_{\text{collision}}}{M}\right)^2 = \frac{\pi^2 d^3}{2^3 M^3 \mathcal{B}} . \quad (8.3.9)$$

From the dynamic evolution of the system we can derive an approximate prediction for the electromagnetic radiation by evaluating the (traceless) electric quadrupole tensor $Q_{ij} = \int d^3\vec{x}\rho(\vec{x})(3x_i x_j - r^2\delta_{ij})$ [214]. In terms of this quadrupole tensor, the total power radiated is given by [214]

$$F_{\text{EM}} = \sum_{ij} \frac{1}{4\pi\epsilon_0} \frac{1}{360c^5} \ddot{Q}_{ij}^2 . \quad (8.3.10)$$

For clarity we have reinstated the factors $4\pi\epsilon_0$ and c^5 here. Using

$$\frac{d^3}{dt^3}(z^2) = 6z\ddot{z} + 2z\dot{z}^2 , \quad (8.3.11)$$

and the equations of motion (8.3.6), (8.3.8) we find

$$F_{\text{EM}} = \frac{\mathcal{B}^3 M^3 Q^2 (1/z - 2/d)}{1920z^4} . \quad (8.3.12)$$

Using $\int dt(\dots) = \int dz/\dot{z}(\dots)$, we can evaluate the time integral up to some cutoff separation, say $z_{\text{min}} = \alpha_b b$, where b is the horizon radius of the initial black hole, $b = M(1 + \sqrt{\mathcal{B}})/2$ and $\alpha_b = \mathcal{O}(1)$ is a constant. This gives,

$$\frac{E_{\text{rad}}^{\text{EM}}}{M} = \mathcal{B}^{5/2} M^{3/2} Q^2 \frac{(d - 2\alpha_b b)^{3/2} (15d^2 + 24d\alpha_b b + 32\alpha_b^2 b^2)}{50400(d\alpha_b b)^{7/2}} . \quad (8.3.13)$$

Emission of gravitational radiation follows from the quadrupole formula, which is a numerical factor 4 times larger, and where the charge is replaced by the mass,

$$\frac{E_{\text{rad}}^{\text{GW}}}{M} = \mathcal{B}^{5/2} M^{7/2} \frac{(d - 2\alpha_b b)^{3/2} (15d^2 + 24d\alpha_b b + 32\alpha_b^2 b^2)}{12600(d\alpha_b b)^{7/2}} . \quad (8.3.14)$$

For $Q = 0, \alpha_b = 1, d = \infty$ we thus obtain

$$\frac{E_{\text{rad}}^{\text{GW}}}{M} = \frac{1}{840} \sim 0.0012 , \quad (8.3.15)$$

in agreement to within a factor of 2 with numerical simulations (see [176] and table 8.1 below; the agreement could be improved by assuming $\alpha_b \sim 1.3$). As a general result of this analysis we find in this approximation,

$$\frac{E_{\text{rad}}^{\text{EM}}}{E_{\text{rad}}^{\text{GW}}} = \frac{Q^2}{4M^2} . \quad (8.3.16)$$

For non-extremal holes $Q < M$, our analytic considerations therefore predict that the energy emitted in electromagnetic radiation is at most 25% of the energy lost in gravitational radiation. As we shall see below, this turns out to be a remarkably good prediction for the results obtained from fully numerical simulations.

8.4 Numerical Results

The numerical integration of the Einstein-Maxwell equations (4.1.14), (8.1.6) has been performed using fourth-order spatial discretisation with the LEAN code, originally presented in [149] for vacuum spacetimes, see section 4.3.

The initial parameters as well as the grid setup and the radiated gravitational and electromagnetic wave energy for our set of binary configurations is listed in table 8.1. All binaries start from rest with a coordinate distance $d/M \simeq 8$ or $d/M \simeq 16$ while the charge-to-mass ratio has been varied from $Q/M = 0$ to $Q/M = 0.98$. Note that identical coordinate separations of the punctures for different values of the charge Q/M correspond to different horizon-to-horizon proper distances. This difference is expected and in fact analysis of the RN solution predicts a divergence of the proper distance in the limit $Q/M \rightarrow 1$.

Table 8.1: Grid structure in the notation of section II E of [149], coordinate distance d/M , proper horizon-to-horizon distance L/M , charge Q/M , gravitational ($E_{\text{rad}}^{\text{GW}}$) and electromagnetic ($E_{\text{rad}}^{\text{EM}}$) radiated energy for our set of simulations. The radiated energy has been computed using only the $l = 2$, $m = 0$ mode; the energy contained in higher-order multipoles such as $l = 4$, $m = 0$ is negligible for all configurations.

Run	Grid	d/M	L/M	Q/M	$E_{\text{rad}}^{\text{GW}}$	$E_{\text{rad}}^{\text{EM}}$
d08q00	$\{(256, 128, 64, 32, 16, 8) \times (2, 1, 0.5), 1/80\}$	8.002	11.56	0	5.1×10^{-4}	–
d08q03	$\{(256, 128, 64, 32, 16, 8) \times (2, 1, 0.5), 1/80\}$	8.002	11.60	0.3	4.5×10^{-4}	1.3×10^{-5}
d08q04	$\{(256, 128, 64, 32, 16, 8) \times (2, 1, 0.5), 1/80\}$	8.002	11.65	0.4	4.0×10^{-4}	2.1×10^{-5}
d08q05c	$\{(256, 128, 64, 32, 16, 8) \times (2, 1, 0.5), 1/64\}$	8.002	11.67	0.5	3.3×10^{-4}	2.7×10^{-5}
d08q05m	$\{(256, 128, 64, 32, 16, 8) \times (2, 1, 0.5), 1/80\}$	8.002	11.70	0.5	3.4×10^{-4}	2.7×10^{-5}
d08q05f	$\{(256, 128, 64, 32, 16, 8) \times (2, 1, 0.5), 1/96\}$	8.002	11.67	0.5	3.4×10^{-4}	2.7×10^{-5}
d08q055	$\{(256, 128, 64, 32, 16, 8) \times (2, 1, 0.5), 1/80\}$	8.002	11.70	0.55	3.0×10^{-4}	2.89×10^{-5}
d08q06	$\{(256, 128, 64, 32, 16, 8) \times (2, 1, 0.5), 1/80\}$	8.002	11.75	0.6	2.6×10^{-4}	2.97×10^{-5}
d08q07	$\{(256, 128, 64, 32, 16, 8) \times (2, 1, 0.5), 1/80\}$	8.002	11.87	0.7	1.8×10^{-4}	2.7×10^{-5}
d08q08	$\{(256, 128, 64, 32, 16, 8) \times (2, 1, 0.5), 1/80\}$	8.002	12.0	0.8	9.8×10^{-5}	1.8×10^{-5}
d08q09	$\{(256, 128, 64, 32, 16, 8) \times (2, 1, 0.5), 1/80\}$	8.002	12.3	0.9	2.6×10^{-5}	5.5×10^{-6}
d08q098cc	$\{(256, 128, 64, 32, 16, 8) \times (2, 1, 0.5), 1/64\}$	8.002	12.3	0.98	7.0×10^{-7}	2.1×10^{-7}
d08q098c	$\{(256, 128, 64, 32, 16, 8) \times (2, 1, 0.5), 1/80\}$	8.002	13.1	0.98	4.3×10^{-7}	1.4×10^{-7}
d08q098m	$\{(256, 128, 64, 32, 16, 8) \times (2, 1, 0.5), 1/96\}$	8.002	13.1	0.98	3.4×10^{-7}	1.0×10^{-7}
d08q098f	$\{(256, 128, 64, 32, 16, 8) \times (2, 1, 0.5), 1/112\}$	8.002	13.0	0.98	4.0×10^{-7}	9.5×10^{-8}
d08q098ff	$\{(256, 128, 64, 32, 16, 8) \times (2, 1, 0.5), 1/128\}$	8.002	13.0	0.98	4.05×10^{-7}	8.75×10^{-8}
d08q098fff	$\{(256, 128, 64, 32, 16, 8) \times (2, 1, 0.5), 1/136\}$	8.002	13.1	0.98	3.73×10^{-7}	8.41×10^{-8}
d16q00	$\{(256, 128, 64, 32, 16) \times (4, 2, 1, 0.5), 1/64\}$	16.002	20.2	0	5.5×10^{-4}	–
d16q05	$\{(256, 128, 64, 32, 16) \times (4, 2, 1, 0.5), 1/64\}$	16.002	20.3	0.5	3.6×10^{-4}	2.9×10^{-5}
d16q08	$\{(256, 128, 64, 32, 16) \times (4, 2, 1, 0.5), 1/80\}$	16.002	20.7	0.8	1.05×10^{-4}	1.9×10^{-5}
d16q09	$\{(256, 128, 64, 32, 16) \times (4, 2, 1, 0.5), 1/80\}$	16.002	21.0	0.9	2.7×10^{-5}	5.9×10^{-6}

8.4.1 Code tests

Before discussing the obtained results in more detail, we present two tests to validate the performance of our numerical implementation of the evolution equations: (i) single black-hole evolutions in *geodesic slicing* which is known to result in numerical instabilities after relatively short times but facilitates direct comparison with a semi-analytic solution and (ii) convergence analysis of the radiated quadrupole waveforms for simulation d08q05 of table 8.1.

The geodesic slicing condition is enforced by setting the gauge functions to $\alpha = 1$, $\beta^i = 0$ throughout the evolution. The space part of the Reissner-Nordström solution in isotropic coordinates is given by equation (8.1.8) with a conformal factor [215, 216]

$$\psi^2 = \left(1 + \frac{M}{2r}\right)^2 - \frac{Q^2}{4r^2}. \quad (8.4.1)$$

The time evolution of this solution is not known in closed analytic form, but the resulting metric components can be constructed straightforwardly via a simple integration procedure. As expected, we find a time evolution in this gauge to become numerically unstable at times τ of a few M . Before the breaking down of the evolution, however, we can safely compare the numerical and “analytical” solutions. This comparison is shown in figure 8.1 for the γ_{zz} component of the spatial metric and the E^z component of the electric field and demonstrates excellent agreement between the semi-analytic and numerical results.

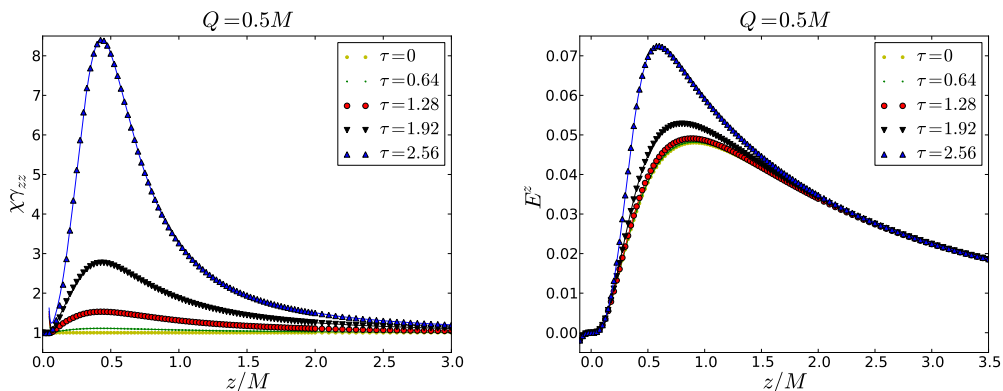


Figure 8.1: The numerical profiles for γ_{zz} and E^z (symbols) obtained in geodesic slicing at various times τ are compared with the semi-analytic results (lines).

For the second test, we have evolved model d08q05 using three different resolutions as listed in table 8.1 and extracted the gravitational and electromagnetic quadrupole ($l = 2, m = 0$) at $R_{\text{ex}} = 100M$. For fourth-order convergence, we expect the differences between the higher resolution simulations to be a factor 2.78 smaller than their coarser resolution counterparts. The numerically obtained differences are displayed with the corresponding rescaling in figure 8.2. Throughout the physically relevant part of the waveform, we observe the expected fourth-order convergence. Only the spurious initial radiation (cf. the discussion at the end of section 8.2) at early times $\Delta t \lesssim -20$ in the figure exhibits convergence closer to

second order, presumably a consequence of high-frequency noise contained in this spurious part of the signal. From Richardson extrapolation of our results we estimate the truncation error of the radiated waves to be about 1%. The error due to extraction at finite radius, on the other hand, is estimated to be 2 % at $R_{\text{ex}} = 100M$.

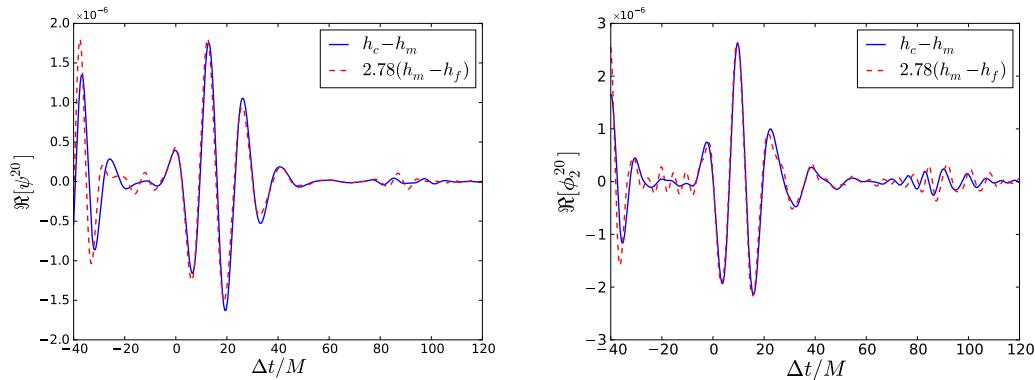


Figure 8.2: Convergence analysis for simulation d08q05 of table 8.1 with resolutions $h_c = M/64$, $h_m = M/80$ and $h_f = M/96$. The panels show differences of the $(2, 0)$ multipoles of the real parts of Ψ_4 (left) and Φ_2 (right) extracted at $R_{\text{ex}} = 100 M$; in each case, the high-resolution differences have been rescaled by a factor 2.78 as expected for fourth-order convergence.

8.4.2 Collisions of two black holes: the “static” components and infall time

We start the discussion of our results with the behaviour of the gravitational and electromagnetic multipoles when the system is in a nearly static configuration, i.e. shortly after the start of the simulation and at late stages after the ringdown of the post-merger hole. At these times, we expect our analytic predictions (8.3.3), (8.3.4) for the monopole and dipole of the electromagnetic field to provide a rather accurate description. Furthermore, the total spacetime charge Q is conserved throughout the evolution, so that the monopole component of Φ_1 should be described by (8.3.3) *at all times*. The quadrupole, on the other hand, is expected to deviate significantly from the static prediction (8.3.4) when the black holes start moving fast.

As demonstrated in figure 8.3, we find our results to be consistent with this picture. Here we plot the monopole and quadrupole of Φ_1 . The monopole part (left panel) captures the Coulomb field and can thus be compared with the total charge of the system. It is constant throughout the evolution to within numerical error and shows agreement with the analytic prediction of equation (8.3.3) within numerical uncertainties; we measure a slightly smaller value for the monopole field than expected from the total charge of the system, but the measured value should increase with extraction radii and agree with the total charge expectation at infinity. This is consistent with the extrapolation of the measured value to infinity as shown in the figure. The quadrupole part (right panel) starts at a non-zero value in

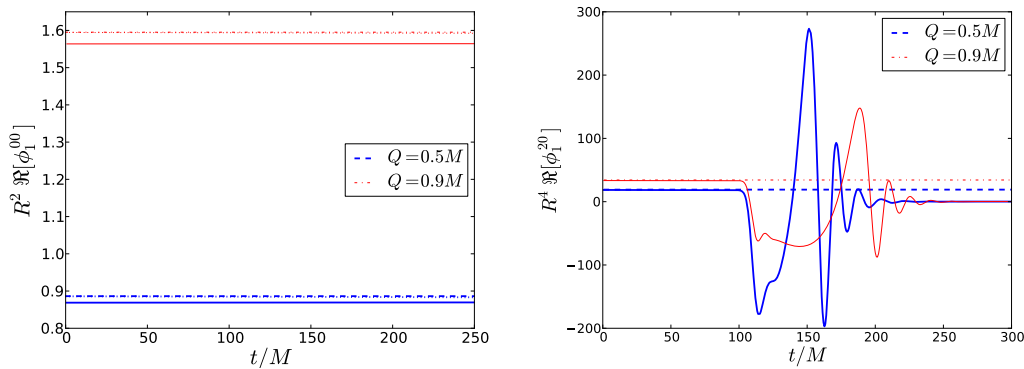


Figure 8.3: Monopole ϕ_1^{00} (left) and quadrupole ϕ_1^{20} (right) of the radial part of the electromagnetic field Φ_1 extracted at $R_{\text{ex}} = 100M$ for simulation d08q05 of table 8.1. The dashed curves show the predictions of equations (8.3.3), (8.3.4) at $R = \infty$ in the static limit. For the monopole case, we also added the curves obtained by extrapolating the results to infinite extraction radius; these curves—dotted lines—essentially overlap with the predictions from equation (8.3.3).

excellent agreement with equation (8.3.4), deviates substantially during the highly dynamic plunge and merger stage and eventually rings down towards the static limit $\phi_1^{20} = 0$ as expected for a spherically symmetric charge distribution.

The analytic approximation of section 8.3 also predicts a value for the time of collision (8.3.9) for a given set of initial parameters. In particular, we see from this prediction that for fixed initial separation d and mass M the collision time scales with the charge as $t_{\text{collision}} \sim 1/\sqrt{\mathcal{B}}$. In comparing these predictions with our numerical results we face the difficulty of not having an unambiguous definition of the separation of the black holes in the fully general relativistic case. From the entries in table 8.1 we see that the proper distance L varies only mildly for fixed coordinate distance d up to $Q/M \approx 0.8$. For nearly extremal values of Q , however, L starts increasing significantly as expected from our discussion at the start of this section. We therefore expect the collision time of the numerical simulations rescaled by $\sqrt{\mathcal{B}}/t_0$, where t_0 is the corresponding time for the uncharged case, to be close to unity over a wide range of Q/M and show some deviation close to $Q/M = 1$. This expectation is borne out in figure 8.4 where we show this rescaled collision time, determined numerically as the first appearance of a common apparent horizon, as a function of Q/M .

8.4.3 Waveforms: infall, merger and ringdown

The dynamical behaviour of all our simulations is qualitatively well represented by the waveforms shown in figure 8.5 for simulations d16q00, d16q05 and d16q09. The panels show the real part of the gravitational (left) and electromagnetic (right) quadrupole extracted at $R_{\text{ex}} = 100M$ as a function of time with $\Delta t = 0$ defined as the time of the global maximum of the waveform. From the classical analysis (8.3.10), we expect the waveforms Ψ_4 , Φ_2 to scale roughly with \mathcal{B} and the mass or charge of the black holes (the scaling with \mathcal{B} is non-trivial,

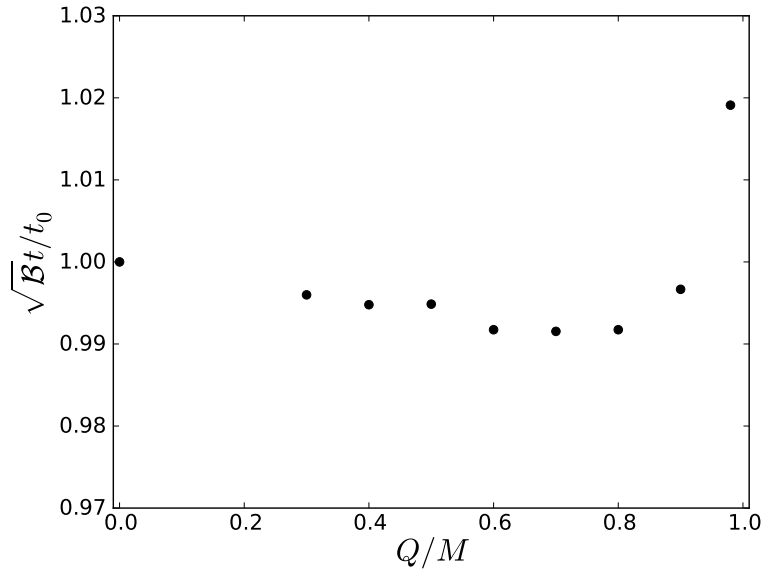


Figure 8.4: Time for apparent horizon formation, re-scaled by the factor $\sqrt{\mathcal{B}}$ and the apparent horizon formation time t_0 for an electrically neutral binary. We note that the change in the quantity we plot is only, at most, of 2%. The coordinate time itself, however, varies by a factor 5 as one goes from $Q = 0$ to $Q = 0.98M$.

but both an analytic estimate and the numerical results indicate the scaling is approximately linear, which we shall therefore use for re-scaling the plots in the figure).

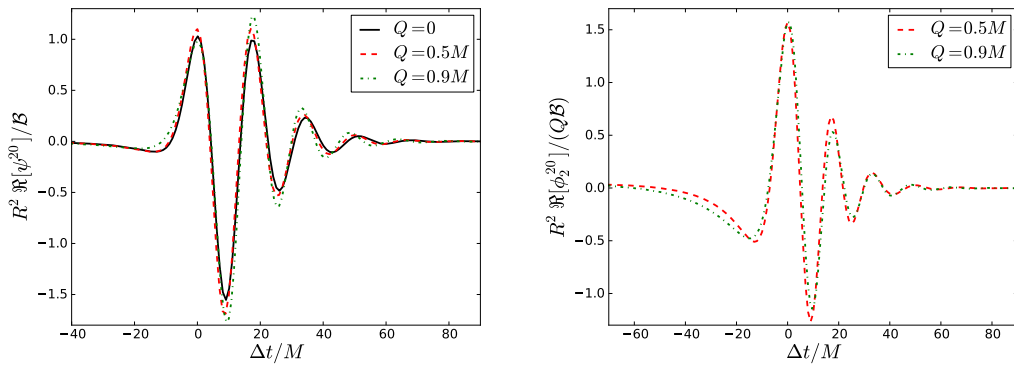


Figure 8.5: Real part of the (2,0) mode of Ψ_4 (left) and Φ_2 (right panel) extracted at $R_{\text{ex}} = 100M$.

The early stage of the signals are marked by the spurious radiation due to the construction of initial data which we ignore in our analysis. Following a relatively weak phase of wave emission during the infall of the holes, the radiation increases strongly during the black-hole merger around $\Delta t = 0$ in the figure and decays exponentially as the final hole rings down into a stationary state. This overall structure of the signals is rather similar for

the electromagnetic and the gravitational part and follows the main pattern observed for gravitational-wave emission in head-on collisions of uncharged black holes [176, 217].

Table 8.2: Comparison of the ringdown frequencies obtained from (i) perturbative calculations [192] and (ii) fitting a two-mode profile to the numerically extracted waveforms. For $Q/M = 0$ the electromagnetic modes are not excited. For values of $Q/M \geq 0.9$ the electromagnetic mode becomes so weak that we can no longer unambiguously identify it in the numerical data.

Q/M	$\omega_{1,2}^{\text{QNM}}$	$\omega_{1,2}^{\text{ext}}$
0	$0.374 - 0.0890i$ $0.458 - 0.0950i$	$0.374 - 0.088i$
0.3	$0.376 - 0.0892i$ $0.470 - 0.0958i$	$0.375 - 0.092i$ $0.481 - 0.100i$
0.5	$0.382 - 0.0896i$ $0.494 - 0.0972i$	$0.381 - 0.091i$ $0.511 - 0.096i$
0.9	$0.382 - 0.0896i$ $0.494 - 0.0972i$	$0.381 - 0.091i$?

The final, exponentially damped ringdown phase is well described by perturbation techniques [192]. In particular, charged black holes are expected to oscillate with two different types of modes, one of gravitational and one of electromagnetic origin. For the case of vanishing charge, the electromagnetic modes are not present, but they generally couple for charged black holes, and we expect both modes to be present in the spectra of our gravitational and electromagnetic waveforms. For verification we have fitted the late-stages of the waveforms to a two-mode, exponentially damped sinusoid waveform

$$f(t) = A_1 e^{-i\omega_1 t} + A_2 e^{-i\omega_2 t}, \quad (8.4.2)$$

where A_i are real-valued amplitudes and ω_i complex frequencies. The results are summarised in table 8.2 for selected values of the charge-to-mass ratio of the post-merger black hole. Real and imaginary part of the fitted frequencies agree within a few percent or better with the perturbative predictions. For the large value Q/M , however, the wave signal is very weak and in such good agreement with a single ringdown mode (the gravitational one) that we cannot clearly identify a second, electromagnetic component. This feature is explained once we understand how the total radiated energy is distributed between the gravitational and the electromagnetic channels. For this purpose, we plot in figure 8.6 the Fourier spectrum of the relevant wavefunctions or, more precisely, their dominant quadrupole contributions obtained for simulation d08q03 $|\bar{\phi}^{20}|^2, |\bar{\psi}^{20}|^2$, where for any function f

$$\bar{f}(\omega) = \int_{-\infty}^{\infty} e^{i\omega t} f(t) dt. \quad (8.4.3)$$

It is clear from the figure that most of the energy is carried in the fundamental gravitational-wave like mode with a peak at approximately $\omega \sim 0.37$, close to the oscillation frequency of the fundamental gravitational ringdown mode; see table 8.2.

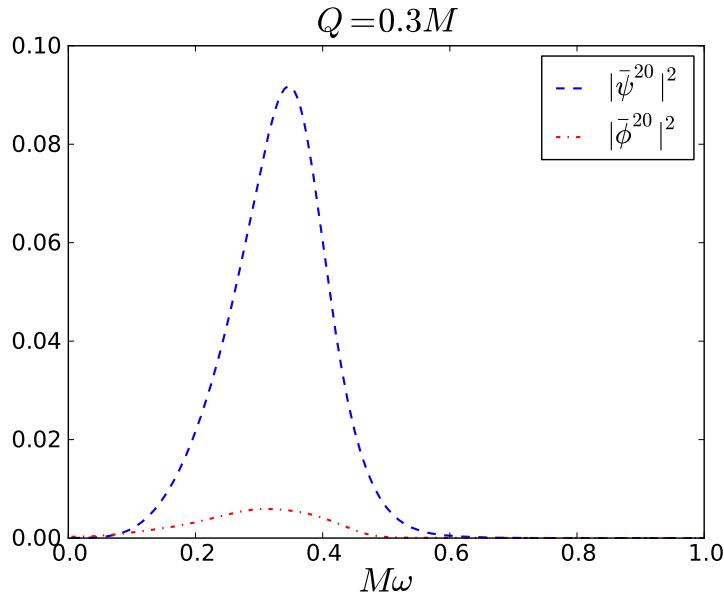


Figure 8.6: Power spectrum for the gravitational (long dashed) and electromagnetic (short dashed) quadrupole extracted from simulation d08q03. Note that the spectrum peaks near the fundamental ringdown frequency of the gravitational mode; cf. table 8.2.

8.4.4 Radiated energy and fluxes

The electromagnetic and gravitational wave fluxes are given by equations (8.2.1) and (8.2.2). We have already noticed from the waveforms in figure 8.5 that the electromagnetic signal follows a pattern quite similar to the gravitational one. The same holds for the energy flux which is shown in figure 8.7 for a subset of our simulations with $Q/M = 0, 0.5$ and 0.9 . From the figure, as well as the numbers in table 8.1, we observe that the energy carried by gravitational radiation decreases with increasing Q/M , as the acceleration becomes smaller and quadrupole emission is suppressed, in agreement with prediction (8.3.14).

This is further illustrated in figure 8.8, which illustrates the radiated energy carried in the gravitational quadrupole and the electromagnetic quadrupole as well as their ratio as functions of the charge-to-mass ratio Q/M . For the case of vanishing charge, the total radiated energy is already known from the literature; e.g. [176]. The value increases mildly with the initial separation as a consequence of the slightly larger collision velocity but is generally found to be close to $E_{\text{rad}}^{\text{GW}}/M = 0.055\%$. Our values of 0.051% for $d/M \simeq 8$ and 0.055% for $d/M \simeq 16$ are in good agreement with the literature. As we increase Q/M , however, $E_{\text{rad}}^{\text{GW}}$ decreases significantly and for $Q/M = 0.9$ (0.98) has dropped by a factor of about 20 (10^3) relative to the uncharged case. For practical reasons, we have explored the largest ratio $Q/M = 0.98$ for the smaller initial separation $d/M \simeq 8$ only; the near cancellation of the gravitational and electromagnetic interaction and the resulting slow-down of the collision lead to a very long infall stage with essentially zero dynamics.

In contrast to the monotonically decreasing gravitational-wave energy, the electromagnetic

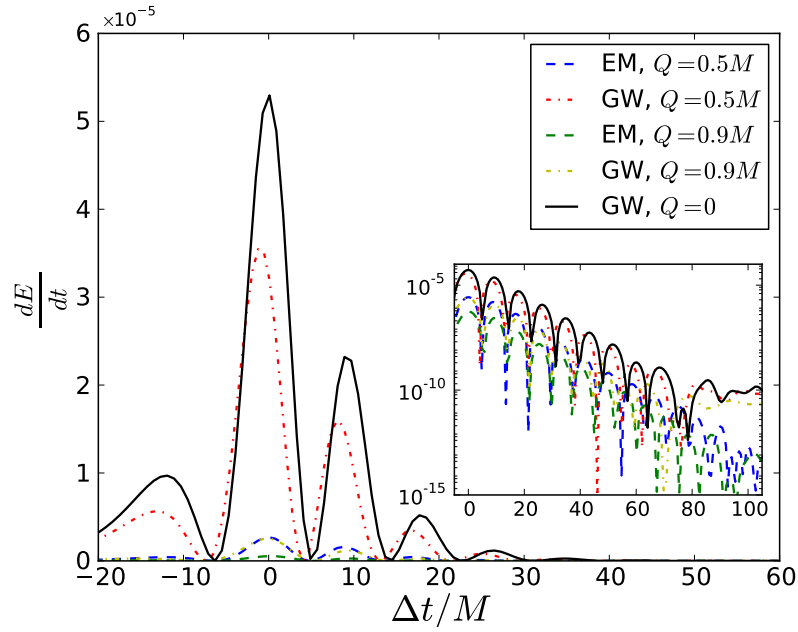


Figure 8.7: Radiated fluxes for simulations d08q05, d08q09 and d08q00 of table 8.1. We have aligned the curves in time such that their global maximum coincides with $t = 0$. The inset shows the exact same plot with the y -axis in logarithmic units.

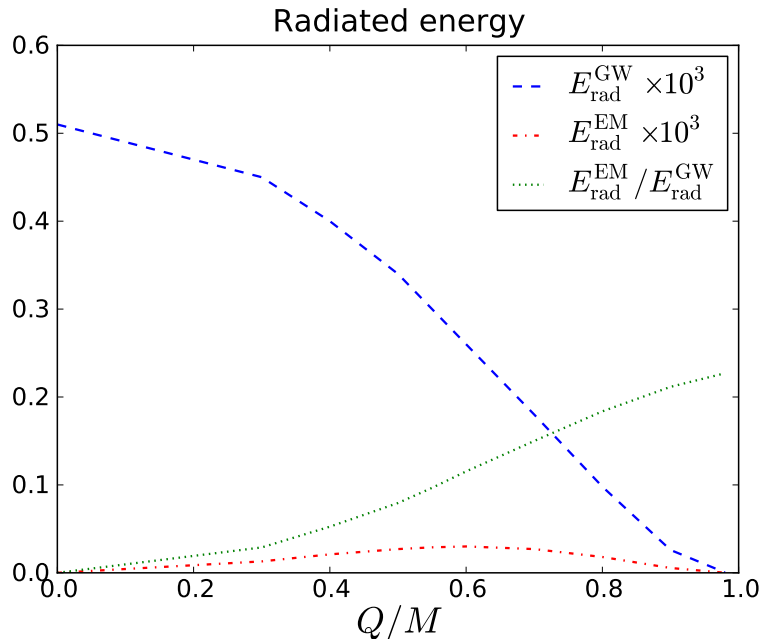


Figure 8.8: Energy radiated in the gravitational and electromagnetic quadrupole as well as the ratio of the two as a function of Q/M .

signal reaches a local maximum around $Q/M = 0.6$, an expected observation as the electromagnetic radiation necessarily vanishes for $Q/M = 0$ (no charge) and $Q/M = 1$ (no acceleration) but takes on non-zero values in the regime in between. Closer analysis of our classical, flat-space calculation (8.3.13) predicts a maximum electromagnetic radiation output at

$$Q_{\max} = \sqrt{\frac{\sqrt{329} - 13}{14}} M \approx 0.605M, \quad (8.4.4)$$

in excellent agreement with the results of our simulations.

We finally consider the ratio of electromagnetic to gravitational wave energy (dotted curve in figure 8.8). As predicted by our analytic calculation (8.3.16), this ratio increases monotonically with Q/M for fixed separation d . A fit of our numerical results yields $E_{\text{rad}}^{\text{EM}}/E_{\text{rad}}^{\text{GW}} = 0.27 Q^2/M^2$ and for our largest value $Q/M = 0.98$, we obtain a ratio of 0.227 to be compared with ~ 0.24 as predicted by equation (8.3.16). Bearing in mind the simplicity of our analytic model in section 8.3, the quantitative agreement is remarkable.

8.5 Conclusions

In this chapter, we performed a numerical study of collisions of charged black holes with equal mass and charge in the framework of the fully non-linear Einstein-Maxwell equations. Our first observation is that the numerical relativity techniques (formulation of the evolution equations, gauge conditions and initial data construction) developed for electrically neutral black hole binaries can be straightforwardly extended to successfully model charged binaries even for nearly extremal charge-to-mass ratios $Q/M \lesssim 1$. In particular, we notice the contrast with the case of rotating black holes with nearly extremal spin which represents a more delicate task for state-of-the-art numerical relativity; cf. references [27, 28] for the latest developments on this front. This absence of difficulties for charged holes is not entirely unexpected. Considering the construction of initial data, for instance, an important difference arises in the customary choice of conformally flat Bowen-York initial data [134] which greatly simplifies the initial data problem. While the Kerr solution for a single rotating black hole does not admit conformally flat slices [136] and therefore inevitably results in spurious radiation, especially for large spin parameters, this difficulty does not arise for charged, but non-rotating black holes; cf. equation (8.4.1) and [215].

The excellent agreement between the classical calculation for the energy emission and the numerical results reported here, allow for an investigation of cosmic censorship close to extremality. If we take two black holes with $M_1 = M_2 = M/2$, $Q_1 = Q_2 = (M - \delta)/2$ and we let them fall from infinity, to first order in δ we get

$$\begin{aligned} Q_{\text{tot}} &= M - \delta \\ M_{\text{tot}} &= M - E_{\text{rad}} \end{aligned} \quad (8.5.1)$$

Now, the classical result (8.3.14) implies that the dominant term for the radiated energy is

$E_{\text{rad}} \sim \mathcal{B}^{5/2} M \sim (\delta/M)^{5/2} M$. Thus we get

$$\frac{Q_{\text{tot}}}{M_{\text{tot}}} \simeq 1 - \frac{\delta}{M} + k \left(\frac{\delta}{M} \right)^{5/2}, \quad (8.5.2)$$

where k is a constant. We conclude that cosmic censorship is preserved for charged collisions of nearly extremal holes ($\delta \ll M$), on account of the much longer collision time, which yields much lower velocities and therefore much lower energy output. The differences between the cases of spinning mergers and charged collisions are interesting. In the former case, naked singularities are avoided by radiation carrying away more angular momentum (via orbital hangup [34]). In the latter case, our results suggest that naked singularities are avoided by the smaller radiation emission, due to the smaller accelerations involved in the infall.

We have here evolved a sequence of binaries, with equal charge-to-mass ratio starting from rest, with Q/M varying from zero to values close to extremality. Starting with the electrically neutral case, where our gravitational wave emission $E_{\text{rad}}^{\text{GW}}/M = 0.055\%$ agrees well with the literature, we observe a monotonic decrease of the emitted gravitational wave energy as we increase Q/M . For our largest value $Q/M = 0.98$, $E_{\text{rad}}^{\text{GW}}$ is reduced by about three orders of magnitude, as the near cancellation of the gravitational and electromagnetic forces substantially slows down the collision. In contrast, the radiated electromagnetic energy reaches a maximum near $Q/M = 0.6$ but always remains significantly below its gravitational counterpart. Indeed, the ratio $E_{\text{rad}}^{\text{EM}}/E_{\text{rad}}^{\text{GW}}$ increases monotonically with Q/M and approaches about 25% in the limit $Q/M \rightarrow 1$. We find all these results to be in remarkably good qualitative *and* quantitative agreement with analytic approximations obtained in the framework of the dynamics of two point charges in a Minkowski background. This approximation also predicts that the collision time relative to that of the uncharged case scales $\sim \sqrt{1 - Q^2/M^2}$ which is confirmed within a few percent by our numerical simulations.

Chapter 9

Final remarks

This probably just goes to show something,
but I sure don't know what.

Calvin
Calvin & Hobbes

Numerical relativity is a fantastic tool to study and explore spacetimes whose exact form is not known.

After decades of efforts, the first stable, long-term evolutions of the orbit and merger of two black holes were finally accomplished in 2005, and since then considerable progress has been made. This field has now reached a state of maturity, and several codes and tools exist that allow one to perform evolutions of black holes—with quite generic initial configurations—in standard four dimensional vacuum gravity.

In addition to the original (main) motivation coming from the two-body problem, it was quickly realised that numerical relativity could be helpful for a much broader range of scenarios, with some motivation coming from fields other than gravity itself.

In this work we have thus worked to extend numerical relativity tools to new frontiers, opening a range of uncharted territory in black hole physics to be explored with contemporary numerical relativity. In particular, we have presented the following:

- (i) a dimensional reduction procedure that allows the use of existing $3 + 1$ numerical codes to evolve higher-dimensional spacetimes with enough symmetry, including head-on collisions in $D \geq 5$ and black hole collisions with impact parameter and spin in $D \geq 6$;
- (ii) a generalisation of the `TWOPUNCTURES` spectral solver, allowing for the computation of initial data for a boosted head-on collision of black hole binaries in higher-dimensional spacetimes;
- (iii) a wave extraction procedure that allows the extraction of gravitational radiation observ-

- ables from numerical evolutions of head-on collisions of black holes in D dimensions;
- (iv) with the above tools, numerical simulations of black hole collisions from rest in five-dimensional spacetimes were successfully evolved, the corresponding wave forms were obtained and total energy released in the form of gravitational waves was computed;
 - (v) evolutions of black holes in non-asymptotically flat spacetimes, including asymptotically de Sitter spacetimes, “boxed” spacetimes with mirror-like boundary conditions, and five-dimensional cylindrical spacetimes;
 - (vi) numerical evolutions of collisions of charged black holes with equal mass and charge, and a calculation of the energy released via emission of gravitational and electromagnetic radiation.

Several open questions and research avenues remain to be explored, and we thus close with a list of natural sequels for this program:

- A systematic investigation of black hole collisions and dynamics in generic dimension. Even though the formalism here presented is valid in arbitrary dimension, the long-term numerical stability of the implementation is a different matter altogether. Currently, only the five-dimensional case seems to be relatively robust, with numerical instabilities occurring in all $D > 5$ cases tried so far. It is possible that such instabilities may be cured with a suitable choice of gauge conditions. These issues remain under investigation.
- Related to the previous point, it could be of interest to systematically investigate the merits and disadvantages, from the point of view of the numerical implementation, of dimensional reduction procedures (such as the one here presented) versus evolution schemes that make use of the Cartoon method.
- The numbers here reported for the total energy loss for the five-dimensional black hole head-on collisions refer to collisions from rest. For the applications described in the Introduction, however, high velocity collisions are the most relevant ones. Such cases do not seem to be as robust as the analogous four dimensional systems, with numerical instabilities appearing when large boost parameters are considered. Investigation on this front is still under way.
- For the Einstein-Maxwell study, a natural step is considering more generic types of initial data, in order to tackle some of the issues discussed in the Introduction. A non-zero boost, for instance, will allow us to study both binary black hole systems that will coalesce into a Kerr-Newman black hole and the impact of electric charge on the dynamics and wave emission (electromagnetic and gravitational) in high energy collisions. A further interesting extension is the case of oppositely charged black holes.

Appendix A

List of publications

This thesis summarises work done in the following publications:

1. **“Numerical relativity for D dimensional axially symmetric space-times: formalism and code tests”**
M. Zilhão, H. Witek, U. Sperhake, V. Cardoso, L. Gualtieri, C. Herdeiro and A. Nerozzi.
[arXiv:1001.2302 \[gr-qc\]](#)
Phys. Rev. D **81**, 084052 (2010)
2. **“Black holes in a box: towards the numerical evolution of black holes in AdS”**
H. Witek, V. Cardoso, C. Herdeiro, A. Nerozzi, U. Sperhake and M. Zilhão.
[arXiv:1004.4633 \[hep-th\]](#)
Phys. Rev. D **82**, 104037 (2010)
3. **“Numerical relativity for D dimensional space-times: head-on collisions of black holes and gravitational wave extraction”**
H. Witek, M. Zilhão, L. Gualtieri, V. Cardoso, C. Herdeiro, A. Nerozzi and U. Sperhake.
[arXiv:1006.3081 \[gr-qc\]](#)
Phys. Rev. D **82**, 104014 (2010)
4. **“Head-on collisions of unequal mass black holes in $D=5$ dimensions”**
H. Witek, V. Cardoso, L. Gualtieri, C. Herdeiro, U. Sperhake and M. Zilhão.
[arXiv:1011.0742 \[gr-qc\]](#)
Phys. Rev. D **83**, 044017 (2011)
5. **“Higher-dimensional puncture initial data”**
M. Zilhão, M. Ansorg, V. Cardoso, L. Gualtieri, C. Herdeiro, U. Sperhake and H. Witek.
[arXiv:1109.2149 \[gr-qc\]](#)
Phys. Rev. D **84**, 084039 (2011)

6. **“Simulations of black holes in compactified spacetimes”**
M. Zilhão, V. Cardoso, L. Gualtieri, C. Herdeiro, A. Nerozzi, U. Sperhake and H. Witek.
J. Phys. Conf. Ser. **314**, 012103 (2011).
7. **“Dynamics of black holes in de Sitter spacetimes”**
M. Zilhão, V. Cardoso, L. Gualtieri, C. Herdeiro, U. Sperhake and H. Witek.
arXiv:1204.2019 [gr-qc]
Phys. Rev. D **85**, 104039 (2012)
8. **“Collisions of charged black holes”**
M. Zilhão, V. Cardoso, C. Herdeiro, L. Lehner and U. Sperhake.
arXiv:1205.1063 [gr-qc]
Phys. Rev. D **85**, 124062 (2012)

The numerical work presented in papers 5, 6, 7 and 8 was performed by the author of this thesis.

Further publications by the author:

1. **“A Double Myers-Perry Black Hole in Five Dimensions”**
C. A. R. Herdeiro, C. Rebelo, M. Zilhão and M. S. Costa.
arXiv:0805.1206 [hep-th]
JHEP **0807**, 009 (2008)
2. **“Mass inflation in a D dimensional Reissner-Nordstrom black hole: a hierarchy of particle accelerators ?”**
P. P. Avelino, A. J. S. Hamilton, C. A. R. Herdeiro and M. Zilhão.
arXiv:1105.4434 [gr-qc]
Phys. Rev. D **84**, 024019 (2011)
3. **“Mathisson’s helical motions for a spinning particle: Are they unphysical?”**
L. F. O. Costa, C. A. R. Herdeiro, J. Natario and M. Zilhão.
arXiv:1109.1019 [gr-qc]
Phys. Rev. D **85**, 024001 (2012)
4. **“NR/HEP: roadmap for the future”**
V. Cardoso, L. Gualtieri, C. Herdeiro, U. Sperhake, *et al.*
arXiv:1201.5118 [hep-th]

Bibliography

- [1] A. Einstein, “On the General Theory of Relativity,” *Sitzungsber.Preuss.Akad.Wiss.Berlin (Math.Phys.)* **1915** (1915) 778–786. (Cited on page 14.)
- [2] A. Einstein, “Explanation of the Perihelion Motion of Mercury from the General Theory of Relativity,” *Sitzungsber.Preuss.Akad.Wiss.Berlin (Math.Phys.)* **1915** (1915) 831–839. (Cited on page 14.)
- [3] A. Einstein, “The Field Equations of Gravitation,” *Sitzungsber.Preuss.Akad.Wiss.Berlin (Math.Phys.)* **1915** (1915) 844–847. (Cited on page 14.)
- [4] A. Abramovici *et al.*, “LIGO: The Laser interferometer gravitational wave observatory,” *Science* **256** (1992) 325–333. (Cited on page 14.)
- [5] B. Caron *et al.*, “The Virgo interferometer,” *Class. Quant. Grav.* **14** (1997) 1461–1469. (Cited on page 15.)
- [6] H. Luck, “The GEO-600 project,” *Class.Quant.Grav.* **14** (1997) 1471–1476. (Cited on page 15.)
- [7] **TAMA Collaboration** Collaboration, M. Ando *et al.*, “Stable operation of a 300-m laser interferometer with sufficient sensitivity to detect gravitational wave events within our galaxy,” *Phys.Rev.Lett.* **86** (2001) 3950, [arXiv:astro-ph/0105473 \[astro-ph\]](#). 5 pages, 4 figures Journal-ref: Physical Review Letters 86 3950 (2001). (Cited on page 15.)
- [8] S. G. Hahn and R. W. Lindquist, “The two-body problem in geometrodynamics,” *Annals of Physics* **29** (1964) 304–331. (Cited on pages 15 and 48.)
- [9] L. Smarr, A. Cadez, B. S. DeWitt, and K. Eppley, “Collision of Two Black Holes: Theoretical Framework,” *Phys. Rev.* **D14** (1976) 2443–2452. (Cited on page 15.)
- [10] K. Eppley, “Evolution of Time Symmetric Gravitational Waves: Initial Data and Apparent Horizons,” *Phys. Rev.* **D16** (1977) 1609–1614. (Cited on page 15.)
- [11] D. Bernstein, D. Hobill, E. Seidel, L. Smarr, and J. Towns, “Numerically generated axisymmetric black hole space-times: Numerical methods and code tests,” *Phys.Rev.* **D50** (1994) 5000–5024. (Cited on page 15.)

- [12] P. Anninos, D. Hobill, E. Seidel, L. Smarr, and W.-M. Suen, “The Headon collision of two equal mass black holes,” *Phys. Rev.* **D52** (1995) 2044–2058, [arXiv:gr-qc/9408041](#). (Cited on page 15.)
- [13] N. Stergioulas and J. L. Friedman, “Nonaxisymmetric neutral modes of rotating relativistic stars,” *Astrophys.J.* **492** (1998) 301, [arXiv:gr-qc/9705056 \[gr-qc\]](#). (Cited on page 15.)
- [14] S. Shapiro and S. Teukolsky, “Collisions of relativistic clusters and the formation of black holes,” *Phys.Rev.* **D45** (1992) 2739–2750. (Cited on page 15.)
- [15] S. A. Hughes, C. R. Keeton, P. Walker, K. T. Walsh, S. L. Shapiro, *et al.*, “Finding black holes in numerical space-times,” *Phys.Rev.* **D49** (1994) 4004–4015. (Cited on page 15.)
- [16] M. W. Choptuik, “Universality and scaling in gravitational collapse of a massless scalar field,” *Phys. Rev. Lett.* **70** (1993) 9–12. (Cited on page 15.)
- [17] L. Lehner, “Numerical relativity: A review,” *Class. Quant. Grav.* **18** (2001) R25–R86, [arXiv:gr-qc/0106072](#). (Cited on page 15.)
- [18] F. Pretorius, “Evolution of Binary Black Hole Spacetimes,” *Phys. Rev. Lett.* **95** (2005) 121101, [arXiv:gr-qc/0507014](#). (Cited on pages 15 and 45.)
- [19] J. G. Baker, J. Centrella, D.-I. Choi, M. Koppitz, and J. van Meter, “Gravitational wave extraction from an inspiraling configuration of merging black holes,” *Phys. Rev. Lett.* **96** (2006) 111102, [arXiv:gr-qc/0511103](#). (Cited on pages 15 and 50.)
- [20] M. Campanelli, C. Lousto, P. Marronetti, and Y. Zlochower, “Accurate evolutions of orbiting black-hole binaries without excision,” *Phys.Rev.Lett.* **96** (2006) 111101, [arXiv:gr-qc/0511048 \[gr-qc\]](#). (Cited on pages 15 and 50.)
- [21] F. Pretorius, “Binary Black Hole Coalescence,” [arXiv:0710.1338 \[gr-qc\]](#). (Cited on page 15.)
- [22] I. Hinder, “The Current Status of Binary Black Hole Simulations in Numerical Relativity,” *Class.Quant.Grav.* **27** (2010) 114004, [arXiv:1001.5161 \[gr-qc\]](#). (Cited on page 15.)
- [23] M. Boyle, D. A. Brown, L. E. Kidder, A. H. Mroue, H. P. Pfeiffer, *et al.*, “High-accuracy comparison of numerical relativity simulations with post-Newtonian expansions,” *Phys.Rev.* **D76** (2007) 124038, [arXiv:0710.0158 \[gr-qc\]](#). (Cited on pages 15 and 115.)
- [24] M. A. Scheel, M. Boyle, T. Chu, L. E. Kidder, K. D. Matthews, *et al.*, “High-accuracy waveforms for binary black hole inspiral, merger, and ringdown,” *Phys.Rev.* **D79** (2009) 024003, [arXiv:0810.1767 \[gr-qc\]](#). (Cited on page 15.)

- [25] C. O. Lousto and Y. Zlochower, “Orbital Evolution of Extreme-Mass-Ratio Black-Hole Binaries with Numerical Relativity,” *Phys.Rev.Lett.* **106** (2011) 041101, [arXiv:1009.0292 \[gr-qc\]](#). (Cited on page 15.)
- [26] U. Sperhake, V. Cardoso, C. D. Ott, E. Schnetter, and H. Witek, “Extreme black hole simulations: collisions of unequal mass black holes and the point particle limit,” *Phys.Rev.* **D84** (2011) 084038, [arXiv:1105.5391 \[gr-qc\]](#). (Cited on page 15.)
- [27] G. Lovelace, M. Boyle, M. A. Scheel, and B. Szilagyi, “Accurate gravitational waveforms for binary-black-hole mergers with nearly extremal spins,” *Class.Quant.Grav.* **29** (2012) 045003, [arXiv:1110.2229 \[gr-qc\]](#). 17 pages, 7 figures, submitted to Classical and Quantum Gravity. (Cited on pages 15 and 129.)
- [28] C. O. Lousto, H. Nakano, Y. Zlochower, B. C. Mundim, and M. Campanelli, “Study of Conformally Flat Initial Data for Highly Spinning Black Holes and their Early Evolutions,” [arXiv:1203.3223 \[gr-qc\]](#). (Cited on pages 15 and 129.)
- [29] F. Pretorius and D. Khurana, “Black hole mergers and unstable circular orbits,” *Class.Quant.Grav.* **24** (2007) S83–S108, [arXiv:gr-qc/0702084 \[GR-QC\]](#). (Cited on page 15.)
- [30] J. Healy, J. Levin, and D. Shoemaker, “Zoom-Whirl Orbits in Black Hole Binaries,” *Phys.Rev.Lett.* **103** (2009) 131101, [arXiv:0907.0671 \[gr-qc\]](#). (Cited on page 15.)
- [31] M. Campanelli, C. O. Lousto, Y. Zlochower, and D. Merritt, “Maximum gravitational recoil,” *Phys.Rev.Lett.* **98** (2007) 231102, [arXiv:gr-qc/0702133 \[GR-QC\]](#). (Cited on page 16.)
- [32] B. Bruegmann, J. A. Gonzalez, M. Hannam, S. Husa, and U. Sperhake, “Exploring black hole superkicks,” *Phys.Rev.* **D77** (2008) 124047, [arXiv:0707.0135 \[gr-qc\]](#). (Cited on page 16.)
- [33] C. O. Lousto and Y. Zlochower, “Hangup Kicks: Still Larger Recoils by Partial Spin/Orbit Alignment of Black-Hole Binaries,” *Phys.Rev.Lett.* **107** (2011) 231102, [arXiv:1108.2009 \[gr-qc\]](#). (Cited on pages 16 and 21.)
- [34] M. Campanelli, C. Lousto, and Y. Zlochower, “Spinning-black-hole binaries: The orbital hang up,” *Phys.Rev.* **D74** (2006) 041501, [arXiv:gr-qc/0604012 \[gr-qc\]](#). (Cited on pages 16 and 130.)
- [35] D. Merritt, M. Milosavljevic, M. Favata, S. A. Hughes, and D. E. Holz, “Consequences of gravitational radiation recoil,” *Astrophys.J.* **607** (2004) L9–L12, [arXiv:astro-ph/0402057 \[astro-ph\]](#). (Cited on page 16.)
- [36] M. Boylan-Kolchin, C.-P. Ma, and E. Quataert, “Core formation in galactic nuclei due to recoiling black holes,” *Astrophys.J.* **613** (2004) L37, [arXiv:astro-ph/0407488 \[astro-ph\]](#). (Cited on page 16.)

- [37] Z. Haiman, “Constraints from gravitational recoil on the growth of supermassive black holes at high redshift,” *Astrophys.J.* **613** (2004) 36–40, [arXiv:astro-ph/0404196](#) [astro-ph]. (Cited on page 16.)
- [38] P. Madau and E. Quataert, “The Effect of gravitational - wave recoil on the demography of massive black holes,” *Astrophys.J.* **606** (2004) L17–L20, [arXiv:astro-ph/0403295](#) [astro-ph]. (Cited on page 16.)
- [39] S. Komossa, “Recoiling black holes: electromagnetic signatures, candidates, and astrophysical implications,” *Adv.Astron.* **2012** (2012) 364973, [arXiv:1202.1977](#) [astro-ph.CO]. (Cited on page 16.)
- [40] U. Sperhake, V. Cardoso, F. Pretorius, E. Berti, and J. A. Gonzalez, “The high-energy collision of two black holes,” *Phys. Rev. Lett.* **101** (2008) 161101, [arXiv:0806.1738](#) [gr-qc]. (Cited on pages 16, 22, and 92.)
- [41] M. Shibata, H. Okawa, and T. Yamamoto, “High-velocity collision of two black holes,” *Phys. Rev.* **D78** (2008) 101501, [arXiv:0810.4735](#) [gr-qc]. (Cited on pages 16, 22, and 92.)
- [42] U. Sperhake *et al.*, “Cross section, final spin and zoom-whirl behavior in high- energy black hole collisions,” *Phys. Rev. Lett.* **103** (2009) 131102, [arXiv:0907.1252](#) [gr-qc]. (Cited on pages 16, 92, and 103.)
- [43] S. Hawking and G. Ellis, *The Large Scale Structure of Space-Time*. Cambridge Monographs on Mathematical Physics. Cambridge University Press, 1975. http://books.google.pt/books?id=QagG_KI7L18C. (Cited on page 16.)
- [44] R. Penrose, “Gravitational collapse: The role of general relativity,” *Riv.Nuovo Cim.* **1** (1969) 252–276. (Cited on page 16.)
- [45] L. Lehner and F. Pretorius, “Black Strings, Low Viscosity Fluids, and Violation of Cosmic Censorship,” *Phys.Rev.Lett.* **105** (2010) 101102, [arXiv:1006.5960](#) [hep-th]. (Cited on pages 16, 20, and 100.)
- [46] R. Gregory and R. Laflamme, “Black strings and p-branes are unstable,” *Phys. Rev. Lett.* **70** (1993) 2837–2840, [arXiv:hep-th/9301052](#). (Cited on pages 16 and 20.)
- [47] H. Okawa, K.-i. Nakao, and M. Shibata, “Is super-Planckian physics visible? – Scattering of black holes in 5 dimensions,” *Phys.Rev.* **D83** (2011) 121501, [arXiv:1105.3331](#) [gr-qc]. (Cited on page 17.)
- [48] R. Emparan and H. S. Reall, “A rotating black ring in five dimensions,” *Phys. Rev. Lett.* **88** (2002) 101101, [arXiv:hep-th/0110260](#). (Cited on page 17.)
- [49] A. Pomeransky and R. Sen’kov, “Black ring with two angular momenta,” [arXiv:hep-th/0612005](#) [hep-th]. (Cited on page 17.)

- [50] H. Elvang and P. Figueras, “Black Saturn,” *JHEP* **0705** (2007) 050, [arXiv:hep-th/0701035](#) [hep-th]. (Cited on page 17.)
- [51] H. Iguchi and T. Mishima, “Black di-ring and infinite nonuniqueness,” *Phys.Rev.* **D75** (2007) 064018, [arXiv:hep-th/0701043](#) [hep-th]. (Cited on page 17.)
- [52] H. Elvang and M. J. Rodriguez, “Bicycling Black Rings,” *JHEP* **0804** (2008) 045, [arXiv:0712.2425](#) [hep-th]. (Cited on page 17.)
- [53] R. Emparan and H. S. Reall, “Black Holes in Higher Dimensions,” *Living Rev. Rel.* **11** (2008) 6, [arXiv:0801.3471](#) [hep-th]. (Cited on page 17.)
- [54] R. Emparan and R. C. Myers, “Instability of ultra-spinning black holes,” *JHEP* **0309** (2003) 025, [arXiv:hep-th/0308056](#) [hep-th]. (Cited on page 17.)
- [55] O. J. Dias, P. Figueras, R. Monteiro, J. E. Santos, and R. Emparan, “Instability and new phases of higher-dimensional rotating black holes,” *Phys.Rev.* **D80** (2009) 111701, [arXiv:0907.2248](#) [hep-th]. (Cited on page 17.)
- [56] M. Shibata and H. Yoshino, “Nonaxisymmetric instability of rapidly rotating black hole in five dimensions,” *Phys.Rev.* **D81** (2010) 021501, [arXiv:0912.3606](#) [gr-qc]. (Cited on page 17.)
- [57] M. Shibata and H. Yoshino, “Bar-mode instability of rapidly spinning black hole in higher dimensions: Numerical simulation in general relativity,” *Phys.Rev.* **D81** (2010) 104035, [arXiv:1004.4970](#) [gr-qc]. (Cited on pages 17, 20, and 61.)
- [58] J. M. Maldacena, “The Large N limit of superconformal field theories and supergravity,” *Adv.Theor.Math.Phys.* **2** (1998) 231–252, [arXiv:hep-th/9711200](#) [hep-th]. (Cited on page 17.)
- [59] A. J. Amsel, D. Marolf, and A. Virmani, “Collisions with Black Holes and Deconfined Plasmas,” *JHEP* **04** (2008) 025, [arXiv:0712.2221](#) [hep-th]. (Cited on page 17.)
- [60] S. S. Gubser, S. S. Pufu, and A. Yarom, “Entropy production in collisions of gravitational shock waves and of heavy ions,” *Phys. Rev.* **D78** (2008) 066014, [arXiv:0805.1551](#) [hep-th]. (Cited on page 17.)
- [61] P. M. Chesler and L. G. Yaffe, “Boost invariant flow, black hole formation, and far-from-equilibrium dynamics in $N = 4$ supersymmetric Yang-Mills theory,” *Phys.Rev.* **D82** (2010) 026006, [arXiv:0906.4426](#) [hep-th]. (Cited on pages 18 and 109.)
- [62] P. M. Chesler and L. G. Yaffe, “Holography and colliding gravitational shock waves in asymptotically AdS5 spacetime,” *Phys.Rev.Lett.* **106** (2011) 021601, [arXiv:1011.3562](#) [hep-th]. (Cited on pages 18 and 109.)
- [63] H. Bantilan, F. Pretorius, and S. S. Gubser, “Simulation of Asymptotically AdS5 Spacetimes with a Generalized Harmonic Evolution Scheme,” *Phys.Rev.* **D85** (2012) 084038, [arXiv:1201.2132](#) [hep-th]. (Cited on pages 18 and 109.)

- [64] G. 't Hooft, “Graviton Dominance in Ultrahigh-Energy Scattering,” *Phys.Lett.* **B198** (1987) 61–63. (Cited on pages 18, 21, and 114.)
- [65] K. S. Thorne, “Nonspherical gravitational collapse: a short review,”. In J. R. Klauder, *Magic Without Magic*, San Francisco 1972, 231–258. (Cited on page 18.)
- [66] M. W. Choptuik and F. Pretorius, “Ultra Relativistic Particle Collisions,” *Phys. Rev. Lett.* **104** (2010) 111101, [arXiv:0908.1780 \[gr-qc\]](#). (Cited on pages 18, 21, and 114.)
- [67] S. Dimopoulos and G. L. Landsberg, “Black Holes at the LHC,” *Phys. Rev. Lett.* **87** (2001) 161602, [arXiv:hep-ph/0106295](#). (Cited on pages 18 and 19.)
- [68] S. B. Giddings and S. D. Thomas, “High energy colliders as black hole factories: The end of short distance physics,” *Phys. Rev.* **D65** (2002) 056010, [arXiv:hep-ph/0106219](#). (Cited on page 18.)
- [69] P. Kanti, “Black Holes at the LHC,” *Lect. Notes Phys.* **769** (2009) 387–423, [arXiv:0802.2218 \[hep-th\]](#). (Cited on page 18.)
- [70] I. Antoniadis, “A Possible new dimension at a few TeV,” *Phys. Lett.* **B246** (1990) 377–384. (Cited on page 18.)
- [71] N. Arkani-Hamed, S. Dimopoulos, and G. R. Dvali, “The hierarchy problem and new dimensions at a millimeter,” *Phys. Lett.* **B429** (1998) 263–272, [arXiv:hep-ph/9803315](#). (Cited on page 18.)
- [72] I. Antoniadis, N. Arkani-Hamed, S. Dimopoulos, and G. R. Dvali, “New dimensions at a millimeter to a Fermi and superstrings at a TeV,” *Phys. Lett.* **B436** (1998) 257–263, [arXiv:hep-ph/9804398](#). (Cited on page 18.)
- [73] L. Randall and R. Sundrum, “A large mass hierarchy from a small extra dimension,” *Phys. Rev. Lett.* **83** (1999) 3370–3373, [arXiv:hep-ph/9905221](#). (Cited on page 18.)
- [74] L. Randall and R. Sundrum, “An alternative to compactification,” *Phys. Rev. Lett.* **83** (1999) 4690–4693, [arXiv:hep-th/9906064](#). (Cited on page 18.)
- [75] P. C. Argyres, S. Dimopoulos, and J. March-Russell, “Black holes and sub-millimeter dimensions,” *Phys. Lett.* **B441** (1998) 96–104, [arXiv:hep-th/9808138](#). (Cited on page 18.)
- [76] T. Banks and W. Fischler, “A model for high energy scattering in quantum gravity,” [arXiv:hep-th/9906038](#). (Cited on page 18.)
- [77] E.-J. Ahn, M. Cavaglia, and A. V. Olinto, “Brane factories,” *Phys. Lett.* **B551** (2003) 1–6, [arXiv:hep-th/0201042](#). (Cited on page 18.)
- [78] A. Chamblin, F. Cooper, and G. C. Nayak, “SUSY production from TeV scale blackhole at LHC,” *Phys. Rev.* **D70** (2004) 075018, [arXiv:hep-ph/0405054](#). (Cited on page 18.)

- [79] J. L. Feng and A. D. Shapere, “Black hole production by cosmic rays,” *Phys. Rev. Lett.* **88** (2002) 021303, [arXiv:hep-ph/0109106](#). (Cited on page 18.)
- [80] E.-J. Ahn, M. Ave, M. Cavaglia, and A. V. Olinto, “TeV black hole fragmentation and detectability in extensive air-showers,” *Phys. Rev.* **D68** (2003) 043004, [arXiv:hep-ph/0306008](#). (Cited on page 18.)
- [81] V. Cardoso, M. C. Espirito Santo, M. Paulos, M. Pimenta, and B. Tome, “Microscopic black hole detection in UHECR: The double bang signature,” *Astropart. Phys.* **22** (2005) 399–407, [arXiv:hep-ph/0405056](#). (Cited on page 18.)
- [82] M. Banados, J. Silk, and S. M. West, “Kerr Black Holes as Particle Accelerators to Arbitrarily High Energy,” *Phys. Rev. Lett.* **103** (2009) 111102, [arXiv:0909.0169 \[hep-ph\]](#). (Cited on page 18.)
- [83] E. Berti, V. Cardoso, L. Gualtieri, F. Pretorius, and U. Sperhake, “Comment on ‘Kerr Black Holes as Particle Accelerators to Arbitrarily High Energy’,” *Phys. Rev. Lett.* **103** (2009) 239001, [arXiv:0911.2243 \[gr-qc\]](#). (Cited on page 18.)
- [84] T. Jacobson and T. P. Sotiriou, “Spinning Black Holes as Particle Accelerators,” *Phys.Rev.Lett.* **104** (2010) 021101, [arXiv:0911.3363 \[gr-qc\]](#). (Cited on page 18.)
- [85] M. Cavaglia, “Black hole and brane production in TeV gravity: A review,” *Int. J. Mod. Phys.* **A18** (2003) 1843–1882, [arXiv:hep-ph/0210296](#). (Cited on page 18.)
- [86] P. Kanti, “Black holes in theories with large extra dimensions: A Review,” *Int. J. Mod. Phys.* **A19** (2004) 4899–4951, [arXiv:hep-ph/0402168](#). (Cited on pages 18 and 67.)
- [87] J. A. Frost *et al.*, “Phenomenology of Production and Decay of Spinning Extra-Dimensional Black Holes at Hadron Colliders,” *JHEP* **10** (2009) 014, [arXiv:0904.0979 \[hep-ph\]](#). (Cited on page 19.)
- [88] M. Cavaglia, R. Godang, L. Cremaldi, and D. Summers, “Catfish: A Monte Carlo simulator for black holes at the LHC,” *Comput. Phys. Commun.* **177** (2007) 506–517, [arXiv:hep-ph/0609001](#). (Cited on page 19.)
- [89] D.-C. Dai *et al.*, “BlackMax: A black-hole event generator with rotation, recoil, split branes and brane tension,” *Phys. Rev.* **D77** (2008) 076007, [arXiv:0711.3012 \[hep-ph\]](#). (Cited on page 19.)
- [90] D.-C. Dai *et al.*, “Manual of BlackMax, a black-hole event generator with rotation, recoil, split branes, and brane tension,” [arXiv:0902.3577 \[hep-ph\]](#). (Cited on page 19.)
- [91] V. Cardoso, L. Gualtieri, C. Herdeiro, U. Sperhake, P. M. Chesler, *et al.*, “NR/HEP: roadmap for the future,” [arXiv:1201.5118 \[hep-th\]](#). (Cited on page 19.)

- [92] M. Choptuik, L. Lehner, I. Olabarrieta, R. Petryk, F. Pretorius, and H. Villegas, “Towards the final fate of an unstable black string,” *Phys. Rev.* **D68** (2003) 044001, [arXiv:gr-qc/0304085](#). (Cited on pages 20 and 61.)
- [93] E. Sorkin and M. W. Choptuik, “Generalized harmonic formulation in spherical symmetry,” *Gen.Rel.Grav.* **42** (2010) 1239–1286, [arXiv:0908.2500 \[gr-qc\]](#). (Cited on page 20.)
- [94] E. Sorkin, “An Axisymmetric generalized harmonic evolution code,” *Phys.Rev.* **D81** (2010) 084062, [arXiv:0911.2011 \[gr-qc\]](#). (Cited on page 20.)
- [95] M. Headrick, S. Kitchen, and T. Wiseman, “A New approach to static numerical relativity, and its application to Kaluza-Klein black holes,” *Class.Quant.Grav.* **27** (2010) 035002, [arXiv:0905.1822 \[gr-qc\]](#). (Cited on page 20.)
- [96] M. Alcubierre, S. Brandt, B. Brügmann, D. Holz, E. Seidel, R. Takahashi, and J. Thornburg, “Symmetry without Symmetry: Numerical Simulation of Axisymmetric Systems using Cartesian Grids,” *Int. J. Mod. Phys.* **D10** (2001) 273–290, [arXiv:gr-qc/9908012](#). (Cited on page 20.)
- [97] H. Yoshino and M. Shibata, “Higher-dimensional numerical relativity: Formulation and code tests,” *Phys. Rev.* **D80** (2009) 084025, [arXiv:0907.2760 \[gr-qc\]](#). (Cited on pages 20, 51, 61, and 82.)
- [98] H. M. S. Yoshino and M. Shibata, “Higher-Dimensional Numerical Relativity: Current Status,” *Prog.Theor.Phys.Suppl.* **189** (2011) 269–310. (Cited on page 20.)
- [99] H. M. S. Yoshino and M. Shibata, “Exploring Higher-Dimensional Black Holes in Numerical Relativity,” *Prog.Theor.Phys.Suppl.* **190** (2011) 282–303. (Cited on page 20.)
- [100] **WMAP Collaboration** Collaboration, E. Komatsu *et al.*, “Seven-Year Wilkinson Microwave Anisotropy Probe (WMAP) Observations: Cosmological Interpretation,” *Astrophys.J.Suppl.* **192** (2011) 18, [arXiv:1001.4538 \[astro-ph.CO\]](#). (Cited on pages 20 and 97.)
- [101] R. M. Wald, “Dynamics in nonglobally hyperbolic, static space-times,” *J. Math. Phys.* **21** (1980) 2802–2805. (Cited on page 20.)
- [102] A. Ishibashi and R. M. Wald, “Dynamics in non-globally-hyperbolic static spacetimes. II: General analysis of prescriptions for dynamics,” *Class. Quant. Grav.* **20** (2003) 3815–3826, [arXiv:gr-qc/0305012](#). (Cited on page 20.)
- [103] A. Ishibashi and R. M. Wald, “Dynamics in non-globally hyperbolic static space-times. III: anti-de Sitter spacetime,” *Class. Quant. Grav.* **21** (2004) 2981–3014, [arXiv:hep-th/0402184](#). (Cited on page 20.)
- [104] H. Witek, V. Cardoso, C. Herdeiro, A. Nerozzi, U. Sperhake, and M. Zilhão, “Black holes in a box: towards the numerical evolution of black holes in AdS,” *Phys.Rev.* **D82** (2010) 104037, [arXiv:1004.4633 \[hep-th\]](#). (Cited on pages 20, 106, and 109.)

- [105] R. C. Myers, “Higher dimensional black holes in compactified space-times,” *Phys. Rev.* **D35** (1987) 455. (Cited on pages 21, 110, and 112.)
- [106] D. Korotkin and H. Nicolai, “A Periodic analog of the Schwarzschild solution,” [arXiv:gr-qc/9403029](#) [gr-qc]. (Cited on pages 21 and 110.)
- [107] A. V. Frolov and V. P. Frolov, “Black holes in a compactified space-time,” *Phys.Rev.* **D67** (2003) 124025, [arXiv:hep-th/0302085](#) [hep-th]. (Cited on pages 21 and 110.)
- [108] T. Harmark and N. A. Obers, “Phases of Kaluza-Klein black holes: A Brief review,” [arXiv:hep-th/0503020](#) [hep-th]. (Cited on pages 21 and 110.)
- [109] C. Palenzuela, M. Anderson, L. Lehner, S. L. Liebling, and D. Neilsen, “Stirring, not shaking: binary black holes’ effects on electromagnetic fields,” *Phys.Rev.Lett.* **103** (2009) 081101, [arXiv:0905.1121](#) [astro-ph.HE]. (Cited on pages 21, 22, and 115.)
- [110] C. Palenzuela, L. Lehner, and S. L. Liebling, “Dual Jets from Binary Black Holes,” *Science* **329** (2010) 927, [arXiv:1005.1067](#) [astro-ph.HE]. (Cited on pages 21 and 114.)
- [111] R. M. Wald, “Black hole in a uniform magnetic field,” *Phys.Rev.* **D10** (1974) 1680–1685. (Cited on pages 21 and 114.)
- [112] R. Blandford and R. Znajek, “Electromagnetic extractions of energy from Kerr black holes,” *Mon.Not.Roy.Astron.Soc.* **179** (1977) 433–456. (Cited on pages 21 and 114.)
- [113] C. Palenzuela, T. Garrett, L. Lehner, and S. L. Liebling, “Magnetospheres of Black Hole Systems in Force-Free Plasma,” *Phys.Rev.* **D82** (2010) 044045, [arXiv:1007.1198](#) [gr-qc]. (Cited on pages 21 and 114.)
- [114] H. Yoshino and R. B. Mann, “Black hole formation in the head-on collision of ultra-relativistic charges,” *Phys.Rev.* **D74** (2006) 044003, [arXiv:gr-qc/0605131](#) [gr-qc]. (Cited on pages 21 and 114.)
- [115] D. M. Gingrich, “Effect of charged partons on black hole production at the large hadron collider,” *JHEP* **0702** (2007) 098, [arXiv:hep-ph/0612105](#) [hep-ph]. (Cited on pages 21 and 114.)
- [116] C. Palenzuela, L. Lehner, O. Reula, and L. Rezzolla, “Beyond ideal MHD: towards a more realistic modeling of relativistic astrophysical plasmas,” *Mon.Not.Roy.Astron.Soc.* **394** (2009) 1727–1740, [arXiv:0810.1838](#) [astro-ph]. (Cited on pages 22 and 115.)
- [117] C. Palenzuela, L. Lehner, and S. Yoshida, “Understanding possible electromagnetic counterparts to loud gravitational wave events: Binary black hole effects on electromagnetic fields,” *Phys.Rev.* **D81** (2010) 084007, [arXiv:0911.3889](#) [gr-qc]. (Cited on pages 22 and 115.)

- [118] P. Mosta, C. Palenzuela, L. Rezzolla, L. Lehner, S. Yoshida, *et al.*, “Vacuum Electromagnetic Counterparts of Binary Black-Hole Mergers,” *Phys.Rev.* **D81** (2010) 064017, [arXiv:0912.2330](https://arxiv.org/abs/0912.2330) [gr-qc]. (Cited on pages 22, 115, and 116.)
- [119] E.ourgoulhon, “3+1 Formalism and Bases of Numerical Relativity,” [arXiv:gr-qc/0703035](https://arxiv.org/abs/gr-qc/0703035). (Cited on pages 22, 25, 27, 29, 30, 32, 38, 41, and 42.)
- [120] M. Alcubierre, *Introduction to 3+1 numerical relativity*. International series of monographs on physics. Oxford Univ. Press, Oxford, 2008. (Cited on pages 22, 35, 45, 54, and 56.)
- [121] T. Baumgarte and S. Shapiro, *Numerical Relativity: Solving Einstein’s Equations on the Computer*. Cambridge University Press, 2010. <http://books.google.co.uk/books?id=dxU10EinvRUC>. (Cited on pages 22, 35, 45, 54, and 56.)
- [122] E. Poisson, *A Relativist’s Toolkit : The Mathematics of Black-Hole Mechanics*. Cambridge University Press, May, 2004. (Cited on page 25.)
- [123] S. M. Carroll, *Spacetime and geometry: An introduction to general relativity*. San Francisco, USA: Addison-Wesley, 2004. (Cited on pages 28 and 54.)
- [124] R. Arnowitt, S. Deser, and C. W. Misner, “The dynamics of general relativity,” in *Gravitation: An introduction to current research*, Witten, L., ed., pp. 227–265. John Wiley, New York, 1962. [arXiv:gr-qc/0405109](https://arxiv.org/abs/gr-qc/0405109). (Cited on page 34.)
- [125] J. W. York, Jr., “Kinematics and dynamics of general relativity,” in *Sources of Gravitational Radiation*, L. L. Smarr, ed., pp. 83–126. 1979. (Cited on page 34.)
- [126] G. B. Cook, “Initial Data for Numerical Relativity,” *Living Rev. Rel.* **3** (2000) 5, [arXiv:gr-qc/0007085](https://arxiv.org/abs/gr-qc/0007085). (Cited on page 35.)
- [127] H. Yoshino, T. Shiromizu, and M. Shibata, “The close limit analysis for head-on collision of two black holes in higher dimensions: Brill-Lindquist initial data,” *Phys. Rev.* **D72** (2005) 084020, [arXiv:gr-qc/0508063](https://arxiv.org/abs/gr-qc/0508063). (Cited on pages 35, 70, 86, and 90.)
- [128] H. Yoshino, T. Shiromizu, and M. Shibata, “Close-slow analysis for head-on collision of two black holes in higher dimensions: Bowen-York initial data,” *Phys. Rev.* **D74** (2006) 124022, [arXiv:gr-qc/0610110](https://arxiv.org/abs/gr-qc/0610110). (Cited on pages 35, 40, 41, 42, 43, 44, and 70.)
- [129] A. Lichnerowicz, “L’integration des equations de la gravitation relativiste et le problème des n corps,” *J. Math. Pures et Appl.* **23** (1944) 37–63. (Cited on page 35.)
- [130] J. W. York, Jr., “Gravitational degrees of freedom and the initial-value problem,” *Phys. Rev. Lett.* **26** (1971) 1656–1658. (Cited on page 35.)
- [131] J. W. York, Jr., “Role of conformal three-geometry in the dynamics of gravitation,” *Phys. Rev. Lett.* **28** (1972) 1082–1085. (Cited on page 35.)

- [132] J. W. York, Jr., “Conformally invariant orthogonal decomposition of symmetric tensors on riemannian manifolds and the initial-value problem of general relativity,” *J. Math. Phys.* **14** (1973) 456–464. (Cited on page 35.)
- [133] D. R. Brill and R. W. Lindquist, “Interaction energy in geometrostatics,” *Phys. Rev.* **131** (1963) 471–476. (Cited on pages 35, 40, 115, and 117.)
- [134] J. M. Bowen and J. W. York Jr., “Time asymmetric initial data for black holes and black hole collisions,” *Phys. Rev.* **D21** (1980) 2047–2056. (Cited on pages 35, 41, 42, and 129.)
- [135] S. Brandt and B. Bruegmann, “A Simple construction of initial data for multiple black holes,” *Phys.Rev.Lett.* **78** (1997) 3606–3609, [arXiv:gr-qc/9703066 \[gr-qc\]](#). (Cited on pages 35, 40, 43, and 44.)
- [136] A. Garat and R. H. Price, “Nonexistence of conformally flat slices of the Kerr spacetime,” *Phys. Rev.* **D61** (2000) 124011, [arXiv:gr-qc/0002013](#). (Cited on pages 43 and 129.)
- [137] S. R. Brandt and E. Seidel, “The Evolution of distorted rotating black holes. 2: Dynamics and analysis,” *Phys. Rev.* **D52** (1995) 870–886, [arXiv:gr-qc/9412073](#). (Cited on page 43.)
- [138] R. J. Gleiser, C. O. Nicasio, R. H. Price, and J. Pullin, “Evolving the Bowen-York initial data for spinning black holes,” *Phys. Rev.* **D57** (1998) 3401–3407, [arXiv:gr-qc/9710096](#). (Cited on page 43.)
- [139] M. Ansorg, B. Bruegmann, and W. Tichy, “A single-domain spectral method for black hole puncture data,” *Phys. Rev.* **D70** (2004) 064011, [arXiv:gr-qc/0404056](#). (Cited on pages 44, 50, 71, 73, 74, 75, 77, 78, and 79.)
- [140] T. Nakamura, K. Oohara, and Y. Kojima, “General Relativistic Collapse to Black Holes and Gravitational Waves from Black Holes,” *Prog.Theor.Phys.Suppl.* **90** (1987) 1–218. (Cited on page 45.)
- [141] M. Shibata and T. Nakamura, “Evolution of three-dimensional gravitational waves: Harmonic slicing case,” *Phys. Rev.* **D52** (1995) 5428–5444. (Cited on pages 45, 47, and 50.)
- [142] T. W. Baumgarte and S. L. Shapiro, “On the numerical integration of Einstein’s field equations,” *Phys. Rev.* **D59** (1999) 024007, [arXiv:gr-qc/9810065](#). (Cited on pages 45, 47, and 50.)
- [143] O. Sarbach, G. Calabrese, J. Pullin, and M. Tiglio, “Hyperbolicity of the BSSN system of Einstein evolution equations,” *Phys.Rev.* **D66** (2002) 064002, [arXiv:gr-qc/0205064 \[gr-qc\]](#). (Cited on page 45.)

- [144] G. Yoneda and H.-a. Shinkai, “Advantages of modified ADM formulation: Constraint propagation analysis of Baumgarte-Shapiro-Shibata-Nakamura system,” *Phys.Rev.* **D66** (2002) 124003, [arXiv:gr-qc/0204002](#) [gr-qc]. (Cited on page 45.)
- [145] H. Friedrich, “Hyperbolic reductions for Einstein’s equations,” *Class.Quant.Grav.* **13** (1996) 1451–1469. (Cited on page 45.)
- [146] P. Anninos, K. Camarda, J. Masso, E. Seidel, W.-M. Suen, *et al.*, “Three-dimensional numerical relativity: The Evolution of black holes,” *Phys.Rev.* **D52** (1995) 2059–2082, [arXiv:gr-qc/9503025](#) [gr-qc]. (Cited on page 49.)
- [147] L. Smarr and J. York, James W., “Kinematical conditions in the construction of space-time,” *Phys.Rev.* **D17** (1978) 2529–2551. (Cited on page 50.)
- [148] M. Alcubierre, B. Bruegmann, P. Diener, M. Koppitz, D. Pollney, *et al.*, “Gauge conditions for long term numerical black hole evolutions without excision,” *Phys.Rev.* **D67** (2003) 084023, [arXiv:gr-qc/0206072](#) [gr-qc]. (Cited on page 50.)
- [149] U. Sperhake, “Binary black-hole evolutions of excision and puncture data,” *Phys. Rev.* **D76** (2007) 104015, [arXiv:gr-qc/0606079](#). (Cited on pages 50, 80, 100, 106, 107, 109, 118, and 121.)
- [150] “Cactus Computational Toolkit.” <http://www.cactuscode.org/>. (Cited on page 50.)
- [151] E. Schnetter, S. H. Hawley, and I. Hawke, “Evolutions in 3D numerical relativity using fixed mesh refinement,” *Class. Quant. Grav.* **21** (2004) 1465–1488, [arXiv:gr-qc/0310042](#). (Cited on page 50.)
- [152] “Mesh refinement with Carpet.” <http://www.carpetcode.org/>. (Cited on page 50.)
- [153] J. Thornburg, “Finding apparent horizons in numerical relativity,” *Phys. Rev.* **D54** (1996) 4899–4918, [arXiv:gr-qc/9508014](#). (Cited on pages 50 and 100.)
- [154] J. Thornburg, “A Fast Apparent-Horizon Finder for 3-Dimensional Cartesian Grids in Numerical Relativity,” *Class. Quant. Grav.* **21** (2004) 743–766, [arXiv:gr-qc/0306056](#). (Cited on pages 50 and 100.)
- [155] H. Kodama, A. Ishibashi, and O. Seto, “Brane world cosmology: Gauge-invariant formalism for perturbation,” *Phys. Rev.* **D62** (2000) 064022, [arXiv:hep-th/0004160](#). (Cited on pages 52, 57, and 58.)
- [156] H. Kodama and A. Ishibashi, “A master equation for gravitational perturbations of maximally symmetric black holes in higher dimensions,” *Prog. Theor. Phys.* **110** (2003) 701–722, [arXiv:hep-th/0305147](#). (Cited on pages 52, 57, 59, and 86.)
- [157] T. Regge and J. A. Wheeler, “Stability of a Schwarzschild singularity,” *Phys. Rev.* **108** (1957) 1063–1069. (Cited on page 52.)

- [158] F. J. Zerilli, “Effective potential for even parity Regge-Wheeler gravitational perturbation equations,” *Phys. Rev. Lett.* **24** (1970) 737–738. (Cited on page 52.)
- [159] V. Moncrief, “Gravitational perturbations of spherically symmetric systems. I. The exterior problem.,” *Annals Phys.* **88** (1974) 323–342. (Cited on pages 52 and 57.)
- [160] E. Newman and R. Penrose, “An Approach to gravitational radiation by a method of spin coefficients,” *J. Math. Phys.* **3** (1962) 566–578. (Cited on pages 52, 54, 56, and 57.)
- [161] R. Hulse and J. Taylor, “Discovery of a pulsar in a binary system,” *Astrophys.J.* **195** (1975) L51–L53. (Cited on page 52.)
- [162] A. Lyne, M. Burgay, M. Kramer, A. Possenti, R. Manchester, *et al.*, “A Double - pulsar system - A Rare laboratory for relativistic gravity and plasma physics,” *Science* **303** (2004) 1153–1157, [arXiv:astro-ph/0401086](https://arxiv.org/abs/astro-ph/0401086) [astro-ph]. (Cited on page 53.)
- [163] M. Kramer and N. Wex, “The double pulsar system: A unique laboratory for gravity,” *Class.Quant.Grav.* **26** (2009) 073001. (Cited on page 53.)
- [164] R. A. Isaacson, “Gravitational Radiation in the Limit of High Frequency. I. The Linear Approximation and Geometrical Optics,” *Phys.Rev.* **166** (1967) 1263–1271. (Cited on page 53.)
- [165] R. A. Isaacson, “Gravitational Radiation in the Limit of High Frequency. II. Nonlinear Terms and the Effective Stress Tensor,” *Phys.Rev.* **166** (1968) 1272–1279. (Cited on page 53.)
- [166] C. W. Misner, K. S. Thorne, and J. A. Wheeler, *Gravitation*. W. H. Freeman, 1973. (Cited on pages 53 and 54.)
- [167] R. P. Geroch, A. Held, and R. Penrose, “A space-time calculus based on pairs of null directions,” *J.Math.Phys.* **14** (1973) 874–881. (Cited on page 55.)
- [168] M. Durkee, V. Pravda, A. Pravdova, and H. S. Reall, “Generalization of the Geroch-Held-Penrose formalism to higher dimensions,” *Class.Quant.Grav.* **27** (2010) 215010, [arXiv:1002.4826](https://arxiv.org/abs/1002.4826) [gr-qc]. (Cited on page 55.)
- [169] L. Lehner and O. M. Moreschi, “Dealing with delicate issues in waveforms calculations,” *Phys.Rev.* **D76** (2007) 124040, [arXiv:0706.1319](https://arxiv.org/abs/0706.1319) [gr-qc]. (Cited on page 56.)
- [170] E. T. Newman and K. P. Tod, “Asymptotically Flat Space-Times,” in *General Relativity and Gravitation II*, A. Held, ed., p. 1. 1980. (Cited on pages 56 and 57.)
- [171] E. Berti, M. Cavaglia, and L. Gualtieri, “Gravitational energy loss in high energy particle collisions: Ultrarelativistic plunge into a multidimensional black hole,” *Phys. Rev.* **D69** (2004) 124011, [arXiv:hep-th/0309203](https://arxiv.org/abs/hep-th/0309203). (Cited on pages 59 and 86.)
- [172] J. Thornburg, “Event and apparent horizon finders for 3+1 numerical relativity,” *Living Rev.Rel.* **10** (2007) 3, [arXiv:gr-qc/0512169](https://arxiv.org/abs/gr-qc/0512169) [gr-qc]. (Cited on page 60.)

- [173] R. M. Wald and V. Iyer, “Trapped surfaces in the Schwarzschild geometry and cosmic censorship,” *Phys.Rev.* **D44** (1991) 3719–3722. (Cited on page 60.)
- [174] R. Wald, *General Relativity*. University of Chicago Press, 1984. <http://books.google.com.br/books?id=9S-hzg6-moYC>. (Cited on page 60.)
- [175] M. Zilhão, H. Witek, U. Sperhake, V. Cardoso, L. Gualtieri, C. Herdeiro, and A. Nerozzi, “Numerical relativity for D dimensional axially symmetric space-times: formalism and code tests,” *Phys.Rev.* **D81** (2010) 084052, [arXiv:1001.2302](https://arxiv.org/abs/1001.2302) [gr-qc]. (Cited on pages 61 and 81.)
- [176] H. Witek, M. Zilhão, L. Gualtieri, V. Cardoso, C. Herdeiro, A. Nerozzi, and U. Sperhake, “Numerical relativity for D dimensional space-times: head-on collisions of black holes and gravitational wave extraction,” *Phys.Rev.* **D82** (2010) 104014, [arXiv:1006.3081](https://arxiv.org/abs/1006.3081) [gr-qc]. (Cited on pages 61, 84, 85, 86, 120, 126, and 127.)
- [177] M. Zilhão, M. Ansorg, V. Cardoso, L. Gualtieri, C. Herdeiro, U. Sperhake, and H. Witek, “Higher-dimensional puncture initial data,” *Phys.Rev.* **D84** (2011) 084039, [arXiv:1109.2149](https://arxiv.org/abs/1109.2149) [gr-qc]. (Cited on pages 61 and 71.)
- [178] F. R. Tangherlini, “Schwarzschild field in n dimensions and the dimensionality of space problem,” *Nuovo Cim.* **27** (1963) 636–651. (Cited on page 62.)
- [179] R. P. Geroch, “A Method for generating solutions of Einstein’s equations,” *J. Math. Phys.* **12** (1971) 918–924. (Cited on pages 62 and 91.)
- [180] K. R. P. Sjodin, U. Sperhake, and J. A. Vickers, “Dynamic cosmic strings. I,” *Phys. Rev.* **D63** (2001) 024011, [arXiv:gr-qc/0002096](https://arxiv.org/abs/gr-qc/0002096). (Cited on page 62.)
- [181] U. Sperhake, K. R. P. Sjodin, and J. A. Vickers, “Dynamic cosmic strings. II: Numerical evolution of excited cosmic strings,” *Phys. Rev.* **D63** (2001) 024012, [arXiv:gr-qc/0003114](https://arxiv.org/abs/gr-qc/0003114). (Cited on page 62.)
- [182] M. W. Choptuik, E. W. Hirschmann, S. L. Liebling, and F. Pretorius, “An Axisymmetric Gravitational Collapse Code,” *Class. Quant. Grav.* **20** (2003) 1857–1878, [arXiv:gr-qc/0301006](https://arxiv.org/abs/gr-qc/0301006). (Cited on page 62.)
- [183] C. C. Chiang, S. C. Lee, and G. Marmo, “Curvature Tensor For Kaluza-Klein Theories With Homogeneous Fibers,” *Phys. Rev.* **D32** (1985) 1364. (Cited on pages 62 and 64.)
- [184] Y. M. Cho, “Dimensional Reduction by Isometry,” *Phys. Lett* **186B** (1987) 38. (Cited on pages 62, 64, and 91.)
- [185] Y. M. Cho and D. S. Kim, “Higher Dimensional Unification By Isometry,” *J. Math. Phys.* **30** (1989) 1570–1578. (Cited on page 62.)
- [186] M. Abramowitz and I. A. Stegun, *Handbook of Mathematical Functions with Formulas Graphs and Mathematical Tables*. Dover, New York, fifth ed., 1964. (Cited on page 75.)

- [187] S. Dain and H. Friedrich, “Asymptotically flat initial data with prescribed regularity at infinity,” *Commun.Math.Phys.* **222** (2001) 569–609, [arXiv:gr-qc/0102047](#) [gr-qc]. (Cited on page 77.)
- [188] R. J. Gleiser, G. Khanna, and J. Pullin, “Perturbative evolution of conformally flat initial data for a single boosted black hole,” *Phys.Rev.* **D66** (2002) 024035, [arXiv:gr-qc/9905067](#) [gr-qc]. (Cited on page 77.)
- [189] J. Brown, P. Diener, O. Sarbach, E. Schnetter, and M. Tiglio, “Turduckening black holes: An Analytical and computational study,” *Phys.Rev.* **D79** (2009) 044023, [arXiv:0809.3533](#) [gr-qc]. (Cited on page 80.)
- [190] V. Cardoso and J. P. S. Lemos, “Gravitational radiation from collisions at the speed of light: A massless particle falling into a Schwarzschild black hole,” *Phys. Lett.* **B538** (2002) 1–5, [arXiv:gr-qc/0202019](#). (Cited on page 86.)
- [191] V. Cardoso, J. P. Lemos, and S. Yoshida, “Scalar gravitational perturbations and quasinormal modes in the five-dimensional Schwarzschild black hole,” *JHEP* **0312** (2003) 041, [arXiv:hep-th/0311260](#) [hep-th]. (Cited on page 90.)
- [192] E. Berti, V. Cardoso, and A. O. Starinets, “Quasinormal modes of black holes and black branes,” *Class. Quant. Grav.* **26** (2009) 163001, [arXiv:0905.2975](#) [gr-qc]. (Cited on pages 90, 115, and 126.)
- [193] M. Shibata, K.-i. Nakao, T. Nakamura, and K.-i. Maeda, “Dynamical evolution of gravitational waves in the asymptotically de Sitter space-time,” *Phys.Rev.* **D50** (1994) 708–719. (Cited on pages 97 and 98.)
- [194] M. Shibata and M. Sasaki, “Black hole formation in the Friedmann universe: Formulation and computation in numerical relativity,” *Phys.Rev.* **D60** (1999) 084002, [arXiv:gr-qc/9905064](#) [gr-qc]. (Cited on page 97.)
- [195] M. Zilhão, V. Cardoso, L. Gualtieri, C. Herdeiro, U. Sperhake, and H. Witek, “Dynamics of black holes in de Sitter spacetimes,” *Phys.Rev.* **D85** (2012) 104039, [arXiv:1204.2019](#) [gr-qc]. (Cited on page 97.)
- [196] G. McVittie, “The mass-particle in an expanding universe,” *Mon.Not.Roy.Astron.Soc.* **93** (1933) 325–339. (Cited on page 99.)
- [197] K.-i. Nakao, T. Nakamura, K.-i. Oohara, and K.-i. Maeda, “Numerical study of cosmic no hair conjecture. 1. Formalism and linear analysis,” *Phys.Rev.* **D43** (1991) 1788–1797. (Cited on page 100.)
- [198] K.-i. Nakao, K. Yamamoto, and K.-i. Maeda, “Apparent horizons of an N-black-hole system in a space-time with a cosmological constant,” *Phys.Rev.* **D47** (1993) 3203–3213. (Cited on pages 100, 101, and 102.)

- [199] T. Shiromizu, K. Nakao, H. Kodama, and K.-I. Maeda, “Can large black holes collide in de Sitter space-time? An inflationary scenario of an inhomogeneous universe,” *Phys.Rev.* **D47** (1993) 3099–3102. (Cited on page 100.)
- [200] S. A. Hayward, T. Shiromizu, and K.-i. Nakao, “A Cosmological constant limits the size of black holes,” *Phys.Rev.* **D49** (1994) 5080–5085, [arXiv:gr-qc/9309004](#) [gr-qc]. (Cited on page 104.)
- [201] D. R. Brill, G. T. Horowitz, D. Kastor, and J. H. Traschen, “Testing cosmic censorship with black hole collisions,” *Phys.Rev.* **D49** (1994) 840–852, [arXiv:gr-qc/9307014](#) [gr-qc]. (Cited on page 105.)
- [202] D. Shoemaker *et al.*, “Moving black holes via singularity excision,” *Class. Quant. Grav.* **20** (2003) 3729–3744, [arXiv:gr-qc/0301111](#). (Cited on page 106.)
- [203] J. G. Baker, J. Centrella, D.-I. Choi, M. Koppitz, and J. van Meter, “Binary black hole merger dynamics and waveforms,” *Phys. Rev.* **D73** (2006) 104002, [arXiv:gr-qc/0602026](#). (Cited on page 107.)
- [204] E. Berti, V. Cardoso, J. A. Gonzalez, U. Sperhake, M. Hannam, S. Husa, and B. Bruegmann, “Inspiral, merger and ringdown of unequal mass black hole binaries: A multipolar analysis,” *Phys. Rev.* **D76** (2007) 064034, [arXiv:gr-qc/0703053](#). (Cited on pages 107 and 109.)
- [205] K. Kiuchi, Y. Sekiguchi, M. Shibata, and K. Taniguchi, “Longterm general relativistic simulation of binary neutron stars collapsing to a black hole,” *Phys. Rev.* **D80** (2009) 064037, [arXiv:0904.4551](#) [gr-qc]. (Cited on page 108.)
- [206] M. Zilhão, V. Cardoso, L. Gualtieri, C. Herdeiro, A. Nerozzi, U. Sperhake, and H. Witek, “Simulations of black holes in compactified spacetimes,” *J.Phys.Conf.Ser.* **314** (2011) 012103. (Cited on page 110.)
- [207] M. Zilhão, V. Cardoso, C. Herdeiro, L. Lehner, and U. Sperhake, “Collisions of charged black holes,” *Phys.Rev.* **D85** (2012) 124062, [arXiv:1205.1063](#) [gr-qc]. (Cited on page 114.)
- [208] G. Gibbons, “Vacuum Polarization and the Spontaneous Loss of Charge by Black Holes,” *Commun.Math.Phys.* **44** (1975) 245–264. (Cited on page 114.)
- [209] S. Chandrasekhar, *The Mathematical Theory of Black Holes*. Oxford University Press, New York, 1983. (Cited on page 115.)
- [210] L. Blanchet, “Gravitational Radiation from Post-Newtonian Sources and Inspiralling Compact Binaries,” *Living Reviews in Relativity* **9** (2006) no. 4, . <http://www.livingreviews.org/lrr-2006-4>. (Cited on page 115.)
- [211] U. Sperhake, B. Brügmann, D. Müller, and C. F. Sopuerta, “11-orbit inspiral of a mass ratio 4:1 black-hole binary,” *Class.Quant.Grav.* **28** (2011) 134004. [arXiv:1012.3173](#) [gr-qc]. (Cited on page 115.)

- [212] M. Alcubierre, J. C. Degollado, and M. Salgado, “The Einstein-Maxwell system in 3+1 form and initial data for multiple charged black holes,” *Phys.Rev.* **D80** (2009) 104022, [arXiv:0907.1151 \[gr-qc\]](#). (Cited on pages 115 and 117.)
- [213] S. Komissarov, “Multi-dimensional Numerical Scheme for Resistive Relativistic MHD,” *Mon.Not.Roy.Astron.Soc.* (2007) , [arXiv:0708.0323 \[astro-ph\]](#). (Cited on page 115.)
- [214] J. D. Jackson, *Classical Electrodynamics Third Edition*. Wiley, third ed., Aug., 1998. (Cited on pages 118 and 120.)
- [215] J. C. Graves and D. R. Brill, “Oscillatory Character of Reissner-Nordstrom Metric for an Ideal Charged Wormhole,” *Phys.Rev.* **120** (1960) 1507–1513. (Cited on pages 122 and 129.)
- [216] B. Reimann and B. Bruegmann, “Maximal slicing for puncture evolutions of Schwarzschild and Reissner-Nordstrom black holes,” *Phys.Rev.* **D69** (2004) 044006, [arXiv:gr-qc/0307036 \[gr-qc\]](#). (Cited on page 122.)
- [217] H. Witek, V. Cardoso, L. Gualtieri, C. Herdeiro, U. Sperhake, and M. Zilhão, “Head-on collisions of unequal mass black holes in D=5 dimensions,” *Phys.Rev.* **D83** (2011) 044017, [arXiv:1011.0742 \[gr-qc\]](#). (Cited on page 126.)